

**ATOMIC FORCE MICROSCOPY
INVESTIGATIONS OF PEPTIDE
SELF- ASSEMBLY**

Victoria L. Sedman BSc MSc

Thesis submitted to the University of Nottingham
for the degree of Doctor of Philosophy

September 2006

Abstract

The ability of short peptide fragments to self-assemble in isolation as amyloid and amyloid-like structures has prompted their use as model systems for the study of amyloid formation and recently also for their utilisation as novel nanofibrillar material. The atomic force microscope (AFM) is used here to investigate the self-assembly of two peptide systems and the development of strategies to directly manipulate and control the structures they form.

The studies presented in Chapter 2 address the self-assembly of a peptide fragment of the human amylin polypeptide; amylin (20-29). In the opening study we use *ex situ* AFM imaging to characterise the early stages of amylin (20-29) fibril formation. High-resolution images reveal that following an initial lag phase, fibrils displaying a globular appearance are formed, which over time are replaced by flat ribbon-like fibrils with no periodicity displaying a range of polymorphic structures and assemblies. Following on from these findings, we investigate the influence of solution conditions on amylin (20-29) fibril formation utilising *in situ* AFM imaging. Altering the pH and electrolyte composition affords a range of morphologies including, truncated and long branched or unbranched flexible fibrils and globular aggregates.

Following on from this characterisation chapter, in Chapter 3 a strategy to assemble specifically functionalised fibrillar material from chemically modified amylin (20-29) peptides was investigated. Azide and alkyne moieties were successfully coupled to the amylin (20-29) peptides. *Ex situ* AFM imaging and Congo red binding confirmed that the additional steric bulk had no detrimental effects on the fibril forming capacity of the peptides.

Finally, in Chapter 4 the focus turns to the self-assembly of a dipeptide of phenylalanine which corresponds to the core recognition motif of the β -amyloid polypeptide. Here, the AFM is used to study the physical properties of the well-ordered, discrete, hollow nanotubes which are formed. Their chemical stability in organic solvents and considerable thermal stability under both dry and wet heating conditions is revealed. Finally, the use of strong magnetic fields to directly control and orientate the diphenylalanine nanotubes was examined by AFM.

The results presented throughout this thesis demonstrate the versatility of self-assembling peptides for the generation of fibrillar nanostructures that can be directly modified and controlled to generate novel architectures and functionalised well-ordered nanomaterials.

Acknowledgements

I would like to thank my supervisors, Professor Saul Tendler and Dr Stephanie Allen, for their various contributions towards this thesis and their constant support throughout.

There are many within the School of Pharmacy whom I wish to thank for their help and guidance throughout this project. To begin, I would like to thank the other academics within the LBSA for their various contributions and support. Many thanks to Dr Weng Chan and Dr Barrie Kellam for their advice and guidance during the synthesis of the peptides and all in the Medicinal Chemistry group for their help and patience with my steep chemistry learning curve. To Dr Cath Ortori for her assistance and infallible knowledge of mass spectrometry and HPLC. To Dr Xinyong Chen for his help and vast knowledge of the AFM and to Dr Frank Rutten for his assistance with the TOF SIMS data acquisition.

I also wish to thank my collaborators in the diphenylalanine nanotube study Dr Ehud Gazit and Lihi Adler-Abramovich at the University of Tel Aviv, Israel, and Professor Laurence Eaves and Dr Richard Hill in the School of Physics and Astronomy here at Nottingham. Many thanks also to Prof. Richard Bowtell of the School of Physics and Astronomy, for the use of the 3 and 7 Tesla MRI magnets and for his assistance with their use.

I would like to thank all the lovely friends I have made in Nottingham who have shown me there's life outside the PhD world. Especially to those in the LBSA, both past and present, who have made my time in the lab so memorable and have helped me see it through to the end with a smile.

And finally to four very special people. I thank my Mum and Dad for their never-ending support and faith in me. To Dawn for her constant sisterly cheer and wisdom in the ways of thesis survival. And Eleanor for always being there with a smile and a cup of tea and without whom life would have been so very much different.

Contents

LIST OF ABBREVIATIONS	i
-----------------------------	---

1. INTRODUCTION

1.1	Native Protein Structural Hierarchy	1
1.2	Folding pathways.....	2
1.3	Protein misfolding	4
1.4	Amyloid and Disease	5
1.5	General characteristics of amyloid	6
1.5.1	Amyloid structure	7
1.5.2	Amyloid fibril morphology.....	11
1.6	Fibrillisation pathway	12
1.6.1	Driving forces and stabilising interactions	13
1.6.2	Core amyloidogenic fragments	14
1.7	The study of amyloid.....	17
1.8	Atomic force microscopy (AFM).....	20
1.8.1	AFM imaging modes	22
1.8.1.1	Contact mode.....	22
1.8.1.2	Tapping mode.....	23
1.8.1.3	Non-contact	24
1.8.2	Force distance measurements	24
1.9	The characterisation of amyloid by AFM	25
1.9.1	<i>Ex situ</i> and <i>in situ</i> imaging	26
1.9.2	Kinetic studies	27
1.9.3	Investigating the physical properties of amyloid.	28
1.10	Amyloid and the nanoscientist	30
1.11	Thesis outline	32

2. CHARACTERISATION OF AMYLIN (20-29) FIBRILS BY *EX SITU* AND *IN SITU* AFM IMAGING

2.1	Introduction	34
------------	---------------------------	-----------

2.2	Experimental.....	37
2.2.1	Materials	37
2.2.2	Method	37
2.2.2.1	Solid phase peptide synthesis	37
2.2.2.2	Liquid chromatography mass spectrometry	38
2.2.2.3	HPLC.....	39
2.2.2.4	Congo red assay.....	39
2.2.2.4.1	<i>Optical microscopy and birefringence</i>	40
2.2.2.5	<i>Ex situ</i> AFM imaging	40
2.2.2.6	<i>In situ</i> AFM imaging of amylin (20-29) fibrils	40
2.2.2.6.1	<i>Sample Preparation</i>	40
2.2.2.6.2	<i>AFM Imaging</i>	41
2.2.2.7	AFM image analysis.....	41
2.3	Results.....	42
2.3.1	Solid phase peptide synthesis	42
2.3.2	HPLC	43
2.3.3	Congo red assay	45
2.3.4	AFM <i>ex situ</i> imaging	45
2.3.4.1	Preliminary <i>ex situ</i> AFM images.....	45
2.3.4.2	Fibril morphology.....	47
2.3.4.2.1	<i>Amylin (20-29) at t=18 hours</i>	50
2.3.4.2.2	<i>Fibril Variation with Time</i>	51
2.3.4.2.3	<i>Fibril Morphology at 48 hours</i>	55
2.3.5	AFM <i>in situ</i> imaging.....	59
2.3.5.1	Ultrapure Water	61
2.3.5.2	Tris HCl.....	62
2.3.5.3	Potassium chloride	65
2.3.5.4	Magnesium chloride	68
2.3.5.5	Sodium acetate	68
2.3.5.6	Sodium acetate and potassium chloride system	75
2.3.5.7	Sodium acetate and magnesium chloride system.....	78
2.3.5.8	Sodium citrate.....	81
2.3.5.9	Sodium citrate and potassium chloride system	84
2.3.5.10	Sodium citrate and magnesium chloride system	87

2.3.6	Summary of results from <i>in situ</i> imaging	89
2.4	Discussion	90
2.4.1	Preliminary <i>ex situ</i> AFM imaging	90
2.4.2	<i>In situ</i> AFM.....	93
2.5	Conclusion	100

3. MODIFICATION OF AMYLIN (20-29) PEPTIDES

3.1	Introduction	102
3.2	Experimental.....	106
3.2.1	Materials	106
3.2.2	Method	107
3.2.2.1	Solid phase peptide synthesis	107
3.2.2.2	Coupling of azide group to N-terminus.....	108
3.2.2.2.1	2-Azidoacetic acid synthesis	108
3.2.2.2.2	2-Azidoacetic acid coupling.....	110
3.2.2.3	Coupling of alkyne to N-terminus.....	110
3.2.2.4	Side chain deprotection and resin cleavage.....	111
3.2.2.4.1	Reverse-phase HPLC	111
3.2.2.5	Preliminary fibrillisation assay.....	111
3.2.2.6	Copper (I) catalysed 1,3-dipolar cycloaddition reaction assay	112
3.2.2.7	AFM imaging	113
3.2.2.8	Congo red assay.....	113
3.2.2.8.1	Optical microscopy and Birefringence	114
3.3	Results.....	114
3.3.1	Azide- amylin (20-29) peptide synthesis	114
3.3.2	Alkyne-amylin (20-29) peptide synthesis.....	117
3.3.3	Preliminary AFM study of fibrillisation	120
3.3.4	Congo red assay	125
3.3.5	Copper (I) Catalysed Cycloaddition	125
3.3.5.1	1 mM Copper (I).....	125
3.3.5.1.1	<i>t</i> =0 hours.....	125
3.3.5.1.2	<i>t</i> =18 hours.....	131

3.3.5.2	5 mM Copper (I).....	135
3.3.5.2.1	<i>t</i> =0 hours.....	137
3.3.5.2.2	<i>t</i> =18 hours.....	137
3.4	Discussion	142
3.5	Conclusion	146

4. AFM STUDY OF DIPHENYLALANINE NANOTUBES

4.1	Introduction	148
4.2	Experimental	152
4.2.1	Materials	152
4.2.2	Method	152
4.2.2.1	Preparation of peptide samples.....	152
4.2.2.2	AFM imaging and data analysis.....	152
4.2.2.3	Air AFM imaging.....	153
4.2.2.4	Solution AFM imaging.....	153
4.2.2.5	AFM imaging of autoclaved samples.....	154
4.2.2.6	<i>In situ</i> heat imaging	154
4.2.2.7	<i>Ex situ</i> heat imaging	155
4.2.2.8	Optical microscopy imaging of AFM cantilever following high-temperature AFM imaging	155
4.2.2.9	TOF SIMS	155
4.2.2.10	Magnetic anisotropy	155
4.2.2.10.1	<i>Diphenylalanine nanotubes</i>	155
4.2.2.10.2	<i>Amylin (20-29) fibrils</i>	156
4.2.2.10.3	<i>AFM imaging and data analysis</i>	156
4.3	Results	157
4.3.1	AFM imaging of diphenylalanine nanotubes	157
4.3.2	AFM imaging of autoclaved diphenylalanine nanotubes.....	158
4.3.3	<i>AFM in situ</i> heat imaging	162
4.3.4	<i>AFM ex situ</i> heat imaging	162

4.3.5	Optical microscopy images of AFM cantilever following high-temperature AFM imaging	167
4.3.6	TOF-SIMS analysis	167
4.3.7	Magnetic Anisotropy	170
4.4	Discussion	175
4.5	Conclusion	180
5.	GENERAL CONCLUSIONS	181
	REFERENCES	187
	APPENDIX A - ANIMATIONS	217
	APPENDIX B – TOF-SIMS spectra for PDMS	218

List of Abbreviations

3D	Three dimensional
AFM	Atomic force microscopy
Amylin (20-29)	The peptide fragment of the amylin polypeptide corresponding to residues 20 to 29 in the human sequence.
ANS	1-anilinonaphthalene-8-sulphonate
β -Amyloid	β -amyloid polypeptide, generic phrase for the two (β (1-40) and β (1-42)) commonly found peptides in Alzheimer's <i>in vivo</i> amyloid deposits
$\text{BrCH}_2\text{CO}_2\text{H}$	Bromoacetic acid
CD	Circular dichroism
Cu (I)	Copper in the 1 st oxidation state
DCM	dichloromethane
DIPEA	<i>N,N</i> -diisopropylethylamine
DMF	dimethylformamide
EM	Electron microscopy
Fmoc	9-fluorenylmethyloxycarbonyl
FTIR	Fourier transform infra red spectroscopy
HATU	<i>N</i> -[(dimethylamino)-1H-1,2,3-triazolo[4,5-b]pyridin-1-ylmethylene]- <i>N</i> -methylethanaminium hexafluorophosphate N-oxide
HFIP	1,1,1,3,3,3-hexafluoro-2-propanol
HOPG	Highly-ordered pyrolytic graphite
HPLC	High performance liquid chromatography
KCl	Potassium chloride
LC-MS	Liquid chromatography mass spectrometry
MgCl_2	Magnesium chloride
MgSO_4	Magnesium sulphate
MS	Mass spectrometry
$\text{N}_3\text{CH}_2\text{CO}_2\text{H}$	2-Azidoacetic acid
$\text{Na}_3\text{C}_6\text{H}_5\text{O}_7$	Sodium citrate

NaCH ₃ COO	Sodium acetate
NaCl	Sodium chloride
NaN ₃	Sodium azide
NMP	<i>N</i> -methylpyrrolidone
NMR	Nuclear magnetic resonance
pI	Isoelectric point
RP-HPLC	Reverse-phase high performance liquid chromatography
SEM	scanning electron microscopy
SPPS	Solid phase peptide synthesis
tBu	<i>tert</i> -Butyl group
TEM	transmission electron microscopy
TFA	Trifluoroacetic acid
TGA	thermo-gravimetric analysis
TIPS	triisopropylsilane
TNBS	tri-nitro benzene sulfonate
TOF SIMS	Time-of-flight secondary ion mass spectrometry
Tris HCl	Tris(hydroxymethyl)aminomethane buffer
Trt	Tryl-group

Minds are like parachutes - they only function when open.

Thomas Dewar

Chapter

1

Introduction

Proteins have a wide range of functions within a living cell and are crucial to the maintenance of life. The function of proteins depends on the highly ordered three-dimensional structure of their native folded form. The progression from gene to a correctly folded functional protein can be a precarious journey and the cell has developed a variety of safety nets to prevent or limit any detrimental consequences. However, when these safety features fail, the resultant misfolded protein can have disastrous consequences to the cell. A common feature of a group of mammalian disorders collectively called amyloid or conformational diseases is the aggregation of the incorrectly folded proteins into deposits of fibrillar structures called amyloid.

1.1 Native Protein Structural Hierarchy

Proteins have complex structural hierarchy; the functional protein has a structure folded into several levels of organisation. The physical and chemical properties of each amino acid are conferred by the nature of its side chain, and are therefore of considerable importance in the structure and resultant function of the protein. Folding of the polypeptide chain is driven by non-covalent interactions which form between the different amino acids of the polypeptide chain and is influenced by restrictions imposed from the allowable conformations that the peptide bond can adopt, as well as the flexibility of the amino acids and their side chains.

Secondary structure conformations are stabilised via hydrogen bonds between the side chains of one amino acid to that of another in close spatial proximity but not necessarily neighbouring in the primary sequence of the polypeptide chain. The tertiary structure of the protein is the further folding of the secondary structures

into functional domains which are stabilised by the formation of ionic, disulfide and salt bridges between different residues and by further non-covalent interactions, such as van der Waals forces, hydrogen bonds, etc. The various secondary structure orientations and combinations that can be adopted by the polypeptide chain results in a heterogeneous array of possible structures and this explains how folded proteins can have such functional diversity. The highest level of organisation in a protein is the quaternary structure; referring to the assembly of individual folded polypeptide chains into functional proteins that comprise multimeric assemblies.

1.2 Folding pathways

In the cell, the majority of protein folding occurs within the endoplasmic reticulum, which is the primary location of protein synthesis. Several factors are key to the folding process including:

- Packing and internalisation of hydrophobic amino acid side chains and exclusion of the aqueous environment
- Formation of non-covalent interactions (hydrophobic, electrostatic, hydrogen bonds)

The kinetics and thermodynamic properties of some polypeptide chains results in the formation of a folded structure in the C-terminal portion even before the N-terminal has been synthesised. In such circumstances protein folding is a spontaneous event constrained merely by the speed of the ribosomes. However, not all proteins self-assemble due to either the complexity of the folding event or other factors such as environmental conditions. Under such circumstances the newly synthesised polypeptide chain rapidly collapses to form a folding

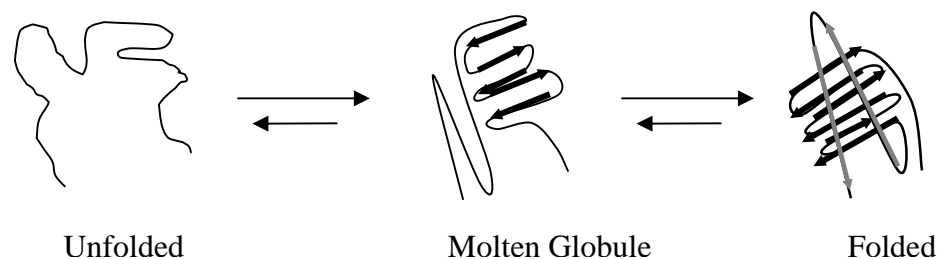


Figure 1.1: Progression of the unfolded nascent polypeptide chain through the molten globule intermediate to the folded functional protein.

intermediate; a partially organised structure called the molten globule. These intermediates enable folding to overcome the various energy and thermodynamic barriers experienced. The molten globule is a group of these intermediates with similar evolving structures rather than a single distinct structure.

The molten globule has several common structural characteristics. It is characterised by a pronounced secondary structure displaying the majority of the structural features of the native protein (figure 1.1). Intramolecular interactions are not properly formed and so the molten globule is lacking in higher order structure and has a loosely packed hydrophobic core. This results in a less compact globular structure than the native folded protein with a radius of gyration 10-30% greater [1]. The less compact structure and exposed hydrophobic core increases the accessibility of the surrounding solvent to the hydrophobic residues. This is a dangerous state for the protein to be in as the hydrophobic surface increases the tendency of the intermediate to form aggregates.

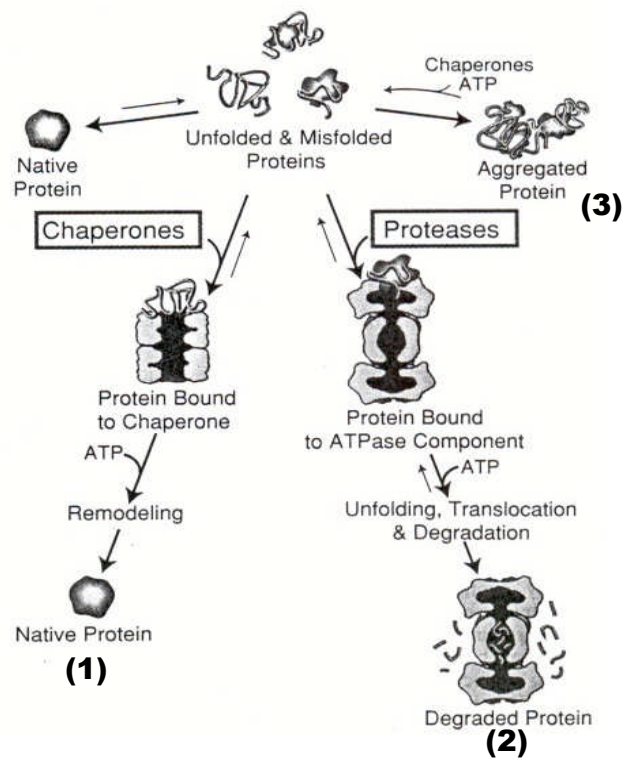


Figure 1.2: Quality control mechanisms employed by the cell to combat unfolded and misfolded proteins. The unfolded or misfolded protein has 3 possible fates in the cell: (1) Refolding by the ATP-dependent molecular chaperones to the correct native protein. (2) Proteolytic degradation or (3) if the misfolded protein escapes detection by the cells quality control system it may aggregate within the cell. Adapted from [2].

To aid the folding process, a group of ATP-dependent catalytic proteins known as molecular chaperones, whose primary role is to prevent protein misassembly and aggregation [3], catalyse protein folding and assist the self-assembly of the molten globules. These catalytic proteins recognise their substrates via the hydrophobic patches exposed in the folding intermediate [4]. By binding the hydrophobic residues they are effectively acting as cloaking devices, masking and preventing the intermediate from forming any unwanted interactions. If the cell deems the misfolded protein to be irretrievable then the proteolytic machinery quickly degrades it. In most instances misfolded proteins are mopped up by the cellular quality control systems. However, certain proteins may escape detection, subsequently forming aggregates of non-functional protein. The exact reason as to why the molecular chaperones and proteases do not recognise these misfolded proteins still remains an area of contention [5].

1.3 Protein misfolding

The key difference between a native protein and its misfolded form is a change in conformation, whether at the secondary, tertiary or quaternary level. Misfolded proteins are unstable within the cell and form an intermediate reminiscent of the molten globule [6]. *In vivo*, the misfolding of a protein may be triggered by any of a number of events such as the result of an intrinsic error in its primary sequence caused during translation, or as a result of mutation in the gene, or misreading of the genetic sequence during transcription. Alternatively it is possible that once the folded protein has been synthesised, a conformational change may be induced by a template misfolded form of the protein (for example the prion protein [7]), or the protein may experience destabilising conditions that lead to either partial or complete unfolding, such as adverse pH, variations in ionic strength and increased temperatures. Specific solvent conditions result in the stabilisation of the molten globule, and consequently the partially folded intermediate retains an exposed hydrophobic core and under these conditions, accumulates, forming insoluble aggregates [8].

During the formation of the correctly folded globular protein, the polypeptide chain collapses to internalise amino acids with hydrophobic side chains (valine,

leucine and isoleucine) within the core of the protein. The resultant structure is soluble in the aqueous environment of the cell or associates with cell membranes. However, if the protein is only partially or misfolded any exposed hydrophobic residues will form interactions with similar surfaces [9]. The hydrophobic interactions can cause any incorrectly folded intermediates to aggregate into fibrillar deposits of varying sizes known as amyloid [10]. A possible role for molecular chaperones in the prevention of amyloid deposition is their ability to induce a conformational change in the precursors of amyloid fibrils [5], preventing their accumulation into toxic insoluble aggregates and instead catalysing the formation of detergent-soluble amorphous and non-toxic aggregates that have been observed under the electron microscope [11].

1.4 Amyloid and Disease

The aggregation and subsequent deposition as amyloid of over 20 different proteins is associated with several mammalian diseases collectively called amyloid or conformational disorders. This group of disorders manifest both as systemic and tissue specific conditions, and include a partial list of human fatal neurodegenerative disorders including Alzheimer's disease, Parkinson's disease and Huntington's chorea, the transmissible spongiform encephalopathies (Kuru, CJD and BSE), Type II diabetes mellitus and other systemic amyloidosis. A common histopathological feature of all these disorders is the deposition of amyloid fibrils as plaques in tissues. These plaques are observed both intracellularly and within extracellular pockets in a range of organs including the liver, spleen, kidneys and brain [12]. Deposition of amyloid is due to several factors and therefore the aetiology of this group of diseases is varied manifesting as genetically inherited, sporadic and infectious disorders (For an excellent overview see Dobson 1999 [13]).

Although the amyloid fibrils are a common factor, it still remains an area of contention whether these aggregates of misfolded protein are the causative agent of the disease state [14]. Current hypothesis suggest that prefibrillar assemblies of the amyloidogenic proteins may actually be the cytotoxic component and directly responsible for cell death [15-17]. Furthermore, the accumulation and aggregation

of these prefibrillar assemblies culminates in the formation of the mature amyloid fibril [17]. There is an increasing amount of evidence supporting this proposal for such neurodegenerative or tissue specific amyloid diseases as Alzheimer's and type-II diabetes mellitus. However, for other systemic amyloidosis it still remains clear that the accumulation of large quantities of insoluble protein aggregates have a direct pathological effect too, causing disruption to organ and tissue functions [18].

Although most amyloid comprises aggregated misfolded or partially folded versions of native protein, not all misfolded proteins become amyloid. In addition, not all amyloid fibrils are associated with disease; in fact several proteins have been shown to form amyloid fibrils *in vivo* with no detrimental effects to the cell and in certain exceptions proves beneficial [19]. Two examples of which are the *Escherichae coli* protein curli [14] and the yeast prion protein Sup35 [20]. Furthermore, amyloid formation is proposed to be a generic feature of the polypeptide chain and that the intermolecular bonds which stabilize amyloid are also intrinsically involved in the folding of the peptide backbone common to all proteins [8, 13, 21].

1.5 General characteristics of amyloid

The formation of the amyloid fibrils is not restricted to a subset of proteins but is in fact a generic feature of the peptide chain and is greatly affected by environmental conditions encountered. Fibril formation is dependent on the accumulation of mis- or partially folded polypeptides exceeding a critical concentration [22] and thus crowding within the cell caused by low clearance or increased production facilitates interactions between misfolded or partially-folded proteins. Variations in the localised environment can affect fibrillisation, such as slight changes in temperature or pH [23].

Although the amyloidogenic proteins are the predominant component of *in vivo* amyloid other molecules are commonly found associated or incorporated within the fibrils. These molecular species are often common to many unrelated amyloid deposits. Among these factors is the serum amyloid-P component (SAP), which is

common to all amyloid found *in vivo* [24] and is proposed to aid amyloid fibrils to escape proteolytic degradation in the cell [25].

Despite the origins of amyloid from a diverse array of proteins, all amyloid fibrils can be characterised by three generic structural criteria. Firstly, amyloid display similar morphologies and are typically long unbranched fibrillar structures. Fibril dimensions are typically less than 10 nm in diameter with lengths in microns scale [26]. Secondly, all amyloid when stained with the azo dye Congo red display a green-gold birefringence under cross-polarised light [27, 28]. This birefringence is directly related to the ordered structural anisotropy of the dye molecule and the core structure of the amyloid fibril. Thirdly, all amyloid have a common structural core; the cross-beta (β) structural conformation.

1.5.1 Amyloid structure

Early X-ray diffraction analysis of amyloid revealed a common diffraction pattern displaying an intense and relatively sharp 4.75 Å meridonal reflection and a weaker and more diffuse equatorial reflection at 9.8 Å [29]. A characteristic diffraction pattern of the cross-beta (β) structural conformation, a common secondary structure conformation found in many proteins [30]. The cross- β structure is a particular folding conformation of β -sheets, in which the constituent β -strands are arranged perpendicular to the fibre axis and the β -sheets arranged parallel. The individual β -strands may be arranged in parallel or antiparallel configurations relative to each other. The 4.75 Å meridonal reflection is generated by the hydrogen bonding spacing between adjacent β -strands, and the face-to-face stacking of the β -sheets gives rise to the equatorial reflection at 9.8 Å. To date all amyloid fibrils including *ex vivo*, *in vitro* and fibrils synthesised from oligopeptides display this common core structure [31].

Further details of the core structure and refinement of a generic amyloid model were gained from synchrotron X-ray diffraction experiments on transthyretin amyloid fibres carried out by Blake and Serpell [32]. The higher-resolution data obtained from the synchrotron X-ray experiments revealed additional very weak meridonal reflections at 3.2, 2.8-9, 2.39-41, 2.22-7 and 2.00-2 Å, which fit a

repeat distance index of 115.5 Å parallel to the fibril axis. Leading to the proposal that the β -strands comprising the cross- β structure of the transthyretin fibril are grouped within this 115.5 Å distance into a novel repeating unit of 24-strands along the axis of the fibril, in which the 24th strand is twisted by 360 degrees relative to the 0th. Corresponding to a well-ordered core structure extending over the entire fibril axis, which is stabilised by hydrogen bonding along the β -sheet helix in which 24 β -strands are arranged with a helical pitch of 115.5 Å, lying parallel to the fibril axis. A molecular model [32] of a single β -sheet helix is presented in figure 1.3 with the helical pitch indicated. The loop regions which join together the individual strands are not shown.

The spacing and intensities of the 10 Å equatorial reflections in the synchrotron X-ray diffraction patterns indicate that a single fibril comprises several of the β -sheet helices stacked face-to-face and perpendicular to the fibril axis. The diffuse reflection is likely to represent the varying distances between individual β -sheets

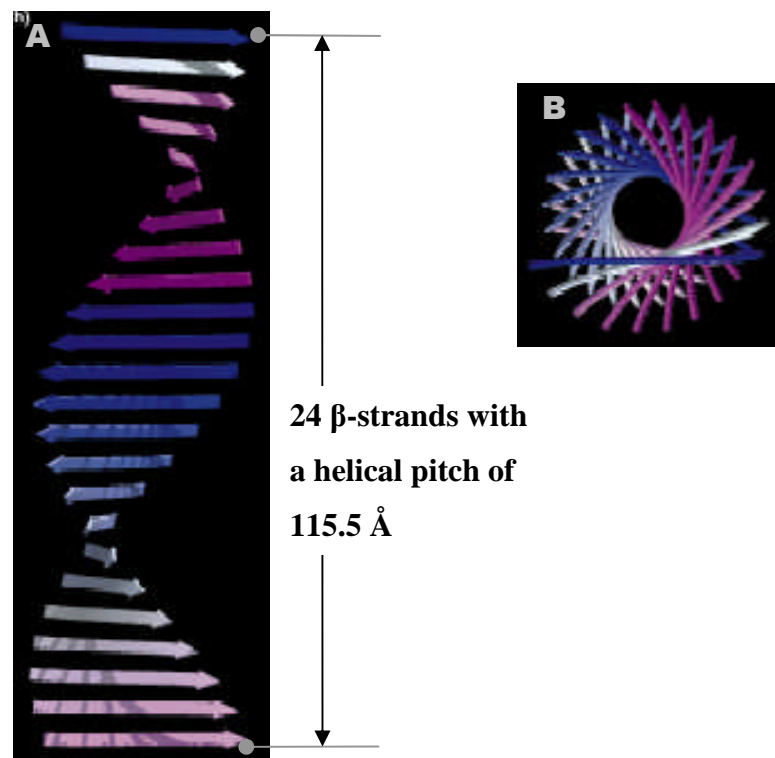


Figure 1.3: An isolated β -sheet helix from the core structure of the amyloid fibril. A: View of the β -sheet helix along the axis of the fibril demonstrating the parallel arrangement of the 24 β -strands within each 115.5 Å helical pitch. **B:** cross sectional view of the β -sheet helix. (Adapted from Blake *et al* '96 [32])

within the fibril, with the distance dependent on the side chain packing of the peptide chains.

Analysis of the X-ray diffraction patterns from other amyloid show similar meridional and equatorial reflections [33, 34]. Consequently it is proposed that this core structure determined for the transthyretin amyloid in which the β -sheets are arranged as a continuous helix configuration within the common cross- β core structure is a generic structural arrangement within amyloid.

Electron microscopy analysis of amyloid combined with the detailed X-ray diffraction data revealed that fibrils display a distinct structural hierarchy with several levels of sub-fibrillar assembly and structural organisation [35-37]. The fibrillar structure comprising several β -sheet helices stacked face-to-face is designated the protofilament and is the lowest structural level of amyloid observable by EM and AFM [35]. Several protofilaments are found coiled together, in the majority, arranged around a hollow, core or channel [35, 38] to form a protofilament. The protofilament is found aggregated together by further coiling or by lateral association into fibrillar deposits. A schematic representation of the various structural levels within amyloid is presented in figure 1.4.

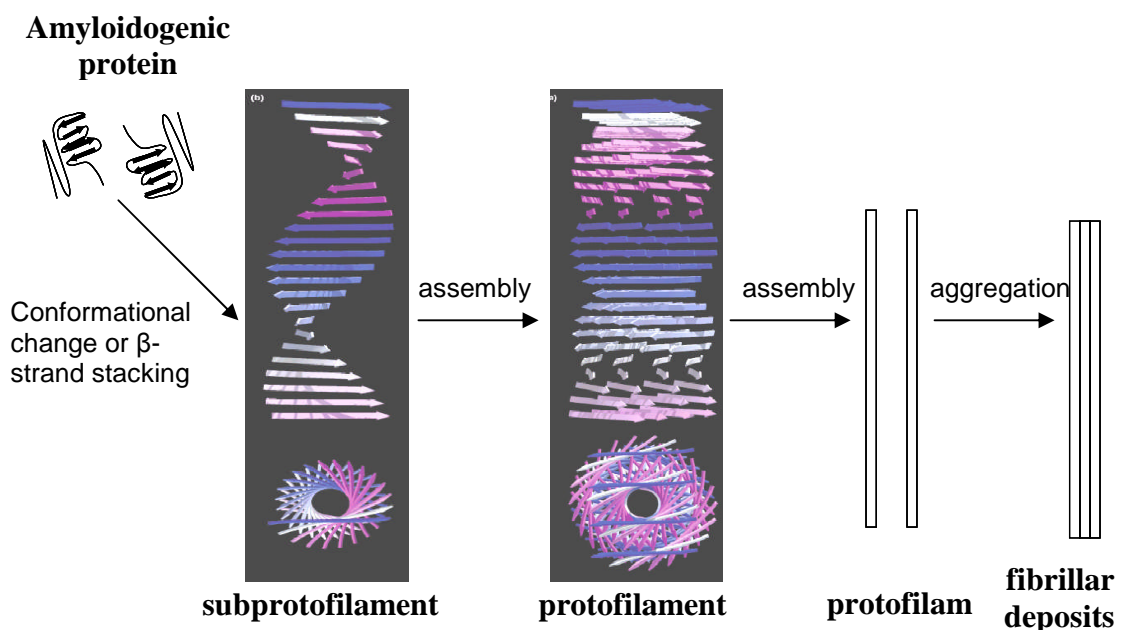


Figure 1.4: Schematic of the structural hierarchy of the amyloid fibril. The cross- β structure of the amyloid fibril includes a hollow channel through the centre of the fibril. The structure of the fibril comprises several well-ordered sub-fibrillar levels.

The core β -sheet structure and hierarchical organisation are proposed to be generic characteristics of amyloid, however the exact number and orientation of protofilaments within the fibril is protein specific and dependent on the sequence of the polypeptide chain. Moreover, not all of the polypeptide chain is incorporated within the folds of the ordered β -sheets, consequently the superfluous and connecting regions influence the interactions and packing arrangements between protofilaments [39, 40]. Furthermore, the orientation of the β -strands within the individual β -sheets is protein specific and may be either antiparallel or parallel.

Summarised in table 1.1 is a list of the suggested structural hierarchy of five different amyloid fibrils as determined from a selection of X-ray diffraction, NMR, EM and AFM studies. In illustration, the proposed structural arrangement

Protein	Associated disease	Mature proto-filament diameter	Structural hierarchy within the mature protofilament	Example references
Aβ-peptide (1-40) & (1-42)	Alzheimer's disease	6-10 nm	5-6 protofilaments 3-5 nm in diameter	[41, 42]
Amylin	Type II diabetes mellitus	8-13 nm	2 to 4 protofilaments 3-5 nm in diameter	[43, 44]
Ig light chain	Light chain amyloidosis	7-8 nm	5 protofilaments 2-3 nm in diameter	[45]
Lysozyme (Asp67His variant)	Autosomal dominant hereditary amyloidosis	8-10 nm	5 protofilaments 3 nm in diameter	[46]
Transthyretin (full length & fragment)	Senile systemic amyloidosis	13 nm	4 protofilaments of 4-6 nm in diameter arranged in pairs	[36, 47]

Table 1.1: Summary of the structural information obtained for five amyloidogenic proteins. Proteins are listed with the associated disease state. The range of dimensions of the mature protofilaments typically observed and the structural hierarchy of species comprising the protofilaments are presented in columns 3 and 4. Examples of the references citing experimental data in support of the structural information are presented in the final column.

models for the polypeptide chains of two dissimilar amyloid proteins within the common cross- β structure of their fibrils are discussed below.

The proposed structural model for protofilaments of the human amylin polypeptide suggests that the polypeptide chain folds in an S-shape with 3 β -strands formed by residues 12-17, 22-27 and 31-37. β -turns allow the polypeptide to fold into the S-conformation with long-range interactions between residues F15, F23 and Y37 [48]. Stacking of the β -strands perpendicular to the fibril axis gives 3 in-register superpleated β -sheets which run parallel to the fibril axis in a cross- β conformation. The S-shaped fold gives rise to a small left-handed rotational twist in the β -sheet [44, 49, 50]. Protofilaments comprising 3 protofilaments arranged with a left handed helical twist are the predominant species [43]. While other structural models have been suggested for the configuration of the β -strands, currently this model is in strongest agreement with experimental observations.

By comparison the model of the fibrils formed by A β (1-40) and (1-42) proteins suggests that protofilaments (>2 nm in diameter) are assembled from pairs of β -sheets. The β -sheet is composed of two β -strands formed from residues 25-30 and 30-40 in an anti-parallel arrangement [41, 51-53]. A β -turn at residues 12-24 enables the two β -strands to form two, in-register, parallel β -sheets in contact via side chain interactions giving rise to the characteristic cross- β X-ray diffraction patterns [54]. The folding of the polypeptide chain is such that the protofilament has a hydrophobic core with one hydrophobic face. EM and X-ray analysis suggest that five or six protofilaments aggregate, most likely driven by hydrophobic forces, into a helical arrangement around a central core channel, 5.5 nm in diameter [38, 41].

1.5.2 Amyloid fibril morphology

As noted earlier, a generic structural feature of amyloid is a long, unbranched fibrillar structure. There is however, a degree of heterogeneity displayed by the morphologies of fibrils formed not only by different proteins but also within the fibril population formed from the same protein species. EM and AFM studies of

amyloid have revealed the polymorphic nature of the amyloid fibril; insulin amyloid forms helically twisted fibrils with four different morphologies dependent on the number of protofilaments present [55], the fibrils formed by lysozyme Asp67His are wavy [26], whereas both human amylin and human A β amyloid exhibit similar heterogeneous polymorphic mature fibrils that may be helical, with left-handed coiling and axial cross-over periodicity of 25-50 nm, twisted ribbons or as ribbon-like arrays [43, 56, 57]. This apparent polymorphic nature is thought to arise not only due to the varying numbers of protofilaments incorporated within the amyloid fibril but may also be directly influenced by environmental conditions [23].

1.6 Fibrillisation pathway

The rate of protein aggregation is greatly dependent on several factors intrinsically linked to the amino acid sequence of the polypeptide chain. With importance on amino acid size, propensity to form β -sheets as well as the hydrophobic nature of the polypeptide sequence [58-60] and growing evidence in favour of aromatic stacking interactions [61-63].

Kinetic studies of amyloid formation indicate a two phase nucleation-dependent mechanism, in which an initial lag phase occurs followed by a period of rapid growth and elongation of fibrils [64-66]. The initial step requires the formation of a nucleus and therefore is dependent on protein concentration and suitable environmental conditions. Following the lag phase, assembly and growth of fibrils occurs rapidly at an exponential rate, limited merely by the availability of the protein.

In the initial lag stage of fibril formation, dimeric or low-oligomeric building blocks further oligomerise to form prefibrillar structures [57, 66-68]. Aggregation and ordered assembly of these structures result in the formation of the protofilament and consequently assembly into protofilaments and fibrillar species.

Seeding of preformed fibrillar aggregates into protein/peptide solutions eliminates the lag phase [69, 70]. Interestingly, 'cross-seeding' of different proteins can

occur, though the level of diversity in the amino acid sequence constrains the efficiency of seeding [70-71]. This sequence specificity may be explained by the long-range interactions that stabilise the amyloid structure. This apparent cross-seeding is likely to explain the species barrier phenomenon associated with the transmissible spongiform encephalopathies; the level of transmission is lowered between different species [73].

1.6.1 Driving forces and stabilising interactions

A fundamental question in amyloid formation which remains in part unanswered focuses on the identification of the driving forces behind self-assembly and aggregation. Not only will answers to this question complete our understanding of amyloid formation but most importantly will aid the development of therapeutic strategies to combat the degenerative amyloid diseases.

Given that the formation of amyloid is a generic feature of the polypeptide chain, it seems highly probable that the interactions and forces involved are intrinsic to the polypeptide backbone. Consequently, the interactions which govern correct protein folding may also be involved in the self-assembly and aggregation of the well-ordered amyloid, considering the same building block is involved in both [13].

Amyloid formation is dominated by a specific pathway of non-specific interactions involving non-covalent molecular recognition and self-assembly. The aggregation pathway commences with the attraction of misfolded or partially folded polypeptide chains by electrostatic and hydrophobic interactions. Regions of the polypeptide chain that would normally be internalised may, in the non-natively folded polypeptide chain, be exposed to the surrounding solvent and thus prone to aggregation driven by such forces [74].

There is also growing evidence in support of the role of aromatic residues in the ordered self-assembly process. Aromatic interaction between the planar ring side chains of the aromatic amino acids are often observed in protein-protein recognition events [75]. The attractive forces between aromatic rings form

interactions that are predominantly entropy driven and thereby provide some of the energetic contribution during the fibril assembly process [60, 62, 75, 76,]. In addition, π - π stacking requires that the planar aromatic side-chains have restricted geometries relative to one another [75]. Consequently, aromatic interactions may also contribute to directionality and ordered arrangement of the polypeptide chain within the β -sheet core.

The aggregated polypeptide chains form oligomeric species which, once reaching a specific size, act as nuclei for the elongation of the fibril. The size of oligomer is entirely protein and condition dependent; oligomers of full-length amylin form oligomers 2 to 6 nm in height before elongating into protofilaments [64], by comparison pre-fibrillar oligomers of A β (1-40) are 4-6 nm in height [56, 77].

Several mechanistic models have been proposed to describe the exact process by which the individual polypeptide/peptide chains form the oligomeric nuclei [66, 78-81], with further suggestion that the mechanism may be amyloid species specific [82]. However all are in agreement that protofilament assembly involves either the longitudinal association of these pre-fibrillar structurally-ordered oligomeric species [64, 83] or by the addition of monomers to the ends of the growing fibril [66].

Once formed the elongating fibril exhibits considerable stability, the major contributor of which is the hydrogen bonding network which exists between individual β -strands within the β -sheet which thus extends along the core structure of the fibril.

1.6.2 Core amyloidogenic fragments

The quest to identify a common factor in the amyloid protein responsible for fibril formation has in part focussed on the identification of sequence motifs within the native proteins. The synthesis of large aggregation prone polypeptide chains is both difficult and expensive. Therefore, shorter fragments of these amyloidogenic polypeptides are often studied as model systems to understand the interactions and mechanisms which govern amyloid assembly [84].

Although no common sequence homology has been demonstrated, key amyloidogenic regions within the individual polypeptide chains have been identified. These sequences are crucial for amyloid formation and intrinsically form part of the β -sheet core of the fibril [85]. In the native, correctly folded polypeptide chain these aggregation ‘hot spots’ are likely to be hidden away within the hydrophobic core of the protein with their side chains involved in stabilising interactions [85].

These amyloidogenic sequences have been identified in the majority of amyloidogenic proteins largely utilising mutagenic (proline and alanine) scanning and through biophysical examination of structures formed by short peptide sequences [86-88]. The short peptide fragments which include the amyloidogenic motifs readily self-assemble into fibrillar structures under a range of conditions. Generally these fibrillar structures still retain the 3 generic amyloid criteria but may often vary, dependent on the size of the fragment, in fibril dimensions and morphology (in example [88-91]). Therefore it may be surmised that the information required for amyloid formation is retained within these key amyloidogenic regions that are incorporated within the cross- β core of the fibril.

For many of the amyloidogenic proteins, there may be several short peptide sequences which are capable of forming amyloid-like fibrils in isolation. However, within most of the proteins there is a key sequence of amino acids without which the whole protein will not form amyloid; referred to as the ‘core amyloidogenic’ motif. For example, rat amylin has considerable sequence homology to the human protein differing by only 6 amino acids, though rat amylin does not form amyloid. Five of the six variations in amino acid sequence between the two homologues have been pinpointed to a 10 amino acid stretch corresponding to residues 20 to 29. Analysis of this region revealed that the central β -strand (residues 22 to 27) within the core cross- β structure of the fibril was formed by this section. Consequently the sequence NFGAIL (residues 22 to 27) has been designated the minimum core amyloidogenic region for amylin.

The information derived on the properties and characteristics of the short fragments provides detail of the interactions which govern the assembly of that specific amino acid sequence. However, when contemplating the assembly interactions which govern the whole polypeptide chain these individual findings must be considered in the context of the influences imposed by the surrounding polypeptide chain. Especially when taken into account that fibrillogenesis of many shorter fragments often require non-physiological conditions. For example, the Alzheimer's polypeptide was recently identified to have a core recognition motif of a simple phenylalanine dipeptide [86]. This dipeptide is the smallest fragment known to self-assemble into fibrillar structures. However, the fibrillar structures that form are large nanotubes (>50 nm in diameter) rather than the smaller biofibrils formed by the full-length A β polypeptide. In fact the smallest fragment of the A β polypeptide known to form biofibrils similar in morphology to the full-length polypeptide fibrils corresponds to residues 16-22, which contains the core diphenylalanine sequence (residues 19-20) [89] clearly demonstrating that the surrounding amino acid sequence can greatly influence the self-assembly packing behaviour.

Although no common motif or homologous amino acid sequence within the amyloidogenic proteins has been identified, in most instances the core amyloidogenic regions often have a greater propensity for certain amino acids; especially residues which are recognised to preferentially form β -sheet structures. In particular the aromatic amino acids such as phenylalanine and tyrosine have a high prevalence in the β -sheet folds. This high incidence of aromatic residues is not thought to be coincidental but may be intrinsic to the driving forces behind the self-assembly pathway of amyloid [62, 92]. In fact some success has been reported with controlling the formation of amyloid by the A β polypeptide using π -stacking inhibitors [93, 94].

However, in a study by Tracz *et al* [95] the effect of replacing Phe23 from the core amyloidogenic region of the amylin polypeptide with leucine or alanine revealed that the charge, size and propensity to form β -sheet were much more influential than retaining the aromatic residue in determining whether fibrils formed from the peptide. This suggests that the driving force is not purely that of

π - π stacking, certainly in amylin, but that aromatic interactions may still play a key role in both the kinetics of self-assembly and structural arrangement within the ordered cross- β core [48].

1.7 The study of amyloid

Many of the advancements made in the study of amyloid have come to fruition due to the development of techniques to isolate *in vivo* amyloid, and from studies of the fibrils formed *in vitro* from polypeptide chains and shorter peptide fragments. The fibrils formed *in vitro* have been demonstrated to be ultrastructurally similar to fibrils found *in vivo* [96].

Presented in table 1.2 is a summary of the most commonly represented techniques utilised in the study of amyloid. Although this list is not exhaustive, the techniques outlined demonstrate the vast wealth of information that has been and can be determined on the structure, properties and kinetics of amyloid fibrils. Evidence obtained from individual techniques may stand alone, however it is rarely taken so and conclusions are generally drawn in context and corroborated by the findings from investigations using a variety of experimental techniques.

This refined list of techniques may be split into those evolved to study amyloid by the histologist and those by the biophysicist. The histology approach to amyloid determination and investigations relies primarily on the use of specific staining and fluorescent labelling. In the majority these have been established as techniques for the study of *in vivo* or *ex vivo* amyloid and subsequently for the detailed study of *in vitro* amyloid too. Congo red dye and the fluorophore Thioflavin T both require the ordered beta-sheet conformation of the amyloid backbone to bind [27, 28, 97, 98]. The green gold birefringence observed under polarised light of Congo red stained samples is seen as a bench mark indicator for the presence of amyloid. Thioflavin T fluorescence is commonly used for kinetic studies of the growth of amyloid in solutions as well as the effects of solution conditions or inhibitors/promoters on the kinetics of fibrillisation.

Technique	Experimental evidence obtained	References
Congo red	<ul style="list-style-type: none"> - Histopathology stain for amyloid - Stained amyloid characteristically displays a green gold birefringence under polarised light 	[27, 28]
Thioflavin T fluorescence	<ul style="list-style-type: none"> - Specific binding to β-sheet structure of amyloid results in fluorescence of the dye - Measurement of fibril growth in solution - Kinetic measurement assays 	[97-99]
X-ray diffraction	<ul style="list-style-type: none"> - Fibril ultrastructure 	[32-34, 54, 100]
Nuclear magnetic resonance	<ul style="list-style-type: none"> - Fibril ultrastructure 	[101-103]
Circular dichroism or Fourier transform infrared spectroscopy	<ul style="list-style-type: none"> - The secondary structures of protein/fibril - Observation of conformational change - Measuring the rate of fibrillogenesis as a function of changing structural conformation 	[8, 104]
Electron microscopy	<ul style="list-style-type: none"> - Study of fibril morphology - <i>Ex situ</i> kinetic study of fibrillogenesis - <i>Ex situ</i> study of environmental conditions effects on fibril formation/morphology - <i>Ex situ</i> study of thermal and chemical stability 	[33, 37, 105]
Atomic force microscopy	<ul style="list-style-type: none"> - Study of fibril morphology - Direct kinetic measurements of fibrillogenesis - <i>In situ</i> study of environmental conditions effects on fibril formation/morphology - Direct observation of thermal and chemical stability - Mechanical properties (image and force measurements) 	[39, 40, 44, 56]

Table 1.2: Summary of the most commonly used techniques for the study of amyloid. Summarised with each technique is a list of the information that can be determined experimentally and examples of work citing such techniques.

The biophysical approach to investigating amyloid seeks to resolve three fundamental issues: fibril structure determination, the mechanism of fibril formation and understanding the kinetics of fibril formation.

X-ray diffraction and nuclear magnetic resonance (NMR) imaging have played an important role in elucidating the ultrastructural organisation of the amyloid fibril, providing detailed evidence on the structural hierarchy exhibited by amyloid and revealing the core cross- β spine common to all amyloid. However, difficulties in forming crystals of pure fibrils for x-ray diffraction analysis has proven a limitation to the extent of information obtained and strategies for improved crystal growth are ongoing. The use of computer modelling and molecular dynamic simulations utilises the information derived from X-ray diffraction patterns and NMR data to generate amyloid structural models and simulations of events during fibrillisation [92, 106, 107].

Circular dichroism (CD) and fourier transform infra red spectroscopy (FTIR) can provide information on the secondary structure conformations of proteins in solution. These techniques have been used to map the changing conformations often observed in solutions of proteins as they aggregate to form amyloid fibrils; from random coil conformations and α -helix content to the characteristic rich β -sheet of amyloid formations. The influence of solution conditions and the presence of potential inhibitory factors on amyloid formation can also be investigated.

The electron microscope (EM) and the atomic force microscope (AFM) are the most widely used instruments for in-depth study of amyloid fibril morphology. Historically, amyloid from a variety of diseased tissue was first observed by electron microscopy in 1959 [10]. With the development of *in vitro* fibrillisation protocols, both the EM and AFM provided detailed studies of the polymorphic nature of fibrils self-assembled from both full-length polypeptides and shorter amyloidogenic peptide sequences. This has enabled the fibril pathway and morphological changes to be studied over a time course allowing events during the fibrillisation pathway to be visualised. Furthermore, morphological studies of the influence of environmental conditions on fibrillisation have provided

information on the interactions which govern self-assembly of the polypeptide and peptide chain into amyloid.

The EM (including scanning electron microscopy (SEM) and transmission electron microscopy (TEM)) is capable of generating very high-resolution images of biological samples. However there are limitations to studying amyloid using the EM: firstly, the requirement for extensive sample preparation in which samples must be dried and stained before imaging, and secondly the inability to image dynamic processes *in situ*; the images generated are of dehydrated samples in their non-native state. By comparison sample preparation for the AFM is extremely easy, requiring physisorption of a sample to a surface. Furthermore, and most importantly, dynamic events such as fibrillogenesis can be directly visualised by liquid imaging; samples are physisorbed to a support substrate and imaged in a liquid environment thus maintaining the sample in a near-native hydrated state. A drawback to imaging in solution using the AFM is that the sample must be sufficiently immobilised to the surface. Therefore conditions which promote physisorption of the sample to the substrate surface must first be identified.

The study of amyloidogenic peptide self-assembly presented in this thesis has primarily utilised the AFM to study the morphology and dynamic behaviour of amyloid biofibrils and nanotubes. Outlined in the sections below is a brief description of the principles of AFM and a discussion of the advances made in understanding of amyloid using the AFM.

1.8 Atomic force microscopy (AFM)

The atomic force microscope (AFM) [108] is a surface biophysical probe capable of generating high-resolution topographical images of surfaces and exploring the interactions between molecules within a sample. In addition force spectroscopy experiments can be performed using the AFM whereby the forces between the tip and sample or interactions between individual molecules can be investigated.

The principle of AFM imaging is analogous to a record player where sound is generated when the stylus moves across the surface of the record. In the AFM, a stylus is attached to a flexible cantilever; at the end of the stylus is a sharp tip, which interacts with the surface of the sample. As the cantilever raster scans backwards and forwards across the surface of the sample, a map of the surface features is generated in the x and y direction. In the simplest imaging method, to build up a topographical map of the sample surface details of variations in the height of the surface are recorded by the movement of the cantilever in the z direction, thus producing a two-dimensional image of the surface topography. The deflections of the cantilever are monitored with atomic-scale sensitivity by an optical lever system; a laser beam directed onto the cantilever is reflected via a mirror to a position sensitive photodiode. A piezoelectric ceramic scanner controls the motion of the cantilever by an electronic feedback mechanism. Presented in figure 1.5 is a schematic of the typical AFM set up.

As the probe raster scans across the surface, the flexible cantilever undergoes deflections due to the attractive and repulsive forces experienced by the tip as a result of the overlapping electron orbitals between the atoms of the sample and the

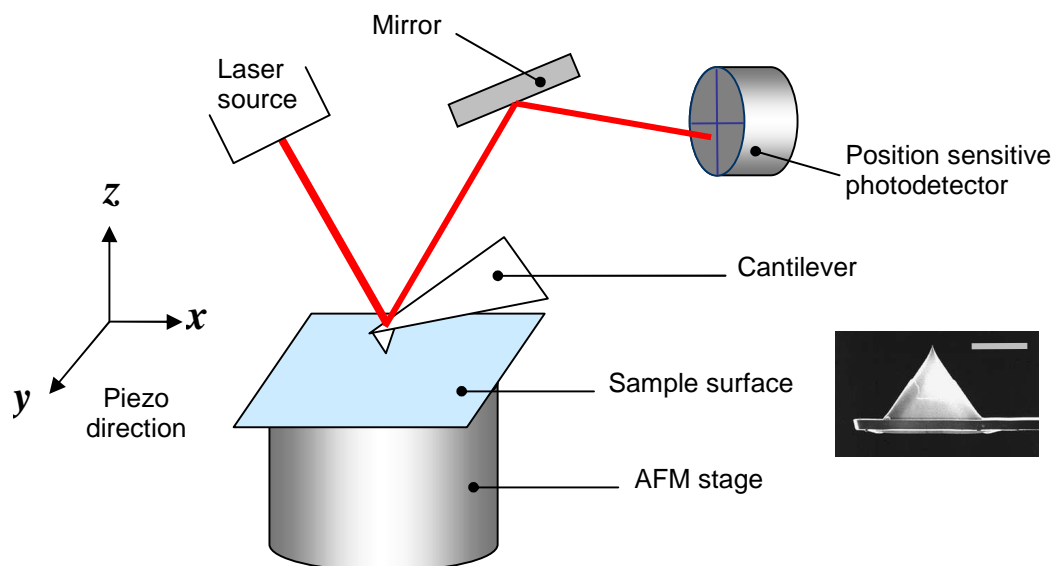


Figure 1.5: Schematic representation of the AFM set up. Image inset is a scanning electron micrograph of the tip at the end of an AFM cantilever (Image from Olympus Corp., scale bar represents 2.4 μm).

tip. Consequently the deflection of the cantilever is a measure of the forces experienced by the tip. AFM cantilevers for biological imaging are very flexible structures with spring constants of less than 1 N/m for contact mode and 2 to 42 N/m for tapping mode imaging. Typically cantilevers are silicon or silicon nitride with lengths ranging from 100-250 μm and tip apexes with radii of curvature of 5 to 40 nm. The optimum resolution of an image is greatly affected by the shape and apex of the tip. Currently the most commonly used commercially available tips are oxide-sharpened pyramid shaped (see inset in figure 1.5). However, the low aspect ratio and shape of these tips may result in the contact occurring between the sides of the tip and the sample feature before the apex of the tip. This causes a tip broadening artefact whereby features appear larger than their true size, in addition two structures lying adjacent might be perceived as one. A solution to this limitation is under development, in which long and narrow carbon nanotubes with high aspect ratios, replace the pyramidal tip [109].

1.8.1 AFM imaging modes

In the conventional AFM, there are three operating modes for image acquisition; contact mode, tapping-mode and non-contact mode. Each mode functions within the different force regimes (attractive and repulsive) of the tip-sample interaction. A brief description of these operating modes is discussed below.

1.8.1.1 Contact mode

In contact mode, the AFM probe is in constant contact with the sample surface. As the tip or sample is raster scanned relative to one another, the repulsive contact forces between the probe and sample cause the cantilever to bend. The z-feedback loop monitors the cantilever deflection and constantly adjusts the height correcting for the deflection and maintaining a constant force on the sample. Images mapping the topography of the surface are generated either by monitoring the changes in z-piezo height or by the movement of the laser caused by changes in the deflection of the cantilever as it is raster scanned across the surface.

The high resolution and fast image acquisition processes used in contact mode are typically associated with the application of high forces and therefore it is

preferentially suited for imaging hard, non-deformable samples. When imaging soft samples in contact mode, such as biomolecules, the lateral forces exerted by the tip can sweep material from the sample surface. Furthermore during air imaging, the adhesive capillary force between the adsorbed liquid layer of the surface and the tip can cause an overall increase in force on the sample [110] which is more likely to deform a soft biomolecular material.

1.8.1.2 Tapping mode

In tapping mode the cantilever is oscillated at or near its resonance frequency (200-400 kHz in air and approximately 10 kHz in liquid) at amplitudes of tens of nanometres when not in contact with the surface. As the tip is moved towards the sample it gently taps the surface as it is raster scanned in an xy direction, only briefly coming into contact with the fragile surface [111-113]. In tapping mode the AFM is operating in both the repulsive and attractive regions of the tip-sample interaction. Variations in the topography of the sample surface result in changes in the oscillation amplitude of the cantilever; lower features will cause increased amplitudes, conversely raised areas result in dampening of the oscillation amplitude. Any resultant variations in the oscillation amplitudes are monitored by a feedback circuit which maintains the amplitude of the freely oscillating cantilever at a constant pre-set value by adjusting the z piezo. The problematic lateral forces of contact mode imaging are no longer experienced as the applied force is periodic and vertical as the tip intermittently comes into contact with the surface. Consequently, tapping mode is the preferred imaging mode for biomolecules and as such all AFM images presented in this thesis have been generated in this operating mode.

Further information about the sample can be achieved by interpretation of the phase shift experienced by the oscillating cantilever as it raster scans across the sample surface. In free air the oscillation amplitude of the cantilever is pre-set at a constant piezo drive voltage, however as the probe raster scans the surface there is a phase lag in the oscillation relative to the driving signal due to tip-sample interactions. The phase lag is recorded and mapped as an image and is referred to as phase imaging [114]. The phase data can provide additional topographical

detail and under certain tapping regimes information can be elucidated on the visco-elastic and adhesive properties of the surface [115-117].

1.8.1.3 Non-contact

In non-contact mode the oscillating tip (at its resonant frequency) never actually touches the sample but is instead kept at a small distance above the sample surface within the long-range van der Waals attractive forces of the tip-sample interaction [118]. As the tip is raster scanned across the surface, gradients in the force are detected by changes in the tip resonant frequency or oscillation amplitude of the cantilever. The major advantage of non-contact AFM is that the technique is non-destructive as the tip does not make contact with the sample, a necessary factor when studying easily deformable biomolecules. However, the attractive forces involved are very small (as little as 10^{-12} N) and less sensitive to probe-sample separation. Consequently, the images generated generally have lower spatial resolution. This is particularly problematic in non-contact imaging in liquid where at small tip-sample distances the van der Waals forces are greatly reduced by more than two orders of magnitude [119, 120].

1.8.2 Force distance measurements

In addition to the imaging capabilities of the AFM, quantitative force measurements of tip and sample interactions can be generated [121]. In an AFM force experiment, the probe is moved vertically at a constant z-piezo velocity towards a sample surface until contact is made and then retracted away. By measuring the deflection experienced by the cantilever a force-distance plot can be generated provided the spring constant of the cantilever is known. Shown in figure 1.6 is a typical force-distance curve in which the y axis is the cantilever deflection force (measured in nN) versus the distance travelled by the z-piezo (measured in nm) on the x axis.

The AFM is one of few techniques (others include optical tweezers, biomembrane-force probe) in which force-distance curves can be generated for single molecule rupture events. This allows the mechanical properties such as individual molecule flexibility and stiffness to be quantified. Furthermore detailed

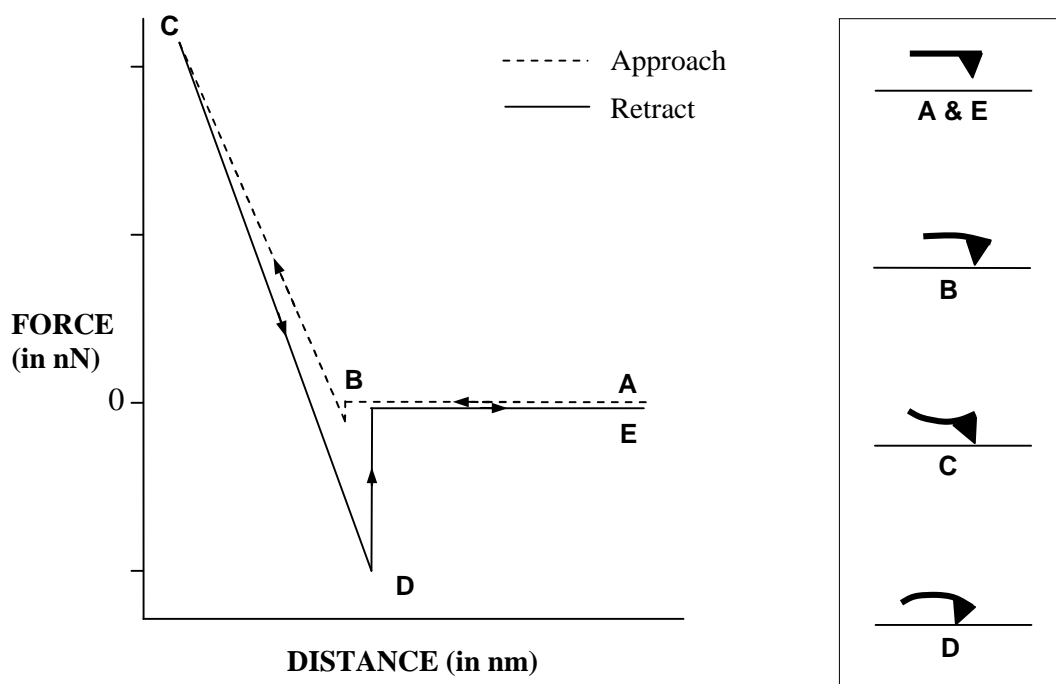


Figure 1.6: Schematic of a typical force-distance curve. **A** The tip approaches the sample surface. At **B** there is “jump to contact” due to attractive van der Waals forces. The cantilever bends as the tip continues forward until point **C**, the predefined maximum load. The tip is retracted and point **D** is the “pull off” force as the tip disengages. At **E** the tip returns back to the start position away from sample contact.

investigations of protein or peptide folding and unfolding events may be mapped as well as protein-protein interactions and protein-ligand binding. For excellent reviews detailing the scope of biomolecular AFM force measurement experiments see [122-124].

1.9 The characterisation of amyloid by AFM

The AFM has extensively been utilised in the study of amyloid and has made possible many advances in our understanding of amyloid. Possibly the greatest achievement facilitated by the AFM is the study of amyloid in a hydrated environment; enabling the direct visualisation of dynamic events during fibrillisation.

The AFM can generate images of samples in solution at static time points as well as dynamically generating a time-lapse sequence of images of fibrils nucleating

and elongating; enabling the study of rates of fibrillogenesis, as well as mapping the progression of variations in morphologies and the development of structural hierarchy. Furthermore, events can be studied under conditions closely exemplifying the native physiological state.

1.9.1 *Ex situ* and *in situ* imaging

Tapping-mode AFM has been successfully utilised for high-resolution imaging in both air (*ex situ*) and in solution (*in situ*) of fibrils formed by a range of amyloidogenic polypeptides and their shorter peptide fragments, including A β [56, 77], amylin [44, 87, 125], Ig light chain [45, 126], and lysozyme [39] as well as the non-disease related Sup35 [81]. Detailed morphological studies can be made and information derived on the helical periodicity, height, and persistence length of the fibril under various environmental conditions [57, 127]. AFM images of β 2-microglobulin have demonstrated that variations in pH promote different fibril morphologies from highly flexible worm like chains to long straight unbranched fibrils and rod-like structures [128, 129]. *In situ* imaging allows the morphology of a fibril in its hydrated state to be studied, thereby enabling the direct visualisation of a fibril in a state near to that expected *in vivo*.

For the acquisition of stable high-resolution images *in situ* the specimen must be sufficiently immobilized to the sample surface. This is often a limiting factor in the imaging of biological samples using tapping mode AFM as suitable conditions must be identified. Various strategies are employed to promote sample immobilisation, including a choice of positively or negatively charged substrate, or by altering the buffer conditions; adsorption is promoted by altering the sample or surface charge through the addition of monovalent or divalent ions [111, 130, 131]. Alternatively samples may be covalently attached to a functionalised surface [132].

The substrate of choice for the study of amyloid is predominantly mica due to its atomically flat surface [40, 56, 133-135]. Other substrates which have been utilised include gold [136] and highly-ordered pyrolytic graphite (HOPG). The atomically flat HOPG is preferentially utilised for orientated and template-directed growth of fibrils due to its crystalline nature [137, 138]. However, it has

been noted that fibrils grown on a substrate support during *in situ* AFM imaging can display different morphologies to counterparts grown in solutions, suggesting that for some systems fibril formation is surface-dependent [135].

Particularly pertinent to the study of amyloid is the ability to mimic the *in vivo* environment. Not only by imaging fibrils at physiological conditions but also by mimicking biomimetic surfaces. Amyloid is believed to preferentially form at the cell membrane where their prefibrillar assemblies act as pores within the membranes leading to disruption of the membrane and loss of cell activity [139-141]. Dynamic AFM imaging of lipid covered substrates in the presence of human amylin and A β (1-42) polypeptide solutions revealed, over a time course, the formation of holes in the lipid rafts which resulted in membrane disruption. Following a lag time fibrillar structures were also observed within the images [140, 142].

An antibody, known as anti-amyloid antibody W01, has been shown by AFM investigations to bind not only to oligomeric species (in this example to β 2-microglobulin prefibrillar oligomers) but also some morphologies of the mature fibril. Indicative therefore that the binding epitope for the antibody is freely available on the oligomeric species but may be masked in some mature fibril morphologies, suggesting fibril self-assembly may follow several distinct pathways [128, 143].

1.9.2 Kinetic studies

The ability to image dynamic events by AFM has facilitated one of the most important advances in the study of amyloid kinetics. The direct observation by tapping mode AFM using time-lapse liquid imaging of amyloid fibril formation [44, 56]. The rates of fibril growth can be measured and correlated with changing morphologies, in addition the direction of growth can be studied [44, 57]. Snapshot events during fibrillisation can be observed using *ex situ* AFM which detail the changing morphology of the fibril and prefibrillar species [135]. Seeding experiments have been performed on solutions of A β polypeptide whereby the effects of pre-formed aggregates on fibril growth can be directly visualised; providing insights into the fibrillisation pathway [57, 144].

The recent development of high-speed AFM capable of generating whole topography and phase images in millisecond rather than minutes at high resolutions [145, 146] has enabled the AFM for the first time to image biological processes in real-time. Currently, studies of the fibrillisation pathways have been limited to time-lapse studies; images of the sample are effectively snap shots of a particular time point taking minutes to generate a full image. Given that the time span of fibrillisation for many amyloid proteins involve hours rather than seconds, time-lapse imaging appears to be more than adequate in the study of amyloid. However, with the development of real-time imaging it may be possible to derive more detailed information on the subtle morphological changes which occur during some of the initial events of fibrillogenesis.

1.9.3 Investigating the physical properties of amyloid.

The thermal and chemical stability of amyloid has often been determined using the traditional methods employed for protein studies namely the use of CD and FTIR in which the loss of secondary structure can be dynamically measured. The EM has also been used to study the effects of heat and chemicals on samples, however these samples must be removed from the conditions, undergo preparative regimes and then imaged, during which valuable information may be lost or masked. However, the AFM is able to combine both strategies, enabling a dynamic study of the changes in morphology with variations in temperature or by the introduction of denaturing chemical agents into the chemically and pH robust liquid cell to allow time-lapse imaging of any resultant artefacts.

The thermal and pressure stability of amyloid fibrils has been investigated by AFM. Samples of transthyretin fibrils after exposure to high hydrostatic pressures and prolonged high temperatures were imaged by *ex situ* AFM, revealing that prefibrillar structures are dissociated by the conditions, however mature fibrils were observed to remain stable [147]. In these experiments, the amyloid samples are treated and then imaged, however modification of the AFM stage with the incorporation of an electronic feedback-controlled heating element would enable samples to be heated from the bottom-up during imaging in air up to ~250 °C or in closed liquid cells up to 100 °C. This would therefore enable, through *in situ*

heat imaging, the effects of temperature to be studied throughout the fibrillation pathway.

Other physical properties of amyloid fibrils have been quantified using the AFM such as persistence length measurements from topography images [128]. Through AFM imaging experiments the ability of Apo CII fibrils to circularise was shown to be intrinsically linked to their flexibility and persistence length [148]. Other amyloid have been noted to circularise: under high pressure conditions insulin fibrils circularise [149], whereas equine lysozyme forms circular amyloid under low pH conditions [150]. The circularised amyloid still retain the ability to bind Congo red and are thought to be another morphological state adopted by amyloid [57].

The small diameter of the AFM tip (~10 nm) and the ability to measure forces with picoNewton sensitivity ideally suits the AFM to measuring the small interaction forces which govern biological polymer assembly and stability and has widely been used to investigate the mechanical properties of many polymer systems from polysaccharides [151] to oligomeric proteins [152, 153]. Similarly the mechanical properties of the amyloid fibril have been investigated to gain a greater understanding of the interactions that govern fibril formation and confer the observed stability within the amyloid plaques. In a study of insulin amyloid the AFM was used to measure the mechanical properties of the fibrils using a nanoindentation method: a fibril is placed over a pore or gap in a substrate (ie between islands on a gold substrate) and the force required to push an AFM tip down onto the fibril is measured, akin to a three-point bending test. This enables information on the Young's, elastic and shear moduli (measure of the stiffness, elasticity and rigidity) of the amyloid fibril to be derived [154].

By utilising the indentation method the elastic properties of β 2-microglobulin fibrils have been identified. Furthermore, individual β -sheets have been 'unzipped' or mechanically peeled away from the fibril and the forces measured using the AFM [155]. In this experiment it was noted that the β -sheets could be reversibly and repeatedly unzipped from the main fibrils of both A β (1-40) and A β (25-35), although the forces required were different for the two polypeptide chains.

Protein secondary structure is an important factor in mechanical strength; β -rich conformations display greater mechanical resistance than α -helical rich, which is attributable to the H-bonding stabilising forces between β -strands [156]. Furthermore, AFM force-extension measurements and molecular dynamic simulations have shown that protein mutants differing by only a few amino acid in their primary sequence, which still display almost identical topology, can exhibit different mechanical resistance due to side chain interactions [157]. Consequently, amyloid fibrils may have considerable mechanical stability due to their β -sheet conformation and therefore it has been hypothesised that fibrils may display characteristic mechanical fingerprints which are dependent on their constituent protein [155].

By studying the mechanical and physical properties of the amyloid fibril a greater understanding of the interactions which govern fibril formation and stability can be achieved. This knowledge will invariably play a key role in the development of therapeutics, which seeks to prevent formation or destabilise the fibril or prefibrillar material.

1.10 Amyloid and the nanoscientist

Advancements in the biotechnology industries have led to the search for more exploitative and readily functionalised building blocks from which novel materials can be built. The vast potential of amyloid structures has not evaded the keen eye of the inquisitive and inventive nanoscientist. As the knowledge and understanding of the many ideal and stable properties of the amyloid fibril have been realised, so too have their apparent ability to be utilised in a wide range of potential applications; a bottom-up approach to novel material fabrication [47, 158, 159].

The recent discussion into the pathogenicity of amyloid has led to the suggestion that the cytotoxic element is the prefibrillar species and not the mature fibrils [15-17]. If this is true then the potential range of possible applications for amyloid may be greater than previously thought possible due to safety concerns, for example *in vivo* as drug delivery vessels or implants.

Predominantly the use of amyloid fibrils for novel biomaterials has focussed on the exploitation of amyloidogenic fragments rather than whole proteins, due to their ease of synthesis and handling. Gold and silver nanowires have been assembled using nanotube scaffolds formed from the dipeptide recognition motif of A β , the Alzheimer's protein [86] and the NM domain of the yeast prion Sup35 [160] for use in microelectronics circuitry.

The synthesis of nanofibrillar materials which can perform or support a specific function is of particular interest to the pharmaceutical and biomedical industries. For example, a Sup35 protein modified with a C-terminally linked green fluorescence protein (GFP) still retained the ability to form fibrillar structures which had green fluorescence [161]. This example demonstrates that proteins and peptides modified with specific functionalities may still retain the ability to form amyloid. Therefore it may be possible to engineer self-assembling fibrils with specific catalytic activity by coupling enzymes to the main protein or alternatively specific functional moieties could be attached to the constituent protein or peptide and thus generate chemically functionalised fibrils.

Furthermore with the proposal that the formation of fibrillar structure with core β -sheet ultrastructure is not limited to a subset of disease related proteins but is in fact a generic feature of the polypeptide chain, new avenues of research are being explored for the development of self-assembling nanofibrillar material from a range of designed amino acid sequences [2, 158, 162-165].

In this introduction a brief overview of the vast world of the amyloid fibril has been discussed from the origins, *in vivo* as misaggregated proteinaceous deposits to manipulation and exploitation as novel nanomaterials. The knowledge derived on the structural, kinetic and physical properties of amyloid using the AFM has been intrinsic to the developing understanding of amyloid fibrillisation. The work presented in this thesis focuses on the study of amyloid and amyloid-like structures using the AFM and a detailed description of the basic principles and functioning parameters of the AFM are also discussed here.

The aims of this PhD project are to investigate the self-assembly of peptides utilizing the AFM, particularly with the view to characterising the morphology, fibrillisation and properties of the fibrillar assemblies which they form. Furthermore, to develop strategies to directly control and exploit these fibrillar structures to explore their potential use as novel nanostructures.

The work presented in this thesis focuses on the fibrillar material self-assembled from peptide fragments of two amyloidogenic proteins: the amylin polypeptide associated with type-II diabetes mellitus and β -amyloid (A β) polypeptide associated with Alzheimer's disease. Specifically the experiments investigate short fragments of these polypeptides comprising the minimal amyloidogenic peptides containing the core recognition motif of the proteins; amylin fragment corresponding to residues 20-29 in the human sequence and residues 19-20 of the human A β polypeptide.

1.11 Thesis outline

The first section of this work focuses on the study and exploitative potential of the amyloid fibrils that self-assemble from amylin (20-29) peptides.

The studies presented in Chapter 2 are concerned with the self-assembly and fibril formation of the amylin (20-29) peptide fragment. Although amylin (20-29) is a commonly studied model peptide fragment, there are no detailed studies that directly visualise fibrillisation and changing morphology in a hydrated state. The opening section of the chapter documents the synthesis of the peptide fragment corresponding to amino acids 20-29 of the human amylin polypeptide by solid phase peptide synthesis. Congo red assay and AFM imaging reveal that the peptide fragments readily self-assemble, forming polymorphic amyloid fibrils. The chapter concludes with an investigation of the influence of solution pH, ionic strength and electrolyte composition on the morphology and fibril forming capabilities of the peptide, which are directly visualised using both *ex situ* and *in situ* AFM imaging.

The experiments presented in Chapter 3 investigate the exploitative potential of the self-assembling amylin (20-29) peptide to produce fibrils decorated with specific functional groups. The amylin (20-29) peptide fragment is synthesised by SPPS with either an azide or alkyne functional group coupled to the N-terminus. High-resolution *ex situ* AFM imaging and Congo red staining probe whether the peptides retain the capacity to form amyloid fibrils.

In the presence of copper (I) catalyst, alkyne and azide functional groups undergo a chemical ligation reaction. Consequently, it may therefore be possible to form stable covalent links between fibrils decorated with these moieties. *Ex situ* AFM imaging is used to investigate the effectiveness of this chemical ligation reaction to produce arrays of covalently linked amylin (20-29) fibrils.

The last section of this thesis focuses on the self-assembly of the second peptide fragment, the dipeptide of phenylalanine; the core recognition motif of the β -amyloid protein. This simple dipeptide of phenylalanine readily forms nanotubes in organic solvent, however these structures are unlike the biofibrils formed from larger fragments of the polypeptide. The nanotubes are large hollow structures with diameters in excess of 200 nm. The successful application of these nanotubes for use as scaffolds for the generation of nanowires has previously been demonstrated. The aim of this study is to further develop our knowledge of the properties of these nanotubes and to develop a means of controlling their assembly. In Chapter 4, *in situ* and *ex situ* tapping-mode AFM is used to investigate the thermal and chemical stability of these nanotubes. Furthermore, the AFM is used to directly visualise the manipulation and ordered orientation of the nanotubes using strong magnetic fields.

Chapter

2

Characterisation of Amylin (20-29) Fibrils by *Ex situ* and *In situ* AFM Imaging

2.1 Introduction

Amylin is a 37 amino acid polypeptide co-secreted with insulin from the pancreatic β -cells of the islets of Langerhans [166]. Amyloid deposits of amylin fibrils are found in over 90% of cases of type II late-onset diabetes mellitus or non-insulin dependent diabetes mellitus (NIDDM) [19, 167, 168]. Whether or not these amyloid deposits are a cause or effect of NIDDM is still largely unclear [169, 170], but increasing evidence supports the hypothesis that pre-fibrillar species of amylin amyloid are cytotoxic *in vitro* [171, 172].

In this chapter, the atomic force microscope is utilised for the characterisation of a self-assembling peptide fragment of the human amylin polypeptide, corresponding to amino acid residues 20 to 29 of the human sequence. Many studies utilising a combination of SEM, TEM and AFM have been undertaken to investigate the morphology and fibrillisation of the full-length amylin polypeptide and several of its peptide fragments [43, 44, 49, 61, 87, 105, 125, 173-177]. These studies have provided evidence that one of the key amyloidogenic regions of the human amylin polypeptide, a 6 amino acid peptide fragment (NH_2 - NFGAIL -COOH), is the smallest amylin fragment capable of self-assembly [87]. Further studies using a combination of EM and turbidity tests have shown that the larger 10 amino acid peptide fragment (NH_2 - SNNFGAILSS -COOH), and the focus of this chapter, self-assembles into fibrils which are similar in morphology to those formed by the full-length polypeptide *in vitro* [48, 100, 102, 176, 178].

Substitution experiments of specific amino acids within the full-length polypeptide revealed that residues within the core amylin (20-29) sequence are

crucial for fibril formation. Substitution of Ser-28 for β -sheet disrupting proline completely inhibited fibril formation [88] and substitution of the aromatic residue Phe-23 for alanine influenced the formation of higher order amyloid aggregates [61]. Together these findings highlight the importance of the amylin (20-29) fragment in fibril formation, however studies of longer amylin fragments reveal that other regions of the polypeptide directly influence the morphology and higher-order fibril assembly of the full-length polypeptide [48, 90, 179, 175].

The major advantage that AFM poses over SEM and TEM is that the sample can be imaged in solution by *in situ* imaging. This enables a dynamic investigation of amyloid in its hydrated state, and thus a study into the kinetics and real-time fibrillisation is possible [44, 56, 57, 177]. Kinetic studies of the fibrillisation of full-length and fragments of amylin have predominantly relied upon the use of turbidity and spectroscopic techniques measuring Congo red, ANS (1-Anilinanaphthalene-8-sulphonate) and Thioflavin-T binding [49, 180-182]. To date time-lapse AFM has only been utilised for the kinetic study of full-length amylin [44, 64] where growth of individual protofilaments, 2.4 nm in height, were observed in Tris buffer elongating at a rate of $1.1 (\pm 0.5) \text{ nm min}^{-1}$. The fibrils had varying morphologies and growth was bi-directional with no significant preference for either end of the growing fibril. Kinetic studies have revealed that fibril formation proceeded through two distinct phases and is nucleation dependent [64]. Fibril elongation followed an initial lag period, the length of which could be influenced by pH and temperature [181].

Although the AFM makes an ideal tool for the study of fibrillisation its use is dependent on sufficient immobilisation of the fibrils to a solid substrate support, particularly during *in situ* imaging. For the study of soft biomolecules such as peptide fibrils the use of tapping-mode AFM, where the tip only briefly comes into contact with the surface, is the most ideal mode of imaging [132, 177, 183]. The minimal forces applied by the tip as it oscillates across the sample surface require only weak immobilisation of the biomolecule to the substrate, enabling biomolecular interactions to freely occur at the surface and thus to be studied.

Immobilisation strategies in the simplest form rely on electrostatic attractions between substrate and biomolecule. Two commonly used substrates in AFM

imaging of amyloid [184] are muscovite mica which carries a net negative charge and gold which has a neutral surface charge. The former substrate is more favoured for AFM imaging due to ease of cleaning during preparation and atom scale flatness, and for this reason is the substrate of choice for the experiments presented in this thesis. For physisorption of a biomolecule to the substrate it may be necessary to manipulate the electrostatic charges on either surface by means of altering the pH or ionic environment. Introduction of co-ions or counterions either in a buffer solution or simply by pre-adsorbing monovalent or divalent salt ions (eg Nickel, Zinc, Cobalt, Magnesium) to the substrate enables the charge on either the substrate or the biomolecule to be masked in favour of physisorption [131]. Time-lapse AFM imaging of full-length amylin to mica was performed in a Tris-HCl buffer at a pH of 7.3 [44]. The isoelectric point of full-length amylin is 8.9 and therefore at this pH the peptide would carry a net positive charge due to protonation of free amine groups of the protein.

Despite the key role of the amylin (20-29) sequence in fibril assembly by the full-length polypeptide no detailed AFM study has been performed on the fragment, and in particular there is no information on the early stages of amylin (20-29) fibril formation or the morphology of the younger fibrils. The work presented in this chapter details the characterisation of fibrils formed by the peptide fragment amylin (20-29) by *in situ* and *ex situ* AFM imaging. The peptide fragment was synthesised using solid phase peptide synthesis (SPPS) and a study was made into purification using reverse-phase high performance liquid chromatography (RP-HPLC). Preliminary high-resolution *ex situ* imaging was used to investigate the polymorphic nature of young amylin (20-29) fibrils. For successful *in situ* AFM imaging of amylin (20-29) fibrils the development of an immobilisation strategy was investigated and initial studies were made into the effects of ionic solution conditions on the morphology, kinetics and fibrillisation of amylin (20-29).

The *ex situ* AFM experiments presented within this chapter are the subject of an article published in the journal *Protein and Peptide Letters* [134]

2.2 Experimental

2.2.1 Materials

All amylin (20-29) was synthesised by SPPS, reagents used in the process were: NovaSyn[®] TGR resin and standard Fmoc protected amino acids were purchased from NovaBiochem; dimethylformamide (DMF) purchased from Rathburn; piperidine, *N*-methylpyrrolidone (NMP), *N,N*-diisopropylethylamine (DIPEA), trifluoroacetic acid (for SPPS), triisopropylsilane (TIPS) and dichloromethane (DCM) were purchased from Sigma-Aldrich; *N*-[[(dimethylamino)-1H-1,2,3-triazolo[4,5-b]pyridin-1-ylmethylene]-*N*-methylmethanaminium hexafluorophosphate N-oxide (HATU) obtained from Perseptive Biosystems, Germany; ethanol, hexane, diethyl ether, acetonitrile (Far UV grade) and trifluoroacetic acid (for HPLC) purchased from Fischer Scientific Chemicals; Sodium chloride were purchased from Sigma-Aldrich.

Reagents used in the AFM studies: sodium citrate (dibasic and monobasic), sodium acetate, potassium chloride (KCl), magnesium chloride (MgCl₂), Tris and Tris HCl all purchased from Sigma Aldrich. Congo red and sodium chloride were purchased from Sigma Aldrich. Ethanol was purchased from Fischer Scientific.

2.2.2 Method

2.2.2.1 Solid phase peptide synthesis

Peptide fragment of human amylin corresponding to residues 20 to 29 (sequence shown below) was synthesised using SPPS.



Adaptations based on the work of Nilsson *et al* [185] for synthesis of amyloidogenic peptides were incorporated into the standard [186] SPPS Fmoc procedure.

The column was packed with 0.1 mmol of an amide Rink resin, NovaSyn[®] TGR resin was solvated initially with *N*-methylpyrrolidinone, and the activation cocktail

containing the coupling reagents, 0.8 mmol DIPEA and 0.4 mmol HATU, solubilised in NMP, mixed with 0.4 mmol of the C-terminal amino acid (serine) and added immediately to the column. Amino acids were loaded with a four-fold excess to ensure maximum yield. Sufficient solvent was added to the column for the resin to be fluid and was left at room temperature on a magnetic stirrer. The first amino acid coupling was left overnight to ensure complete attachment to the resin.

All the amino acids have an Fmoc group protecting the NH₂ group to prevent unwanted formation of peptide bonds. Fmoc deprotection was performed by washing the column with 100% DMF, to remove excess activated amino acids and then with 20% piperidine-DMF solution. Solvent washing of the column was controlled using a LKB Biolynx 4175 Peptide Synthesiser, set to a flow rate of 3 ml/min. Fmoc deprotection and coupling efficiency was monitored spectrophotometrically by absorbance measurements ($\lambda_{280\text{nm}}$) of the column eluent.

Following Fmoc deprotection, the resin was washed with NMP to remove any trace of DMF and the succeeding amino acid with activation cocktail was added. The process was then repeated for each amino acid until the complete sequence was generated. The resin was washed using DMF and DCM over a Buchner funnel and then shrunk using hexane. Cleavage of the peptide chain from the resin and deprotection of side chain groups was performed by the addition of a mixture of 90% v/v trifluoroacetic acid (TFA), 2% v/v triisopropylsilane (TIPS) and 8% v/v water, for 2 hours. The suspension was then filtered and the filtrate evaporated under vacuum. The residual material was titrated with diethyl ether, and the resulting powder (100 mg), consisting of the crude peptide was stored below 4°C.

2.2.2.2 Liquid chromatography mass spectrometry (LC-MS)

Presence and purity of the peptide was determined using LC-MS. Crude peptide was injected onto the column at a concentration of 1 mg/ml in ultrapure water (pH 6, resistivity 18.2 M Ω cm). A C₁₈ analytical column (Bore size 5 μ m) was run at a linear gradient of 25 to 100% solution B (90% v/v acetonitrile and 0.06% v/v

trifluoroacetic acid) over 30 minutes with flow rate of 0.25 ml/min, with detector monitoring eluent at $\lambda_{214 \text{ nm}}$.

2.2.2.3 High performance liquid chromatography (HPLC)

Peptide was purified by reverse-phase HPLC using a C₈ semi-preparative column (bore size 5 μm) on a Beckman Gold System. Solvent A was water and 0.06% v/v trifluoroacetic acid and solvent B, 90% v/v acetonitrile and 0.06% v/v trifluoroacetic acid. Presence of peptide in the eluent was monitored spectrophotometrically by monitoring absorbance at wavelength of 214 nm. The conditions and parameters used for the HPLC purification are a scaled up and developed method based on those used for LC-MS. To achieve more efficient purification, the peptide was loaded at a higher concentration, by dissolving 2 mg/ml of crude peptide in 40% acetonitrile. Criteria for method development were based on improving the resolution of target peak, increasing separation of contaminants and minimising run time. The finalised method was a gradient of 25 to 100 % B over 20 minutes with flow rate of 5 ml/min and injection volume of 200 μl .

HPLC solvents were removed from the purified peptide sample under vacuum using a RotovacTM system and the purified peptide sample lyophilised over 36 hours and stored below 4°C.

2.2.2.4 Congo red assay

The histopathology stain Congo red is commonly used in the detection of amyloid [27] and was used to determine the formation of amyloid fibrils by our amylin (20-29) peptides. A saturated solution of Congo red was prepared using 0.2g of Congo red powder per 100 ml of 80% v/v ethanol solution saturated with sodium chloride. Purified and crude lyophilised peptide samples were suspended in ultrapure water (pH 6, resistivity 18.2 M Ωcm) at concentration of 1 mg/ml. The suspension was aged for 18 and 48 hours at room temperature to ensure maximum allowance for fibrils to form. At each time interval a 10 μl aliquot was dropped onto a clean glass slide and air-dried. Samples were stained for 1 minute by

addition of the saturated Congo red solution. Excess stain was removed by washing with ethanol and the slide air-dried.

2.2.2.4.1 Optical microscopy and birefringence

Birefringence was examined using a Leitz Diaplan light microscope with polarisers and 10 and 25 times magnification objective lens. The polariser lens are set at a 45 degrees to each other, one in the incident beam and the other set above the slide stage between the objective lens and camera. Images of the sample under normal and polarised light were captured using a Nikon 100 digital camera.

2.2.2.5 *Ex situ* AFM imaging

The lyophilized amylin (20 to 29) peptide was solubilised in ultrapure water (pH 6, resistivity 18.2 MΩcm) at a concentration of 1 mg/ml. Samples were left to form fibrils at room temperature up to 48 hours. In some instances, to prevent molecular overcrowding of the AFM scan area, stock solutions were diluted to concentrations of 100 µg/ml in ultrapure water immediately prior to imaging. Aliquots of 10 µl were dropped onto freshly cleaved mica (1 cm²), dried in a N₂ gas stream and imaged immediately. Ultrapure water stored under identical conditions and for the same time period was used as a control preparation; here imaging showed no fibrillar structures. Images presented were generated using a Nanoscope IIIa AFM (Digital Instruments, Veeco Metrology Group, Santa Barbara CA). All imaging was performed in air in tapping mode with scan rates of 1.5-2.5 Hz using silicon TESP tapping probes (supplied by Veeco Metrology Group) mounted on cantilevers with nominal spring constants of 42 N/m (range of 34.4-37.2 N/m) and nominal resonant frequency of 320 kHz (range of 280-360 kHz).

2.2.2.6 *In situ* AFM imaging of amylin (20-29) fibrils

2.2.2.6.1 Sample Preparation

The lyophilised peptide was initially solubilised in ultrapure water (pH 5.6, resistivity 18.2 MΩcm) at a concentration of 1 mg/ml. After 1 hour at room temperature, the sample was diluted to give a final peptide concentration of 100-

200 µg/ml in varying salt solutions and left to incubate at room temperature. All solutions were prepared on day of the experiment from ultrapure water. The salt solutions investigated are summarised in table 2.1, which lists the salt concentrations used and solution pH. Both the potassium chloride and magnesium chloride were acidified by stepwise addition of hydrochloric acid to achieve the desired pH of 4.0. A 30 µl drop of solution was placed onto freshly cleaved mica and an aliquot transferred to an AFM liquid cell immediately prior to imaging.

Ionic content	pH
10-50 mM Tris HCl	7.2
10-100 mM KCl	4.0
100 mM MgCl ₂	4.0
50-150 mM Sodium acetate	5.5
125 mM Sodium acetate with KCl salts	5.5
125 mM Sodium acetate with MgCl ₂ salts	5.0
50-150 mM Sodium citrate	4.0
130 mM Sodium acetate with KCl salts	4.0
125 mM Sodium acetate with KCl salts	4.0
125 mM Sodium acetate with MgCl ₂ salts	4.0

Table 2.1: An overview of the buffer and ion solutions investigated for the immobilisation of amylin (20-29) fibrils to mica.

2.2.2.6.2 AFM Imaging

All images were collected using a Nanoscope IIIa atomic force microscope in tapping mode at scan rates of 2-3 Hz using silicon nitride cantilevers with resonant frequencies of 31-34 kHz and spring constant of 0.08 N/m.

2.2.2.7 AFM image analysis

Data was processed using two computer packages, the analytical processing options from the Nanoscope software version 5.21b48 (Digital Instruments, Veeco Metrology Group, Santa Barbara CA) and SPIP program (Image Metrology ApS USA). Images show topography and phase data (where indicated) with scale bars. Z range contrast scale bars are presented alongside images where

appropriate. The upper z range value is stated above each scale bar with lighter colours indicating higher topographical features and greater phase contrast respectively.

2.3 Results

2.3.1 *Solid phase peptide synthesis*

The ten amino acid peptide fragment corresponding to residues 20-29 of the human amylin polypeptide was successfully synthesised using solid phase peptide synthesis. After each amino acid coupling, an absorption reading of the column eluent was measured using a spectrophotometer to ensure that coupling was successful. However, it was found that after the addition of the third amino acid (leucine) clumping of the resin occurred suggesting the possibility of aggregation of the resin/peptide chain. In order to eliminate this and improve chances of complete coupling, 5 of the ten (bold-type in the sequence below) subsequent amino acids were double coupled.



Double coupling involves the addition of the same amino acid twice: after the first addition and coupling of the amino acid there is no Fmoc deprotection, instead the same amino acid is reapplied to the reaction with coupling activation cocktail, left for a further 2 to 3 hours before the column is washed with DMF, and then the cycle continues with the next amino acid addition following deprotection. This maximises the efficiency of coupling by increasing the tendency of all growing peptide chains to couple with the new amino acid and thus maintaining a high yield of the correct full-length peptide.

Purity of the end product, a white powder (100 mg) was characterised by LC-MS. The real time chromatography UV trace is shown in Figure 2.1a. A positive ion

mass spectrum of the largest peak (at 12.43 minutes) is presented in figure 2.1b and confirms the presence of the target peptide.

Yield : 100 mg (85.7%)

ES-MS : m/z 1008.6 (100 %, $[M]^+$).

2.3.2 HPLC

Purification of the peptide was carried out on a C_{18} preparative column using high performance liquid chromatography. The starting method, based on the conditions used in the LC-MS, was developed by scaling up the conditions utilised in the smaller analytical column to the HPLC preparative column.

In the optimised method, solvents remained the same but with an increased flow rate of 5 ml/min. The sample injection volume was increased to 200 μ l of 2 mg/ml peptide in 40% v/v acetonitrile. The column was washed with a gradient of 25 to 100 % B over 8 minutes, remaining at 100 % B for 5 minutes to ensure release of all bound material, then reduction to 25 % B and run at this ratio for 10 minutes to re-equilibrate the column.

LC-MS analysis of the eluent collected at approximately 5.5 minutes confirmed the presence of the molecular ion corresponding to the peptide. Subsequent analysis of a blank run confirmed all peptide was washed off the column at this time.

Using this method, purified peptide yields were low and combined with the high solvent consumption during the purification process, despite maximum refinement, proved highly inefficient; 3 mg of crude peptide yielded only 0.61 mg of purified peptide.

2.3.3 Congo red assay

The histology stain Congo red is used as a common bench indicator for the presence of amyloid. Positive results are indicated by a green-gold birefringence when viewed under the polarised light microscope. Aged samples of the crude and purified amylin (20-29) in solution were assayed for the presence of amyloid by staining with Congo red and the presence of any birefringence under polarised light noted.

Following incubation of both the crude peptide and the purified peptide in solution for 18 hours, aliquoted samples were dried and stained with Congo red dye. Figure 2.2 presents images of the stained peptide samples: the crude peptide viewed under normal (figure 2.2a) and polarised light (figure 2.2b), and the stained purified peptide sample viewed under normal (figure 2.2c) and polarised light (figure 2.2d). Additionally the samples were left for a further 30 hours to ensure maximum opportunity for amyloid formation. Figure 2.2e shows the crude peptide viewed under normal light and figure 2.2f under polarised light. The stained purified peptide sample viewed under normal light is shown in figure 2.2g and polarised light in figure 2.2h. Both samples under normal light have the red colour of the dye. When the samples were viewed under polarised light the characteristic green gold birefringence is observed for both the crude and purified samples at both time intervals. The birefringence can predominantly be noted around the outer edges of dense aggregates of samples, which form as an artefact of drying.

2.3.4 AFM *ex situ* imaging

The aim of the experiments in the following section was to achieve a detailed study of the morphology of amylin (20-29) fibrils by *ex situ* tapping mode AFM imaging; specifically studying the variation in fibrillar morphology over time with emphasis on younger fibril characterisation.

2.3.4.1 Preliminary *ex situ* AFM images

Preliminary investigations were made into the fibril forming capacity of the crude and purified peptide samples, primarily to evaluate the level of necessity for

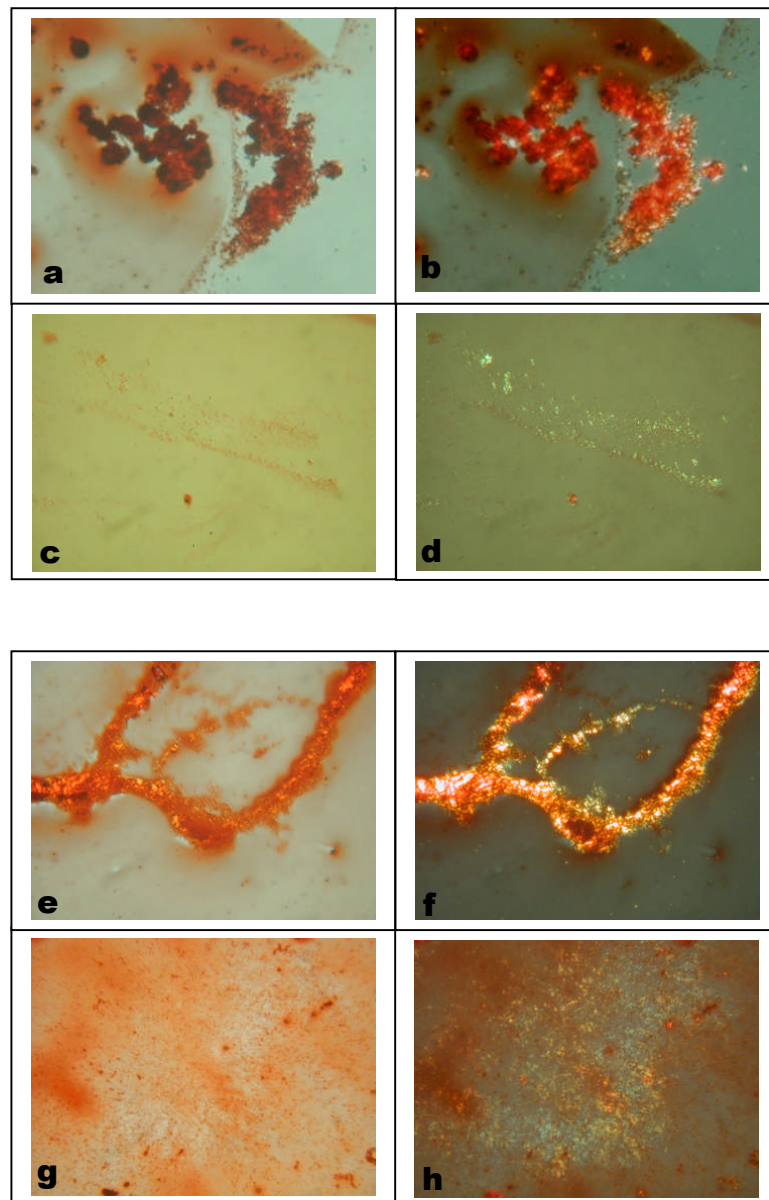


Figure 2.2: Congo red staining of amylin (20-29) samples. Aged for 18 hours crude (a and b) and purified (c and d) peptide samples under normal (left) and polarised (right) light. Aged for 48 hours crude (e and f) and purified (g and h) peptide samples under normal (left) and polarised (right) light. Peptide concentration 1 mg/ml.

purification. Samples of the crude peptide and the purified peptide were stored under identical conditions at room temperature for 18 hours and 48 hours to ensure the maximum time for any fibrillar structures to form. Figure 2.3a is a typical example of the topography (left) and phase (right) image of the crude peptide sample at 18 hours. Individual fibrillar structures can clearly be seen in the high resolution image. Similarly, fibrillar structures are observed in the purified peptide sample at 18 hours (figure 2.3b). In both the purified and crude sample images study of the background mica surface shows a similar extent of deposition of non-aggregated material. This deposited material appears to have had no detrimental influence on fibril formation and subsequent immobilisation to the mica surface.

Figures 2.4a and 2.4b are representative AFM images of the crude and purified samples (respectively) aged and imaged after 48 hours. The samples appear similar in topography with a dense layering of fibrous material on the mica surface. Additionally large dense aggregates are observed irregularly arranged on top of the fibrous layer in both samples.

2.3.4.2 Fibril morphology

Ex situ tapping-mode AFM was used to obtain low and high-resolution images of the morphology of amylin (20-29) fibrils. Figures 2.6 to 2.12 are a representative selection of the topography and phase images generated of peptide fibrils formed in solutions of ultrapure water (concentration 1 mg/ml) aged between 2 and 48 hours and imaged *ex situ* on freshly cleaved mica substrate. To prevent molecular over-crowding of the scan area, it was often necessary to dilute the sample using ultrapure water prior to imaging. Dimensions given are the mean \pm the standard deviation of a sample of randomly selected fibrils within the scan areas.

In control experiments, ultrapure water without peptide was incubated under identical conditions. At the same time as an aliquot of peptide solution was removed and imaged, an aliquot of the control was dropped onto freshly cleaved mica and then imaged, only clear mica surfaces were observed (images not shown).

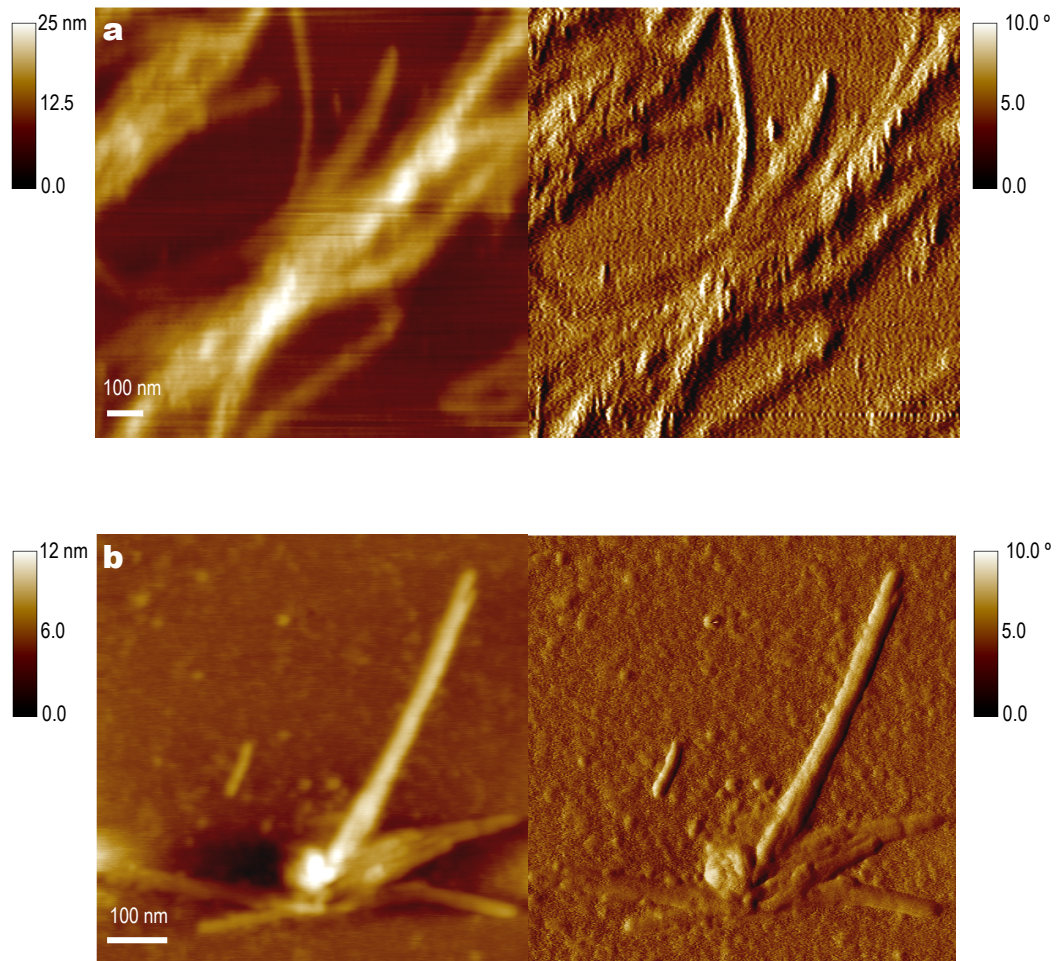


Figure 2.3: *Ex situ* AFM images of the amylin (20-29) peptide sample a) after purification and b) the crude peptide sample at 18 hours. Peptides were solubilised in ultrapure water for 18 hours before aliquot samples were removed and dried onto freshly cleaved mica. The final peptide concentrations were 100 $\mu\text{g/ml}$. Topography images are shown to the left and phase images on the right with z range contrast bar.

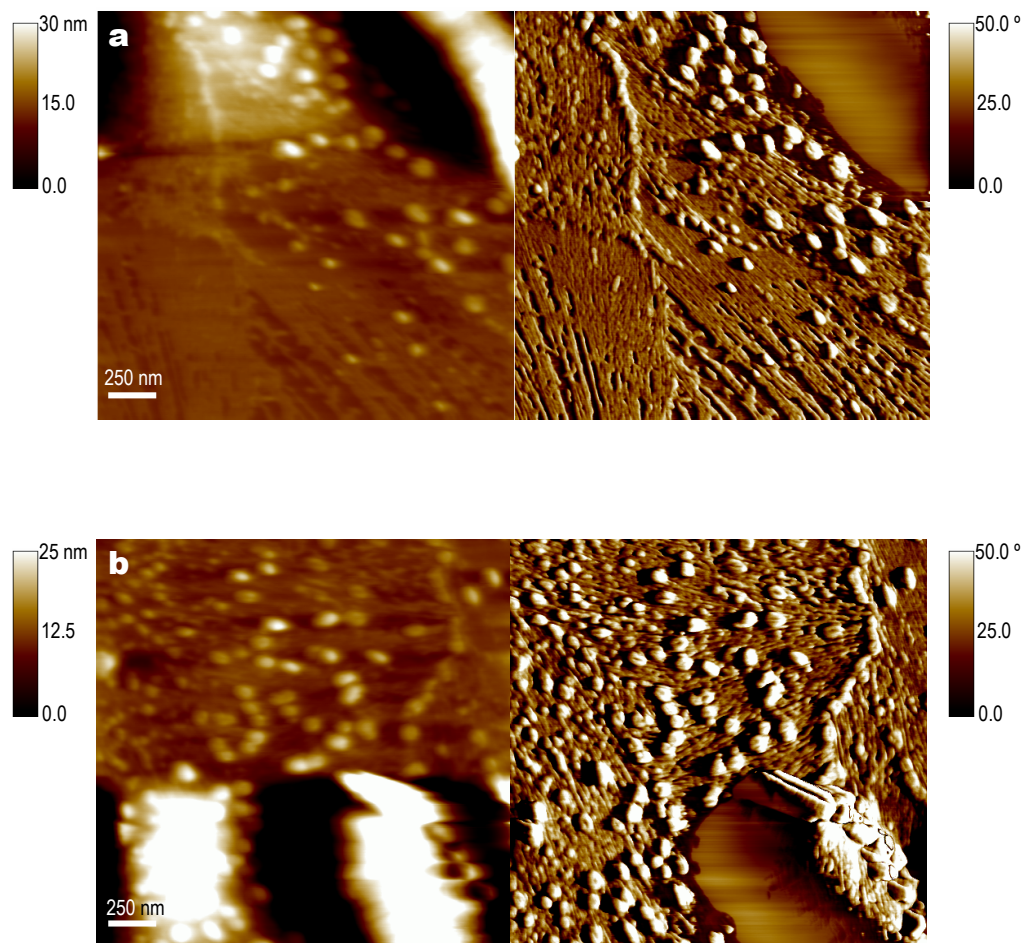


Figure 2.4: *Ex situ* AFM images of the amylin (20-29) peptide sample a) after purification and b) the crude peptide sample at 48 hours. Peptides were solubilised in ultrapure water for 48 hours before aliquot samples were removed and dried onto freshly cleaved mica. The final peptide concentrations were 100 $\mu\text{g/ml}$. Topography images are shown to the left and phase images on the right with z range contrast bars.

2.3.4.2.1 Amylin (20-29) at t=18 hours

The images in figures 2.6-8 are a typical selection of the amylin (20-29) fibrils formed in ultrapure water for 18 hours at a concentration of 1 mg/ml. Immediately prior to imaging in air using tapping-mode AFM, aliquots of solution were diluted to 100 $\mu\text{g/ml}$ before drying onto freshly cleaved mica.

The images shown in figure 2.6a are of a selection of individual fibrils observed in the peptide solutions aged for 18 hours, several different fibril dimensions can be observed. Fibrils were straight (green arrow) and curved (blue arrow), branched (red arrow) or unbranched (black arrow). Figure 2.6b shows a high-resolution image of the boxed area in figure 2.6a, highlighting the end of a fibril. This fibril is 1.195 μm in length with an average width of 26.15(\pm 2.8) nm. At the end of the fibril there is a reduction in height and slight decrease in width (white arrow) compared to the rest of the fibril. The fibril then branches into two arms of similar height but smaller widths (pink arrow). Figure 2.5 is a histogram of the half-height width of a sample selection ($n = 150$) of fibrils found in the 18 hour samples. The mean half-height width is 27.31(\pm 8.36) nm.

Several distinctive morphological features that were encountered during imaging are presented in the topography and phase images presented in figure 2.7. Figure 2.7a shows a high-resolution image of fibrils extending outwards in a fan-like

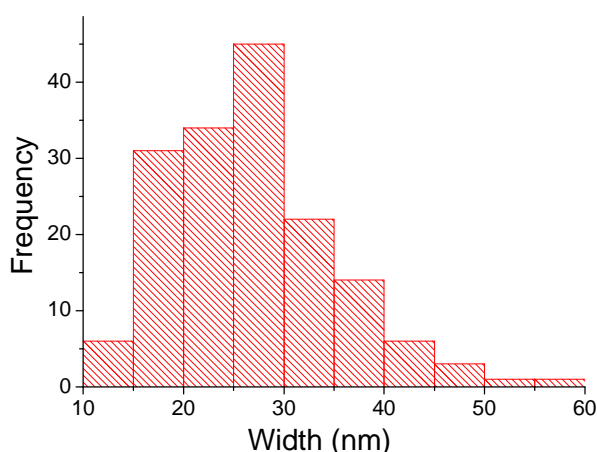


Figure 2.5: Histogram of the half-height width distribution of amylin (20-29) fibrils aged 18 hours. Mean fibril half-height width is 27.31(\pm 8.36) nm ($n = 150$)

manner from a dense central point. Fibrils are of similar width, with average dimensions of $34.4(\pm 8.1)$ nm. A regularly observed feature is the splitting or branching of a single fibril. Branches are generally of equal width and are in most cases as wide as the originating fibril (figures 2.7b and 2.7c). The point at which a fibril splits in two appears to be random, and occasionally the branches rejoin to form a single fibril again (figure 2.7c). A high-resolution image of such a feature can be seen in figure 2.7d, in which the originating fibril is $33.03(\pm 6.83)$ nm, the branches are $24.89(\pm 3.89)$ nm and $28.84(\pm 4.59)$ nm and the remerged fibril is $34.5(\pm 5.30)$ nm.

The phase images presented in to the right in figures 2.7a, 2.8b and c, provide additional complementary information to the topography data on the morphology of the amylin (20-29) fibrils; distinct boundaries between individual fibrils can be elucidated.

Individual protofilaments were also observed organised into higher-order structures. The image shown in figure 2.8a is typical of protofilaments assembled into twisted bundles. The twisting of the bundles appears to have no regular periodicity and displayed variation in the number of protofilaments incorporated within each bundle. Also of note, protofilaments within the twisted bundles could extend out from one bundle to form that of another, generating a network. Furthermore, protofilaments were also observed laterally aligned, forming sheet-like assemblies as demonstrated in the topography and phase image shown in figure 2.8b and at a higher-resolution shown in figure 2.8c. In such cases a more uniform array is produced, and the protofilaments are more linear than in the twisted bundles with no discernable branching.

2.3.4.2.2 Fibril Variation with Time

A preliminary study to investigate the time-scale of amylin (20-29) fibrillogenesis was performed. Aliquot samples were removed from a 1 mg/ml stock solution of amylin (20-29) after successive 2 hour time periods (0, 2, 4, 6 hours), dried onto freshly cleaved mica and imaged in air using tapping mode AFM. The high-resolution topography images are shown in figure 2.9.

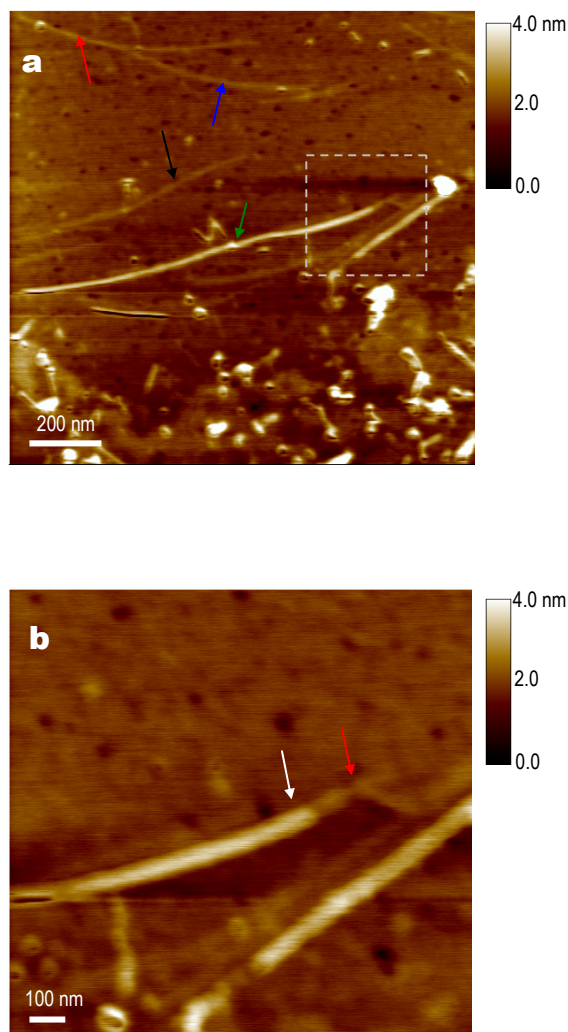


Figure 2.6: *Ex situ* AFM images of individual fibrils of amylin (20-29) stored for 18 hours. Peptides were solubilised in ultrapure water for 18 hours before aliquot samples were removed and dried onto freshly cleaved mica. The final peptide concentration was 100 $\mu\text{g}/\text{ml}$. **Figure 6a** is a topography image, the arrows highlight the range of different fibril morphologies. A higher resolution topography image of the boxed area is shown in **figure 6b**. Arrows indicate two different widths (16.7 (\pm 3.1) nm and 23.9 (\pm 2.6) nm) of the protofilament. Z range contrast bars are shown.

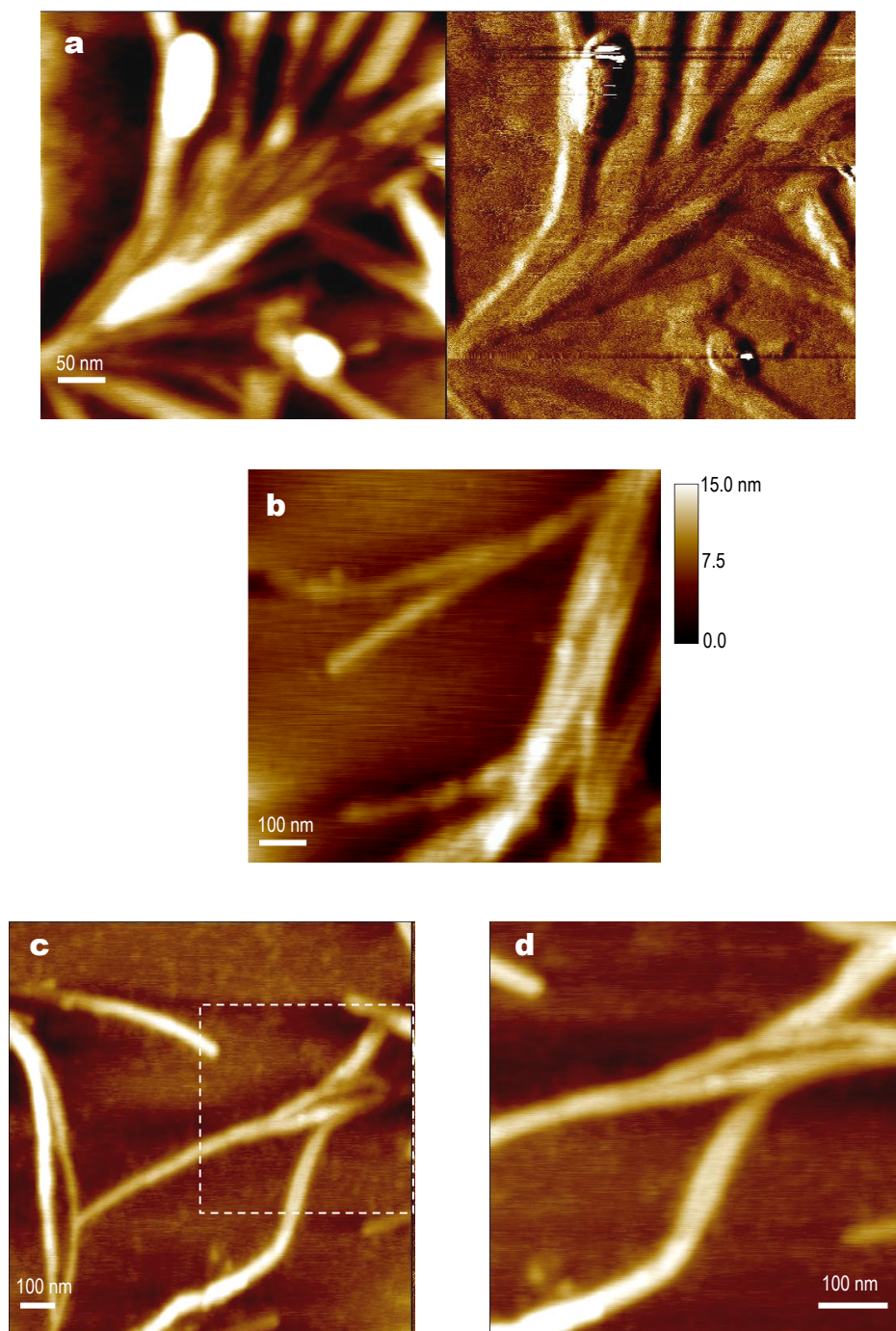


Figure 2.7: High-resolution *ex situ* AFM images of amylin (20-29) fibril morphologies at 18 hours. The final peptide concentration was 100 $\mu\text{g/ml}$ in ultrapure water. **Figure 7a** shows a topography (left) and phase (right) image of fibrils fanning out from a central point. The topography image shown in **figure 7b** is of a fibril splitting or branching. The topography image shown in **figure 7c** is another example of fibril branching, the higher-resolution image of the boxed area shown in **figure 7d** is of a fibril splitting and remerging. Z range contrast bars are shown.

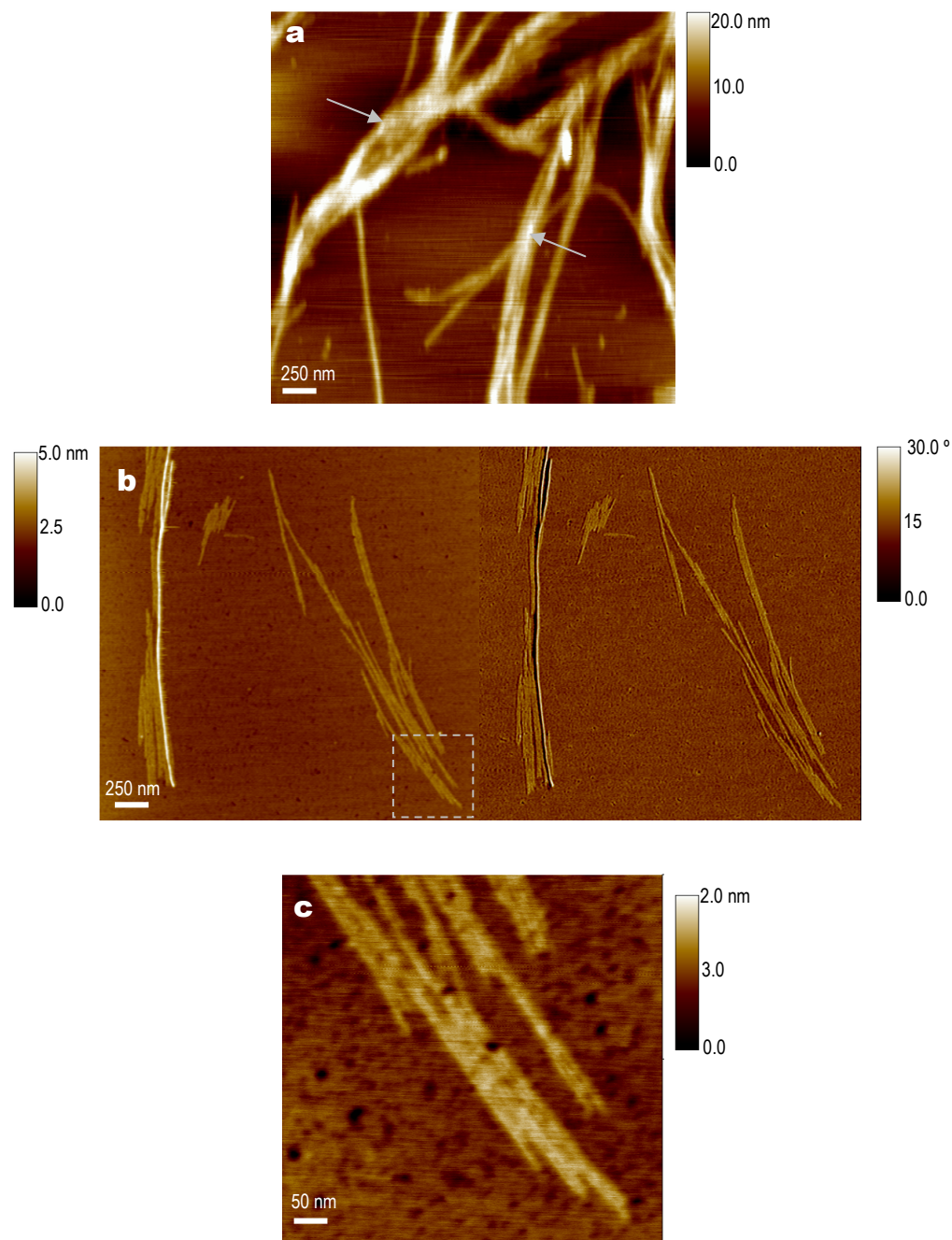


Figure 2.8: *Ex situ* AFM images of higher-order assemblies of amylin (20-29) fibrils aged 18 hours. Final peptide concentration 100 $\mu\text{g/ml}$ in ultrapure water. **Figure 8a** shows a typical topography image of fibrils associated into twisted assemblies. The arrows indicate two bundles with different sizes and morphologies. **Figure 8b** shows a topographic (left) and phase (right) image of laterally associated fibrillar assemblies. **Figure 8c** is a higher-resolution topographic image of the boxed area in figure 8a. Z range contrast bars are shown.

Fibrillar structures were first observed after incubation of the solution for 4 hours (figure 2.9c). Prior to this, no fibrous material was noted. However the mica surface had a granular appearance presumably due to pre-aggregation material, which is still apparent in the higher resolution image in figure 2.9c of the sample at 4 hours but which is dramatically reduced at 6 hours (figure 2.9d). Many of the early protofilaments display a twisting along their axis, giving the structures a globular appearance (figures 2.10 and 2.11). This was more prevalent in the fibrils in the samples aged 6 hours. The twisting periodicity varied between different protofilaments and in some instances had no regular turn. Figure 2.10a and b are typical high-resolution topography images of the protofilaments at 4 hours, with further topographical information detailed in the phase images. At 4 hours the majority of fibrillar structures displayed twisting along their axis; however the periodicity varied amongst the protofilaments in the sample. Figure 2.10c is a cross-sectional profile along the axis of the fibril in the boxed area in figure 2.10b; the measured periodicity is approximately 40 nm with some variation between twists and a fibril half-height width of 20.3 nm. By comparison the fibril in figure 2.10a has a periodicity of approximately 48 nm despite a half-height width of only 10.1 nm. Examples of protofilaments from samples 6 hours old can be seen in the topography image shown in figure 2.11a. This is typical of the sample at this time point and highlights the variation in protofilaments; many display periodicity along their axis whilst the remaining have a featureless morphology. The higher-resolution topography image in figure 2.11b is of the boxed area in figure 2.11a and highlights several protofilaments with periodicity along their axis. Figure 2.11c shows a height cross-sectional profile along the axis of the boxed protofilament in figure 2.11b which has a regular periodicity of approximately 75 nm and maximum half-height width of 26.4 nm and height of 4.1 nm. The twisting periodicity was not observed in solutions of protofilaments incubated for longer periods (18+ hours) (figures 2.7 and 2.8).

2.3.4.2.3 Fibril Morphology at 48 hours

Peptide solutions were stored at room temperature for a further 30 hours in ultrapure water at a concentration of 1 mg/ml, and then aliquots removed, dropped onto freshly cleaved mica and dried immediately prior to imaging in air using

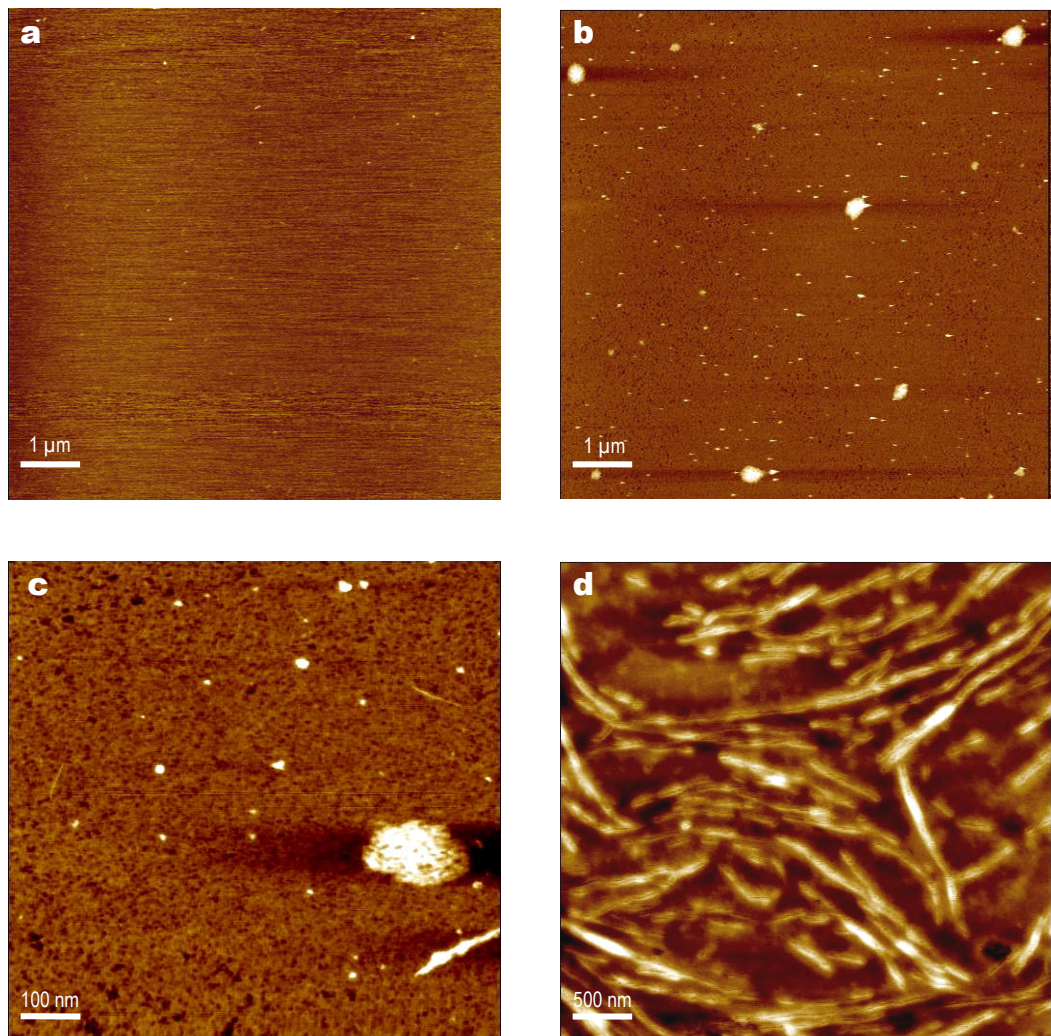


Figure 2.9: *Ex situ* AFM images of amylin (20-29) after 0, 2, 4 and 6 hours incubation. Final peptide concentration was 1 mg/ml in ultrapure water. Topography images are of the peptide sample at **a)** 0 hours, **b)** 2 hours, **c)** 4 hours and **d)** 6 hours.

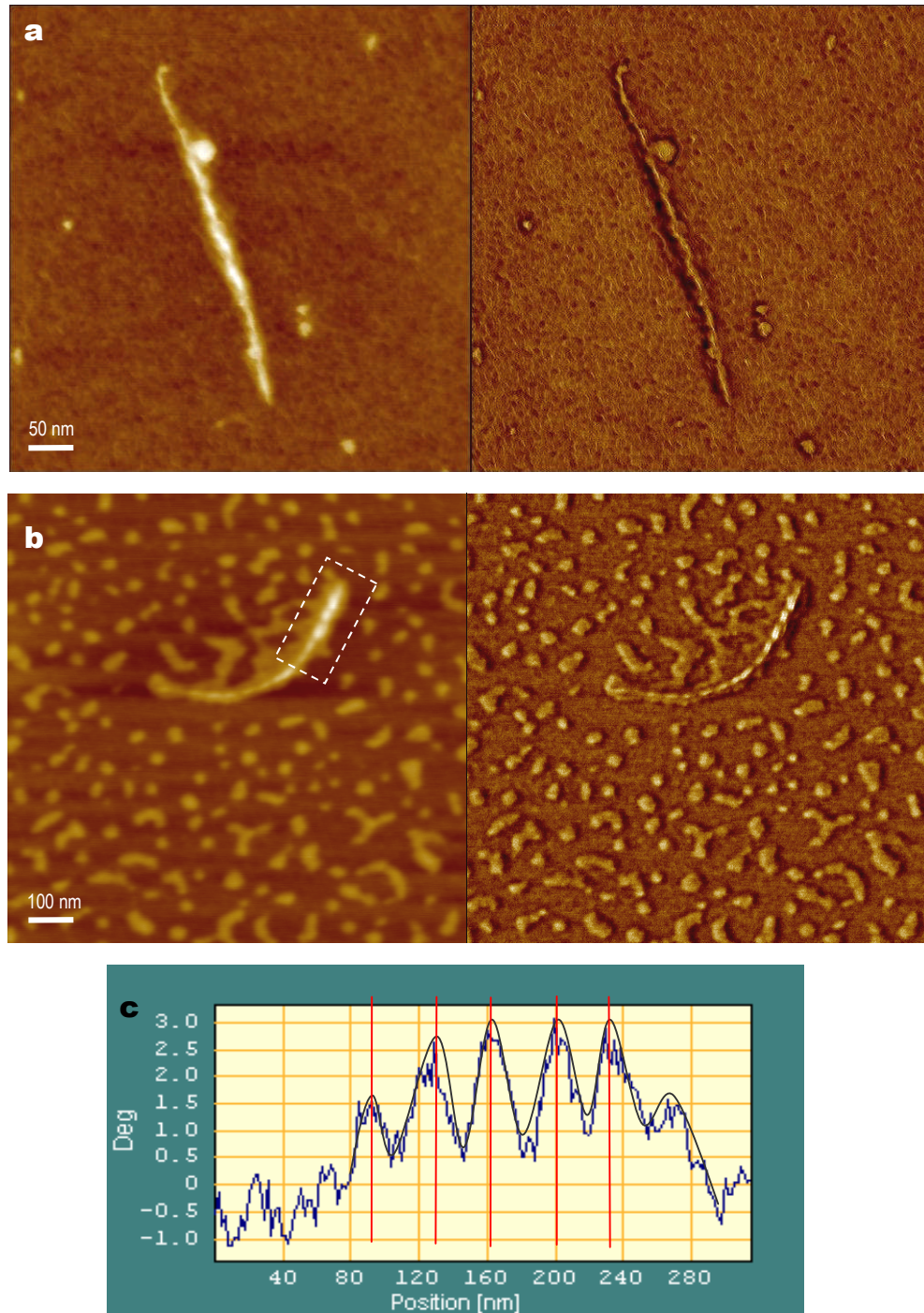


Figure 2.10: *Ex situ* AFM images of amylin (20-29) fibrils aged 4 hours. Final peptide concentration was 1 mg/ml in ultrapure water. The periodicity observed in younger fibrils is demonstrated in the topography (right) and phase (left) images shown in **figure 10a** and **figure 10b**. **Figure 10c** is a line plot along the axis of the fibril in the box of figure 10b, showing an example of the regular periodicity observed in younger fibrils.

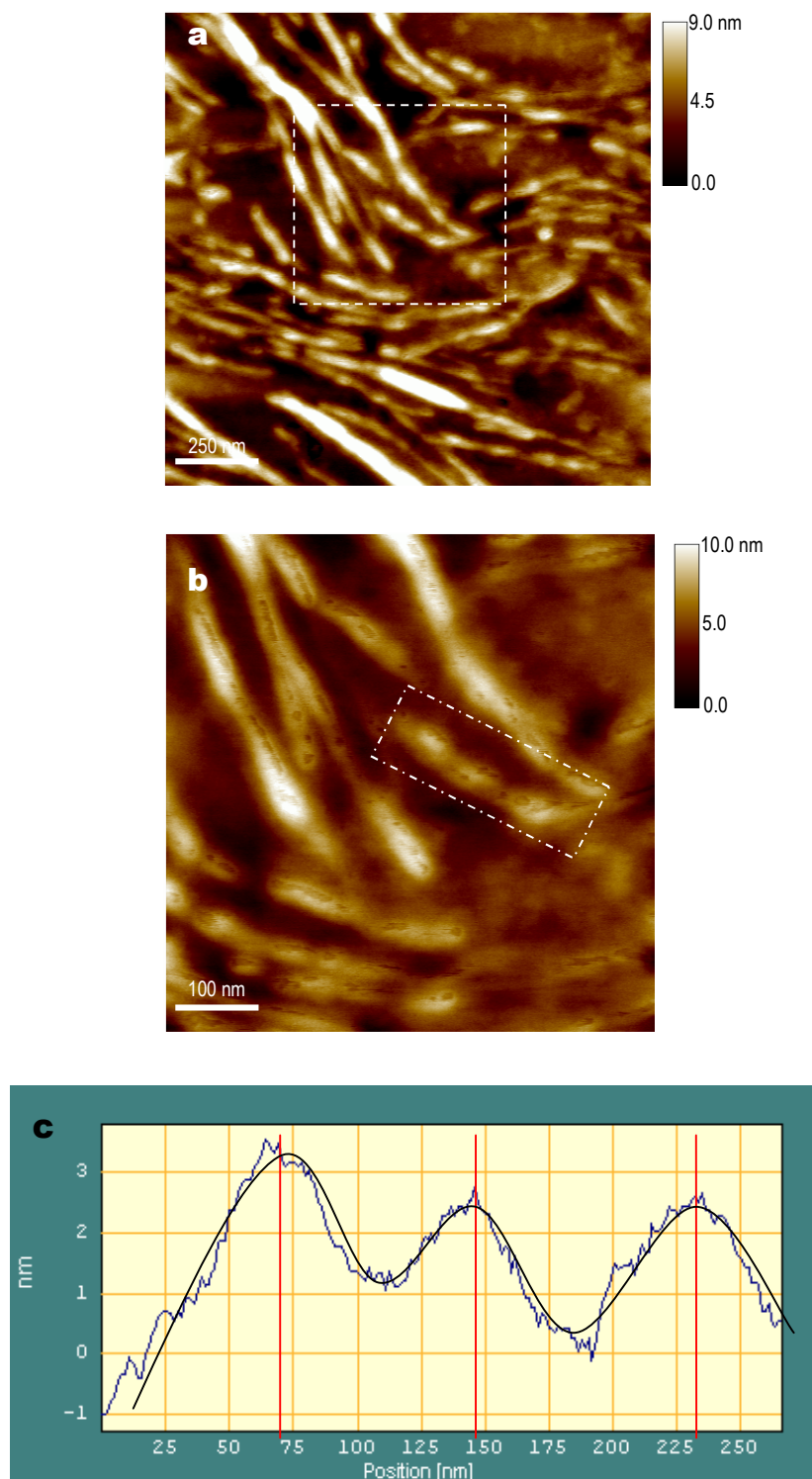


Figure 2.11: *Ex situ* AFM images of amylin (20-29) fibrils aged 6 hours. The final peptide concentration was 1 mg/ml in ultrapure water. **Figure 11a** shows a topography image, a higher-resolution topography image of the boxed area is shown in **figure 11b**. Z range contrast bars are shown. **Figure 11c** is a line profile of the height variations along the axis of the fibril in the box of figure 11b, showing an example of the periodicity observed in younger fibrils.

tapping mode AFM. Typical topography and phase images are shown in figure 2.12.

In most samples, a fibrous layer was observed (Figure 2.12) covering the entire sample area and appeared much denser than previously seen in the samples aged 18 hours. In the upper portion of figure 2.12a, higher raised aggregates can be seen on the denser portion of the fibril surface layer. The aggregates are of varied dimensions with no discernable morphology. There is no regularity to the location of the aggregates on the surface layer and it is not apparent whether these are aggregates which have adsorbed to the preformed fibrils or a mis-aggregated clump bulging outwards from a fibril. Figure 2.12b is a higher-resolution topography and phase image of the fibrous layer, several of the protofilaments are broken, a likely effect of the drying process. The mean half-height width of protofilaments at 48 hours was 33.7 (± 6.9) nm and height of 2.19 (± 0.54) nm. In Figure 2.12, several general features are worth noting, firstly that the fibrils appear to be layered in sections in which they are laterally assembled with no twisting and coiling, and second that the majority of fibrils appear straight and unbranched. Although these layering features could be a characteristic of aged fibrils, it is also possible that this may be an artefact of drying, especially the tendency for the fibrils to layer in a unidirectional manner.

The images displayed in Figures 2.12c and d are of an area on the perimeter of the fibrous layer. The topographical image of a fibrillar structure extending away from the layer is shown in figure 2.12c. The topography image suggests that the structure is a single fibril; however a zoom in of the structure indicates a bundle of at least 3 fibrils (figure 2.12d). The bundle is 1.78 μm in length and 52 nm wide, with the widths of the individual fibrils being 25.4, 26.6 and 30.7 nm. The fibrils within the bundle are straight with a regular uniform surface along their entire axis and no noticeable surface features.

2.3.5 *AFM in situ imaging*

The aim of the following experiments was to study amylin (20-29) fibrils in a hydrated form by AFM liquid imaging. A variety of salt solutions were investigated to determine the necessary conditions for physisorption of the amylin

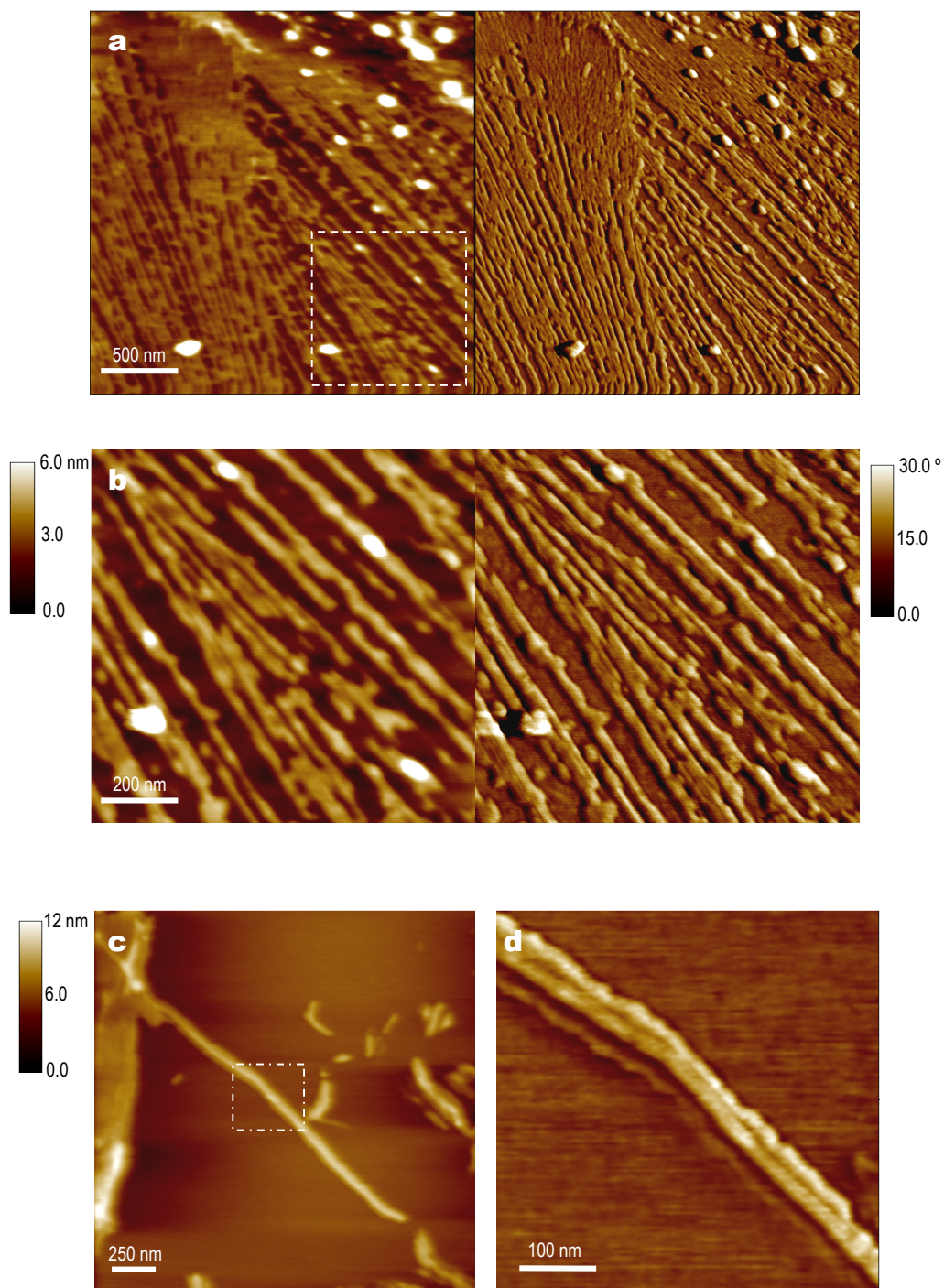


Figure 2.12: *Ex situ* AFM images of amylin (20-29) fibrils aged 48 hours. The final peptide concentration was 1 mg/ml in ultrapure water. **Figure 12a** shows a topography (left) and phase (right) image, a higher-resolution topography (left) and phase (right) image of the boxed area is shown in **figure 12b**. **Figure 12c** shows topography image at the perimeter of the fibrous area, a higher-resolution topography image of the boxed area is shown in **figure 12d**. Z range contrast bars are shown.

(20-29) fibrils to muscovite mica. An overview of the buffers and ionic species investigated are listed in table 2.2. Only a few of the conditions investigated provided a suitable environment for the immobilisation of the peptide material to the substrate, which was necessary for stable and reproducible AFM imaging.

Ionic content	pH
10 & 50 mM Tris HCl	7.2
10, 50, & 100 mM KCl (acidified)	4.0
100 mM MgCl ₂ (acidified)	4.0
50, 100, 150 mM Sodium acetate	5.5
125 mM Sodium acetate and 30 mM KCl	5.5
125 mM Sodium acetate and 30 mM MgCl ₂	5.0
50, 100, 150 mM Sodium citrate	4.0
130 mM Sodium acetate and 30 mM KCl	4.0
125 mM Sodium acetate and 30 mM KCl	4.0
125 mM Sodium acetate and 30 mM MgCl ₂	4.0

Table 2.2: Concentrations and pHs of the buffer and ion solutions investigated for the immobilisation of amylin (20-29) fibrils to mica.

2.3.5.1 Ultrapure Water

The images displayed in figure 2.13 are typical topography images observed when amylin (20-29) at a concentration of 125 µg/ml was imaged in ultrapure water after 18 hours (figure 2.13a and b). No fibrillar structures were observed physisorbed to the mica surface at either 18 or after the sample was left for a further 6 hours (images not shown). Control images of ultrapure water stored under identical conditions revealed clear mica (figure 2.13c).

Taking into account the air imaging experiments in the previous section in which fibrillar structures readily form in ultrapure water, it is likely that the immobilisation of the fibrils rather than impaired formation is the reason for these findings. Therefore it may be surmised that ultrapure water is not sufficient to

enable immobilisation of the amylin (20-29) fibrils to mica and thus further investigations were required.

2.3.5.2 Tris HCl

The study by Goldsbury *et al* 1999 [44] followed the fibrillisation of full-length amylin on mica substrate using 10 mM Tris HCl (pH 7.3) system and so was deemed a good starting strategy for imaging the amylin (20-29) fragment fibril in solution. Figure 2.14a shows a typical topography image of the amylin (20-29) sample (peptide concentration 100 µg/ml) after 8 hours in 10 mM Tris HCl at pH 7.2. No fibrillar structures are observed, instead the mica surface has a mottled appearance, which may be aggregated material that has not undergone fibrillisation. To increase the ionic strength of the Tris ions, the imaging concentration was increased to 50 mM. At 50 mM Tris HCl pH 7.2 small clumped aggregates are observed, however no fibrillar structures are observed (Figure 2.14b).

The isoelectric point for amylin (20-29) has been calculated to be 5.2. Therefore at pHs below this value, the peptides would have an overall positive charge. The surface of muscovite mica has an overall net negative charge, therefore using an ionic environment with a pH below 5.2, physisorption of the peptides and fibrils to the mica surface should be promoted. The topography image presented in figure 2.14c is of amylin (20-29) in 10 mM Tris HCl at pH 5.0. In similarity to the higher pH images, no fibrils are observed in the sample and the mica surface has a deposition of aggregated material. Figure 2.14d is a low-resolution topography image of a control solution of 10 mM Tris HCl at pH 5.0 with no amylin (20-29) present. As expected the mica surface appears clear with no material deposition.

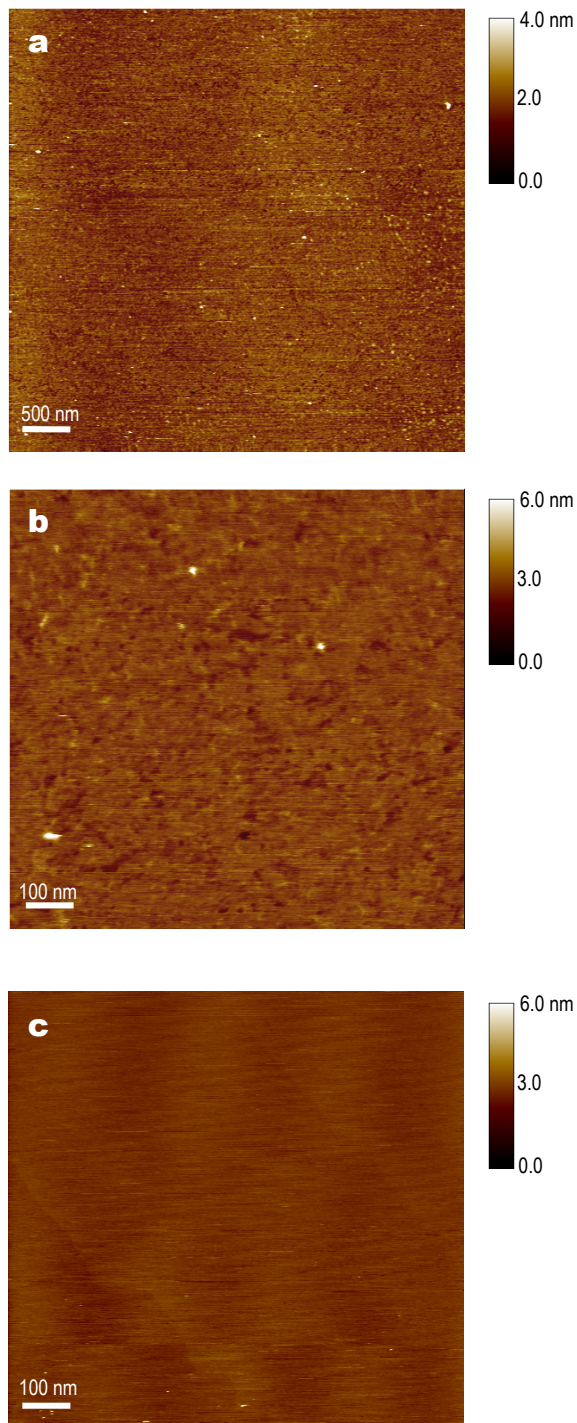


Figure 2.13: *In situ* AFM images of amylin (20-29) fibrils in ultrapure water at 18 hours. The final peptide concentration was 125 $\mu\text{g/ml}$. **Figure 13a** shows a topography image, a higher resolution topography image is shown in **Figure 13b**. **Figure 13c** is a topography image of the control solution. Z range contrast bars are shown.

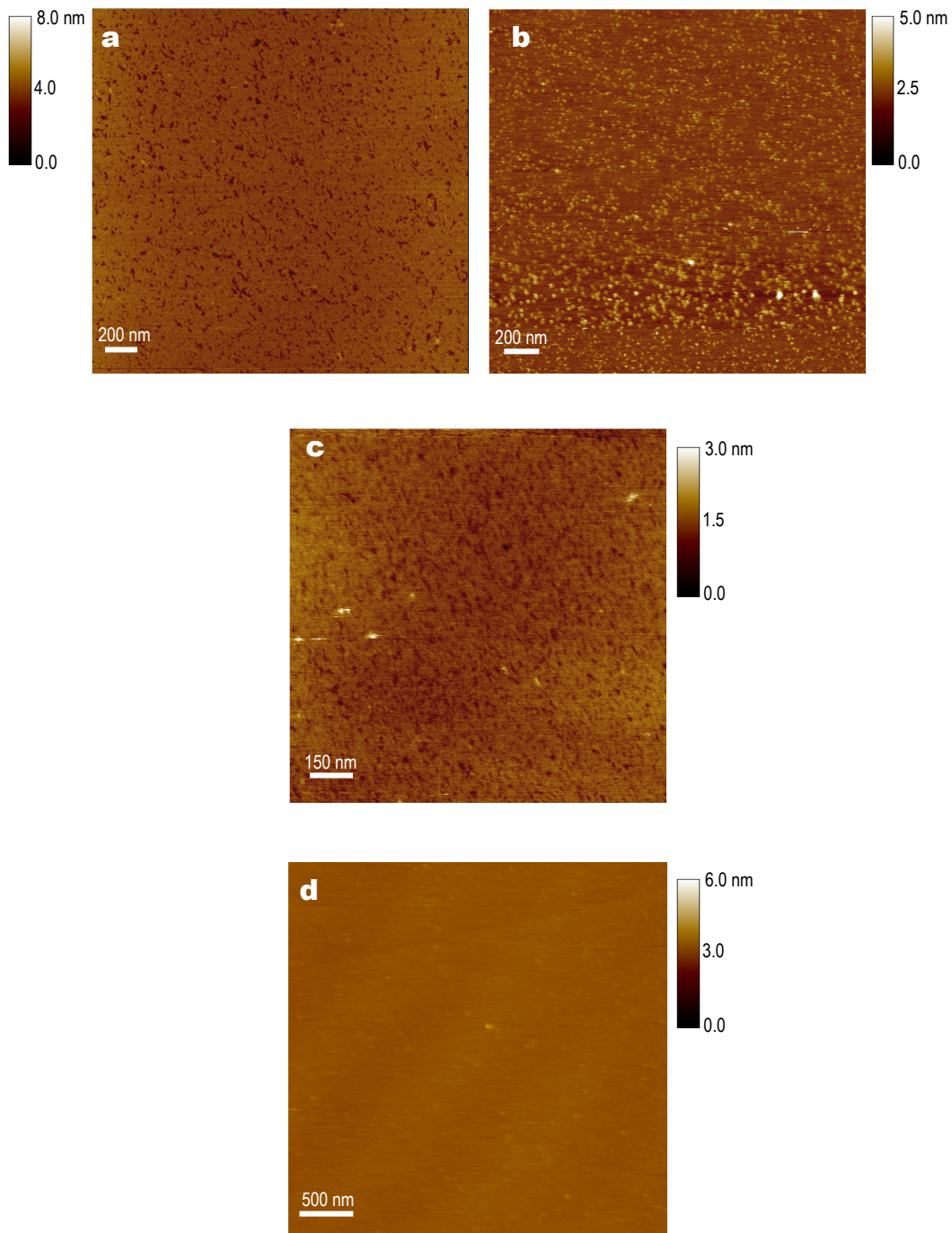


Figure 2.14: *In situ* AFM images of amylin (20-29) fibrils 10 mM and 50 mM Tris HCl. Peptide solutions were aged for 8 hours before imaging. The final peptide concentration for all was 100 $\mu\text{g/ml}$. **Figure 14a** shows a topography image of peptide in 10 mM TrisHCl at pH 7.2 and **figure 14b** shows a topography image of peptide in 50 mM TrisHCl pH 7.2. **Figure 14c** shows a topography image of peptide in 10 mM TrisHCl pH 5.0. **Figure 14d** is a topography image of the control sample. Z range contrast bars are shown.

2.3.5.3 Potassium chloride

The rationale behind the following set of experiments was to investigate the ability of ionic solutions with pH's lower than the isoelectric point of amylin (20-29) to facilitate the physisorption of the peptide fibrils to a mica surface.

The topography image shown in figure 2.15a is typical of the low-resolution liquid images of amylin (20-29) in solutions of 10 mM potassium chloride pH 4. The amylin sample was prepared in ultrapure water and then diluted to 100 µg/ml in the potassium chloride (KCl) solution after 4 hours and imaged in solution after 8 hours. The mica surface has a granular appearance which is most likely peptide material and not potassium salts agglomerates as the solution was filtered through a 0.2 µm filter prior to use and were not observed in control samples.

To determine whether the KCl had interfered with the self-assembly of the amylin (20-29) fibrils, aliquot samples were removed after 6 ½ hours and dried onto freshly cleaved mica. Figure 2.15b and c are typical low and high-resolution (respectively) images of the dried sample. A dense mat of clearly defined fibrillar structures is observed covering the entire sample surface. The high-resolution image shows the protofilaments to have no discernable surface topographies, and are flat ribbon-like structures with many having extending branches and dimensions in the same range as previously observed. Worthy of note is the apparent lack of globular material seen in the liquid images.

To determine whether a higher concentration of the monovalent salts would facilitate physisorption, the experiment was repeated at the same pH but the ionic strength of the KCl solution was increased 5 fold. Figure 2.16a, b and c are typical high-resolution topography images of the fibrillar structures observed in the solution at 8 hours, with peptide concentration of 100 µg/ml. Fibrils were observed only as individual structures with no lateral or coiling aggregation of several fibrils together. Fibrils were generally observed as flexible rods, either branched (figure 2.16b) or unbranched fibril of width 10.67 nm and height of 1.66 nm can be seen in figure 2.16c, with half-height widths of 10.5 and 13.7 nm and heights 1.66 and 1.75 nm (respectively).

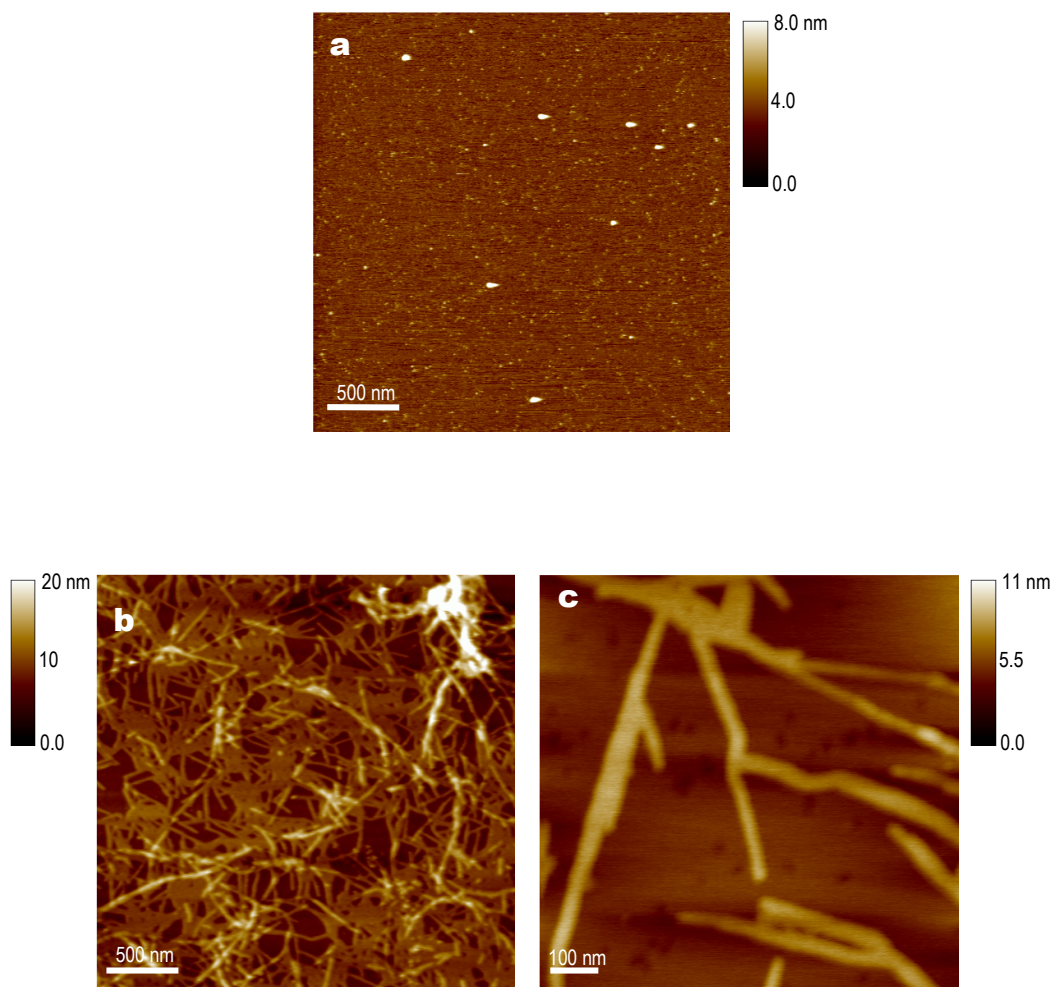


Figure 2.15: *In situ* and *ex situ* AFM images of amylin (20-29) fibrils in 10 mM KCl pH 4. Peptide solutions were aged for 8 hours before imaging. The final peptide concentration was 100 $\mu\text{g/ml}$. **Figure 15a** shows an *in situ* topography image. **Figure 15b** shows a topography image of the same sample after drying in N_2 gas stream and imaging in air (sample aged 6½ hours). A higher-resolution topography image of the dried sample is shown in **figure 15c**. Z range contrast bars are shown.

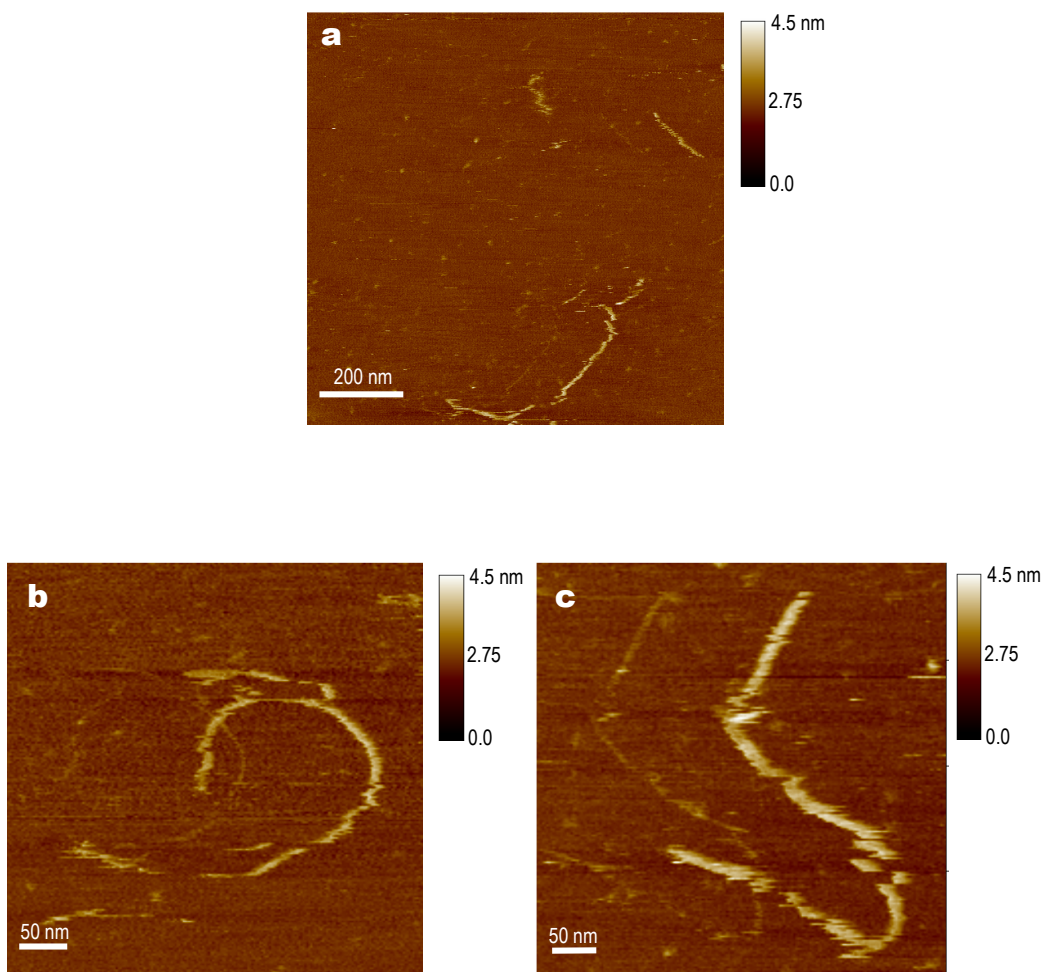


Figure 2.16: *In situ* AFM images of amylin (20-29) fibrils in 50 mM KCl pH 4. Peptide solutions were aged for 8 hours before imaging. The final peptide concentration was 50 $\mu\text{g/ml}$. **Figure 16a** shows a topography image. Higher-resolution topography images of individual fibrils are shown in **figure 16b** and **figure 16c**. Z range contrast bars are shown.

Although the solution conditions have enabled imaging of the fibrils, a double-tipping effect was observed in all the images generated. Furthermore, the images are unstable due to insufficient adsorption of the fibrils to the surface which has caused the structures to appear broken. To overcome these issues the concentration of the solution was increased further to 100 mM KCl, however no fibrillar structures were observed at this higher KCl concentration. Furthermore, on increasing the peptide concentration to 200 µg/ml no fibrillar material was observed.

2.3.5.4 Magnesium chloride

Typical low and high-resolution topography images are presented in figure 2.17 of amylin (20-29) at 8 hours in a solution of magnesium chloride (MgCl₂). The peptide concentration was 100µg/ml in a 30 mM MgCl₂ solution at pH of 4. No fibrillar structures were observed in the MgCl₂ solution during imaging however the mica surface did have aggregates of material across the surface. This aggregated material is likely to be peptide-based as the MgCl₂ solution was filtered to 0.2 µm prior to use and were not observed in control samples in the absence of peptide. In the higher-resolution image (figure 2.17b), one can see that the globular materials are very low structures with no distinct surface regularity and of varying dimensions, and most likely to be aggregated peptide deposits.

2.3.5.5 Sodium acetate

Following the limited success with simple monovalent and divalent ionic solutions, more complex buffer solutions were investigated. Sodium acetate buffer (pH 5.5) at three different concentrations of 50, 100 and 150 mM were studied.

No fibrillar structures were observed at 8 hours in the 50 mM sodium acetate, instead a dense layer of material was present covering the entire mica surface. Figure 2.18a is a typical topography image of amylin (20-29) at a concentration of 150 µg/ml in 50 mM sodium acetate. The mat of material contains some holes, but no individual fibrillar structures could be elucidated at either low or high resolution. With the intention of reducing the dense coverage of material the peptide concentration was lowered to 100 µg/ml. Figure 2.18b is typical of the topography images observed; a dense layer of material has still formed on the surface and no distinguishable fibril features were apparent. From these images it

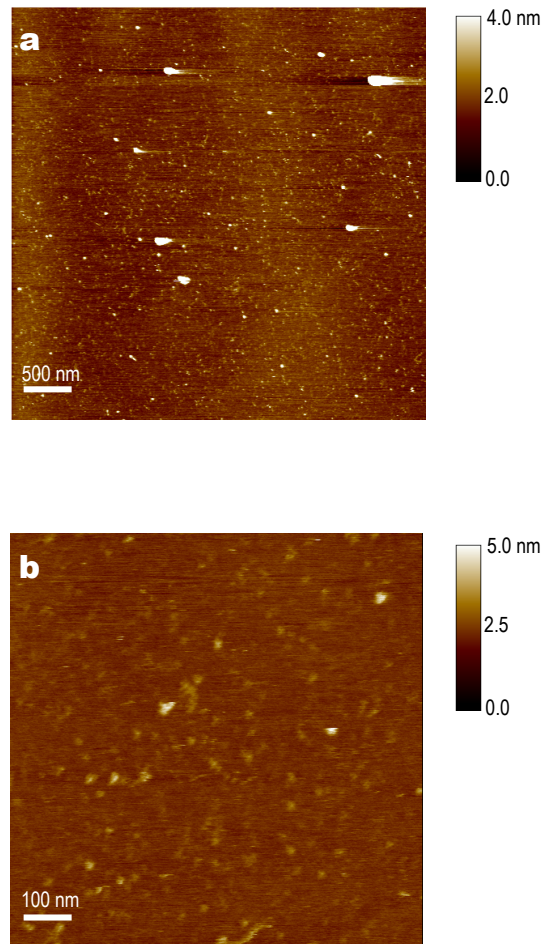


Figure 2.17: *In situ* AFM images of amylin (20-29) fibrils 30 mM MgCl₂ pH 4. Peptide solutions were aged for 8 hours before imaging. The final peptide concentration was 100 µg/ml. **Figure 17a** shows a topography image, a higher-resolution topography image is shown in **figure 17b**. Z range contrast bars are shown.

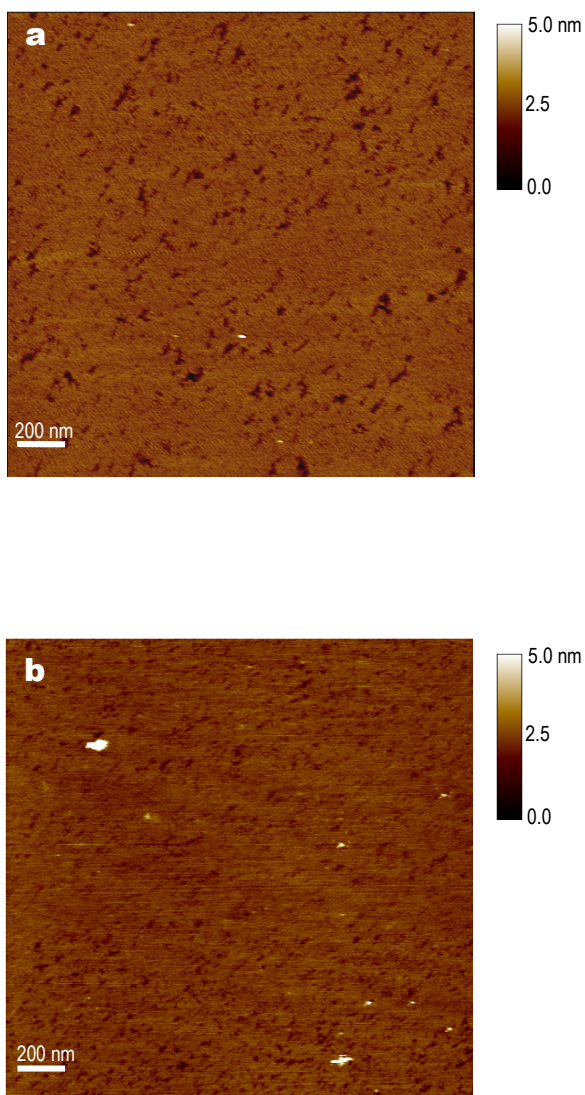


Figure 2.18: *In situ* AFM images of amylin (20-29) fibrils 50 mM sodium acetate pH 5.5. Peptide solutions were aged for 8 hours before imaging. **Figure 18a** shows a topography image of the sample at a final peptide concentration of 150 µg/ml. To reduce molecular overcrowding of the scan area the peptide concentration was reduced to 100 µg/ml, **figure 18b** shows a topography image of the sample. Z range contrast bars are shown.

is not clear whether the sodium acetate has interfered with fibril formation and thus no fibrils are formed or that there are fibrils present but that the individual fibrils are not resolvable by the AFM tip aperture due to dense aggregation and packing together on the surface.

On increasing the sodium acetate concentration to 100 mM success was achieved in imaging individual fibrillar structures. A selected sample of the successive topography images captured during the course of the study are shown in figure 2.19a to f. An animation of these images can be found in Appendix A. The images were collected over approximately 2 ½ hours when the peptide solution was aged between 5 to 7 ½ hours, the exact length of minutes is noted against the individual image. The peptide concentration was 100 µg/ml. Fibrils appear to originate from a dense clump and elongate outwards retaining the same width and height along the entire axis. Fibrils were flat ribbon-like structures with widths in the range of 10-15 nm and heights of 2-4 nm. Individual fibrils often appeared granular along their surface but did not generate branches from a central axis, instead several fibrils elongated from the same nucleating clump. An unfortunate artefact of AFM imaging in solution is drift, despite efforts to maintain the same position on the mica during the course of imaging there was some drift experienced. A red cross marks the same spot on the mica surface in each of the images shown in figure 2.19a-f. Figure 2.19g is a control topography image of the 100 mM sodium acetate solution in the absence of peptide, no fibrillar structures are present.

A study of the kinetics of fibril formation was performed on a random sample of protofilaments from these images. The change in length of the fibrils was measured over time and plotted as a graph shown in figure 2.19h. The average increase in length was calculated per minute and varied between fibril from approximately 2 to 10 nm min⁻¹. The growth of fibrils could be bidirectional and it was often noted that the growth was suppressed if another fibril blocked the path of the elongating fibril. This may be a reason for the variation in fibril rates as a growing fibril once blocked by another would not undergo any further increase in length over the time period.

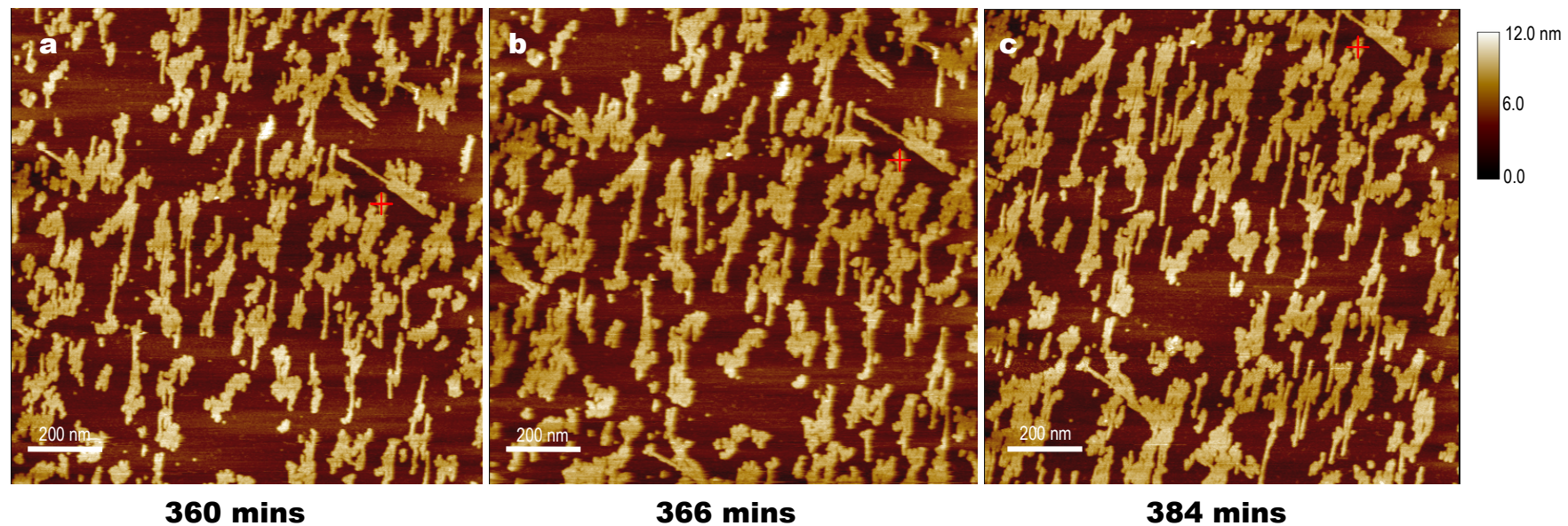
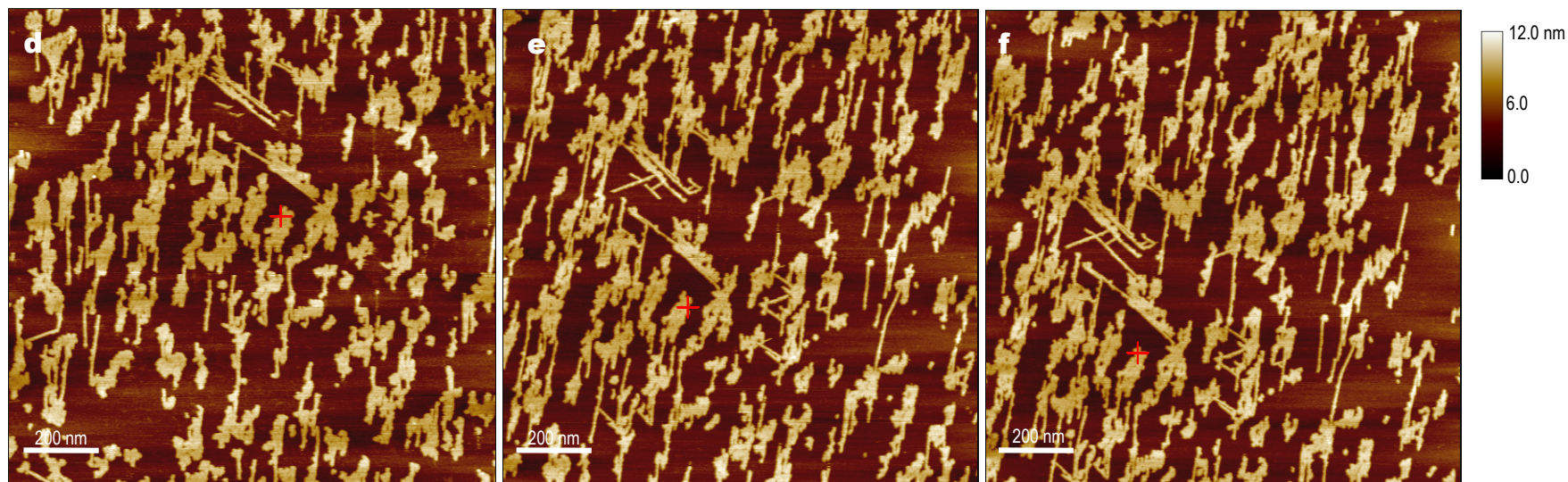


Figure 2.19: *In situ* AFM images of amylin (20-29) fibrils in 100 mM sodium acetate pH 5.5. The final peptide concentration was 100 $\mu\text{g/ml}$. **Figures 19a-f** are successive topography images with the age of the solution shown in minutes below. The red cross highlights the same point on the mica surface in each image. Z range contrast bars are shown. The line graph shown in **figure 19g** is the change in length with time of 7 randomly chosen fibrils within the scan area. The rate of fibril elongation is shown as nm per min. **Figure 19h** shows a topography image of the control sample. Z range contrast bar is shown.



393 mins

403 mins

409 mins

(Figure 2.19 continued: *In situ* AFM images of amylin (20-29) fibrils in 100 mM sodium acetate pH 5.5)

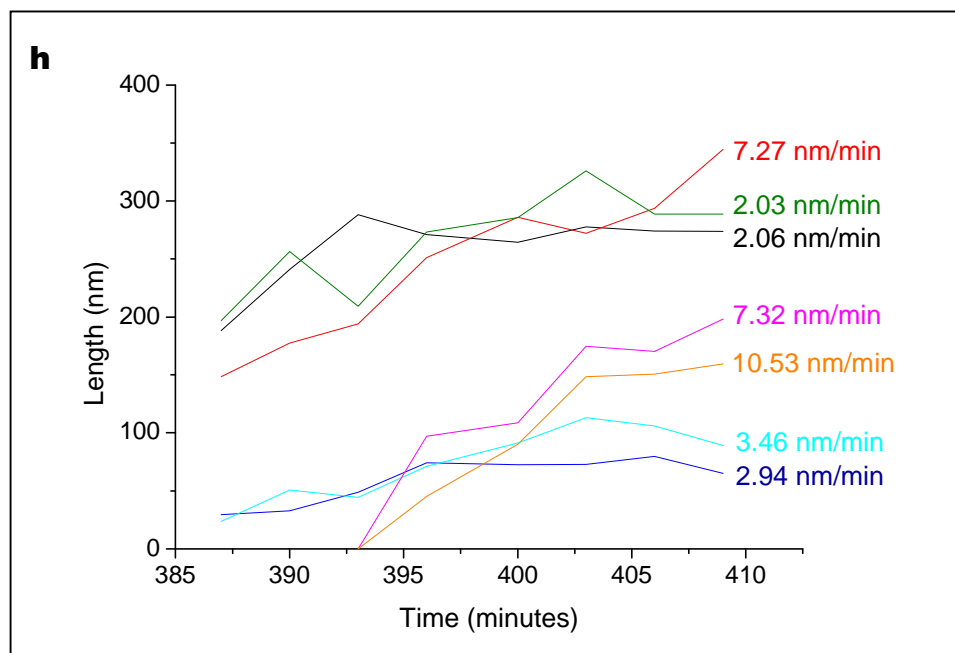
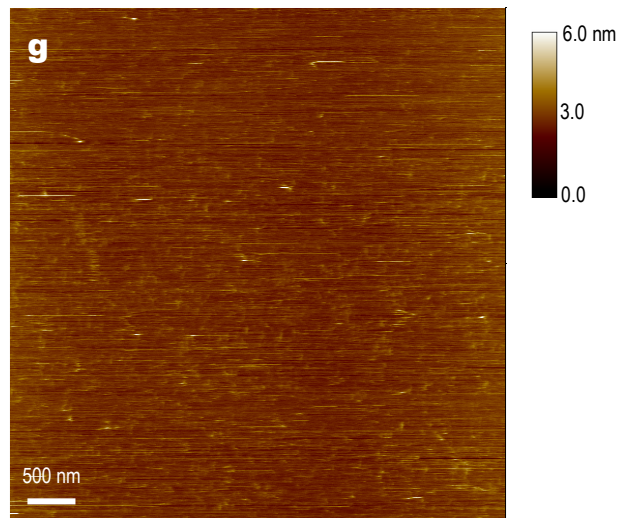


(Figure 2.19 continued: *In situ* AFM images of amylin (20-29) fibrils in 100 mM sodium acetate pH 5.5)

The concentration of sodium acetate was increased further to 150 mM (pH 5.5). A typical low-resolution topography image of 150 $\mu\text{g/ml}$ amylin (20-29) in 150 mM sodium acetate at 8 hours is shown in figure 2.20a and a higher-resolution image of the boxed area is shown in figure 2.20b. No fibrillar structures were present at this higher buffer concentration; however the mica surface has a grainy appearance. To determine whether the higher sodium acetate concentration had interfered with fibrillisation a sample was removed and dried onto freshly cleaved mica, the topography images are shown in figure 2.20c and a higher-resolution image is shown in figure 2.20d. The dried sample revealed that fibrils are still forming in 150 mM sodium acetate concentration, however large aggregates of varying size and morphology were frequently observed too. These aggregates are most likely amorphous aggregates of peptide rather than buffer salts as the solution was filtered to 0.2 μm prior to use.

2.3.5.6 Sodium acetate and potassium chloride system

Given the differing dimensions and morphologies of the fibrillar structures observed in the sodium acetate buffer solutions to those observed in the KCl ion solution, a further experiment was devised to investigate the electrostatic effects of a buffer with a monovalent ion on the fibril formation of amylin (20-29).

Clear high-resolution images of the amylin (20-29) fibrils were produced using a 125 mM sodium acetate and 30 mM potassium chloride system. Figure 2.21a is a typical low-resolution topography image of the fibrillar structures observed in the sample at 18 hours with a peptide concentration of 150 $\mu\text{g/ml}$. A high-resolution topography image of the boxed area in figure 2.21a is presented in figure 2.21b and a zoomed in 3D representation of the surface is shown in figure 2.21c. The fibrils were unbranched and ribbon-like structures with no apparent surface morphology. Fibrils appear to preferentially aggregate together forming isolated clumps directly onto the mica surface. Unlike the aggregation patterns observed in fibrils self-assembled in water and imaged in air, no twisting or coiling of the fibrils into bundles was observed. However, here the fibrils have a propensity to laterally align (highlighted by arrow in figure 2.21c). Individual fibrils have considerable flexibility with the ability to freely form curves and loops and to overlap one another on the surface.

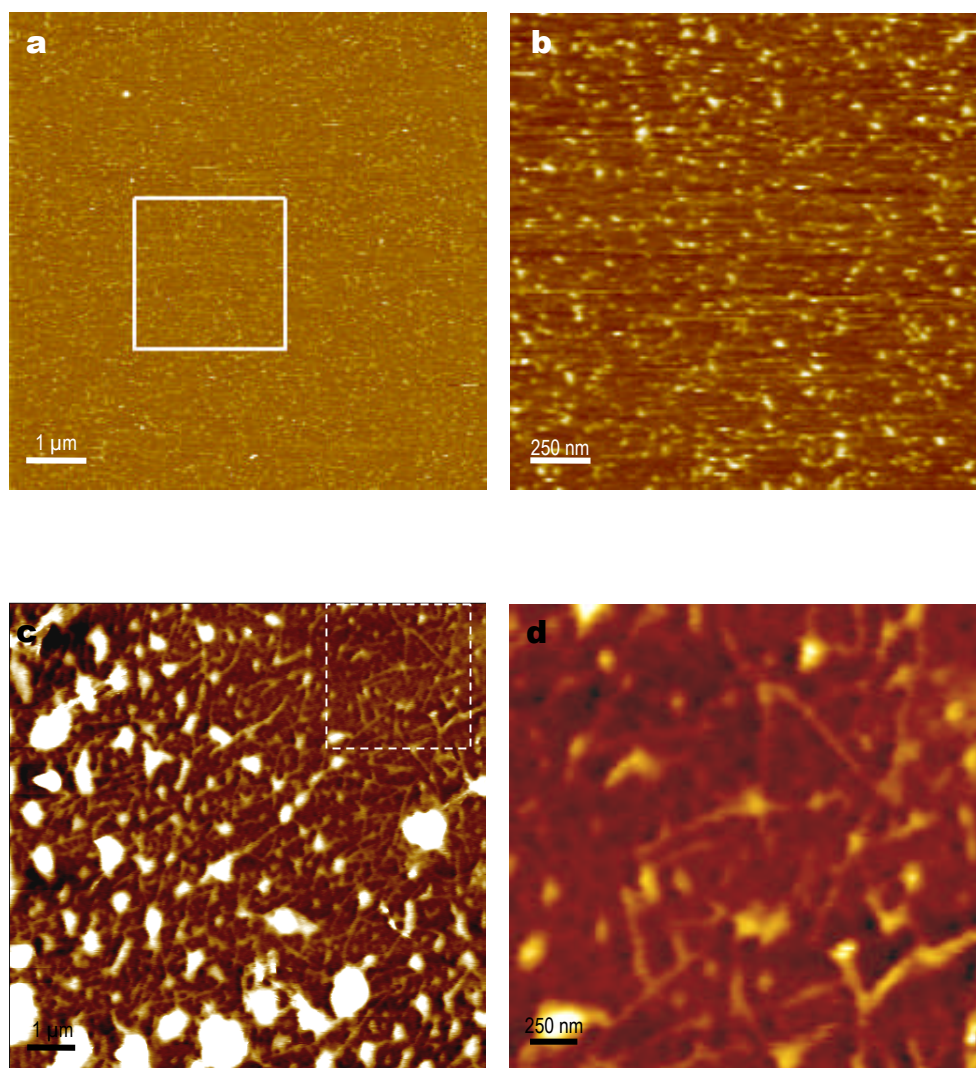


Figure 2.20: *In situ* and *ex situ* AFM images of amylin (20-29) fibrils 150 mM sodium acetate pH 5.5. Peptide solutions were aged for 8 hours before imaging. The final peptide concentration was 150 $\mu\text{g}/\text{ml}$. **Figure 20a** shows a topography images with a higher-resolution topography image of the boxed area is shown in **figure 20b**. **Figure 20c** shows a topography image of the sample after drying. **Figure 20d** shows a digital zoom image of the boxed area in fig 20c.

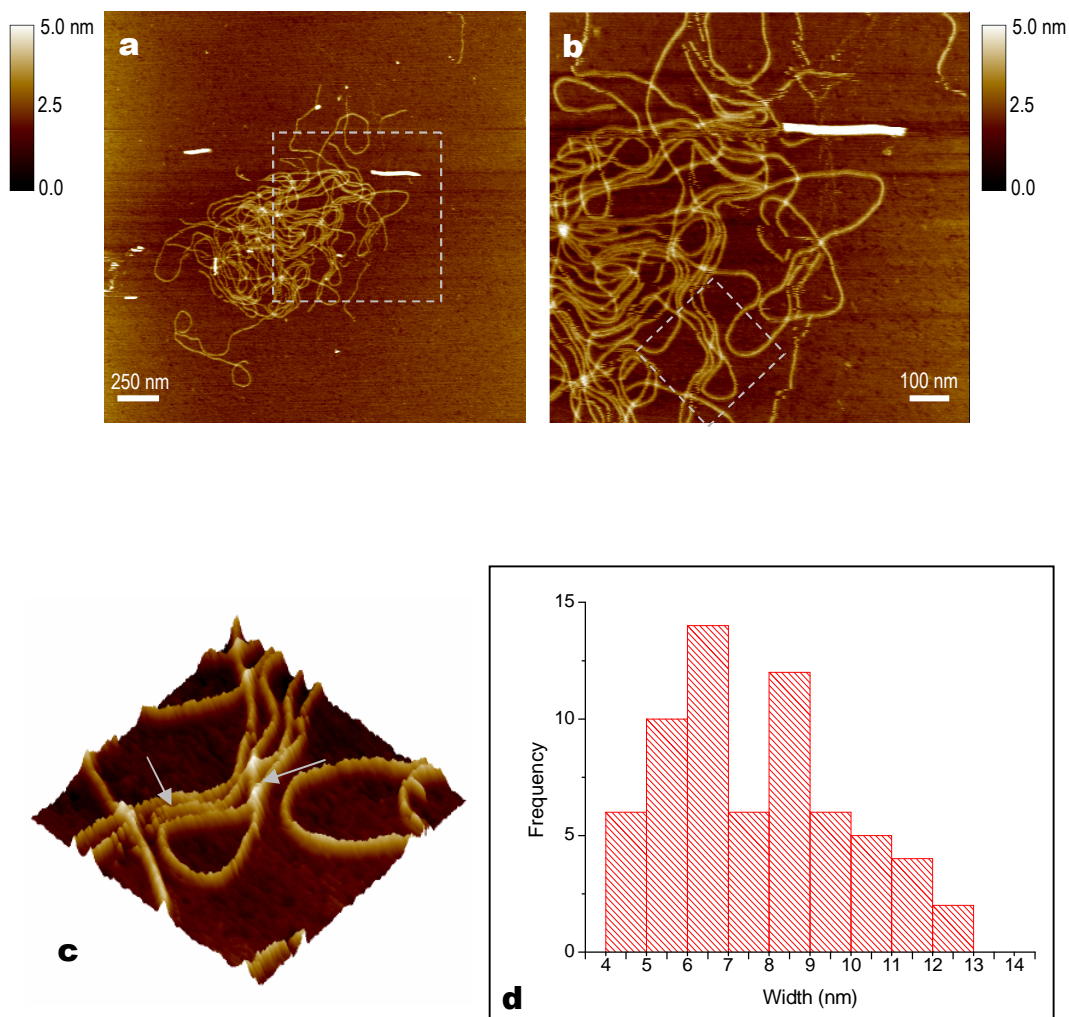


Figure 2.21: *In situ* AFM images of amylin (20-29) fibrils 125 mM sodium acetate and 30 mM KCl at pH 5.5. Peptide solutions were aged for 8 hours before imaging. The final peptide concentration was 150 $\mu\text{g/ml}$. **Figure 21a** shows a topography image of the sample, a higher-resolution topography image of the boxed area is shown in **figure 21b**. A 3D representation of the topography image in figure 21b is shown in **figure 21c**. **Figure 21d** is a histogram of the frequency distribution of fibril half-height widths in the sample. Z range contrast bars are shown.

The histogram in figure 2.21d shows the half-height width distribution for the fibrils in 125 mM sodium acetate and 30 mM potassium chloride, the mean width was calculated as 8.27 (± 2.17) nm and mean height of 1.5 (± 0.21) nm.

2.3.5.7 Sodium acetate and magnesium chloride system

The topography image shown in figure 2.22a is typical of the low-resolution information obtained from samples of 200 $\mu\text{g/ml}$ amylin (20-29) in 125 mM sodium acetate with 30 mM magnesium chloride at 8 hours. A dense covering of globular structures can be observed. A high-resolution topography image shown in figure 2.22b and the 3D topography representation (figure 2.22c) reveal that the structures are densely aggregated together and are several layers thick. Furthermore, it can be observed that the globular structures are sufficiently stable in their multilayer packing to remain fully bound to one another even during the raster scanning of the tip during imaging. The globular structures vary in dimension with widths ranging from 30 to 100 nm. In control samples of sodium acetate and magnesium chloride no such structures are observed, and therefore it is surmised that these globular features comprise aggregated peptide material.

Previous results have not revealed any similar structures in solutions of amylin (20-29) peptide with either sodium acetate (figure 2.19-21) or magnesium chloride (figure 2.18). In these samples amylin (20-29) was placed directly at time = 0 into a solution of sodium acetate and MgCl_2 . Therefore to determine whether the MgCl_2 in combination with sodium acetate was interfering with the fibrillisation of amylin (20-29), the addition of MgCl_2 to the fibrillisation mixture was delayed until 4.5 hours and 6 hours. The rationale behind these timings was based on the preliminary *ex situ* imaging study in which the first observation of small fibrils was recorded at approx 4 hours with a significant increase in the number of fibrils at 6 hours (figure 2.9). Therefore by addition of MgCl_2 at these time points, fibrils should already be formed. If no fibrils are observed then it may be assumed that the MgCl_2 /sodium acetate combination has a unique aggregating effect on the pre-formed fibrils.

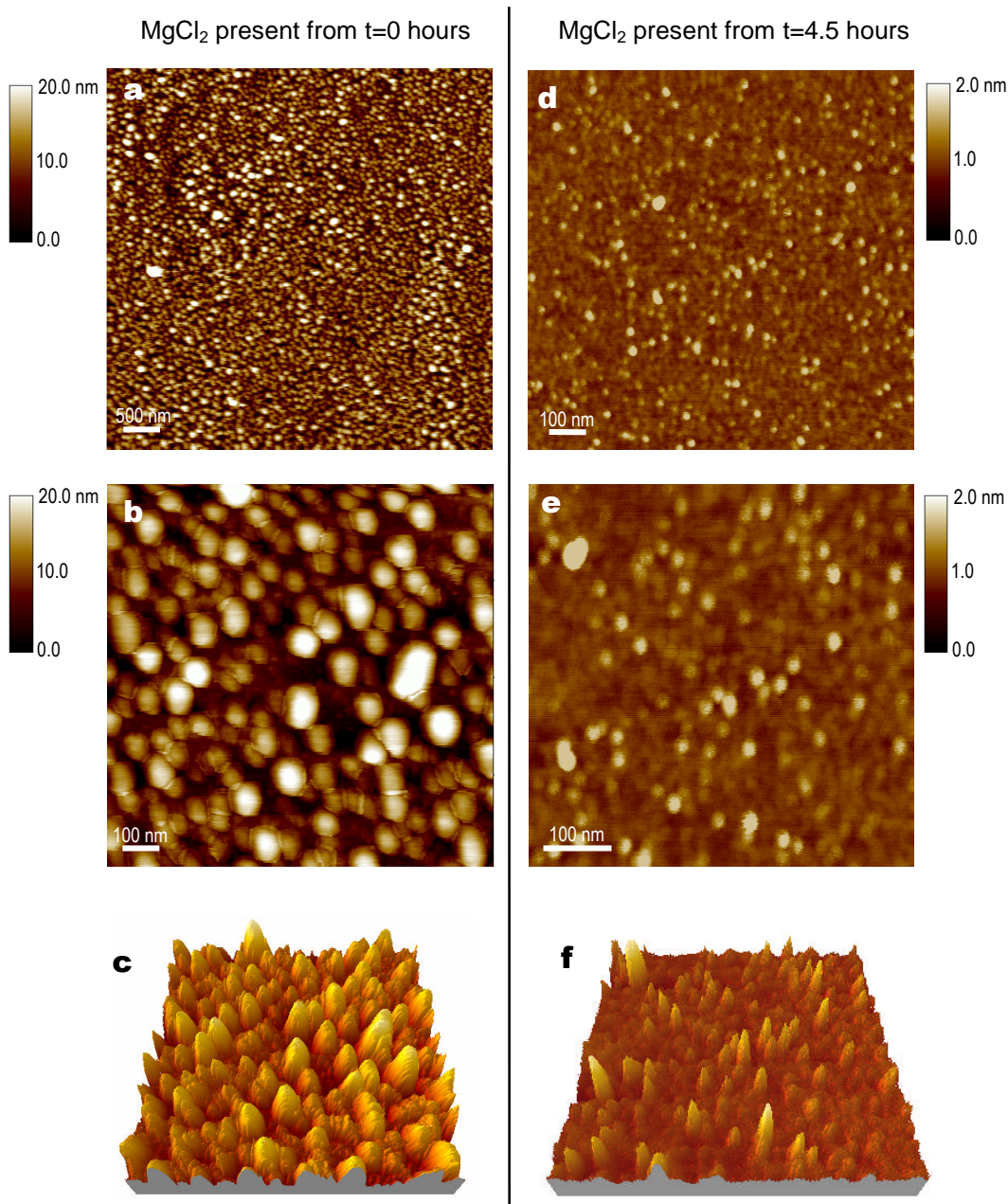


Figure 2.22: *In situ* AFM images of amylin (20-29) fibrils in 125 mM sodium acetate and 30 mM MgCl₂. The final peptide concentration was 200 µg/ml. **Figure 22a** shows a topography image of the peptide sample when MgCl₂ was added at t= 0 hours. A higher resolution topography image of the sample is shown in **figure 22b** and a 3D representation of the surface is shown in **figure 22c**. **Figure 22d** shows a topography image of the peptide sample when MgCl₂ was added at t= 4.5 hours. A higher resolution topography image of the sample is shown in **figure 22e**, and **figure 22f** is a 3D representation of the surface. Z range contrast bars are shown. *Continued on next page.*

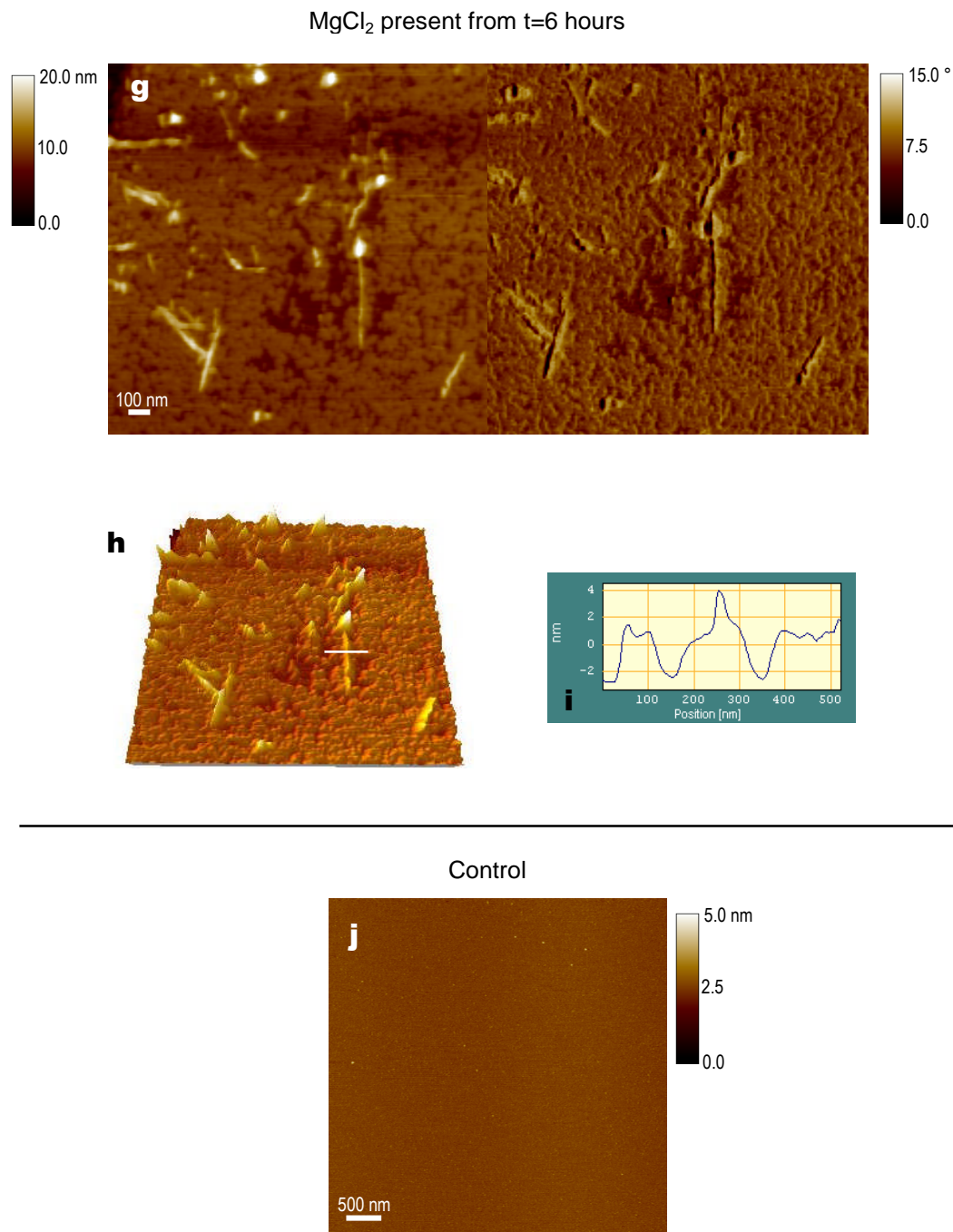


Figure 2.22 (continued): *In situ* AFM images of amylin (20-29) fibrils in 125 mM sodium acetate and 30 mM MgCl₂. The final peptide concentration was 200 µg/ml. **Figure 22g** shows a topography (left) and phase (right) image of the peptide sample when MgCl₂ was added at t= 6 hours. Z range contrast bars are shown. A 3D representation of the surface is shown in **figure 22h** and a cross-sectional profile shown in **figure 22i**. **Figure 22j** shows a topography image of the control sample. Z range contrast bars are shown.

The high-resolution topography images shown in Figure 2.22 d and e are of the globular structures observed when 30 mM MgCl₂ was added to a solution of amylin (20-29) in 125 mM sodium acetate after 4.5 hours and then imaged up to 8 hours. These globular structures are slightly smaller, have a more spherical appearance but are not as densely packed (figure 2.22f) as previously seen in the samples with MgCl₂ present from 0 hours (figures 2.22 a-c); however no fibrillar structures were observed.

Conversely when the experiment was repeated using identical conditions but the MgCl₂ was added at 6 hours fibrillar structures were observed. Figure 2.22g is a high-resolution topography image (left) of the sample at 8 hours, further topographical information can be obtained from the phase image to the right. A 3D representation of the sample surface is shown in figure 2.22h. The fibrils appear to be adsorbed to monolayer of material covering the mica surface. Dimensions are greater than previously observed for amylin (20-29) fibrils and are in the range of 25 to 40 nm in width. The cross-sectional profile (figure 2.22i) shows that the monolayer is approximately 2.8 to 3.2 nm thick and is in the same height range as the fibrils adsorbed to its surface. A control topography image in the absence of peptide is shown in figure 2.22j.

2.3.5.8 Sodium citrate

Sodium citrate was selected for its lower pH buffering capacity and was investigated at 3 concentrations of 50, 100 and 150 mM at pH 4. Typical high-resolution topography images of amylin (20-29) at a concentration of 150 µg/ml imaged in each of the solutions are shown in figure 2.23.

As can be seen in the topography image presented in figure 2.23a, at 50 mM sodium citrate fibrillar structures were observed adsorbed to the mica surface in samples aged 8 hours. During imaging in 50 mM sodium citrate, despite using low scan rates and scan area of 1 µm, it was found that topographical features generally appeared blurred and undefined. Due to this imaging artefact, features may appear larger than their true dimension.

On repeating the experiment using a higher concentration of 100 mM sodium citrate a combination of fibrillar structures and non-descript aggregates were observed on the mica surface. Figure 2.23b is a typical high-resolution image of the topographical structures observed at 8 hours. The aggregates are alike in appearance to those observed in 100 mM sodium acetate (figure 2.19) and the fibrillar structures appear to originate from the aggregates in a similar manner. Figure 2.23c is a higher-resolution image of the boxed area in figure 2.23b, all fibrils appear to be projecting from an aggregate of material. Fibril dimension are comparable to those observed in the sodium acetate and potassium chloride images (figure 2.21) in the range of 5 to 10 nm. Given the small dimensions of the fibrillar structures, it is possible that the aperture of the AFM tip is too large (mean NPS tapping-mode tip radius is 15 nm (Olympus)) to resolve topographical features within the aggregates. Therefore it is possible that these aggregates may not be single structures but instead are an agglomeration of laterally aligned truncated protofilaments or pre-fibrillar intermediates.

However, when the peptide sample was imaged at a higher concentration of 150 mM buffer, no fibrillar structures were observed, even after 24 hours in solution. Figure 2.23d is typical of the high-resolution topography images of the sample at 24 hours, adsorbed to the mica surface are aggregates with a range of sizes. It can be assumed that as the control images of sodium citrate with no peptide present produced clear images (images not shown) that these aggregates comprise of peptide material. Following imaging of the liquid sample, the mica was dried and imaged. Figure 2.23e is the tapping-mode air image of the mica section. Large quantities of fibrils can be seen which suggests that the 150 mM sodium citrate solution does not prevent fibrillisation, but that the higher concentration is not conducive to imaging of the amylin (20-29) fibrils.

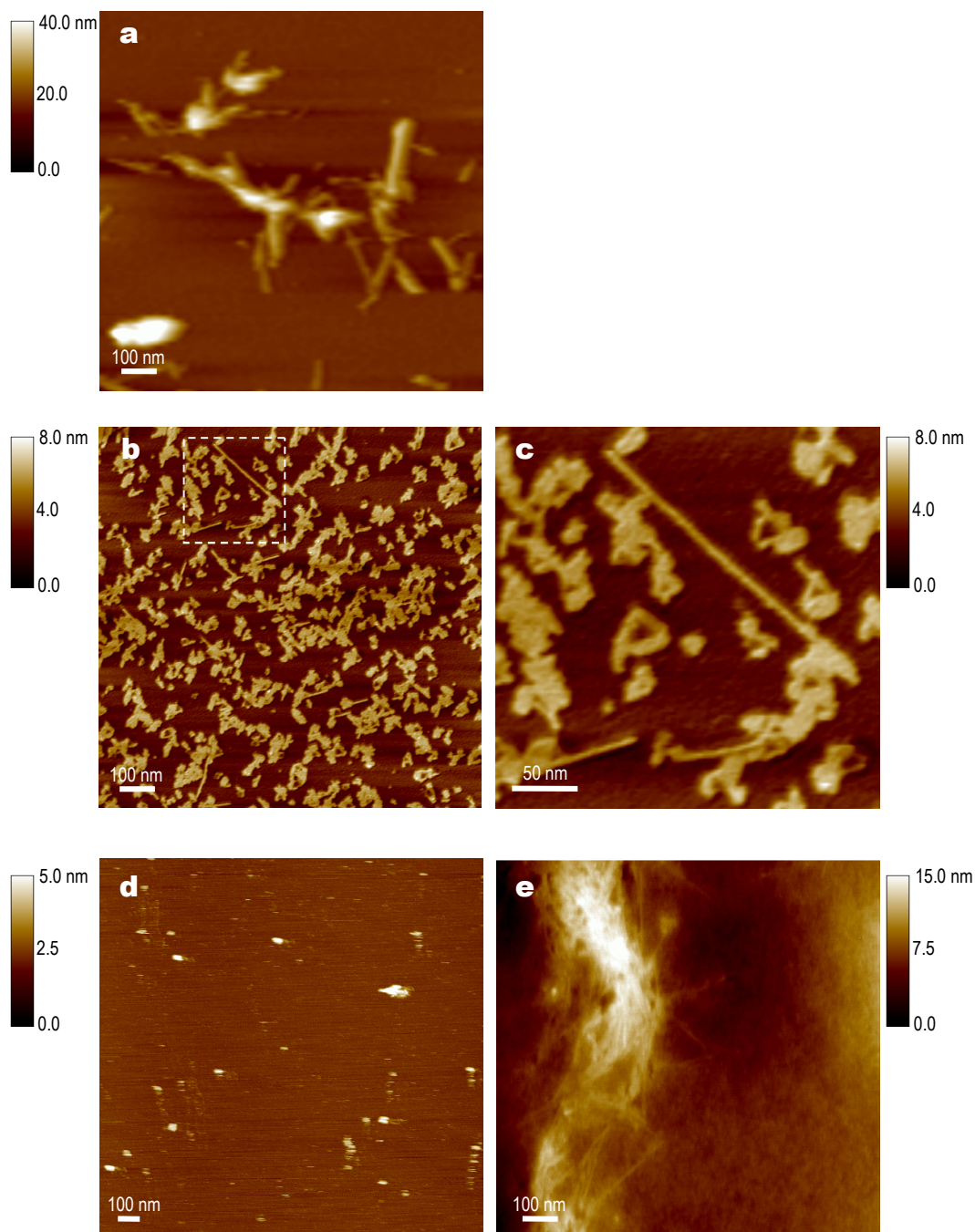


Figure 2.23: *In situ* AFM images of amylin (20-29) fibrils in 50, 100 and 150 mM sodium citrate at pH 4.0. The final peptide concentration was 150 $\mu\text{g/ml}$. **Figure 23a** shows a topography image of amylin (20-29) fibrils in 50 mM sodium citrate. **Figure 23b** shows a topography image of amylin (20-29) fibrils in 100 mM sodium citrate, a higher-resolution image of the boxed area is shown in **figure 23c**. **Figure 23d** shows a topography image of amylin (20-29) fibrils in 150 mM sodium citrate at 24 hours and **figure 23e** shows an *ex situ* topography image of the same sample after drying. Z range contrast bars are shown.

2.3.5.9 Sodium citrate and potassium chloride system

The topography images presented in figure 2.24 are typical of the fibrillar structures observed in 125 mM sodium citrate and 30 mM potassium chloride solution. The fibrils were straight and unbranched with a smooth outer topography at 18 hours, displaying considerable flexibility, and in some instances with the ability to bend almost as a hairpin. Figure 2.24b is a zoom topography image showing an area of high fibrillar aggregation. The 3D representation (figure 2.24c) of the same area shows that the height at what appears to be the epicentre of the aggregation is not the cumulative height of the surrounding fibrils. Therefore, indicative that this point may be a nucleation point from which the fibrils originate rather than several fibrils overlapping on the surface. Such a feature was observed previously during *ex situ* imaging (figure 2.7a).

Fibrillar dimensions had a half-height width distribution (figure 2.24d) with mean of 18.03 (± 2.13) nm. The fibrils displayed a height distribution with mean of 1.5 (± 0.23) nm. These dimensions suggest that the fibrils have a flat ribbon-like appearance.

The blurred edges of the fibrils and noise within the image suggest that the fibrils were not fully adsorbed to the mica surface, remaining slightly flexible within the solution whilst the AFM tip was scanning the surface. In fact, prolonged imaging of the sample was not possible due to aggregation of material to the tip which resulted in double-tipping and considerable noise distortion during imaging. The background has a mottled appearance (figure 2.24b) indicating that the aggregated fibrils are layered on top of a dense layer of material. It can be assumed that this surface layer contains peptide material as control images in the absence of amylin (20-29) show only clear mica surfaces (images not shown).

A time-lapse study of fibrils in 130 mM sodium citrate and 30 mM potassium chloride was performed between 0 and 8 ½ hours; successive topography images are shown in figure 2.25a to f. There is little change in the fibril dimensions over the time course; however the topography images highlight the flexibility in the fibrils.

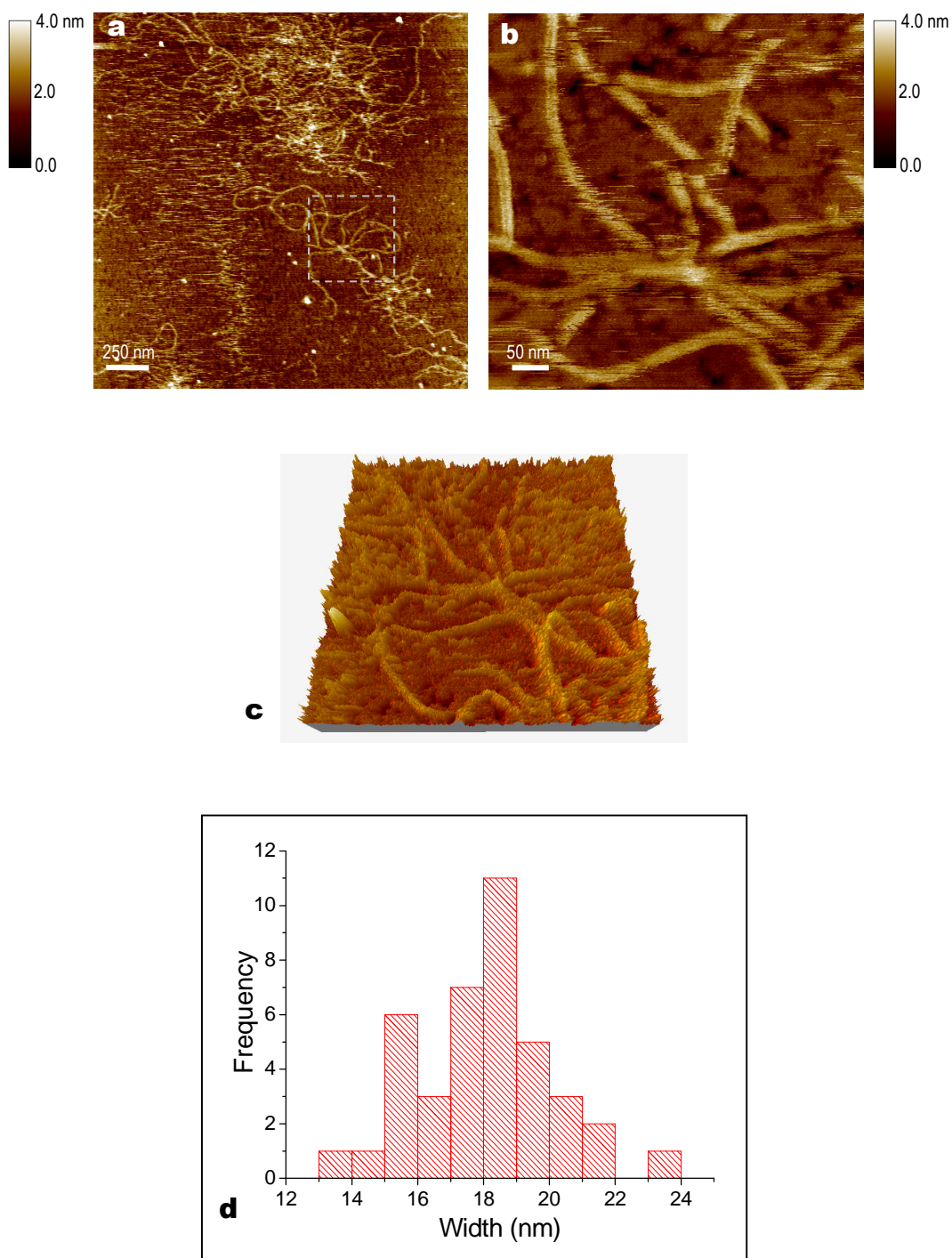


Figure 2.24: *In situ* AFM images of amylin (20-29) fibrils 130 mM sodium citrate and 30 mM KCl at pH 4. Samples imaged at 18 hours, KCl added at $t = 0$ hours, the final peptide concentration was 150 $\mu\text{g}/\text{ml}$. **Figure 24a** shows a topography image of the peptide sample, a higher-resolution topography image of the boxed area is shown in **figure 24b**. Z range contrast bars are shown. A 3D representation of the surface is shown in **figure 24c**. **Figure 24d** is a histogram of the frequency distribution of fibril half-height widths in the sample.

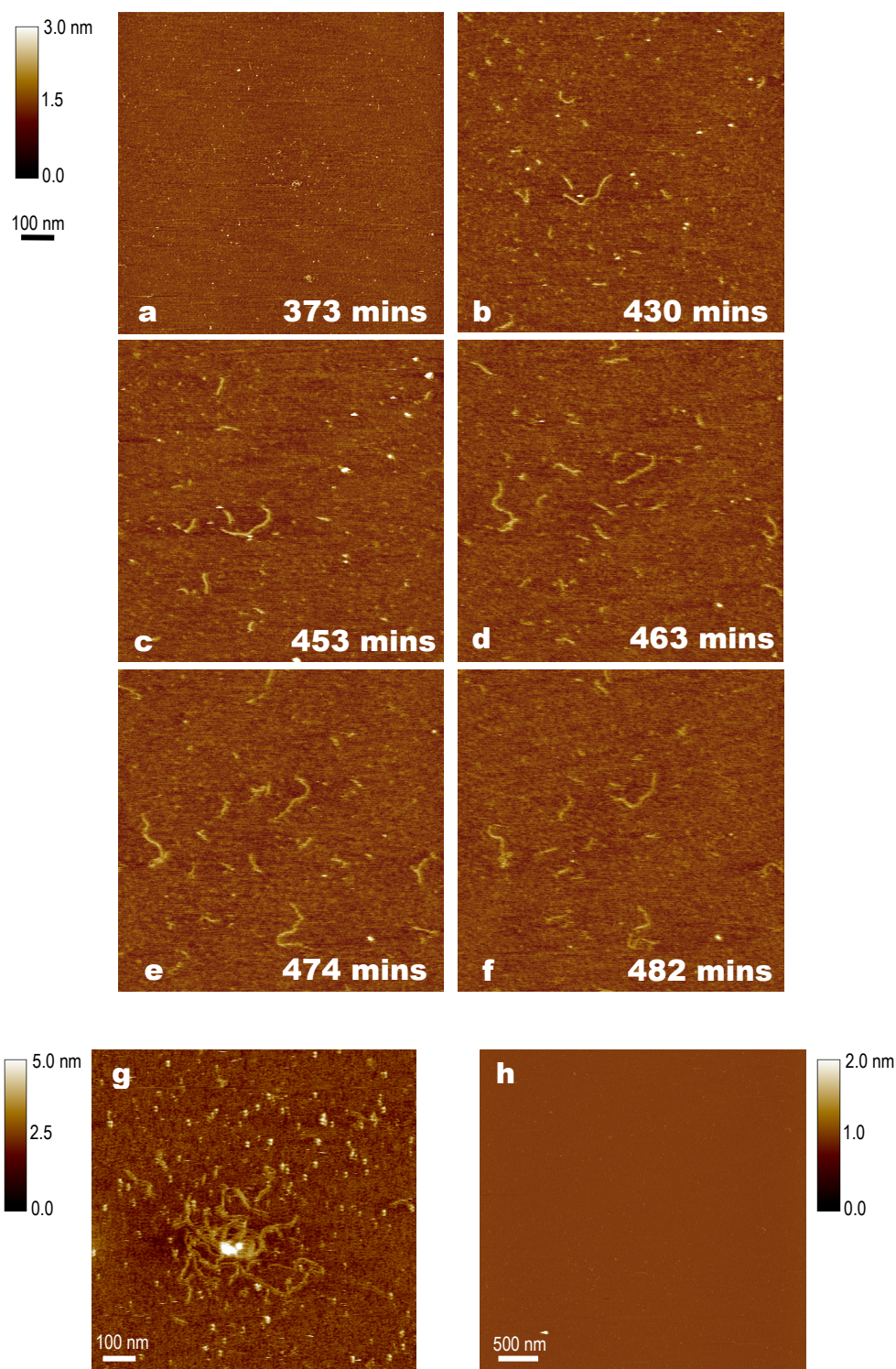


Figure 2.25: AFM images of amylin (20-29) fibrils 125 mM sodium citrate and 30 mM KCl at pH 5.5. KCl added from $t = 0$ hours, imaging started after 6 hours. The final peptide concentration was 250 $\mu\text{g/ml}$. The topography images shown in **figures 25a-f** are of the same location on the mica surface collected over the time course, the time of image capture is shown in minutes. **Figure 25g** shows a topography image of the sample at 18 hours. **Figure 25h** shows a topography image of the control sample. Z range contrast bars are shown.

2.3.5.10 Sodium citrate and magnesium chloride system

When amylin (20-29) was imaged in solution of 100 mM sodium citrate and 30 mM MgCl₂ (pH 4) images show that there was widespread deposition on the surface of globular structures, no fibrillar structures were observed. Figure 2.26a is a typical high-resolution topography image of the sample at 8 hours; a 3D representation of the surface has been generated and is presented in figure 2.26b. The globular structures, although not as well defined are similar to those observed in 150 mM sodium acetate and 30 mM MgCl₂ solutions. The apparent lack of definition in the globular features may be attributed to slight drift and double-tipping occurring during imaging. The structures vary in width but display a similar height measurement as is highlighted in the 3D image and cross-sectional profile (figure 2.26c); height of structures was in the range of 1.2 to 1.6 nm. These globular structures are not aggregates of buffer salts as the solutions were filtered to 0.2 μm prior to imaging. Furthermore a typical control image of the 150 mM sodium acetate and 30 mM MgCl₂ solution with no peptide present is shown in figure 2.26d; both the topography image and phase data show clear mica surfaces.

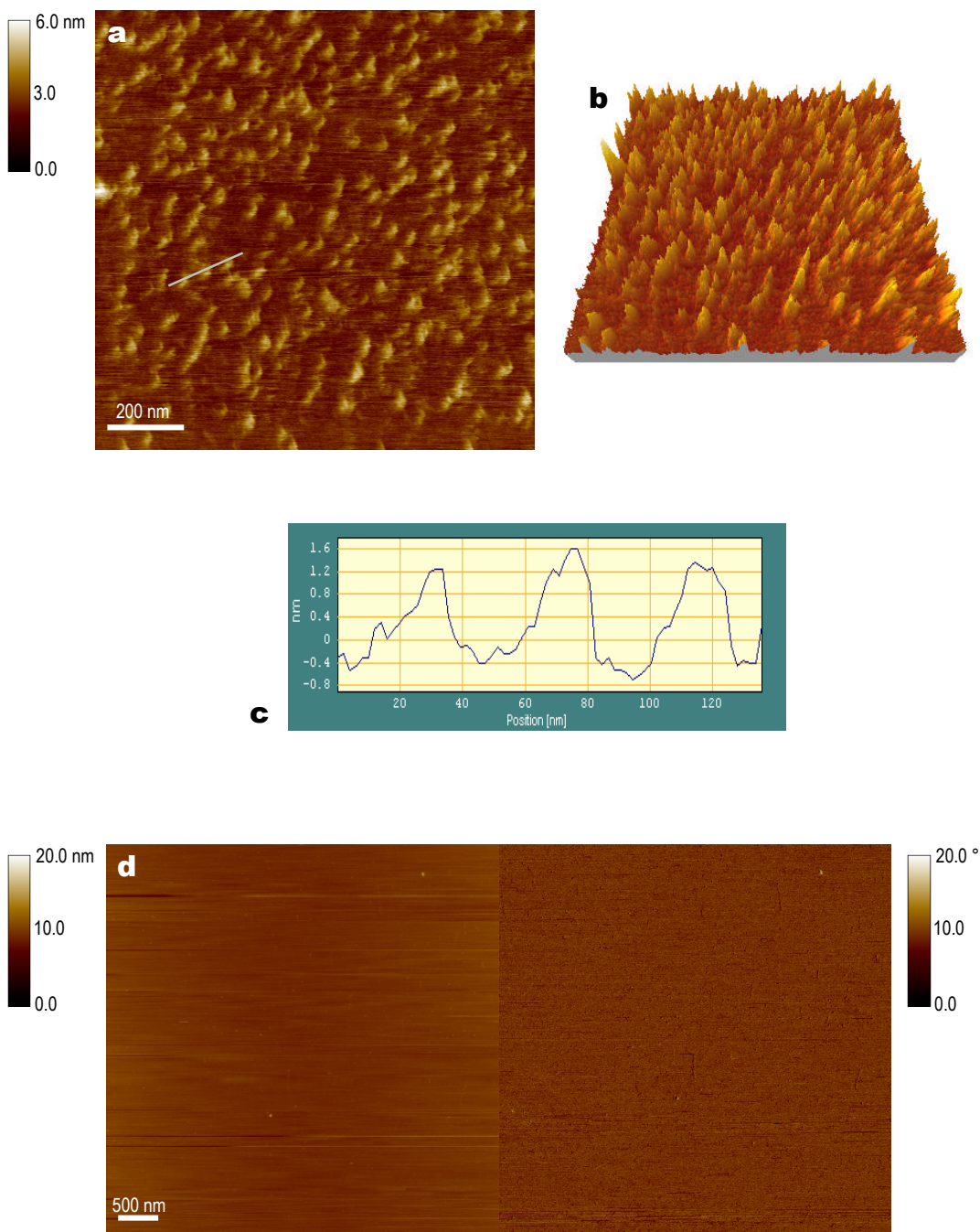


Figure 2.26: *In situ* AFM images of amylin (20-29) fibrils in 100 mM sodium citrate and 30 mM MgCl_2 pH 4. MgCl_2 added at $t = 0$ hours. The final peptide concentration was 250 $\mu\text{g/ml}$. **Figure 26a** shows a topography image captured at 8 hours, a 3D representation of the surface is shown in **figure 26b**. **Figure 26c** is a cross-sectional profile of the features highlighted by the line in figure 26a. **Figure 26d** shows a topography (left) and phase (right) image of the control sample. Z range contrast bars are shown.

2.3.6 Summary of results from *in situ* imaging

Listed in table 2.3 below is a summary of the findings and observations made during *in situ* AFM imaging of amylin (20-29) under various environmental conditions.

Ionic content	pH	Fibrils	Observations
Ultrapure water	5.6	No	
10 mM Tris HCl	7.2	No	
50 mM TrisHCl	7.2	No	
10 mM KCl	4.0	No	Fibrils observed in dried sample
50 mM KCl	4.0	Yes	Loosely immobilised. Long flexible fibrils
100 mM KCl	4.0	No	
30 mM MgCl ₂	4.0	No	
50 mM sodium acetate	5.5	No	
100 mM sodium acetate	5.5	Yes	Fibrils observed elongating from aggregates of truncated fibrils
150 mM sodium acetate	5.5	No	Fibrils observed in dried sample
125 mM sodium acetate and 30 mM KCl	5.5	Yes	Long flexible unbranched ribbons
125 mM sodium acetate and 30 mM MgCl ₂	5.0	No/Yes	Globular aggregates. Fibrils observed when MgCl ₂ added after 6 hours
50 mM sodium citrate	4.0	Yes	Short fibrils
100 mM sodium citrate	4.0	Yes	Predominantly truncated laterally assembled fibrils with longer fibril projections observed
150 mM sodium citrate	4.0	No	Fibrils observed in dried sample
125 mM sodium citrate and 30 mM KCl	4.0	Yes	Long flexible unbranched ribbons
130 mM sodium citrate and 30 mM KCl	4.0	Yes	Long flexible unbranched ribbons
125 mM sodium citrate and 30 mM MgCl ₂	4.0	No	Globular aggregates

Table 2.3: Summary of the observations noted during *in situ* AFM imaging of amylin (20-29) samples under a range of pH and ionic environments.

2.4 Discussion

The first section of this chapter deals with the successful synthesis of the 10 amino acid peptide fragment corresponding to residues 20 to 29 of the human amylin polypeptide using Fmoc solid phase peptide synthesis (figure 2.1). Preliminary *ex situ* AFM images presented of amylin (20-29) fibrils formed in ultrapure water suggest that the fibrils are freely forming and display similar morphologies irrespective of whether the peptide proceeded through a HPLC purification step or not. When taken into consideration that the purity of the crude peptide sample, as estimated by LC-MS, was approximately 80 % with the remaining 20 % attributed to residual solvents rather than incomplete peptide chains it was decided not to proceed with this purification step. Particularly in this regard was the fact that purification was time consuming and produced low yields of pure peptide with no observable benefits.

Comparison of the AFM images of crude peptide after both 18 hours and 48 hours in solution with similar images of the purified peptide sample (figure 2.3 and 2.4) clearly shows that any impurities present in the crude sample have had no detrimental effect on the formation of fibrillar structures by the peptides. In the background of the 18 hour image (figure 2.3) non-fibrillar debris that is physisorbed to the mica surface is observed, and to greater extent in the crude peptide sample. However, this material does not prevent fibrillisation, and may simply be amorphous aggregates of peptide which had yet to elongate into fibrillar formations. Furthermore, the Congo red assay performed on both crude and purified samples corroborates these AFM data as a green/gold birefringence (a positive for the presence of amyloid) was observed after staining in both samples (figure 2.2).

2.4.1 Preliminary *ex situ* AFM imaging

The representative AFM images presented in this chapter demonstrate the polymorphic nature of the fibrils formed by the peptide fragment of amylin (20-29). The following section discusses the preliminary experiments performed using tapping-mode *ex situ* AFM imaging of amylin 20-29 fibrils aged up to 48 hours. We refer to *ex situ* as samples which have been removed from a stock sample at

specific time points and dried in an N₂ air stream onto freshly cleaved mica. Therefore these images present information on the morphology of the fibrillar structures at snapshots in time.

Electron microscopy studies by Goldsbury's group [49] show mature (aged more than 48 hours) amylin (20-29) fibrils to be straight and rod like structures; however, currently there is no published information on fibrils from solutions stored for less than 24 hours. Here we have investigated the morphology of fibrils from solutions stored for shorter time periods.

Our findings suggest that protofilaments form after a lag period of 4 hours in solution (figure 2.9), and that these early fibrils have a cable-like appearance with varied periodicity dependent on the fibril (Figures 2.10 and 11). The majority of fibrils observed between 18 and 48 hours in solution were straight rod-like structures (figures 2.6, 2.7-8 & 2.12) which were observed individually or further associated within higher-order assemblies displaying a range of morphologies. Fibrils could be seen individually as well as assembled into bundles that were irregularly coiled or laterally aligned. Branching of fibrils into two new fibrils was frequently observed (figure 2.7). Branching of fibrils has been reported for other amyloid and has been suggested that branching is further proof of the structural hierarchy of amyloid; as two sub-fibrillar species, i.e. protofilaments or protofilaments, aggregate together to form the mature fibril, branching occurs when the two constituent sub-fibrillar species are not associated together, with one forming a branch and the other the main stem [40]. A common feature also noted was thinning at the end of a fibril. Again, an explanation for this could be that the thicker fibril is comprised of several lower order sub-fibrillar structures and the thinner end is a single overhanging constituent protofilament.

The observation of higher-ordered association of fibrils either by lateral alignment or twisting into coils and bundles has previously been noted in formations of full-length amylin protofilaments [43, 187], in which it was noted that two similar populations exist; protofilaments that coil with distinct axial periodicity and a second group in which the protofilaments laterally align [43]. These data are suggestive that the interactions governing the formation of higher-order structures

in the full-length protofilaments may be retained within the shorter peptide fragment of amylin (20-29). Although it is not known whether these higher-order assemblies are due to an artefact of the sample preparation method, this phenomenon has been previously observed both by EM and AFM in which sample preparation in the two techniques is different [34, 43, 44]. Therefore further study of the aggregation properties of amylin (20-29) would prove beneficial to clarify this point, particularly investigation of aggregation patterns in solutions, which is dealt with in the following section of this chapter.

Periodicity along the axis of a fibril was only observed in young samples (4 and 6 hours); some fibrils appeared to comprise globular structures with irregular periodicity. However, this was not observed in any of the solutions of fibrils aged for longer periods. This is suggestive of the fact that over the time course these younger protofilaments mature into fibrils which do not display any periodicity. These findings are not mirrored by fibrils formed from full-length and other longer fragments of human amylin in which mature fibrils retain the twisted cable-like appearance with a regular periodicity of the nascent protofilament [43, 44, 49]. However, the straight rod-like appearance of the older amylin (20-29) fibrils is in agreement with published EM images of amylin (20-29) fibrils [49, 87, 88, 90] which had been aged in solution for at least 24 hours.

The observation that younger protofilaments display a periodicity, which disappears when they mature into older fibrils, indicates the morphology of amylin (20-29) protofilaments may vary during growth. Furthermore, it is possible that the structures observed in the preparations aged for 4 and 6 hours are nascent intermediates of the protofilament and a lower-order structure. This suggestion provides further support for the proposal that all amyloid have a generic highly ordered structural hierarchy in which the amyloid fibril is formed from the aggregation of protofilaments that are assemblies of protofilaments comprising of several subprotofilaments [33]. Our *ex situ* observations provide evidence that amylin (20-29) forms protofilaments that display this hierarchy, and therefore the ability to form the highly organized and structured amyloid fibril, is intrinsically retained within the fragment of amylin (20-29).

Analysis of the fibril sizes revealed that those incubated for 6 and 18 hours displayed a population distribution with mean widths of 27.31 (± 8.36) nm (figure 2.6). Whereas after 48 hours there was some evidence of higher-order structures, with an additional population of individual fibrils exhibiting widths of approximately 50 nm. In EM studies findings have suggested that the amylin (20-29) peptide forms additional lower order 3.6 nm wide protofilaments that laterally assemble into ribbons [49]. Similar protofilaments with dimensions of 5 nm have also been recorded in full-length and other fragments of amylin samples [43, 49]. It is possible that such structures are present here but not visible in these AFM images due to the limitations caused by the sharpness of the AFM tip; the apex of the cantilever tips used for these experiments have a radii of approximately 20 nm and therefore may not distinguish between protofilaments which are themselves expected to be only 5 nm in width. Furthermore, when recording dimension measurements one must take into account the effects of AFM tip convolution in which features appear broader. As a result width dimensions may be an overestimate of the true value, however height measurements are accurate. Nonetheless, these measurements suggest that the protofilaments formed by amylin (20-29) are flat ribbon-like structures. This provides further evidence that this fragment of amylin forms fibrillar structures similar in morphology to those formed by full-length amylin [49].

2.4.2 *In situ AFM*

Several interesting aggregation patterns and fibril morphologies were observed in the *ex situ images*, including the aggregation of fibrils into irregular twisted bundles or as lateral arrays and dense sheets. However, one may question whether these observations are an intrinsic aggregation motif of amylin (20-29) fibrils or merely an artefact of drying. The AFM is an ideal tool for the imaging of biomolecules due its capacity to image in an aqueous environment. In the following discussion the development of a system for the immobilization and imaging of amylin (20-29) fibrils in solution using the AFM is examined and the subsequent study on the influence of the aqueous ionic environment on fibril formation and morphology. Additionally, our preliminary study into the kinetics of fibrillisation of amylin (20-29) by time-lapse AFM imaging will be discussed.

2.4.2.1 Immobilisation strategy

The initial starting point for designing an immobilisation strategy was based on the system used by Goldsbury *et al* 1999 [44] for the study of full-length amylin fibrils. The time-lapse study of amylin fibrils was performed in solutions of 10 mM Tris HCl at pH 7.3 using mica as the substrate. However, when these conditions were recreated in our own experiments, no amylin (20-29) fibrils were observed, instead a dense matt of material was immobilised to the mica surface (figure 2.15a) and the constituent material did not resemble the expected (based on *ex situ* imaging) fibrillar structures. Furthermore when the concentration of Tris HCl was raised to 50 mM only amorphous material was observed (figure 2.15b). These findings are not wholly unexpected given the differences in amino acid sequence between the full-length 37 amino acid long polypeptide and our 10 amino acid peptide fragment. The full length amylin polypeptide has an estimated pI of 8.90 by comparison to a pI of 5.24 for amylin (20-29), therefore in solutions of Tris HCl at a pH 7.3 one would expect the net charge on the peptide fragment, and thus conferred to the fibrils, to be negative resulting in repulsion from the negatively charged mica surface [133, 188, 189] and no immobilisation.

Consequently, further investigations were required, with the selection of the solutions and concentration variations shown in table 2.2. These studies show that for immobilisation and imaging, only 4 ionic environments proved fruitful. These systems were based around sodium acetate and sodium citrate buffer alone or in combination with KCl and MgCl₂ salts. The sodium acetate solutions were pH 5.5 and the sodium citrate pH 4. Fibrillar structures were observed in solutions solely comprising sodium acetate (100 mM, pH 5.5) and sodium citrate (50 & 100 mM, pH 4) (figure 2.19 and 2.23 respectively). In solutions of the monovalent salt, KCl at a concentration of 50 mM and pH 4, images of the fibrils were captured, however double-tipping and unstable structures were observed (figure 2.16). However, by the additional presence of either sodium acetate or sodium citrate, the imaging quality and resolution was greatly improved (figures 2.21 and 2.24). In general, the images captured in sodium acetate with KCl were clearer with higher resolution, and topographical features appeared more stable during scanning. By contrast, whilst imaging in solutions of the divalent salt MgCl₂ no

fibrillar structures and only loosely bound irregular material with no distinct morphology was observed (figure 2.18). By comparison in EM studies of full-length amylin, fibril morphologies varied dependent on pH and ionic solution. Short rapidly forming fibrils were noted in low concentrations of sodium citrate and long extended fibrils displaying periodicity in low concentrations of sodium acetate [90].

Overall, several conclusions can be drawn from this initial study into the surface binding of the amylin (20-29) fibrils to a mica substrate. In general, the results demonstrate that the ionic strength of a solution plays an important role in the immobilisation of the fibrils to the mica. For fibril surface binding the ionic environment should be such that either the negative charge of the mica surface or the charge of the peptide fibril (the overall charge of the fibril is conferred by the ionisable groups of the peptide monomers, namely the terminal $-NH_3$ and $-COOH$ group) is sufficiently masked by the electrolytes present in the solution so that stable adhesive van der Waals forces of attraction will dominate the fibril-mica surface interaction.

Our findings indicate that in solutions with low ionic concentrations of sodium acetate and sodium citrate buffer alone amylin (20-29) fibrils are observed bound to the substrate surface. However, when the ionic strength of the buffers was increased no surface binding of the fibrils was observed. In a similar pattern, fibrils in solutions of acidified KCl at pH 4.0 require ionic concentrations of 50 mM to bind to the mica surface, but on raising the ionic strength further the fibrils no longer physisorb to the surface. At the lower ionic concentration the electrical double layer formed by the monovalent K^+ ions within the solution bulk was sufficient to mask the repulsive forces arising from like charges on the fibril and substrate surfaces. This screening reduces the distance between the charged surfaces enabling the van der Waals forces of attraction to dominate and thus surface binding. In solution the K^+ ions which are exposed on the basal surface of the mica disassociate giving rise to the negative charge on the mica surface. In electrolyte solutions these K^+ ions can be replaced by the cations from the solution [188, 189], consequently as the ionic strength of the KCl solution was increased

further a diffuse layer of cations formed at the mica surface resulting in the repulsion of the positively charged peptide fibril and no surface binding.

2.4.2.2 Effects of the ionic environment

The fibrillar structures observed in solutions of both the sodium acetate and sodium citrate with KCl salts displayed similar long, flat ribbon-like morphologies and had considerable flexibility. Some fibrils branched into arms with the same dimensions: however the majority were unbranched with no noticeable surface features. Analysis of the fibril half-height widths revealed a normal distribution in size, but with varying mean values (figures 2.21 and 2.24). The fibrils in sodium acetate and KCl ranged in width from 4 to 13 nm with a mean of 8.27 (± 2.17) nm and height mean of 1.5 (± 0.21) nm. Conversely, the fibrils imaged in sodium citrate and KCl were almost double the width with a mean of 18.03 (± 2.13) ranging from 13 to 24 nm, however the height mean was the same at 1.5 (± 0.23) nm.

This apparent difference in fibril widths may be a consequence of tip convolution where topographical features appear broader than their true dimensions and is a consequence of the shape of the tip. It is possible that the tip used to image the sodium citrate and KCl solution had a higher aspect ratio in comparison to that used for the sodium acetate imaging. Given that the height measurements are similar for both solution conditions this is the most likely conclusion and therefore it is unlikely that the pronounced difference in widths is due to solution conditions alone. However, it is possible that the difference in solution pH and the ions present in solution may have attributed to some of the difference in dimensions. Especially when taken into account that the dimension measurements are based on a sample from a combination of several experiments where different tips have been used. It is possible that the change in pH, or citrate cation compared to acetate anion may have influenced the association of sub-hierarchical species into the observed fibrillar structures. The role of aromatic interactions and hydrophobic bonding has been well documented in the formation of amylin fibrils [92, 107, 176, 190]. These interactions and the side chains of residues are all influenced by the ionic environment.

Interestingly, similar aggregation patterns were noted in the *in situ* (both sodium acetate and sodium citrate with KCl aged 18 hours) images and the *ex situ* data, proof that the lateral alignment and propensity to clump together is an inherent feature of the fibrils and not an artefact of drying. However, aggregation of fibrils occurred more prominently by lateral association with twisting and coiling of fibrils together not as commonly observed in the solution images. This may be a result of lower order protofilaments associating and interacting laterally to form the visible fibril rather than by intertwining and coiling. Additionally, no periodicity was noted in younger fibrils (figure 2.19) imaged *in situ*, however this may be a limitation of tip sharpness and image resolution. The apparent aggregation and clumping of fibrils into pockets on the mica surface gives further indication of the hydrophobic nature of the fibrils and the electrostatic interactions governing their behaviour in solution.

In preparations of amylin (20-29) in sodium acetate and MgCl_2 a unique observation of globular aggregates were seen densely packed on the mica surface. The widths of the globular aggregates range from 30 to 110 nm with mean surface area of $3.57 (\pm 1.8) \times 10^3 \text{ nm}^2$. By comparison, these widths are much larger than the dimensions measured for the fibrils imaged *in situ*. On investigation it was found that these globular structures formed when MgCl_2 was present in the initial solution at time 0, but weren't observed in peptide solutions of either sodium acetate alone or MgCl_2 only. Furthermore that when amylin (20-29) was initially placed into solutions of sodium acetate and then 30 mM MgCl_2 was added after 4½ hours, globular structures were still observed, but in general had smaller dimensions and were not as densely packaged on the surface. However, when the experiment was repeated with MgCl_2 added to solutions of pre-formed fibrils (after 6 hours in sodium acetate solution) no globular structures were observed. Instead fibrils were observed physisorbed on top of a single layer of material on the mica surface (figure 2.22g). The point at which fibrils form in solutions of amylin (20-29) had been pinpointed based on our *ex situ* imaging data (figure 2.9) to be between 4 hours, where a very small population of fibrils was observed, to a larger population at 6 hours. Therefore at 6 hours it is highly probable that a significant number of protofilaments have already formed and are present in the solution. This is in fact what was observed; on addition of MgCl_2 to the solution

of sodium acetate and amylin (20-29) at 6 hours fibrillar structures were seen. Therefore, it can be surmised that sodium acetate with $MgCl_2$ has no detrimental effects on the preformed fibrils and is sufficient to facilitate surface binding of the fibrils. However, by addition of $MgCl_2$ to the sodium acetate and peptide solution prior to fibril formation (time = 0 to ~4 hours), the combination of ionic species is such that the aggregation of amylin (20-29) results in only globular aggregate formation. Similarly, although less well defined, globular structures were also observed (figure 2.26) in solutions of sodium citrate and amylin (20-29) when $MgCl_2$ was present from time = 0, which were not observed in solutions of sodium citrate and peptide.

These findings suggest that electrostatic interactions play an important role in amylin (20-29) fibril formation and aggregation. Furthermore, that the phenomena noted are a result of ionic environmental effects on the peptide induced by the presence of the $MgCl$ rather than impaired physisorption of fibrils to the mica surface. It also follows that the globular structures are formed as a result of electrostatic interactions due to the introduction of the divalent cation, Mg^{2+} which are unfavourable to fibril formation. An explanation for this observation maybe in the formation of non-covalent complexes that are coordinated by the Mg^{2+} cations between charged groups on the peptides. Binding of the Mg^{2+} cations may have a two-fold consequence, firstly the cation complexes with and masks the charged terminal carboxylate group on the peptide. Consequently screening any repulsion experienced by like charges on the monomeric peptides may reduce the intermolecular interactions needed for the promotion of the beta-sheet conformation necessary for fibril formation. Secondly, the formation of cross-linking ionic complexes between individual peptides may prevent the formation of pre-fibrillar species and instead results in the fast aggregation of the peptides into amorphous aggregates as observed in figure 2.22 and 2.26. Divalent cations have previously been reported to mediate the formation of low mass oligomeric species by stabilising through complexation or by aiding the conformational change associated with several of the self-assembling proteins through the formation of similar metal ion complexes. However, unlike the findings presented here these low oligomeric species proceeded, and in some instances at accelerated rates, to form fibrillar structures [191, 192].

Presented in figure 2.27 is a schematic summary of the variety of different morphologies observed in samples of amylin (20-29) under the different environmental conditions investigated within this chapter.

The influence of solution environment on fibril formation has been documented for several other amyloidogenic proteins. The promotion of different fibril morphologies has been observed on alterations in pH and electrolyte concentration; morphologies included globular aggregates, spherulites, toroidal structures, worm-like and rod-like chains as well as longer fibrils [126-128, 193]. The formation of these polymorphic structures has been suggested to occur due to the promotion of different assembly pathways by the solution environment. Suggestive that the self-assembly of the polypeptide into amyloid proceeds via

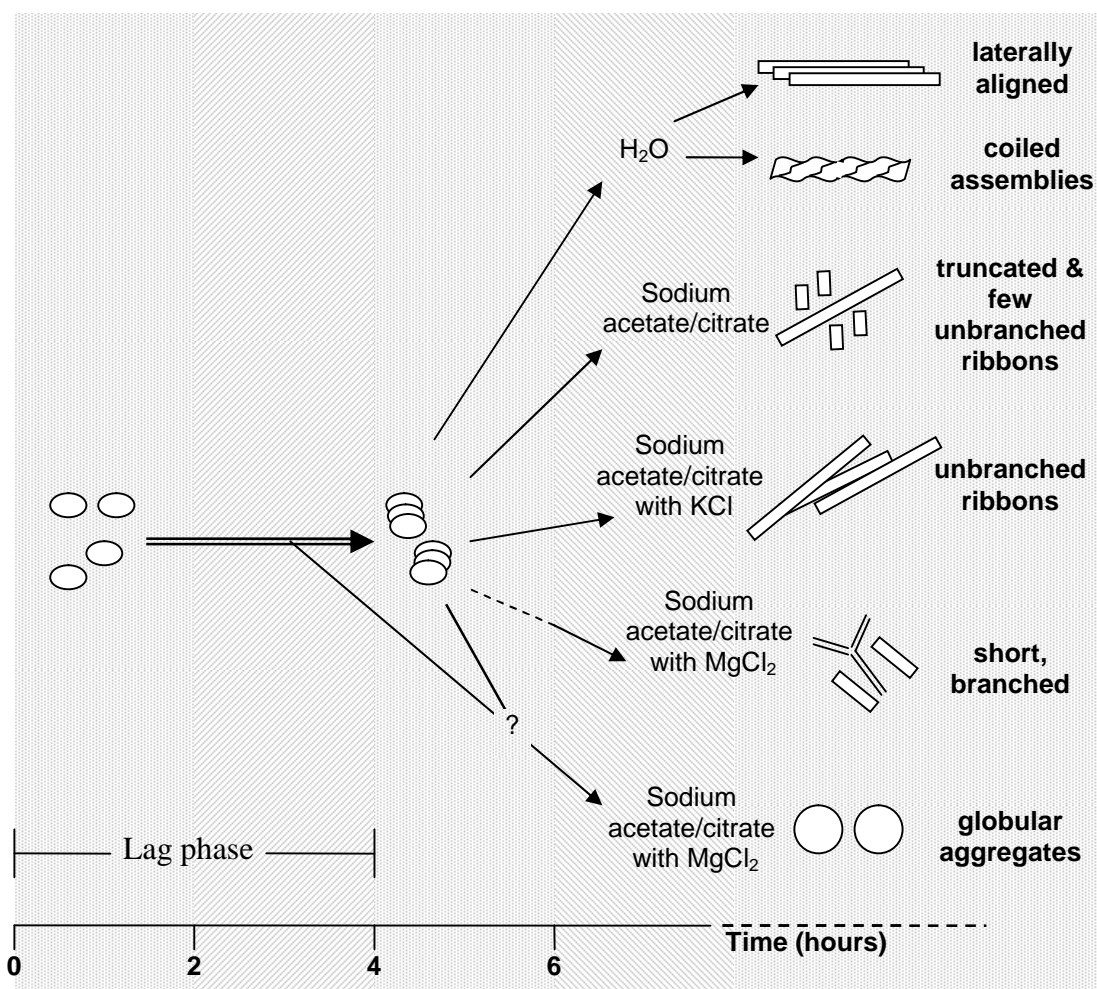


Figure 2.27: Summary of the morphologies of amylin (20-29) observed under various environmental conditions during AFM imaging.

any of several competitive kinetic pathways [128] and that the observed structures may be directly-nucleating pre-fibrillar intermediates or off-pathway assemblies of the various pathways.

2.4.2.3 Kinetic study

The preliminary studies investigating the kinetics of formation of amylin (20-29) fibrils by *in situ* imaging in 100 mM sodium acetate pH 5.5 solution, revealed that growth rates varied dependent on the fibril and ranged from 2 to 11 nm min⁻¹. These rates are much faster in comparison to the published rate of 1.1 nm min⁻¹ as determined by time-lapse AFM for full-length amylin [44]. A faster rate of formation is not unexpected given the shorter chain length of the amylin (20-29) peptide. The peptide in comparison to the full-length chain would require less packaging and therefore there is a higher probability that the peptides free in the surrounding solution will be in the correct steric conformation for interaction with the growing peptide fibril on the sample surface. Similarly to full-length amylin, we also observed longitudinal elongation of fibrils occurring from either end of a fibril with no apparent polar preference. A two phase model has been proposed for the growth of fibrils by full-length amylin where lateral growth from a preformed nucleus of oligomers precedes a second phase of longitudinal growth of mature fibrils [64]. This hypothesis appears to fit with the observations presented in figure 2.19, where clear aggregates are observed in pre-formed clumps and from these fibrils grow longitudinally. Furthermore, during *ex situ* imaging of samples formed in water, fibrils were observed growing out from a central nucleating point (figure 2.7).

2.5 Conclusion

Amylin (20-29) peptide fibrils self-assemble in a range of electrolyte solutions to form fibrillar structures which display polymorphic assemblies. Using a combination of *ex situ* and *in situ* tapping-mode AFM imaging we have demonstrated the change in fibril morphology with time and under the influence of various electrolyte solution environments. Additionally, as a consequence of solution conditions, a possible off-pathway globular aggregate formation has been

identified. Suggestive that the ionic environment may be used to influence the morphology of fibrils by inducing different amyloid folding pathways. Furthermore, we have been able to image for the first time amylin (20-29) fibrils in solution and perform kinetic studies on the fibrillisation.

Chapter

3

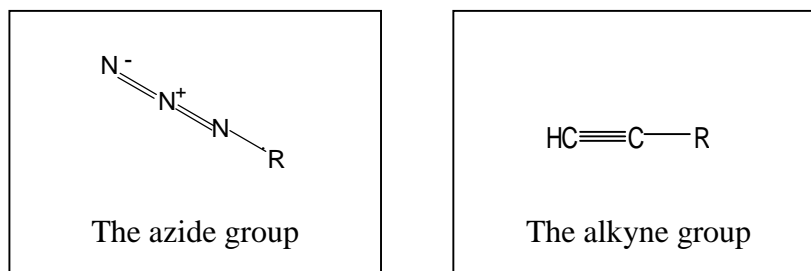
Modification of amylin (20-29) peptides

3.1 Introduction

In the previous chapter we have shown that the peptide fragment of amylin corresponding to residues 20-29 of the human polypeptide readily forms fibrils under a selection of solution environments. The fibrils that form display a range of morphologies and display a propensity to aggregate together. The aggregation of the fibrils was driven by non-covalent interactions and could, to some extent, be controlled by the surrounding solution conditions. However, the ability to directly manipulate the fibrils by controlling fibrillisation or surface immobilisation in a predictable and orientated manner, as well as forming strongly linked assemblies would enable these fibrils to be used in a broad range of potential applications from peptide scaffolds to functionalised surfaces or matrices.

A wide range of strategies are available and have been successfully utilised for the control and exploitation of peptide fibrils and peptide-based assemblies including, template-directed growth using highly-ordered surfaces [137], nanolithography [194, 195] and self-assembled monolayers [196-198]. One strategy for the manipulation of peptide-based systems is the exploitation of specific functional groups already present on the biomolecule or by the introduction of a specific moiety [47, 199, 200].

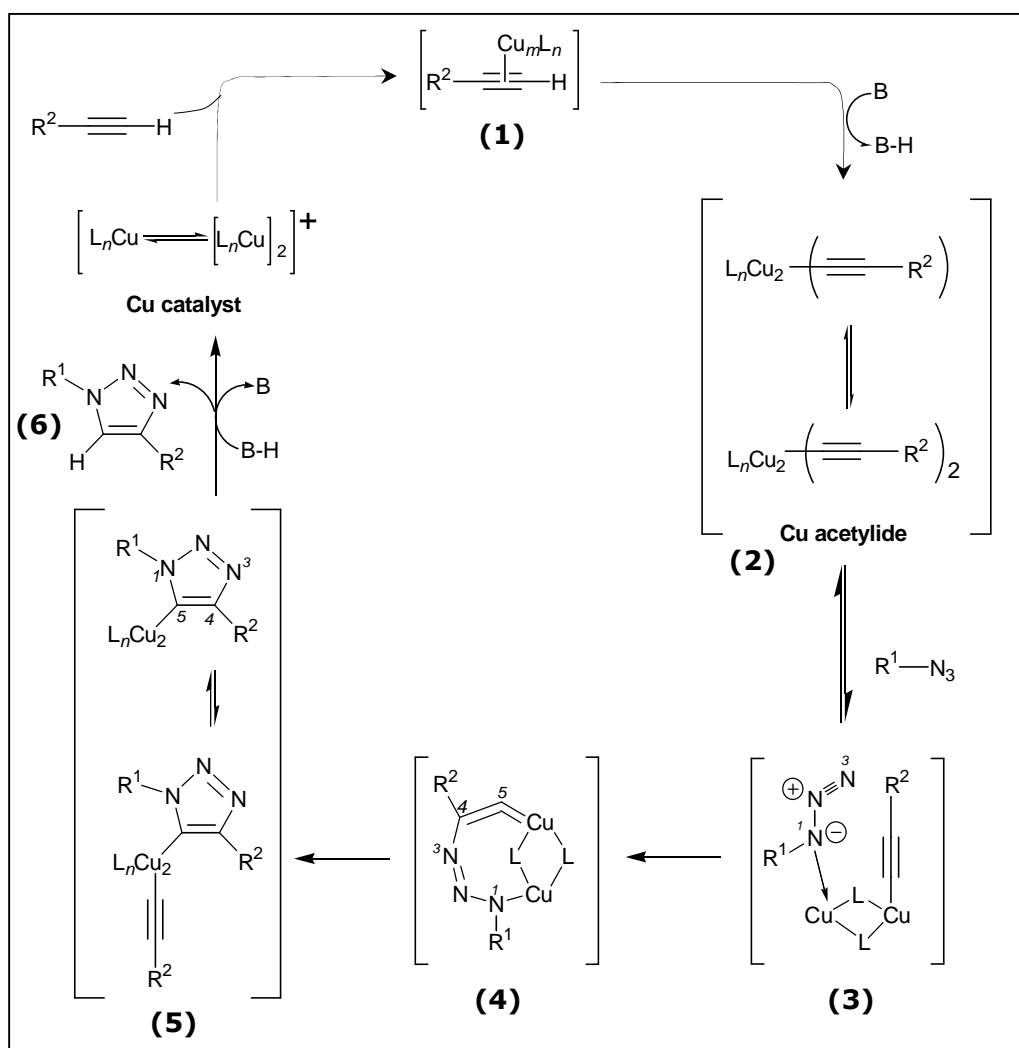
In this chapter the potential for the directed control of amylin (20-29) fibrils by the introduction of specific functional moieties to the peptide is explored. Specifically by the chemical modification of the amylin (20-29) peptide during synthesis by the coupling of two functional groups to the N-terminal of the peptide. The functional groups are an azide and an alkyne group. The azide



moiety is a linear molecule of three nitrogen atoms with an orthogonal double bond in which there is a delocalised cloud of four π -electrons over the three nitrogen atoms. The electrons of the central nitrogen atom are sp hybridised allowing some bending of the bonds within the linear structure, making the molecule an ideal nucleophile [201]. The alkyne moiety is a hydrocarbon containing a carbon-carbon triple bond. The carbon atoms in the triple bond are sp hybridised and overlap of the orbitals forms a delocalised cloud of π electrons around the carbon-carbon bond [202].

A terminal alkyne (dipolarophile) and azide (1,3 dipole) group can undergo fusion to form a 1,4-disubstituted 1,2,3-triazole, in the presence of a copper (I) catalyst, by means of the Huisgen 1,3-dipolar cycloaddition reaction mechanism [203, 204]; more popularly known as 'click chemistry'. The 1,2,3-triazole group is a thermally and hydrolytically stable five-membered aromatic heterocycle [204] comprising heteroatoms at position 1,2 and 3, in this instance nitrogen atoms. By coupling of either an azide or alkyne group to the N-terminal of the amylin (20-29) peptide, the aim was to generate fibrils assembled from these functionalised peptides. Furthermore, to investigate the use of the cycloaddition reaction chemistry to form strong covalent links between the fibrils in the form of the 1,2,3-triazole ring in an attempt to synthesise higher-ordered structures. The proposed mechanism [204-206,] for the copper (I)-catalysed 1,3-dipolar cycloaddition reaction of an azide and terminal alkyne is presented in scheme 3.1. The mechanism favours an indirect ligation through a series of intermediates rather than the direct formation of the triazole ring.

The stepwise catalytic cycle initiates with the formation of a copper (I) acetylide species (**1**) via alkyne π complexation which requires ligand dissociation and deprotonation. The copper (I) acetylide species exists as a family of interchanging



Scheme 3.1: Proposed catalytic cycle for the Cu (I) catalysed cycloaddition reaction of terminal alkynes and azides. Source Bock *et al* (2006) [205].

species in solution **(2)**. For catalysis to proceed, it is thought that two metal centres, one or two alkyne ligands and other labile ligands for competitive 1,3 dipole binding are required. The pathway proceeds through the activation of the azide functionality by the second copper atom of the copper (I) acetylide complex **(3)**. Simultaneously, the reactivity of the acetylide towards cyclization is increased by the further π complexation of terminally bound acetylide to a proximal copper atom. A copper acetylide-azide species is generated by the displacement of one ligand by an azide. Cyclization of the complex to produce a metallocycle **(4)** occurs by the nucleophilic attack of carbon 4 of the acetylide at nitrogen 3 of the azide. The bound azide is thus in an optimum position within the metallocycle for the subsequent ring contraction, which proceeds by the transformation of the metallocycle into a triazole-copper derivative **(5)**. The reaction cycle ends by

protonation of the triazole-copper derivative which affords the 1,2,3-triazole product (**6**) and regeneration of the copper catalyst species.

The triazole ring, as with many products of 1,3-dipolar cycloaddition reactions [207, 208] forms as a mixture of two possible regioisomers a 1,4-disubstituted or 1,5-disubstituted 1,2,3 triazole. However, Rostovtsev *et al* [204] note that in the copper (I) catalysed reaction, formation of the triazole ring proceeds regioselectively favouring the formation of the 1,4 isomer. The regiospecificity of the product is determined by the energy levels of the molecular orbitals of the dipolarophile and 1,3 dipole. In the cycloaddition reaction bonding occurs by interaction of the highest occupied molecular orbital (HOMO) of one component, which may be either the 1,3-dipole or the dipolarophile, and the lowest unoccupied molecular orbital (LUMO) of the complementary group in the pairing. The combination with the smallest energy gap will bind and results in either formation of the 1,4 or 1,5 regioisomer. In the copper (I) catalysed reaction, the copper initially binds to the alkyne and the energy of the LUMO of the coordinated alkyne is reduced. This has two outcomes, firstly the reaction proceeds regioselectively whereby the predominant isoform is the 1,4-disubstituted 1,2,3 triazole and secondly, there is an overall increase in the energy of the system and thus copper acts as a catalyst to speed up the reaction [203, 204, 207, 209].

Copper (I)-catalysed 1,3 cycloaddition reactions of azides and alkynes have previously been utilised for a range of biological applications, including use in the bioconjugation of labels and ligands on cell-surfaces [210, 211], as well as for fluorescent labelling of proteins and peptides [212, 213]. Furthermore, this form of click chemistry has previously been investigated for utilisation in peptide-based systems for the generation of peptide scaffolds, in which a range of peptides with varying sequences and lengths (up to 12-mer) were synthesised with terminal azide groups [214]. These peptides were site-selectively ligated to a resin-bound cyclic peptide scaffold using the cycloaddition reaction by formation of the 1,4 disubstituted 1,2,3 triazole between the terminal azide of the peptides and site-specific alkyne groups on the cyclic peptide scaffold. Although there is no current literature on the direct use of the 1,3-dipolar cycloaddition of azide and alkynes in

peptide fibril nanostructures, collectively these few examples suggests that the chemistry may be compatible with the larger peptide structures. Therefore, it is proposed that incorporation of the azide and alkyne functionalities into the amylin (20-29) fibrils would enable a range of possible future applications. For example, the formation of triazole rings between fibrils could be exploited in the production of a covalently linked fibrillar matrix, alternatively the functional groups and chemistry could be utilised as a means of covalently linking the fibrils to an azide or alkyne functionalised surface for covalent immobilisation of the fibrils.

The experiments presented in this chapter are preliminary investigations on the use of the 1,3-dipolar cycloaddition reaction of azide and alkynes for the manipulation of amylin (20-29) fibrils. The experimental design aims to answer two fundamental questions. Firstly, what influence will the introduction of additional steric bulk (in the form of the azide or alkyne functional group) to the terminal of the amylin (20-29) peptide have on fibril formation? Secondly, are the functional groups sufficiently exposed on the outer surface of the fibrils, and in close enough proximity for the copper (I) catalysed cycloaddition reaction to proceed for 1,2,3-triazole ring formation? The AFM will be utilised in the study to investigate the properties and fibrillisation of these modified peptides.

3.2 Experimental

3.2.1 *Materials*

Amylin (20-29) was synthesised by SPPS, reagents used in the process were: NovaSyn® TGR resin and standard Fmoc protected amino acids which were purchased from NovaBiochem; dimethylformamide (DMF) purchased from Rathburn; piperidine, *N*-methylpyrrolidinone, *N,N*-diisopropylethylamine (DIPEA), 2,4,6-trinitrobenzenesulphonic acid (TNBS), trifluoroacetic acid (for SPPS), triisopropylsilane (TIPS) and dichloromethane (DCM) were purchased from Sigma-Aldrich; *N*-[(dimethylamino)-1H-1,2,3-triazolo[4,5-b]pyridin-1-ylmethylene]-*N*-methylmethanaminium hexafluorophosphate *N*-oxide (HATU) obtained from Perseptive Biosystems, Germany; ethanol, hexane, diethyl ether,

acetonitrile (Far UV grade), and trifluoroacetic acid (for HPLC) purchased from Fischer Scientific Chemicals; sodium chloride and magnesium sulphate were purchased from Sigma-Aldrich. Bromoacetic acid, Sodium azide and propionic acid were purchased from Sigma-Aldrich. For the Congo red assay, Congo red and sodium chloride were from Sigma Aldrich and ethanol from Fischer Scientific Chemicals. For the cycloaddition assay Copper (II) Sulphate pentahydrate and L-Ascorbic Acid were from Sigma-Aldrich and ethanol was purchased from Fischer Scientific.

3.2.2 *Method*

3.2.2.1 **Solid phase peptide synthesis**

The peptide fragment of human amylin corresponding to residues 20 to 29 (for the sequence see Chapter 2) was synthesised using solid phase peptide synthesis (SPPS). The same SPPS protocol to that outlined in chapter 2 was followed, with the exception that Fmoc protecting groups were removed manually (see below).

The column was packed with 0.1 mmol of an amide Rink resin, NovaSyn® TGR. Resin was solvated initially with *N*-methylpyrrolidinone (NMP). The activation cocktail containing the coupling reagents, 0.8 mmol DIPEA and 0.4 mmol HATU, solubilised in NMP, was mixed with 0.4 mmol of the C-terminal amino acid (serine) and added immediately to the reaction vessel. Amino acids were loaded with a four-fold excess to ensure maximum yield. Sufficient solvent was added to the reaction vessel for the resin to be fluid and was left at room temperature on a magnetic stirrer. The first amino acid coupling was left overnight to ensure complete attachment to the resin.

Following each new amino acid coupling a tri-nitro benzene sulfonate (TNBS) test was performed to determine whether complete coupling had occurred. A small sample of resin was removed from the reaction vessel and washed several times with ethanol to remove any unbound amino acids. A few drops of DIPEA and TNBS in equal quantity were added in sufficient volume, and the colour of the resin beads and solution observed. In the event of incomplete coupling, the

free amines present will result in the beads appearing red. Conversely, when the coupling has proceeded fully, the beads and solution are colourless. In the event of incomplete coupling the reaction was allowed to proceed for a further 1-2 hours until no red beads and solution was observed.

Following complete coupling of the amino acid, any excess coupling solvent was removed from the reaction vessel by vacuum and the resin washed 5 times with an excess volume of NMP. Fmoc deprotection of the serine amino group in preparation for the coupling of the next amino acid was performed by washing the reaction vessel with 100% DMF, to remove excess activated amino acids. Sufficient deprotection reagent of 20% piperidine-NMP solution was added to cover the resin and left with N₂ gas bubbling through to ensure complete mixing for 15-30 minutes.

Following Fmoc deprotection, the resin was washed with NMP (5 times excess bed volume) to remove any trace of deprotection reagent and the next amino acid in the sequence was added with the activation cocktail. The process was then repeated for each amino acid until the complete sequence was generated. Following the final Fmoc deprotection, the resin was washed using DMF and DCM over a Buchner funnel and then shrunk using hexane.

Prior to cleavage of the peptide from the resin an additional step was included to add either the alkyne moiety or azide moiety to the N-terminal of the peptide chain. The resin was divided in half, with a small portion set aside for mass spectrometry analysis of the peptide sequence.

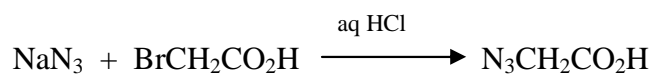
3.2.2.2 Coupling of azide group to N-terminus

The azide moiety was introduced to the N-terminus of the amylin (20-29) peptide in the form of azidoacetic acid. The initial step in this process was the synthesis of the azidoacetic acid.

3.2.2.2.1 2-Azidoacetic acid synthesis

2-Azidoacetic acid (N₃CH₂CO₂H) was synthesised according to the methodology of Dyke *et al* [215] from sodium azide (NaN₃) and bromoacetic acid

(BrCH₂CO₂H). Great care was taken during the synthesis to minimise the risk of explosion whilst using the highly explosive azides.



A saturated aqueous solution of sodium azide (780.42 mg) was mixed in a 2:1 ratio with bromoacetic acid (833.7 mg), and stirred continuously for 24 hours in an ice bath. The reaction mixture was then acidified to pH 5 by the addition of aqueous hydrogen chloride. Thin layer chromatography was performed as an indicator for the presence of product (azidoacetic acid) and reagents during and at the end of the reaction.

The 2-azidoacetic acid product was extracted by salting out with a saturated quantity of sodium chloride. The aqueous layer was extracted using diethyl ether several times and the combined organic layers were dried over anhydrous magnesium sulphate. Final traces of water and diethyl ether were removed under vacuum. The final product obtained was 60 mg of a yellow oil. Characterisation of the end product was performed by electron-spray liquid chromatography mass spectrometry (LC-MS), H¹-nuclear magnetic resonance (NMR) and infrared spectroscopy (IR).

3.2.2.2.1.1 LC-MS

Mass spectra were obtained using a Micromass LCT Mass spectrometer with autosampler. The sample was prepared by dissolving in acetonitrile/water solution. Samples were analysed by negative ion electron spray.

3.2.2.2.1.2 ¹H-NMR

H¹-NMR spectra were acquired on a Bruker 400 MHz instrument (Bruker, UK). The samples were prepared in deuterated chloroform (CDCl₃). All chemical shifts are relative to a tetramethylsilane (TMS) internal standard.

3.2.2.2.1.3 IR spectroscopy

Transmission infrared spectra were acquired on a Nicolet Avatar 360 FT-IR instrument using NaCl discs. Mid-IR spectra were acquired over the range 400 – 4000 cm⁻¹.

3.2.2.2.2 2-Azidoacetic acid coupling

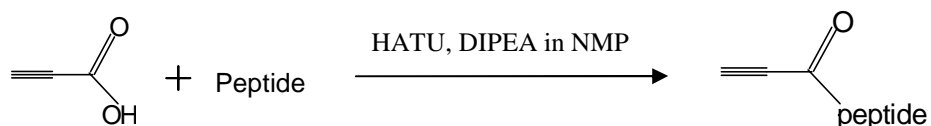
In preparation for the coupling of the azide moiety to the N-terminus of the amylin (20-29) peptide chain, 150 mg of peptide bound resin was resolvated and washed with NMP.



A three-fold excess of 2-azidoacetic acid (30 mg) and the activation cocktail containing the coupling reagents, 0.8 mmol DIPEA and 0.4 mmol HATU, solubilised in NMP, was added immediately to the reaction vessel. The reaction was left bubbling through with N_2 gas for 3 hours. A TNBS test was performed on a small sample of resin to ensure full coupling of the azide group to the peptide chain had occurred. Following successful coupling of the azide moiety to the amylin (20-29) peptide the side groups were deprotected and the peptide chain cleaved from the resin as outlined below.

3.2.2.3 Coupling of alkyne to N-terminus

The alkyne moiety was introduced to the amylin (20-29) in the form of propiolic acid ($C_3H_2O_2$). Coupling of the peptide chain with the propiolic acid requires the formation of a peptide bond between the NH_2 group of the N-terminal serine of the amylin (20-29) peptide chain and the carboxylic acid group of the propiolic acid.



A portion of the peptide-bound resin (213.1 mg) was resolvated with sufficient NMP and washed with several bed volumes. A three-fold excess of propiolic acid (450 μ l) and the activation cocktail containing the coupling reagents, 0.8 mmol DIPEA and 0.4 mmol HATU, solubilised in NMP, was added immediately to the reaction vessel. The reaction was left bubbling through with N_2 gas for 3 hours. A TNBS test was performed on a small sample of resin to ensure full coupling of the

propionic acid to the peptide chain had occurred. Following successful coupling, the side chain protecting groups were deprotected and the alkyne-peptide chain was cleaved from the resin as outlined below.

3.2.2.4 Side chain deprotection and resin cleavage

Cleavage of the peptide chain from the resin and deprotection of side chain groups was performed by the addition of a mixture of 90% v/v trifluoroacetic acid (TFA), 2% v/v triisopropylsilane (TIPS) and 8% v/v water, for 2 hours. The suspension was then filtered and the filtrate evaporated under vacuum. The residual material was titrated with diethyl ether, and the resulting powder consisting of the crude peptides were stored below 4°C. The successful synthesis of the two target peptides was confirmed by electro-spray mass spectrometry (Micromass LCT Mass spectrometer).

3.2.2.4.1 Reverse-phase high performance liquid chromatography

The crude peptides were analysed on a reverse-phase C18 (Hypersil BDS, bore size 4.6 mm, supplied by Shandon,UK) column. The solvent system employed comprised: A = 0.06 % trifluoroacetic acid in ultrapure water (pH 6, resistivity 18.2 MΩcm), B = 0.06% trifluoroacetic acid in 90% acetonitrile/ 10% ultrapure water. Presence of the peptide in the eluent was monitored spectrophotometrically at $\lambda_{214\text{nm}}$. The crude peptides were dissolved in 60 % v/v acetonitrile to a concentration of 2 mg/ml. The gradient of 30 to 100 % B over 30 minutes with flow rate of 5 ml/min and injection volume of 200 μl .

3.2.2.5 Preliminary fibrillation assay

A preliminary study to determine the fibrillation capabilities of both forms of the functionalized amylin (20-29) peptides was performed. The lyophilized azide- and alkyne form of the amylin (20-29) peptide were solubilised in ultrapure water (pH 6, resistivity 18.2 MΩcm) at a concentration of 300 $\mu\text{g/ml}$. Samples were left to form fibrils at room temperature for 18 hours before aliquots were removed and dried under N_2 onto freshly cleaved mica and imaged using the AFM.

3.2.2.6 Copper (I) catalysed 1,3-dipolar cycloaddition reaction assay

Investigations to establish the viability of the alkyne- and azide- coupled moiety on the peptide fibrils for the copper (I) catalysed cycloaddition reaction for the formation of triazole groups was performed. The assay conditions employed for the cycloaddition reaction were based on the methodologies from the work of Link & Tirell [210], Rostovtsev *et al* [204] and Wang *et al* [211].

The cycloaddition reaction requires the presence of copper as a catalyst which must be in the +1 oxidation state. Here we use the +2 oxidised form of copper in the form of $\text{CuSO}_4 \cdot 5\text{H}_2\text{O}$, which is reduced *in situ* by the reducing agent ascorbic acid in a 2:1 water and alcohol solution according to the method of Rostovtsev *et al* [204].

The lyophilised azide- and alkyne- peptides were solubilised in ultrapure water to a concentration of 1 mg/ml and left for 18 hours to ensure formation of fibrils. After this initial incubation, aliquot samples of the peptides were removed and placed into eppendorfs containing either 1 mM or 5mM copper sulphate with 5 mM or 25 mM (respectively) ascorbic acid in a 2:1 mix of water and ethanol (referred to hereafter as copper (I) solution) to give a final peptide concentration of 300 $\mu\text{g}/\text{ml}$. The eppendorfs contained either azide-peptide or alkyne-peptide or a 50:50 mix of both forms of peptide. Samples were continuously mixed for a further 8 hours at room temperature, before aliquot samples were removed and dropped onto freshly cleaved mica and dried under N_2 before imaging.

To investigate whether the cycloaddition reaction would prevent fibrillisation of the amylin (20-29) peptides, the experiment was repeated with the exception that 1 mM or 5 mM copper sulphate with ascorbic acid in a 2:1 mix of water and ethanol was added to a 50:50 mix of both forms of the peptide (final peptide concentration 300 $\mu\text{g}/\text{ml}$) at time 0 hours. Samples were continuously mixed for 18 hours at room temperature, aliquot samples were then removed, dropped onto freshly cleaved mica, and dried under N_2 before imaging.

3.2.2.7 AFM imaging

All AFM imaging was performed in air using the Nanoscope IIIa (Digital Instruments, Veeco Metrology Group, Santa Barbara CA) in tapping mode. Silicon TESP tapping probes (supplied by Veeco Metrology Group) mounted on cantilevers with nominal spring constants of 42 N/m (range of 34.4-37.2 N/m) and nominal resonant frequency of 320 kHz (range of 280-360 kHz) were used. All imaging was performed at a final peptide concentration of 300 µg/ml. Aliquots of 10 µl were dropped onto freshly cleaved mica (1 cm²), dried in a N₂ gas stream and imaged immediately. Control preparations of ultrapure water (pH 6, resistivity 18.2 MΩcm) and solutions of copper sulphate with ascorbic acid in a 2:1 mix of water and ethanol were stored under identical conditions and for the same time period; here imaging showed no fibrillar structures. AFM image analysis

Data was processed using two computer packages, the analytical processing options from the Nanoscope software version 5.21b48 (Digital Instruments, Veeco Metrology Group, Santa Barbara CA) and SPIP program (Image Metrology ApS USA). Images show topography and phase data (where indicated), contrast scale bars are presented alongside images where appropriate. The upper z range value is stated above each scale bar with lighter colours indicating higher topographical features and greater phase contrast respectively.

3.2.2.8 Congo red assay

The formation of amyloid fibrils by the functionalised amylin (20-29) peptides was investigated using the histopathology stain, Congo red. A saturated solution of Congo red was prepared using 0.2g of Congo red powder per 100 ml of 80% v/v ethanol solution saturated with sodium chloride. Both forms of the lyophilised peptides were suspended in Ultrapure water (pH 6, resistivity 18.2 MΩcm) at a concentration of 1 mg/ml. The suspension was aged for 18 hours at room temperature to ensure maximum allowance for fibril formation and a 10 µl aliquot was removed and dropped onto a clean glass slide and air-dried. Samples were stained for 1 minute by the addition of the saturated Congo red solution. Excess stain was removed by washing with ethanol and the slide air-dried.

3.2.2.8.1 Optical microscopy and Birefringence

Birefringence was examined using a Leitz Diaplan light microscope with polarisers and 10 and 25 times magnification objective lens. The polariser lens are set at an angle of 45 degrees to each other, one in the incident beam and the other set above the slide stage between the objective lens and camera. Images of the sample under normal and polarised light were captured using a Nikon 100 digital camera.

3.3 Results

3.3.1 Azide- amylin (20-29) peptide synthesis

An azide group was added to the N-terminal of the amylin (20-29) peptide by formation of a peptide bond by reacting 2-azidoacetic acid with the resin-mounted peptide in the presence of the coupling activation cocktail. 2-azidoacetic acid was successfully synthesised from sodium azide and bromoacetic acid. Characterisation of the yellow end product is listed below, $^1\text{H-NMR}$ and IR (liquid) spectra are presented in figures 3.1 and 3.2 respectively.

Yield: 60 mg (60 %)

MS (ES): 100.06 (M^-)

$\nu_{\text{max}}(\text{NaCl})$: 2116.26 (N_3), 1731 ($\text{C}=\text{O}$), 1420 (C-OH in plane bending),
1284-1221 (C-O stretching), 946 ($-\text{OH}$ bending), 877 and 3158-
3459 ($-\text{OH}$ stretching) cm^{-1}

$\delta_{\text{H}}(400\text{MHz}, \text{CDCl}_3)$: 4.0 ppm (2H, s, CH_2)

10.6 ppm (1H, s, COOH)

Collectively the mass spectroscopy, $^1\text{H-NMR}$ and IR characterisation indicate that the yellow oil end product is azidoacetic acid. There was no evidence observed in the characterisation spectra for the presence of any unreacted reactants or intermediates in the end product.

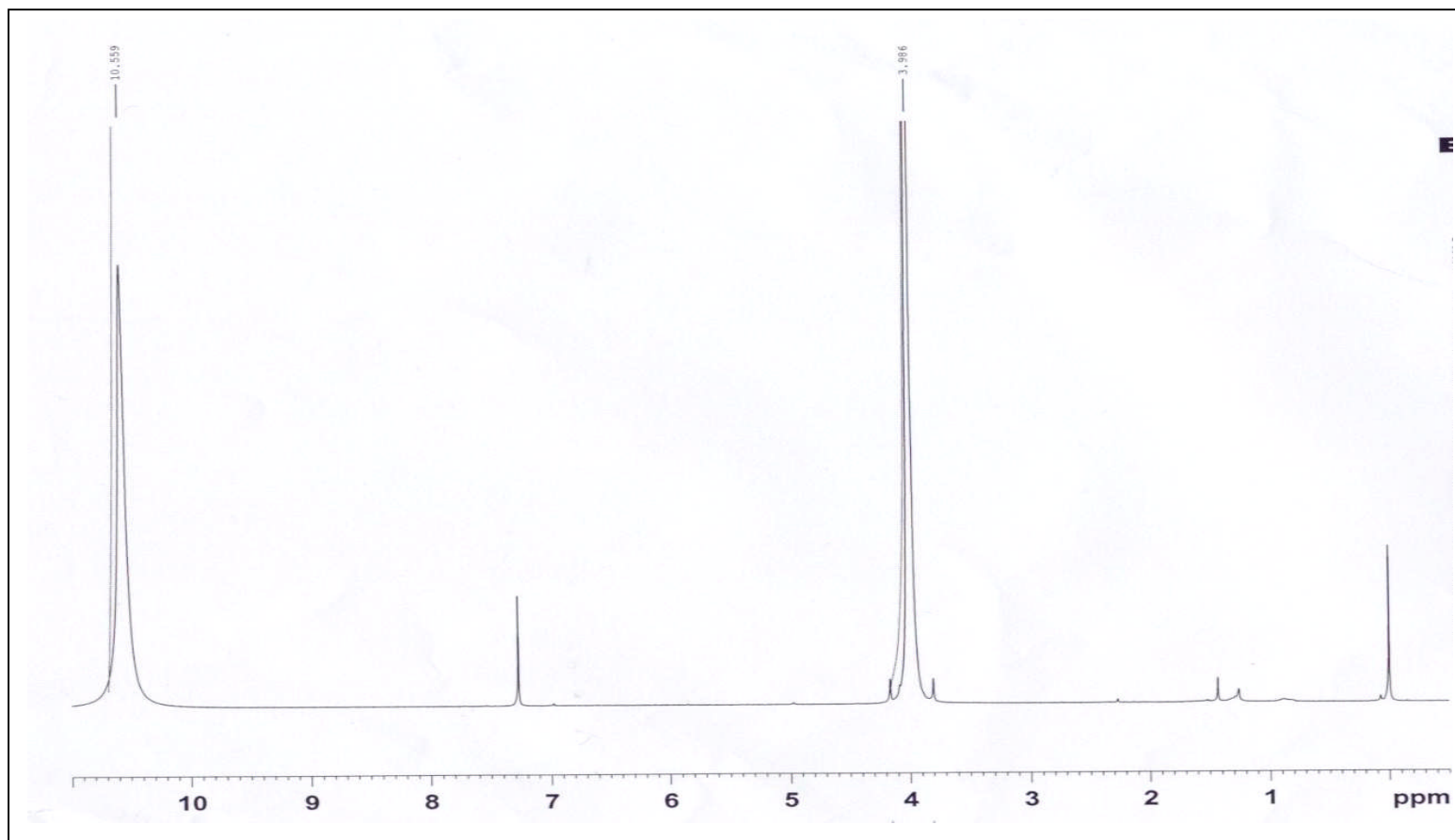


Figure 3.1: $^1\text{H-NMR}$ spectrum of 2-azidoacetic acid. Integrated 400 MHz $^1\text{H-NMR}$ spectrum of the yellow oil product from the 2-azidoacetic acid synthesis. Solvent used was CDCl_3 with TMS standard. The singlet signal at 4.0 ppm is consistent with that expected for the methylene proton of the 2-azidoacetic acid and broad singlet at 10.6 ppm corresponds to the hydroxyl proton. The signal at 7.0 ppm is consistent with that observed for CHCl_3 , a protonated form of the solvent.

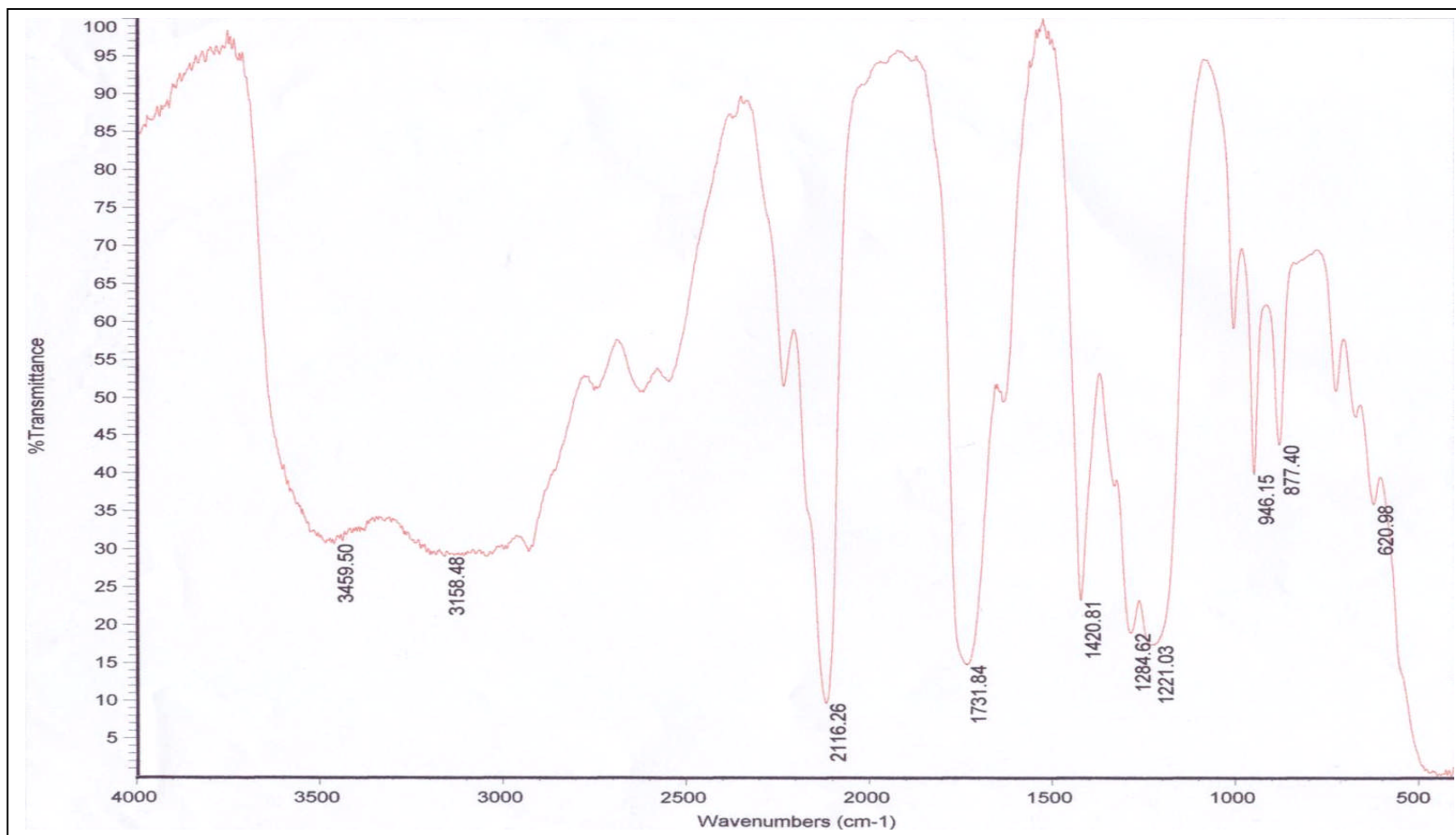


Figure 3.2: Infra Red Spectroscopy spectrum of 2-azidoacetic acid. The mid -IR spectrum of the yellow oil product from the synthesis of 2-azidoacetic acid. Spectrum was generated using the Nicolet Avatar 360 FT-IR using NaCl discs. The characteristic resonance of the N₃ group is observed at of 2116.26 cm⁻¹ wavelength.

Coupling of the azidoacetic acid to the second half of the resin proceeded successfully and the negative mass spectrum of the azide-form of the amylin (20-29) peptide is shown in figure 3.3. ES-MS: m/z 1089.52 ((M-3H), 100%), 1090.52 ((M-2H), 58 %) and 1091.2 ((MH), 25 %). The molecular fragments (M-3H) and (M-2H), can be accounted for by the deprotonation of amino acid side chain groups (alcohol group of serine) and the carboxylic acid of the peptide chain.

Presented in figure 3.4 is a RPHPLC chromatogram typical of that obtained during RPHPLC analysis on the azide-amylin (20-29) peptide. The chromatogram is dominated by a peak at 10.75 minutes close to the solvent front (5 minutes), corresponding to the target peptide. Several smaller peaks with less than 15 % intensity are also observed at later time points.

3.3.2 *Alkyne-amylin (20-29) peptide synthesis*

Coupling of the alkyne moiety to the amine group of N-terminal serine residue of the amylin (20-29) peptide fragment was successfully performed by SPPS. A positive ion mass spectrum of the alkyne-amylin (20-29) sample is presented in figure 3.5. ES-MS : m/z 1061.19 (46 %, [MH]).

Presented in figure 3.6 is a RP-HPLC chromatogram typical of that obtained during RP-HPLC analysis on the alkyne-amylin (20-29) peptide. The solvent front is observed at 5 minutes, followed by a dominant peak at 14.6 minutes corresponding to the target peptide and lower intensity (<30 %) peak at 15.5 minutes.

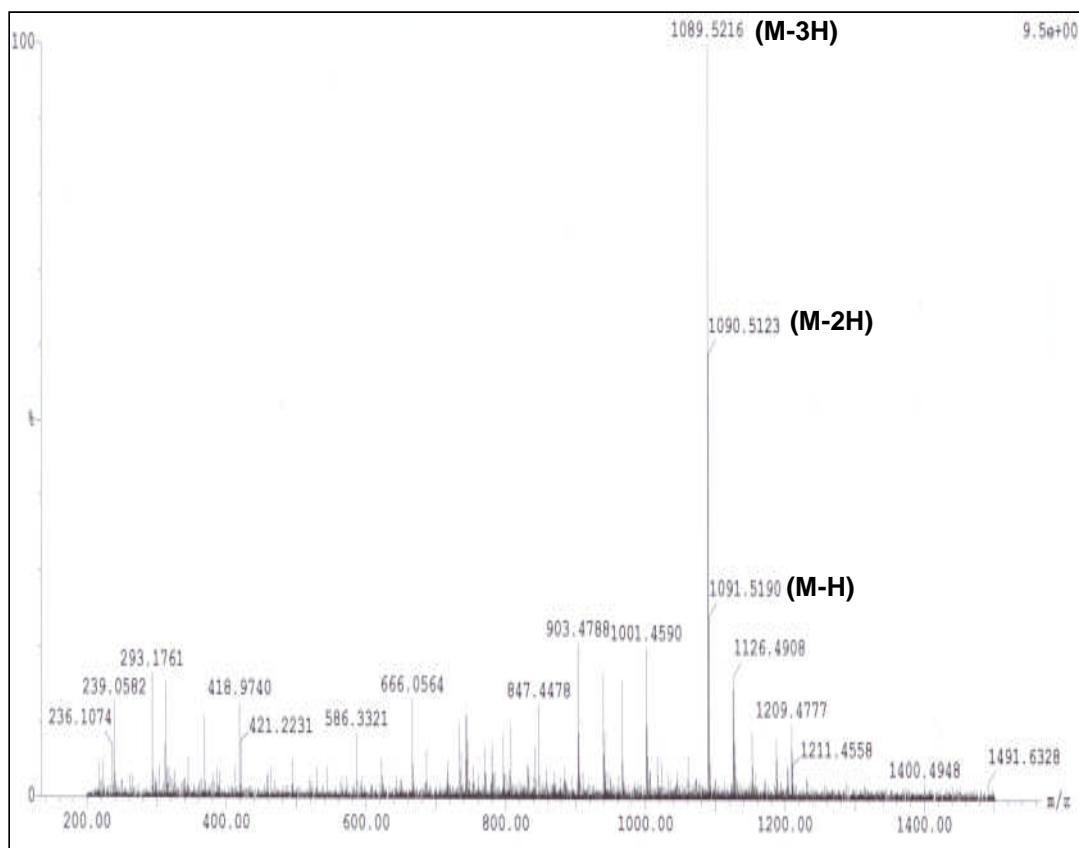


Figure 3.3: LC-MS spectrum for the azide-form of amylin (20-29) peptide. Negative ionisation spectrum. The parent ion (M-H) is observed at m/z 1091.51 (25%). Two peaks of higher intensity correspond to deprotonated forms of the ion, at m/z 1090.51 (58%, (M-2H)) and 1089.52 (base peak, (M-3H))

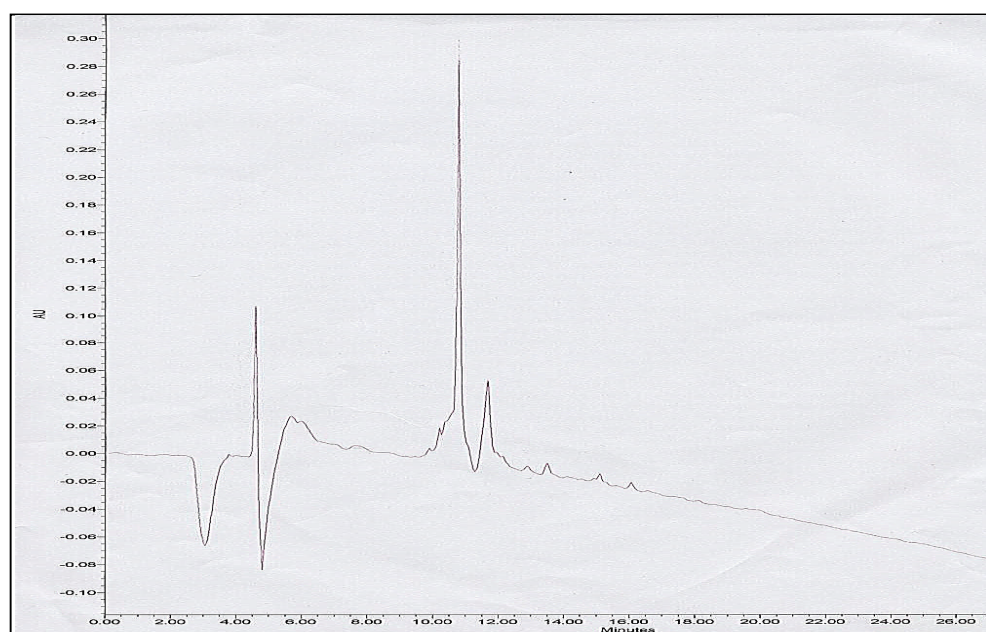


Figure 3.4: RP-HPLC chromatogram for azide-amylin (20-29) peptide. The major peak at 10.75 minutes corresponds to the target peptide. Smaller peaks of later eluting impurities are also observed.

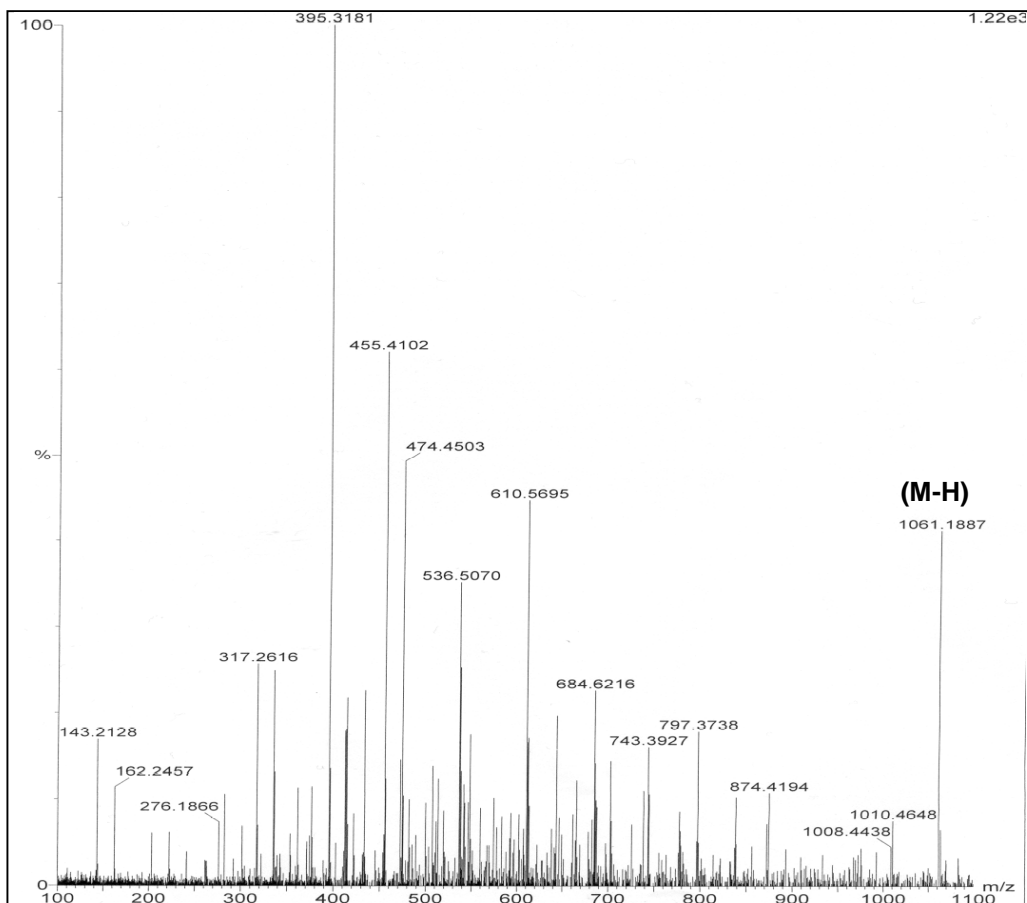


Figure 3.5: LC-MS spectrum for the alkyne-form of amylin (20-29) peptide. Positive ionisation spectrum. The parent molecular ion, [M-H], was observed at m/z 1061.19 corresponding to the expected molecular weight of the alkyne-amylin (20-29) ion

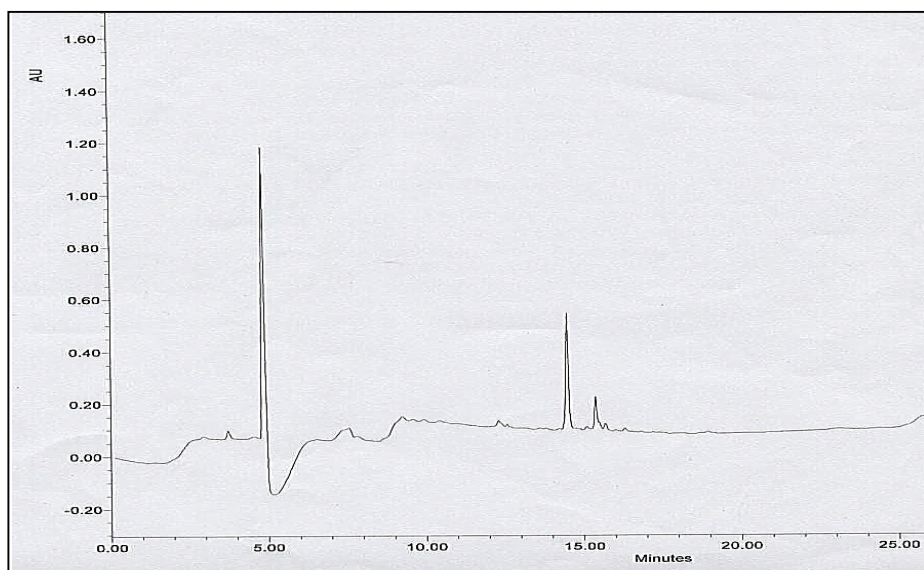


Figure 3.6: RP-HPLC chromatogram for alkyne-amylin (20-29) peptide. A major peak is present at 14.6 minutes, with later eluting smaller (< 30%) peak at 15.5 minutes. Method: gradient of 30 to 100 % B over 30 minutes with flow rate of 5 ml/min.

3.3.3 *Preliminary AFM study of fibrillisation*

A preliminary study to investigate the influence of the azide and alkyne moieties on fibrillisation of amylin (20-29) peptide was performed. Peptide samples were prepared in ultrapure water at a final peptide concentration of 300 $\mu\text{g/ml}$ and aged for 24 hours at room temperature before imaging by tapping-mode *ex situ* AFM. Samples of either the azide or alkyne forms of the peptide and a 50:50 mix of both forms of the peptide were investigated.

The AFM images presented in figure 3.7 are typical of the azide-amylin (20-29) only sample. In the low resolution topography and phase image shown in Figure 3.7a it can clearly be seen that the functionalised peptide has retained the ability to self-assemble and form fibril structures. Several distinct morphologies of fibrils can be observed in the azide-amylin (20-29) sample. The high resolution topography and phase image shown in figure 3.7b is a zoom in of the lower mid section of figure 3.7a and highlights the variation in the two population morphologies.

The majority of the fibrillar structures observed were short, flattened ribbon-like fibrils with mean half-height widths of 10.2 (± 2.8) nm and heights of 1.58 (± 0.38) nm. The fibrils were predominantly laterally aligned on the mica surface with a propensity to associate together in single layers. Several truncated fibrils were observed individually, enabling a clearer view of the topography of the fibrils. The surfaces of the fibrils appear globular and less uniform than similarly aged fibrils of non-functionalised amylin (20-29) observed previously (figures 2.6, 2.7-8).

A second less abundant population of larger fibrils was observed in the sample. These structures displayed greater half-height widths and heights but which varied significantly within the sample. In the majority of these larger fibrils a periodicity along the fibril axis can be observed. The longitudinal cross-section along the

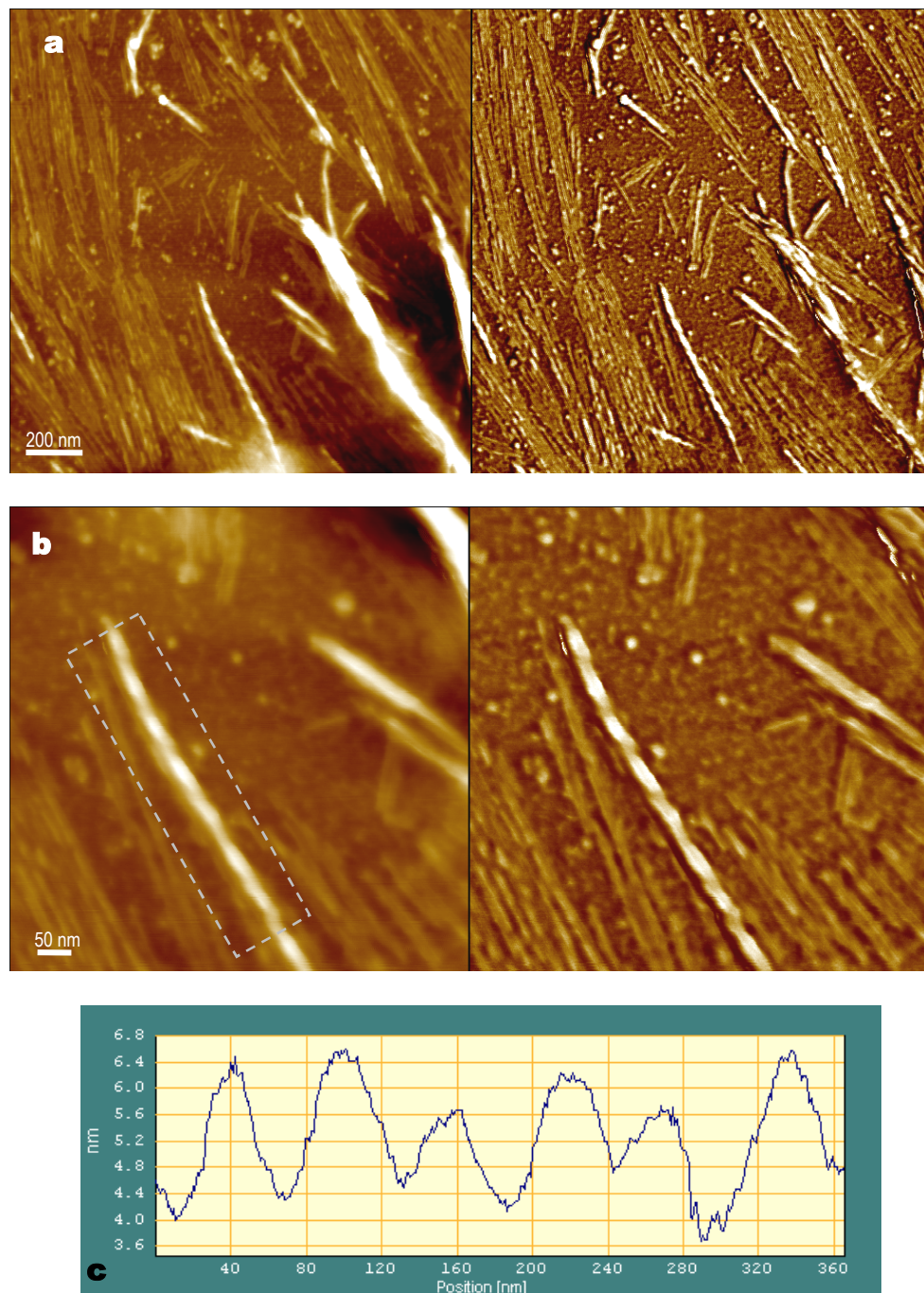


Figure 3.7: *Ex situ* AFM images of azide amylin (20-29) sample. Samples were aged for 24 hours in ultrapure water before aliquots were dried onto freshly cleaved mica. The final peptide concentration was 200 $\mu\text{g/ml}$. **Figure 7a** shows typical topography (left) and phase (right) images of the sample. **Figure 7b** shows a higher-resolution topography (left) and phase (right) images, a line profile along the axis of the boxed fibril is shown in **figure 7c** and demonstrates the periodicity of the fibril twist. Z range contrast bars are shown.

fibril axis highlighted by the box in figure 3.7b can be seen in figure 3.7c. A regular periodicity can be observed along the fibril axis and is approximately 55 nm. However, in other fibrils this periodicity was not always as regular and varied in twist.

The AFM images presented in figure 3.8 are representative of the images generated of the alkyne-amylin (20-29) sample. In contrast to the azide-amylin (20-29) sample, no periodicity was observed in the fibrillar structures found in the alkyne-amylin (20-29) only sample. However, in similarity, two distinct morphologies were observed which displayed similar topographies.

One morphological type is illustrated by the fibrillar structures observed in the low resolution topography image shown in figure 3.8a. Individual fibrils have associated into larger fibrillar structures which have a dense network of material. Figure 3.8b shows a zoomed in section of this network; the phase data provides further detailed information on the constituent fibrils which comprise these fibrillar structures. These larger structures comprise differing numbers of fibrils which are laterally aggregated. Several of which over the lengths of the structure have a non-uniform twist along the axis.

The second class of fibril morphology is typified by the fibrils shown in the high-resolution topography image presented in figure 3.8c. The fibrils are observed individually or loosely laterally associated on the mica surface. Individual fibrils are flat ribbon-like structures with mean half-height widths of 11.28 (± 2.16) nm and mean height of 1.29 (± 0.30) nm. In similarity to the fibrils formed from azide-amylin (20-29), the surface morphology of the fibrils is in most instances non-uniform with a slight globular appearance displaying an irregular periodicity.

The images presented in figure 3.9 are representative of the low (figure 3.9a) and high-resolution (figure 3.9b) images of the fibrillar structures formed in samples comprising a 50:50 mix of both azide and alkyne-amylin (20-29) peptides. Two distinct morphologies of fibrils can be observed. The first are single-layered, laterally aligned fibrils. The second are aggregated groups of fibrils formed into larger fibrillar structures, which have entangled forming a network. The first morphological population comprises of fibrils with half-height widths in the range

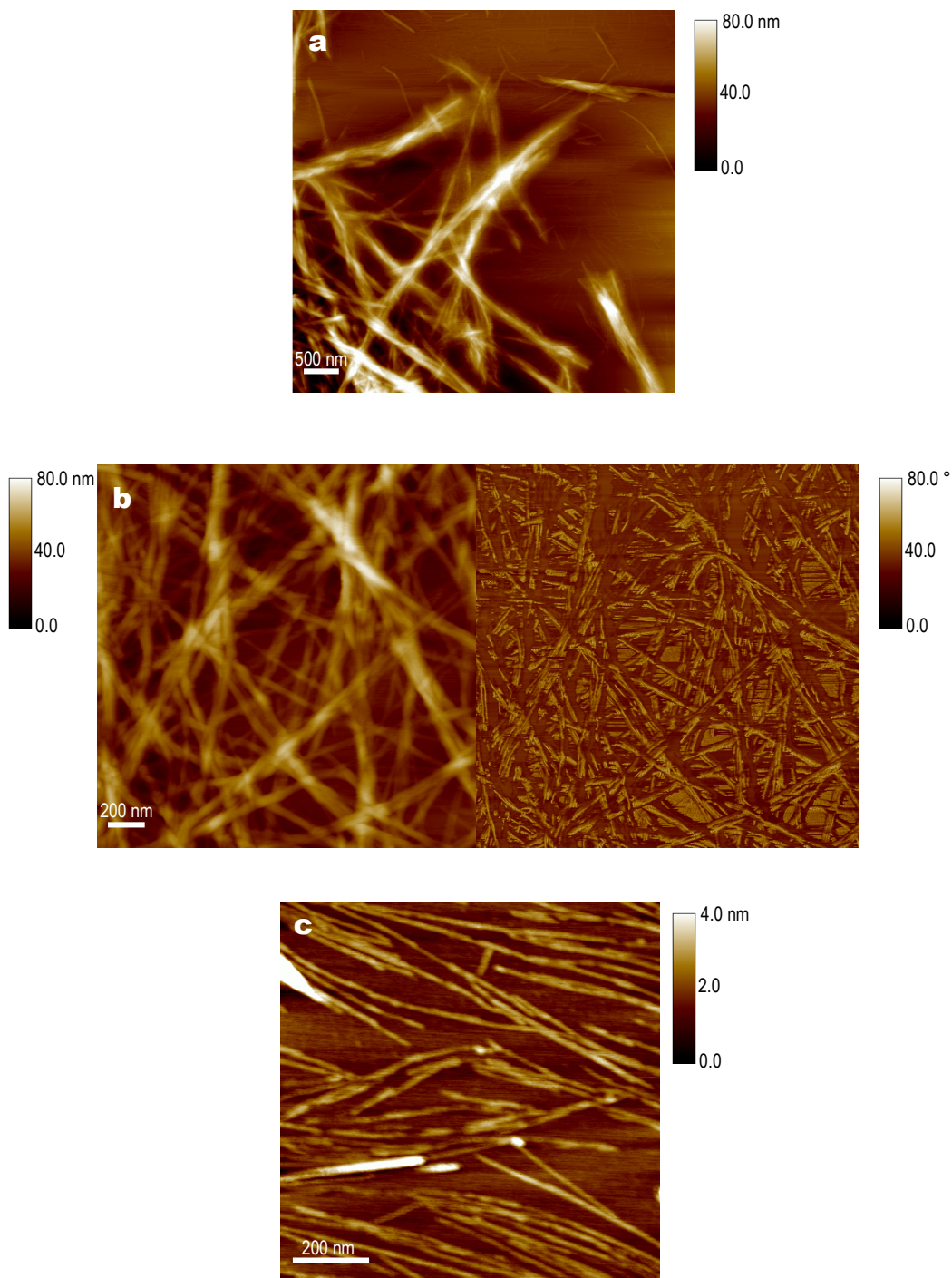


Figure 3.8: *Ex situ* AFM images of alkyne amylin (20-29) sample. Samples were aged for 24 hours in ultrapure water before aliquot samples were dried onto freshly cleaved mica. The final peptide concentration was 200 $\mu\text{g/ml}$. **Figure 8a** shows a topography image of the sample. **Figures 8b** and **8c** are typical higher-resolution topography (left) and phase (right) images demonstrating the variation in fibril morphologies observed. Z range contrast bars are shown.

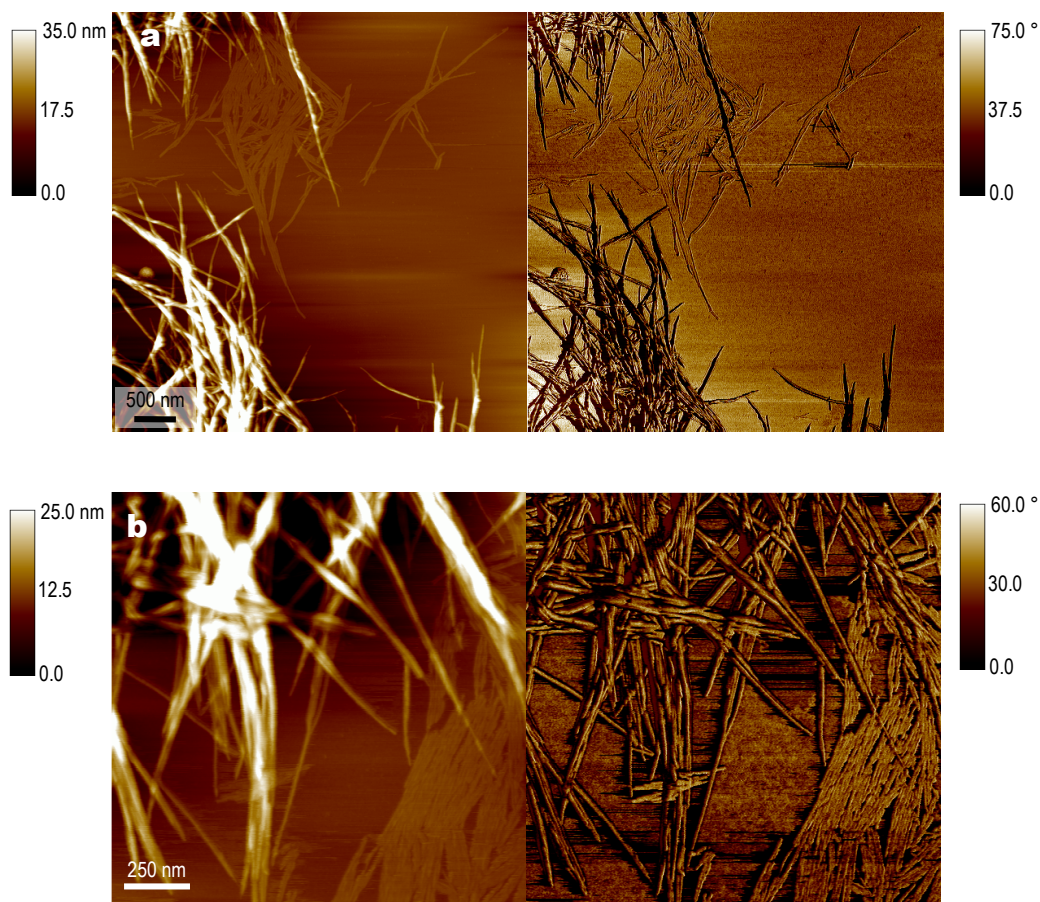


Figure 3.9: *Ex situ* AFM images of 50:50 mix of azide and alkyne amylin (20-29) samples. Equal quantities of both peptides were solubilised in ultrapure water and aged for 24 hours, before aliquot samples were dried onto freshly cleaved mica. The final peptide concentration was 300 $\mu\text{g/ml}$. **Figure 9a** shows a typical topography (left) and phase (right) image of the sample. Higher-resolution topography (left) and phase (right) images of the sample are shown in **figure 9b**. Z range contrast bars are shown.

7 to 12 nm and heights of approximately 1.4 nm. By comparison, the smallest resolvable fibrils displaying the second morphological type are wider with dimensions in the range of 19 to 30 nm.

3.3.4 Congo red assay

To establish whether the fibrillar structures formed by the azide and alkyne forms of amylin (20-29) have retained the common amyloid structure, samples were assayed using Congo red staining; the histopathology stain for the detection of amyloid. Under polarized light amyloid stained with Congo red dye will display a green gold birefringence [27]. Samples of the azide-form and alkyne-form of amylin (20-29) in ultrapure water were aged for 18 hours to ensure sufficient time for fibril formation. Aliquot samples were dried and stained with the Congo red dye and the appearance of birefringence noted under polarized light. The optical micrographs shown in figures 3.10a and b are of the stained azide form of the amylin (20-29) under non-polarised and polarized light, respectively. A green gold birefringence can be observed under the polarized light. The micrographs presented in figures 3.10c and d are of the alkyne-form of the amylin (20-29) peptide under non-polarised and polarized light, respectively; a green gold birefringence is observed.

3.3.5 Copper (I) Catalysed Cycloaddition

Following the successful fibrillisation of the functionalised amylin (20-29) peptide, an AFM study of the peptides under the copper (I) catalysed cycloaddition reaction conditions was performed. The study comprises several conditions in which the peptides are either initially ($t = 0$ hours) solubilised in 1 mM and 5 mM equivalent of copper (I), or allowed to preform into fibrils prior to addition at 18 hours ($t = 18$ hours) of the 1 mM and 5 mM equivalent of copper (I) cycloaddition reaction mixture.

3.3.5.1 1 mM Copper (I)

3.3.5.1.1 Fibrillisation in the presence of Cu (I) ($t = 0$ hours)

After incubating the azide-form and alkyne-form of the amylin (20-29) peptide in isolation in 1 mM copper sulphate with ascorbic acid solution for 18 hours, fibrillar structures were observed in both samples. These results provide evidence

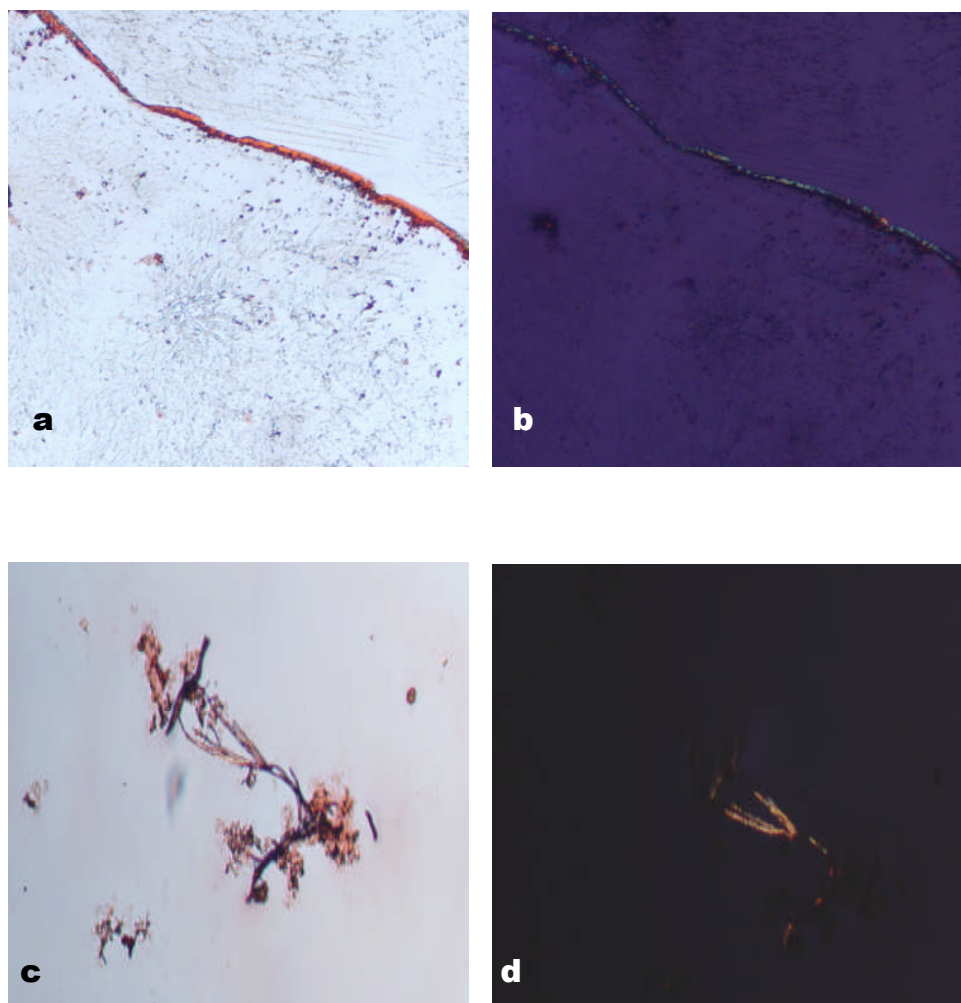


Figure 3.10: Congo red assay of azide- and alkyne- amylin (20-29) peptide. Peptide samples were aged for 18 hours in ultrapure water, before aliquot samples were removed, dried and stained with Congo red solution. **Figures 10 a** and **b** show samples of the azide-amylin (20-29) samples under normal and polarised light respectively. **Figures 10 c** and **d** show samples of the alkyne-amylin (20-29) samples under normal and polarised light respectively.

that neither the copper salts nor any of the components (ascorbic acid, ethanol) of the cycloaddition reaction mixture inhibit the formation of fibrils by the functionalized amylin (20-29) peptide. The AFM topography images presented in figure 3.11 are typical of the azide-amylin (20-29) peptide (figure 3.11a and b) and alkyne-amylin (20-29) peptide (figure 3.11c and d) samples at 18 hours.

In similarity to the fibrils formed by the peptides in the absence of copper salts, the fibrils have flattened ribbon-like morphologies. The azide-amylin (20-29) fibril samples display a mean half-height width of 10.97 (± 1.8) nm and height of 2.69 (± 0.31) nm. By comparison, the average half-height width of the fibrils from the alkyne-amylin (20-29) sample was 18.33 (± 2.7) and mean height of 1.84 (± 0.51) nm.

Figure 3.11a is a topography image typical of the fibrils formed by the azide-amylin (20-29) peptide. The fibrils captured in the high-resolution topography image in figure 3.11b demonstrate the uniform and smooth topography of the fibrils. In the upper portion of the group of fibrils highlighted by the arrow in figure 3.11b, two fibrils are observed twisted together. This form of association was infrequently observed in the samples and the majority of fibrils were observed individually or with some propensity to associate together laterally. The mica surface appeared clear of physisorbed non-fibrillar material except for small pockets of amorphous debris which can be observed in the background of the images. All solutions were filtered through 0.2 μm gauze prior to use, therefore it is likely that the debris is dried salt deposits or non-fibrillised peptide material.

Typical fibrillar material observed in the alkyne-amylin (20-29) peptide samples is presented in the topography image shown in figure 3.11c. Fibrils were rarely observed individually, but instead were predominantly associated together in aggregates of several fibrils that interconnected to form networks of loosely coiled or laterally grouped larger structures. Figure 3.11d is a higher-resolution topography image and demonstrates the uniform and smooth topography of the individual alkyne-amylin (20-29) fibrils.

Collectively the images presented above in figure 3.11 demonstrate that the presence of the copper (I) solution is not inhibitive to the formation of fibrils by either forms of the amylin (20-29) peptide. Therefore the next stage in this set of experiments, was to perform the cycloaddition reaction assay, combining both forms of the functionalized amylin (20-29) peptide in the presence of copper (I) salts. Equal quantities of both forms of the peptide were solubilised together in the cycloaddition copper solution and mixed continuously for 18 hours. Aliquots of both samples were removed, dropped onto freshly cleaved mica and imaged in air using tapping mode AFM. Presented in figures 3.12 are a typical selection of the images that were generated.

Two distinct fibril morphologies were observed. Figure 3.12a is a typical topography image of the first morphology type, where lower-order fibrils are predominantly observed assembled into larger higher-order fibrillar structures. These structures showed considerable variation in dimension ranging in half-height widths from 55 to 130 nm and average height of $9.7 (\pm 3.2)$ nm. The lower-order fibrils are resolvable in these structures giving them a non-uniform surface topography. In some instances a distinct periodicity can be observed where several lower-order fibrils are entwined together. A typical example of this is shown in figure 3.12b which is a digital zoom of the central boxed area in figure 3.12a; the fibril has a distinct globular appearance with a slightly irregular but distinct periodicity. Figure 3.12c is a digital zoom of the upper boxed area in figure 3.12a, the lower-order fibrils are resolvable within the higher-order structures but do not display any periodicity and do not appear to be coiled around one another.

The second morphology is typified by the fibrils present in the topography image presented in figure 3.12d. Fibrils are thinner and shorter, and laterally align into layers one fibril thick. This population of fibrils had a mean half-height width of $16.7 (\pm 3.02)$ and height of $1.75 (\pm 1.1)$ nm. Figure 3.12e is a high-resolution zoom of the boxed area in figure 3.12d highlighting the differences in dimensions and morphologies between the two types of fibril.

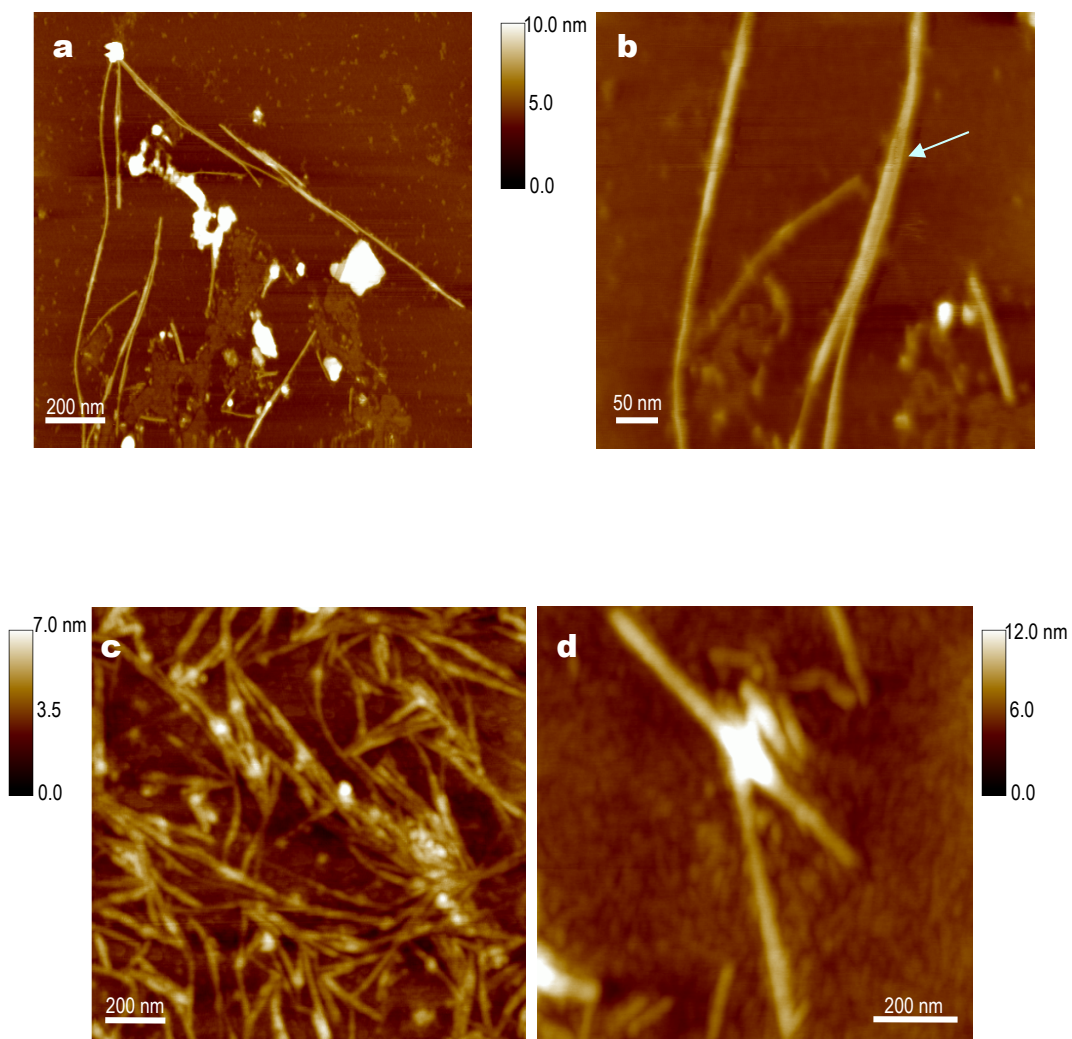


Figure 3.11: *Ex situ* AFM images of 1 mM Cu⁺ present from 0 hours azide and alkyne amylin (20-29) samples. Peptide was solubilised in 1 mM Cu⁺ salt solution, at 18 hours aliquot samples were dried onto freshly cleaved mica. The final peptide concentration was 300 µg/ml. Topography images of the azide peptide sample are shown in **figure 11a** and higher-resolution in **figure 11b**. Topography images of the alkyne peptide sample are shown in **figure 11c** and **figure 11d**. Z range contrast bars are shown.

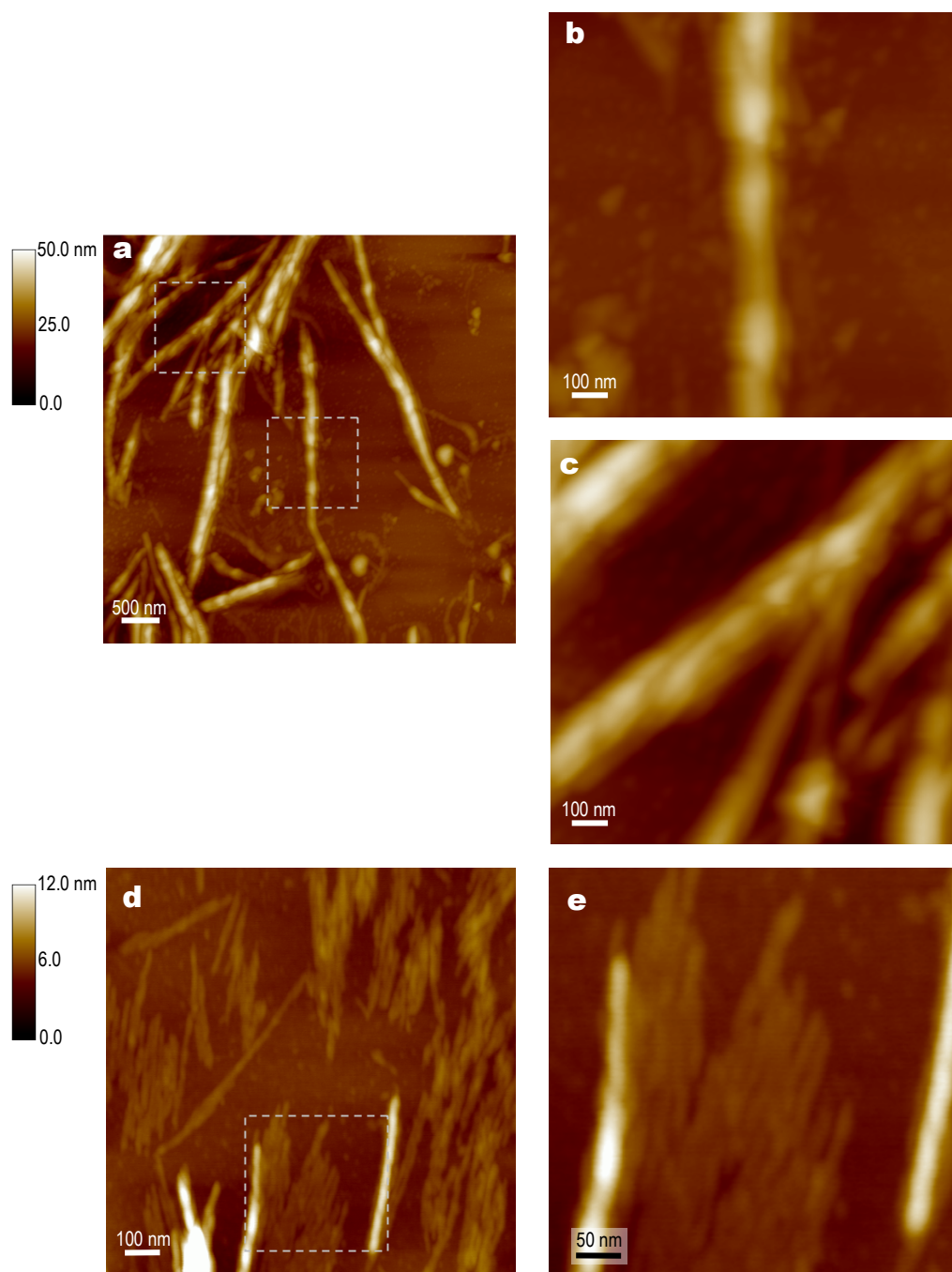


Figure 3.12: *Ex situ* AFM images of 50:50 mix of both peptides in 1 mM Cu^+ present from 0 hours. Peptide was solubilised in 1 mM Cu^+ salt solution, at 18 hours aliquot samples were dried onto freshly cleaved mica. The final peptide concentration was 300 $\mu\text{g/ml}$. **Figure 12a** is a topography image of the peptide sample, higher-resolution topography images of the boxed areas are shown in **figure 12b** highlighting a typical fibril displaying periodicity, and **figure 12c** highlighting fibrils with no periodicity. **Figure 12d** is a topography image, a higher-resolution topography image of the boxed area is shown in **figure 12e**, demonstrating the different fibril morphologies. Z range contrast bars are shown.

3.3.5.1.2 Addition of Cu (I) to solutions of pre-formed fibrils (t =18 hours)

An additional assay was performed to investigate the influence of the cycloaddition reaction on pre-formed fibrils of the azide and alkyne amylin (20-29) either in isolation or in combination. Peptide solutions were prepared initially in ultrapure water and aged for 18 hours at which point the samples were diluted to a final peptide concentration of 300 $\mu\text{g/ml}$ by the addition of the cycloaddition 1 mM copper sulphate with ascorbic acid in water/ethanol and mixed continuously for a further 8 hours.

The images shown in figure 3.13 are of the samples containing azide-amylin (20-29) only peptide. Figure 3.13a is typical of the low-resolution topography images of the fibrillar structures formed. Fibrils were long and ribbon-like in appearance and were observed individually or aggregated as interconnected assemblies. The half-height widths of individual fibrils were greater than previously observed with a mean of 30.24 (± 2.6) nm, but displayed a similar mean height of 1.15 (± 0.27) nm.

In the majority, aggregation of fibrils was by lateral association into interconnected networks of irregular bundles. A typical example of this aggregation pattern can be seen in the high-resolution topography image presented in figure 3.13b. Many of the fibrils associated into these bundles were shorter than the fibrils observed individually.

As with the samples formed in the absence of copper, the twisting of several fibrils into one structure was observed. Figure 3.13c is a high-resolution topography and phase image showing the association of two fibrils (10.8 nm and 13.8 nm) into a single fibril (15.0 nm) by coiling. The phase image enables the two constituent fibrils to be clearly seen. The profile inset is of the cross-section along the axis of the coiled portion of the fibril, the regular periodicity of the twisted fibrils is approximately 32 nm.

An interesting phenomena which was unique to this sample, was the presence of small, dense aggregated balls of fibrils. A typical example of these formations is presented in the high-resolution topography and phase image shown in figure

3.13d. The cross-sectional profile of the fibril ball, shown by the line in the topography image, is presented in the inset panel. As can be seen from the profile, the structure is more a mound on the mica surface than a ball. There is variation in height across the structure with a maximum height of 9.5 nm. Together with the additional topographical details offered by the phase image, these ‘balls’ appear to be formed from irregular bundles of overlapping fibrils analogous to a loose and unevenly wound ball of string. Several ‘ends’ of the constituent fibrils can be seen projecting outwards from the central mass together with longer individual fibrils. Some fibril balls appear more densely packed together than others, however the AFM images do not provide any detailed information on how or why these fibril balls have formed.

Presented in figure 3.14 are images of the alkyne-amylin (20-29) only sample following addition of the cycloaddition reaction mixture at 18 hours. Figure 3.14a is a high-resolution topography and phase image of the lateral assembly of the alkyne-amylin (20-29) fibrils. The phase data provides further topographical detail of the lateral assemblies and enables individual fibrils which are tightly packed within the assemblies to be elucidated. Several fibrils can be seen emerging from the large aggregates, these individual fibrils display heights with a mean of 1.84 (± 0.56) nm. By comparison, the heights of the fibrillar aggregates range from 2.9 to 8.4 nm in height, suggestive that the fibrils are aggregating laterally both side by side and stacked upwards. In the previous examples of lateral assembly of fibrils from either form or mixes of the peptide, aggregation has only been noted side-by-side and not by stacking to form layers several fibrils thick.

Figure 3.14b is a low-resolution topography and phase image, the boxed area has been zoomed in digitally and is shown in figure 3.14c. These images highlight a different type of aggregation pattern of the alkyne-amylin (20-29) fibrils, in which fibrils are observed projecting from a dense central area. Unlike the fibril balls noted in the azide-only samples (figure 3.13d), these dense central points do not have any resolvable ordered structure or surface topography, are more tightly packed, and are considerably greater in height (> 20 nm). However, it is possible

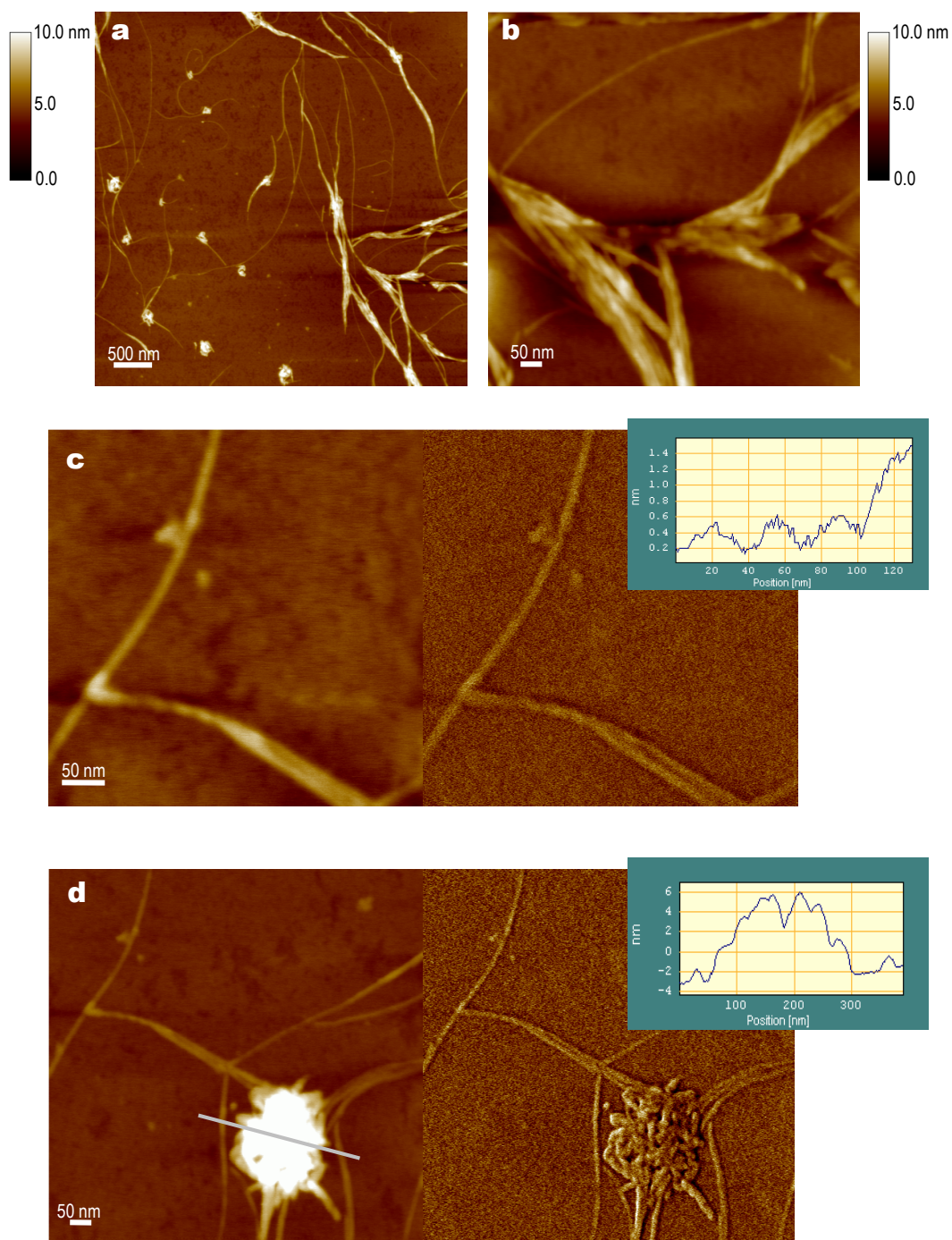


Figure 3.13: Ex situ AFM images of 1 mM Cu⁺ present from 18 hours azide-amylin (20-29) sample. Peptide was solubilised initially in ultrapure water, at 18 hours Cu⁺ salts were introduced. Samples were aged for 8 hours in copper solution before drying onto freshly cleaved mica. The final peptide concentration was 300 µg/ml. **Figure 13a** is an *ex situ* topography image of the peptide sample. Z range contrast bars are shown. Higher-resolution topography images highlighting individual features are shown in **figure 13b** (topography), **figure 13c** (topography and phase) and **figure 13d** (topography and phase). Insets are cross-sectional profiles.

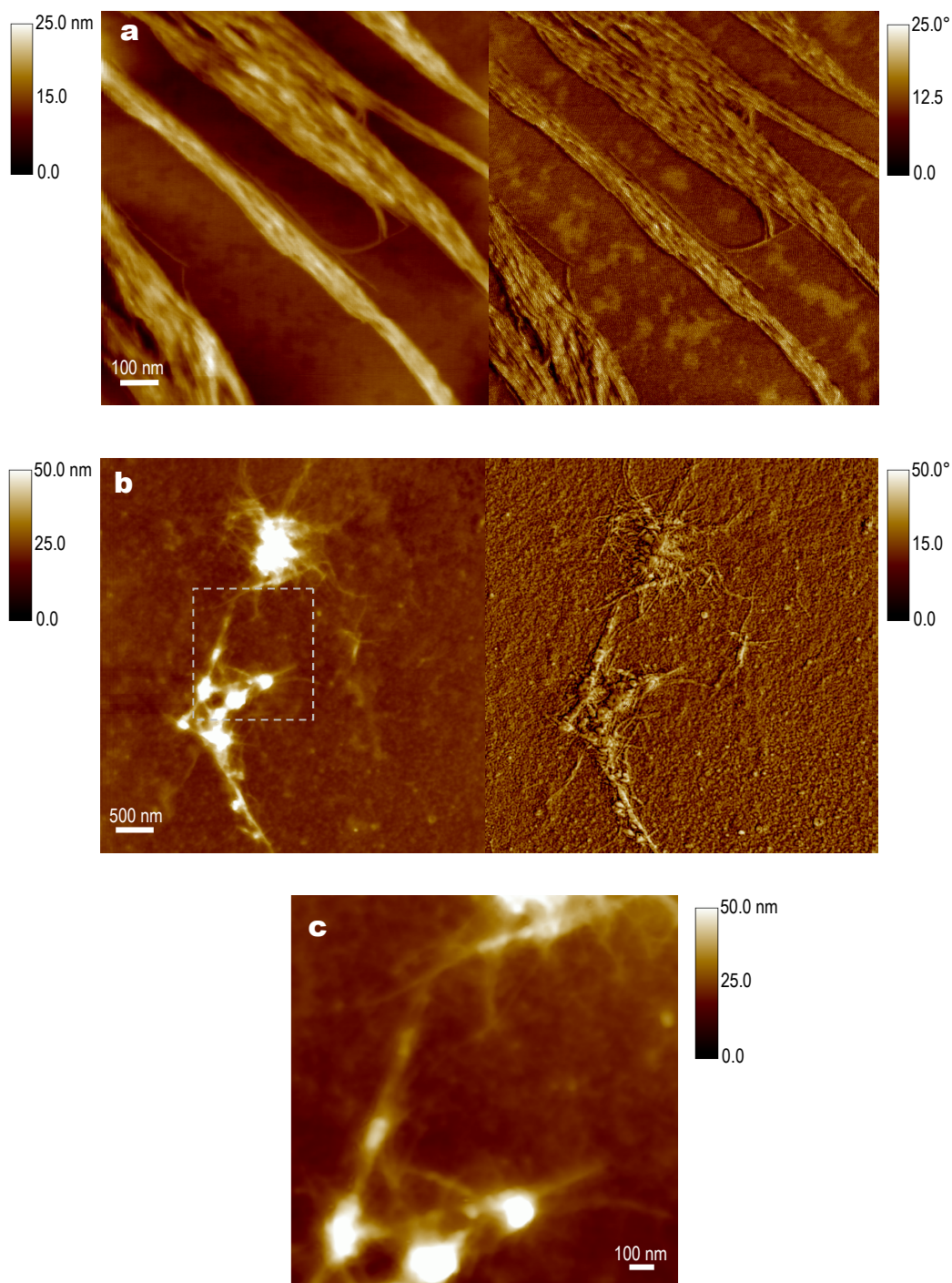


Figure 3.14: Ex situ AFM images of 1 mM Cu⁺ present from 18 hours alkyne–amylin (20-29) sample. Peptide was solubilised in ultrapure water, at 18 hours Cu⁺ salts were introduced. Samples were aged for 8 hours in copper solutions before drying onto freshly cleaved mica. The final peptide concentration was 300 µg/ml. **Figure 14a** shows a high-resolution topography (left) and phase (right) image of the peptide sample. **Figure 14b** shows a topography (left) and phase (right) image of a different fibril morphology type, a higher-resolution 1.6 µm x 1.6 µm topography image of the boxed area is shown in **figure 14c**. Z range contrast bars are shown.

that these structures are similar to the fibril balls but tighter packing results in unresolvable structure.

The topography images shown in figure 3.15 are representative of those generated for samples containing equal quantities of both forms of the peptide, which were allowed to form fibrils in ultrapure water before the addition of the cycloaddition copper solution at 18 hours, after which time the solution was mixed continuously for a further 8 hours. Figure 3.15a is a low-resolution topography image of the fibrils observed. Despite consistently using the same peptide concentration (300 $\mu\text{g/ml}$), fibrils were observed infrequently in the samples. Fibrils were present either individually or as small groups aggregated together in a manner typical of those shown in figure 3.15a. Individual fibrils are long and flat structures with smooth surface topographies. Dimensions of the fibrils were larger than that measured for the same sample but in the absence of copper and had a mean half-height width was 33.7 (± 6.4) nm and mean height of 3.80 (± 1.4) nm. Several examples of fibrils grouped together by intertwining of several fibrils to form larger fibrillar structures can be found in the image in figure 3.15a. The fibrils highlighted by the boxed area are an example of this; a higher-resolution topography image in of this area is shown in figure 3.15b. Three individual fibrils can be seen emerging from a larger structure at the bottom of the image, one of which branches higher up to produce a fibril with the same dimensions. The original fibril is then observed coiling together with another of the starting fibrils to form a single structure again. The digitally zoomed in area shown in figure 3.15c is another example where the coiling of several fibrils to form a larger structure is evident due to the unraveling or loose coiling of the constituent fibrils. The fibril marked with an arrow in this group appears to have regions of different thickness (19.7 nm, 31.3 nm and 20.2 nm), which may be evidence of further structural hierarchy, given that the smaller thickness dimensions are in keeping with those seen in figure 3.12.

3.3.5.2 5 mM Copper (I)

In the current literature investigating the applications and mechanisms of this 1,3 dipolar cycloaddition reaction the concentration of copper (I) salts employed

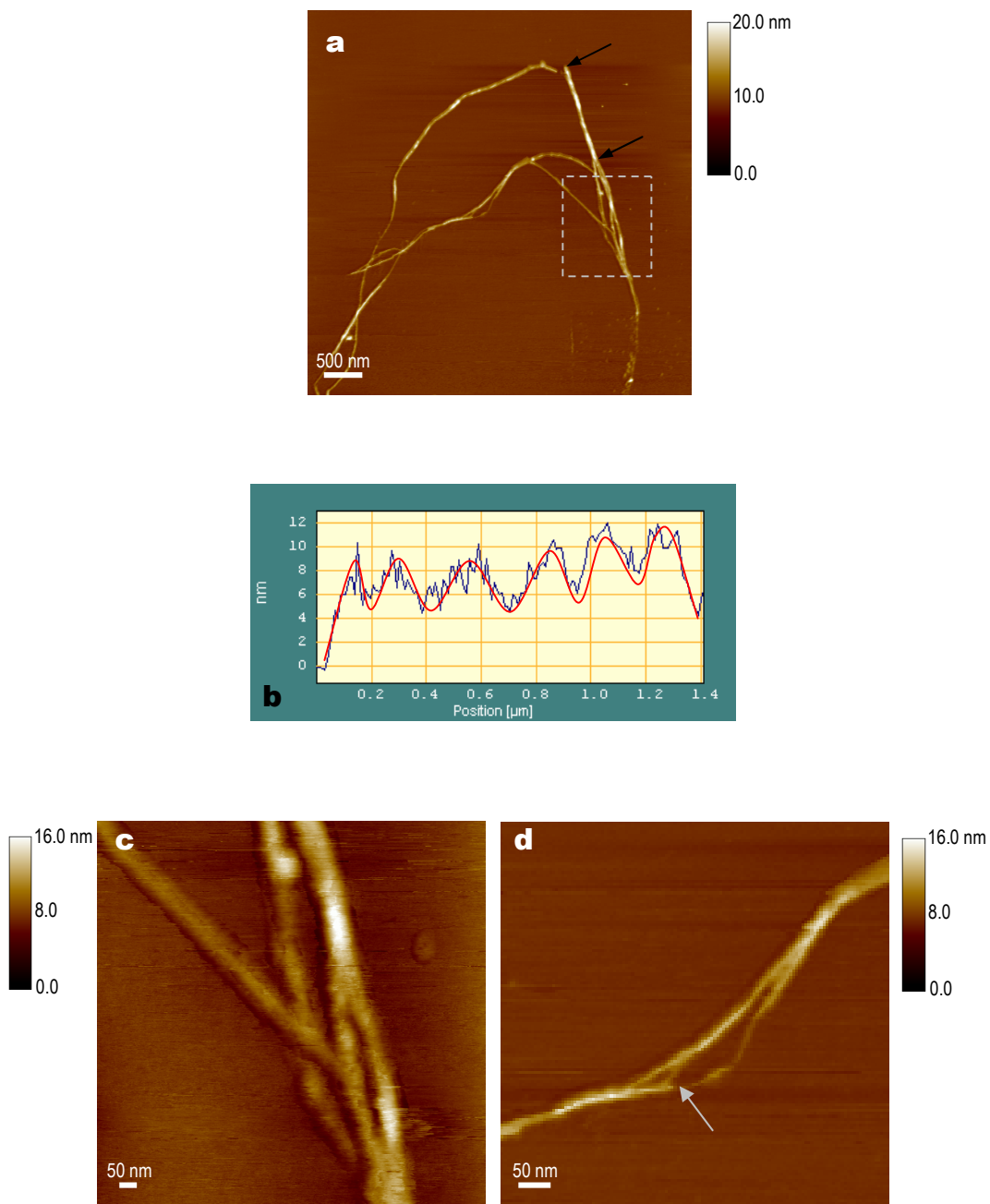


Figure 3.15: *Ex situ* AFM images of 50:50 mix of both peptides in 1 mM Cu^+ present from 18 hours. Peptide was solubilised in ultrapure water, at 18 hours Cu^+ salts were introduced. Samples were aged for 8 hours in copper solution before drying onto freshly cleaved mica. The final peptide concentration was 300 $\mu\text{g}/\text{ml}$. **Figure 15a** shows a topography image, a line profile along the axis of the fibril between the arrow markers is shown in **figure 15b**, demonstrating the periodicity of the twist. A higher-resolution topography image of the boxed area is shown in **figure 15c**. The arrow in the high-resolution topography image shown in **figure 15d** highlights a lower-order fibril. Z range contrast bars are shown.

range from 0.5 mM to 2 mM [204, 211, 213, 214, 216]. Given that no change in fibril morphology or assembly has been observed here for copper concentrations of 1 mM, a follow-up experiment was performed to assay the effects of a five-fold increase in copper concentration on fibril formation and assembly.

3.3.5.2.1 Fibrillisation in the presence of Cu (I) (t=0 hours)

Presented in figure 3.16 are typical AFM images in air of samples of 50:50 mix of both forms of amylin (20-29) peptide solubilised in solutions of 5 mM copper sulphate with ascorbic acid in ethanol/water and aged for 18 hours. The low-resolution topography and phase image shown in figure 3.16a are typical of the fibrils formed under these conditions. Fibrils were flat ribbon-like structures which aggregated together in large dense pockets on the mica surface. Similar densely packed regions were observed in the samples containing no copper and in the alkyne-only peptide samples. Fibril width and length dimensions are equivalent to those measured in samples in the absence of copper and in 1 mM copper, with mean half-height width of 17.59 (± 2.7) nm. However an increase in fibril heights with a mean of 5.54 (± 1.95) nm was observed.

The high-resolution topography and phase image presented in figure 3.16b is a zoom in to the perimeter of one of the dense aggregate pockets and reveals more morphological detail of the individual fibrils. The surface topography of the fibrils is not as smooth as that observed in any of the previous samples. In the phase image, the fibril surfaces appear fragmented, which may provide further support that the fibrils are the assembly of lower-order fibrillar structures that are resolvable in this image. The lower-order fibrils appear in most instances to be truncated structures.

3.3.5.2.2 Addition of Cu (I) to solutions of pre-formed fibrils (t =18 hours)

The images presented in figure 3.17 are of samples of a 50:50 mix of both forms of amylin (20-29) peptide in which the 5 mM copper cycloaddition reaction mixture was not added until 18 hours, at which point it was left for a further 8 hours before imaging. In the low-resolution topography and phase image

presented in figure 3.17a, two distinct types of fibril morphology and aggregation pattern can be seen and are similar to those observed in the samples in the absence of copper. The first type are low lying fibrils that laterally align as a tightly packed blanket with few gaps forming a uniform single thickness layer on the mica surface. The fibrils display a mean half-height width of 20.8 (± 3.52) nm and height of 2.25 (± 0.74) nm. In contrast, fibrils displaying the second type of morphology aggregate together to form irregular, larger interconnected bundles. The bundles that are deposited on the top of the laterally aligned fibril layer, in general, cause disruption to the underlying layer and clear mica can be observed (exemplified in the bottom right corner of the phase image in figure 3.17a). The fibrils are larger and have a mean half-height of 38.10 (± 6.60) nm and mean height of 6.53 (± 2.59). The higher-resolution topography image shown in figure 3.17b demonstrates the differences in size and aggregation pattern of the two types of morphologies and highlights the dense packing of the laterally aligned fibrils. The smooth and uniform surface topography of the fibrils from both morphologies can be seen clearly in the high-resolution image shown in figure 3.17c.

To allow for comparisons to be drawn, frequency distributions of the half-height widths and height measurements of the fibrillar structures formed in samples containing both forms of the peptide in 0, 1, and 5 mM copper have been plotted and are presented in figure 3.18. The histograms shown in figures 3.18a and b are the frequency distributions of the half-height widths of fibrils observed in samples where the copper catalyst was present from 0 hours and 18 hours respectively. The histogram presented in figures 3.18c and d are fibril height frequency distributions of samples where the copper catalyst was present from 0 hours and 18 hours respectively.

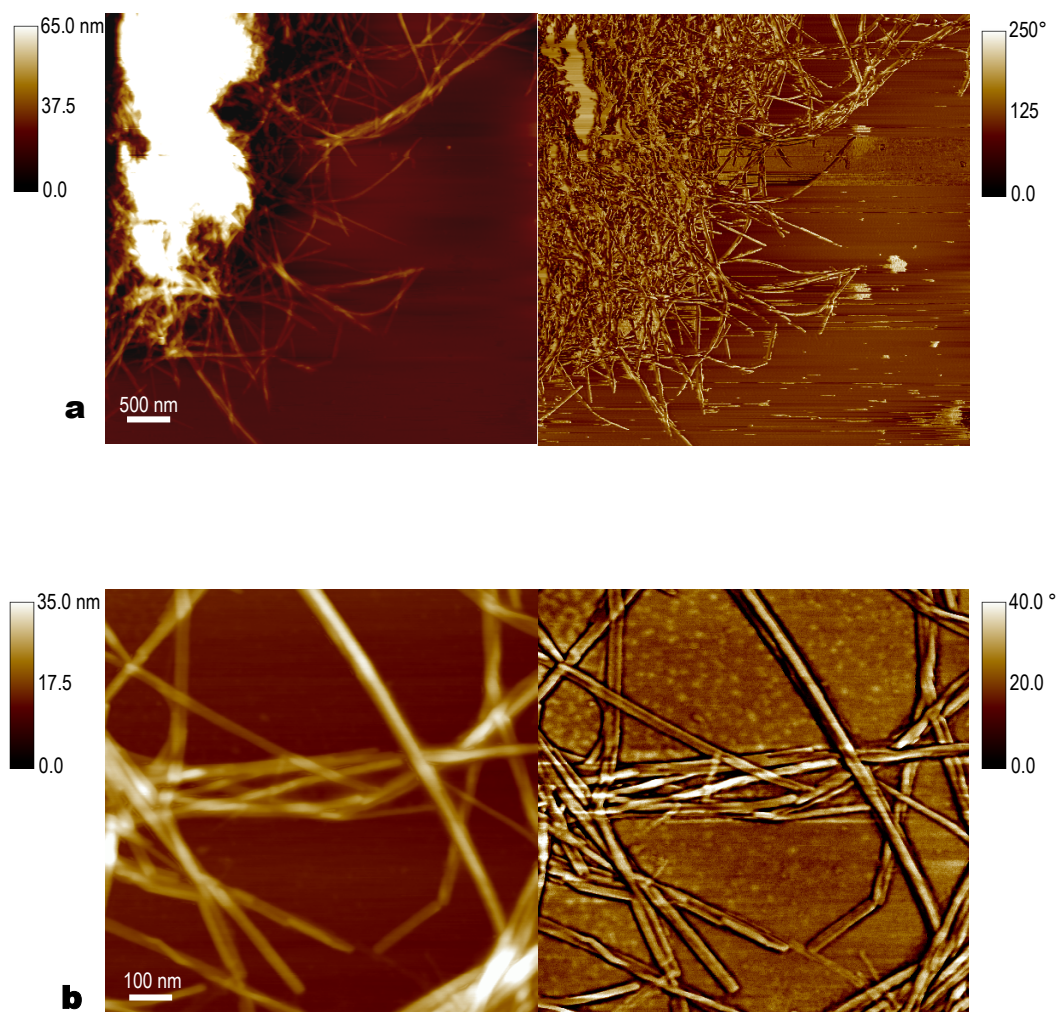


Figure 3.16: Ex situ AFM images of 50:50 mix of both peptides in 5 mM Cu⁺ present from 0 hours. Peptide was solubilised in 5 mM Cu⁺ salt solution, at 18 hours aliquot samples were dried onto freshly cleaved mica. The final peptide concentration was 300 µg/ml. **Figure 16a** shows a topography (left) and phase (right) image of the peptide sample. A higher-resolution topography (left) and phase (right) image of an area in the top centre is shown in **figure 16b**. Z range contrast bars are shown.

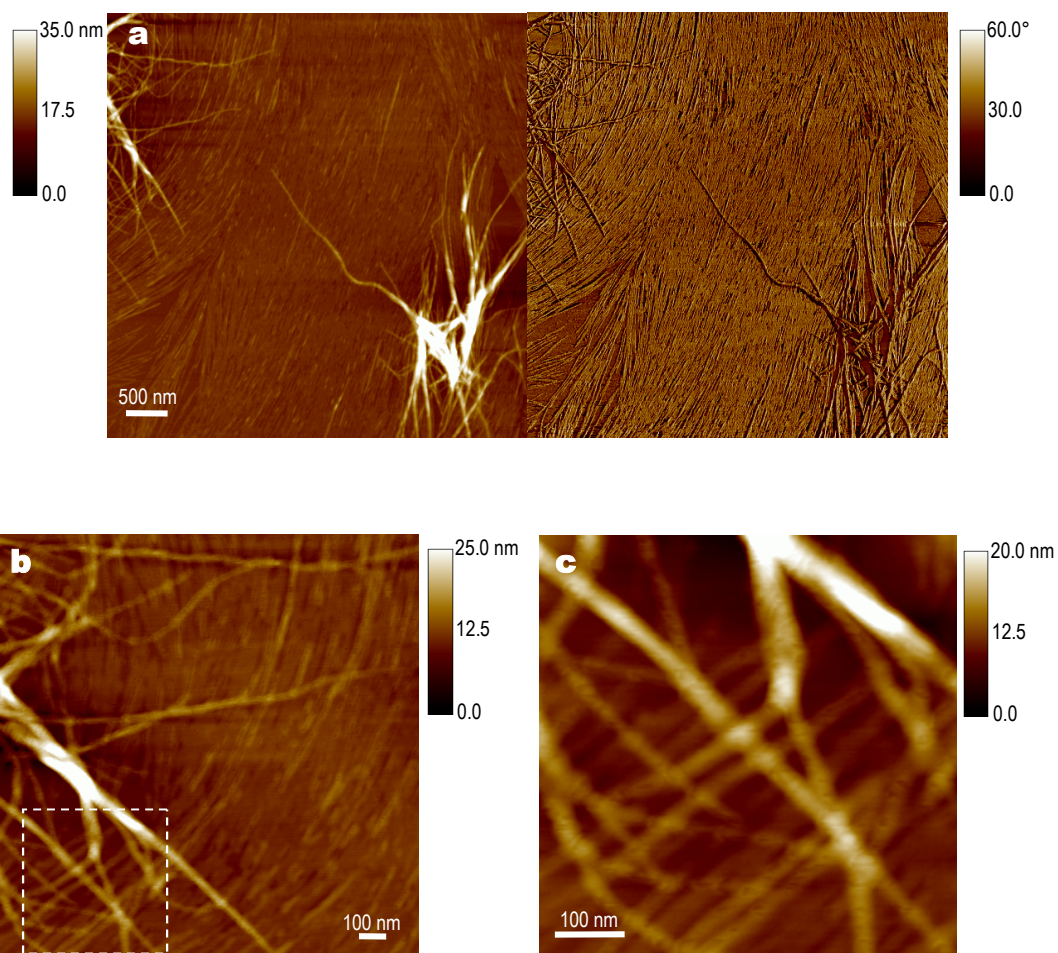


Figure 3.17: *Ex situ* AFM images of 50:50 mix of both peptides in 5 mM Cu⁺ present from 18 hours. Peptide was solubilised in ultrapure water, at 18 hours Cu⁺ salts were introduced. Samples were aged for 8 hours in copper solution before drying onto freshly cleaved mica. The final peptide concentration was 300 µg/ml. **Figure 17a** shows a topography (left) and phase (right) image of the peptide sample. A higher-resolution topography image is shown in **figure 17b** demonstrating the different fibril morphologies, a high-resolution topography image of the boxed area is shown in **figure 17c**. Z range contrast bars are shown.

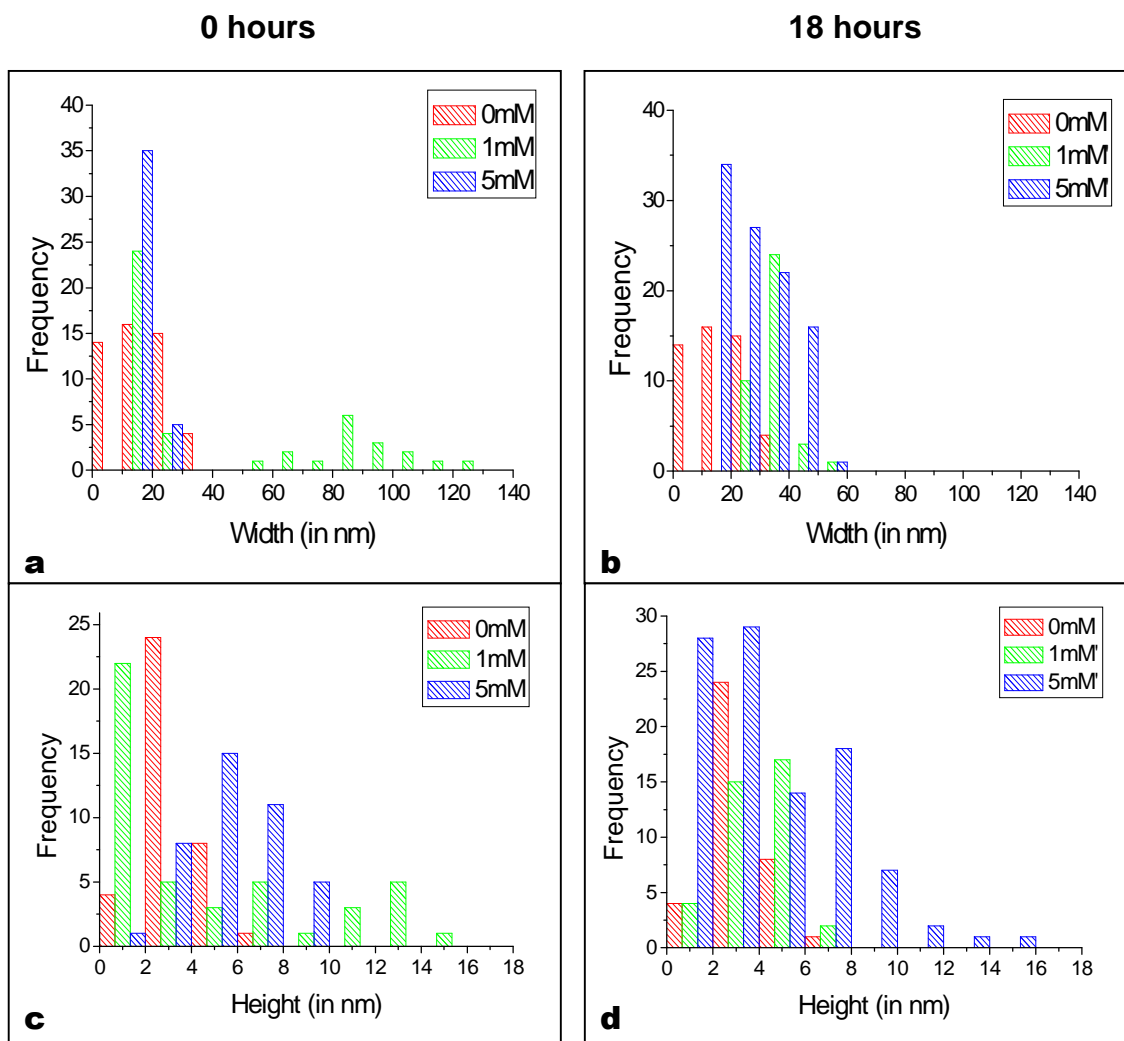


Figure 3.17: Histograms showing the frequency distribution of amylin (20-29) fibril widths and heights in copper catalyst concentrations of 0, 1 and 5 mM. Histograms of the frequency distribution of fibril half-height widths formed in copper solutions present from **a)** 0 hours and **b)** 18 hours. Histograms of the frequency distribution of fibril heights formed in copper solutions present from **c)** 0 hours and **d)** 18 hours. Fibril widths and heights were measured from AFM *ex situ* images of samples containing mixtures of both azide and alkyne forms of amylin (20-29) with either 0 or 1 or 5 mM copper catalyst solution added either prior to fibril formation at 0 hours or to pre-formed fibril samples at 18 hours.

3.4 Discussion

In this chapter the effects on fibrillisation of the introduction of an azide and terminal alkyne functional group to the amylin (20-29) peptide has been investigated by AFM and Congo red staining. In addition, the use of the 1,3 dipolar cycloaddition reaction of azide and alkynes to form 1,2,3 triazole rings has been studied for the formation of covalent links between the fibrils of the functionalized amylin (20-29) peptide.

Solid phase peptide synthesis was successfully used in the synthesis of amylin (20-29) peptides with either an azide group or alkyne group coupled to the N-terminus. Synthesis of the azide-form of the peptide required the initial synthesis of 2-azidoacetic acid from bromoacetic acid and sodium azide, which comprises the azide functional group and carboxy group for peptide bond formation. IR spectroscopy, NMR and MS analysis of the product identified the successful synthesis of the 2-azidoacetic acid, which was coupled to the N-terminal serine of the amylin (20-29) peptide. In a one step synthesis the alkyne moiety in the form of propiolic acid was coupled to the N-terminal serine of the amylin (20-29) peptides. MS analysis clarified the presence and purity of the azide-form and alkyne-form of the peptide.

Preliminary *ex situ* AFM investigations revealed that both azide and alkyne forms of the amylin (20-29) peptide readily form fibrils in ultrapure water. The fibrils were flattened ribbon-like structures that had a tendency to aggregate laterally or into densely tangled clumps or as irregular twisted coils. Following Congo red staining of samples aged 18 hours, a green gold birefringence was observed under polarized light for both the azide-form and alkyne-form of the amylin (20-29) peptide. Indicative therefore, that the fibrils formed by the azide- and alkyne-amylin (20-29) peptides have retained the amyloidogenic structure necessary for Congo red binding [27, 217].

Furthermore, the introduction of the copper catalyst in the cycloaddition reaction solution at either concentration of 1 or 5 mM did not have any detrimental effects on the formation of fibrils (figures 3.11, 3.13, 3.14, 3.16 and 3.17). Under both

copper concentrations and in the absence of copper, the predominant fibril morphologies and assemblies mirrored those observed in the preliminary *ex situ* AFM study and can be similarly separated into two distinct morphological classes. The first, displayed a tendency to associate together laterally in single or denser layers. The second class showed a propensity to assemble into larger fibrillar structures either by entwined or irregular associations.

Similar fibril morphologies were observed in the samples irrespective of copper concentration or whether the copper catalyst had been present throughout fibrillisation, or introduced to samples of pre-formed fibrils at 18 hours. Furthermore, the range of morphologies observed within the samples containing only one form of the amylin (20-29) peptide (figures 3.11, 3.13 & 3.14), with the exception of the small population of fibril 'balls' observed in the azide-only amylin samples (figure 3.13), can clearly be seen in the samples comprising a mix of both forms of the peptide in the presence of the copper catalyst (figures 3.12, 3.15-17). Consequently, given that these observed morphologies and aggregation patterns are also commonly observed in non-functionalised amylin (20-29) fibrils (see Chapter 2), these findings suggest that the introduction of the copper (I) catalyst either during fibrillisation, or to pre-formed fibrils results in no change in morphology or aggregation patterns of the fibrils.

However, although no apparent changes in the morphology of the fibrils or aggregation patterns were observed directly, variations in fibril dimensions were noted. By comparison of the dimensions of non-functionalised amylin (20-29) fibrils (mean width of 27.31 (\pm 8.4) nm and height 1.66 (\pm 1.0) nm), with the functionalized amylin (20-29) fibrils formed in the absence of copper catalyst, we see that the latter display significantly smaller widths, but similar heights. Indicative therefore, that the azide and alkyne moieties are exerting some influence on the packaging of fibrils. The model for amylin fibril ultrastructure proposes formation occurs by the association of sub-fibrillar species into a structural hierarchy, in which the peptides aggregate as a beta-sheet into protofilaments. Several protofilaments then associate into protofilaments which group together laterally or by coiling into the fibril [43, 44, 49]. It is therefore conceivable that the additional bulk of the azide and alkyne moieties are

influencing the aggregation of these sub-fibrillar species by limiting the number of protofilament or protofilaments which associate into the observed species.

The frequency of fibrils (in all samples irrespective of the presence of copper) displaying a periodicity along the axis was considerably greater than expected based on a comparison with the fibrils formed by non-functionalised amylin (20-29) presented in Chapter 2, in which periodicity was only observed in younger fibrils and not the more mature species at 18 hours. Therefore, providing further support that the functional groups may be influencing the assembly and packing of the fibrils, either by promoting the coiling of fibrils into higher-order structures or that the additional bulk of the functional moieties results in the looser packing of sub-fibrillar structures into the fibrils and thus the periodicity of the packing is resolvable by the AFM tip.

Furthermore, frequency distributions (see histograms in figure 3.18) of fibril dimensions in samples containing both forms of the peptide in the presence of the copper catalyst show a broadening and shift in population distribution, which was dependent on the copper concentration. Two trends were noted, firstly when the copper catalyst was present during fibrillisation (ie present from 0 hours, figures 3.18a and c) at both the 1 and 5 mM concentration a shift and increase in fibril height was observed. Furthermore an additional population of fibrillar structures with greater half-height widths and heights were observed in the samples in which 1 mM copper was present. Secondly, when the fibrils were allowed to pre-form prior to the addition of the copper catalyst (ie copper added at 18 hours, figure 3.18b and d), when in the presence of both concentrations of the copper catalyst there was a more pronounced increase and broadening in the distribution of the fibrillar dimensions. However, the additional population noted in the 1mM sample was no longer observed.

When considering these findings, it is apparent that the presence of the copper catalyst both during fibrillisation and when added to the pre-formed fibril samples is inducing a change in the fibril dimensions within the samples. However, the increased fibrillar dimensions were not matched with the observation of any novel morphologies or aggregation patterns within the samples. It is therefore probable

that the observed increases in fibrillar dimensions are a consequence of the formation of a few triazole linkers between fibrils but at a low efficiency of formation.

Any future investigation into the success of this cross-linking reaction should be verified by exploration of the sample using IR spectroscopy or by NMR characterisation. Formation of the triazole cross-linker could be identifiable in an IR spectrum by a loss of the azide ($-N_3$) and carbon triple bond bands characteristic of the two reactants and the appearance of bands corresponding to the triazole ring vibration and C-N and N=N bonds of the triazole. The presence of a 1,2,3 triazole ring would induce a chemical shift to ~ 8.5 p.p.m (corresponding to the C-H of the ring structure) in an 1H -NMR spectrum [218].

A factor which may prove limiting to the success of the cycloaddition reaction to link the azide and alkyne moieties on individual fibrils would be the presentation of the functional groups in a sterically favourable manner for the reaction to proceed and triazole ring formation. Unfavourable steric presentation of the reacting moieties may provide a possible explanation for the apparent lack of any novel aggregation patterns or wide-spread network formation in the samples of functionalized amylin (20-29) fibrils. Several factors may influence whether the triazole ring forms: the azide and alkyne moieties must be present on the outside of the fibril, be in a sterically favourable orientation, and the azide and alkyne pairing must be in close enough spacial proximity for the reaction to proceed. Additionally, the 1,2,3 triazole ring is a planar 5-membered heterocycle which is constrained by the bonds and electron densities between its constituent atoms [219]. Thus the formation of triazole linkers between fibrils may be restricted conformationally and sterically by the allowable bond angles within the ring and in addition by the 1,4 bonds linking the peptide chain to the ring. Given that similar morphologies were observed even in the samples where an excess of copper catalyst was present (5 mM concentration), it seems unlikely that the availability of the catalyst played any limiting factor in the progression of the reaction. In the published literature the range of copper (I) catalyst concentrations used for the cycloaddition reaction have employed concentrations 2.5 to 10 times

less than this excess value and achieved successful catalysis [204, 211, 213, 214, 216].

Previous studies incorporating copper catalysed 1,3-dipolar cycloadditions of azides and alkynes have fallen short of our ambition to link large biomolecular structures; focusing on bioconjugation of proteins [211] and cells [210, 216] expressing the azide or alkyne on specific amino acids with dyes or ligands functionalized with the complementary group. In these instances only one triazole ring was formed per linkage of a small ligand to the larger supramolecule and thus no restraint was placed on the probability of other azide and alkynes being in close enough proximity for further ligations to occur, as might be expected in our experiment. Given the hydrophobic, aromatic and H-bonding interactions that govern fibril assembly [61, 62, 95, 176, 190], any change in fibril aggregation might be expected to require the formation of several triazole linkers to enforce any noticeable change in aggregation pattern or morphology.

Consequently, one may surmise that the 1,3-dipolar cycloaddition click chemistry may not be the effective choice for the synthesis of covalently linked fibrillar networks of amylin (20-29) without better understanding and the ability to control the presentation of the azide and alkyne functionalities on the fibrils. However, more success may be found in the decoration of the functionalized fibrils with function specific ligands, as previously demonstrated in the decoration of viral coat proteins [211] and bacterial and yeast cells [210, 216]. Or alternatively, for use in the immobilization of fibrils to an azide or alkyne functionalized support or scaffold [214]. In each example the frequency of complementary functional groups available on the surface would be greater and the probability of more favourable positioning for the formation of the 1,2,3 triazole ring increased.

3.5 Conclusion

Amylin (20-29) peptides were successfully synthesized with an alkyne or azide moiety coupled to the N-terminal amino acid residue. AFM images of samples of the azide and alkyne forms of the amylin (20-29) reveal that both readily self-assemble to form fibrillar structures, thus indicating that the introduction of an

alkyne and azide moiety does not interfere with the fibrillation of the peptide. Furthermore, the fibrils formed by the azide and alkyne amylin (20-29) peptide resembled the morphologies of non-functionalised amylin (20-29) peptides. Our aim to form 1,2,3 triazole ring cross-linkers between these functionalised fibrils by the 1,3 cycloaddition reaction of the azide and alkyne moieties proved to be of some success but with an apparent low efficiency of formation. Despite the lack of any observable novel fibril morphologies, networks or aggregation patterns, an increase and shift in population distribution of the fibril dimensions was noted, suggestive that some triazole linkers may have formed between fibrils producing larger fibrillar structures. The findings presented in this chapter provide a good foundation on which future studies can build for the possible application of the 1,3-dipolar cycloaddition of azide and alkyne for the functionalisation of amyloid-forming peptides and synthesis of organized nanostructures.

Chapter

4

AFM Study of Diphenylalanine Nanotubes

The studies in this chapter focus on the characterisation by AFM of the structures formed by the second of the two peptide systems, the diphenylalanine peptide.

4.1 Introduction

In the quest to fully understand the formation of amyloid and the development of potential therapeutics to combat the range of associated diseases, studies of short peptide fragments have been investigated to identify the minimal amyloidogenic fragment within the amyloid forming proteins [87, 174]. One such strand of research led to the discovery that the core recognition motif of the β -amyloid polypeptide, a simple dipeptide of phenylalanine [86], is the smallest known unit to self-assemble into discrete tubular structures. Furthermore, these nanotubes retain many of the characteristics of the biofibrils formed from the full-length β -amyloid polypeptide; birefringence under polarised light upon Congo red staining and β -sheet like conformation as determined by FT-IR [86].

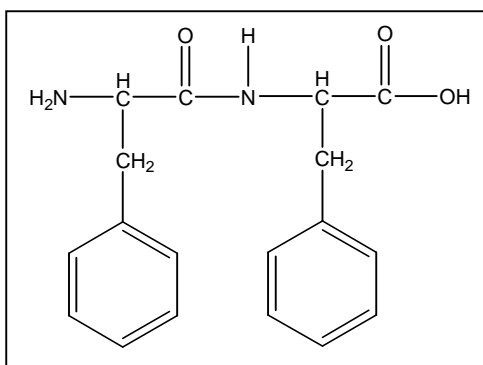


Figure 4.1: The structure of diphenylalanine. The structure of the dipeptide comprising the L-isomer of phenylalanine.

The diphenylalanine nanotubes are discrete, hollow water-filled structures with uniform morphologies [86, 220], ranging in dimensions from 100 to 1500 nm in diameter. The nanotubes are water soluble and have walls which display a degree of porosity [221]. The nanotubes require only mild conditions to efficiently assemble and thus are ideal materials for large scale, low cost manufacture. In addition, the nanotubes have many inherent physical properties which make them ideal building blocks for a range of bionanomaterials displaying high persistence lengths, a high degree of strength with an average point stiffness of 160 N/m and considerable rigidity by comparison to other bionanomaterials with Young's modulus of 19 GPa [220]. By comparison the Young's modulus of microtubules, hollow tube proteins which form part of the cytoskeleton of eukaryotic cells is approximately 1 GPa [222].

The diphenylalanine nanotubes have proven successful as novel materials in a wide range of applications from microelectronics to biosensors. For example, the diphenylalanine nanotubes have been used as enzymatically digestible scaffolds for the synthesis of silver nanowires for microelectronics [86], in the formation of peptide nanotube platinum-nanoparticle composites [221] and as part of electrochemical biosensor platforms [223, 224]. Furthermore, the potential ease with which the peptide nanotubes can be biologically and chemically modified will further broaden their application as novel specifically functionalised materials. The generation of peptides of diphenylalanine with an N-terminally attached Fmoc group have been shown to readily self-assemble into tubular structures displaying a higher degree of flexibility, and which form as a rigid hydrogel [225]. Hydrogels are of particular interest for use as tissue engineering scaffolds due to the capacity to support cell growth and the ease of decoration with growth promoting ligands [163, 226-228].

The exact structural organisation of the diphenylalanine molecules within the nanotubes still remains to be elucidated. A model for the formation of the diphenylalanine nanotubes is outlined in figure 4.2 [86, 229] and proposes that the nanotubes form in a similar manner to fullerenes and carbon nanotubes by the formation of a two-dimensional sheet stabilized by aromatic ring interactions. The energetic contribution and ordered assembly of the diphenylalanine molecules

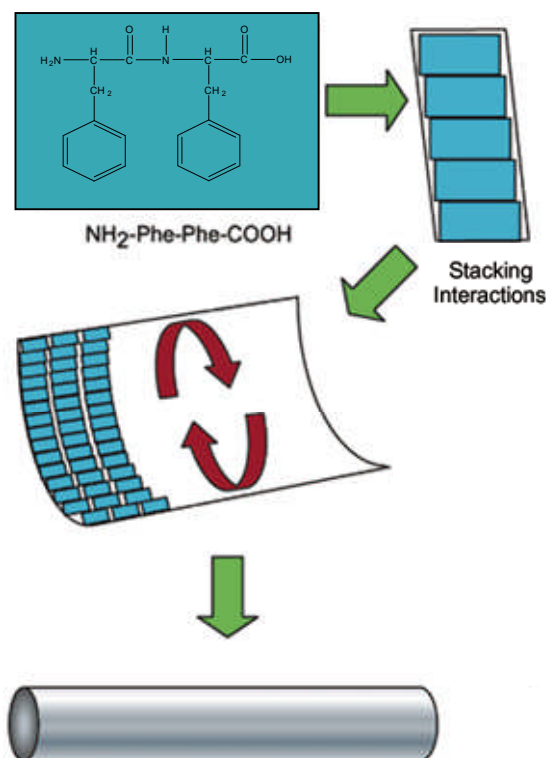


Figure 4.2: Model for the formation of the diphenylalanine nanotubes. (Source Reches and Gazit 2004 [229]) Ordered stacking of diphenylalanine into a two dimensional sheet is driven by π - π stacking interactions, closure of the sheet into the tubular structure is further stabilised by aromatic interactions and H-bonding.

into an extended β -sheet is driven by the π - π interaction of the aromatic ring side chains. The tubular structure is formed by the closure of the extended β -sheet and is further stabilised by aromatic interactions and H-bonding [229].

The importance of the aromatic ring in peptide nanotube formation may also confer many ideal properties to the nanotubes. Aromatic clusters on the surface and active sites of a range of thermophilic enzymes are key in conferring thermal stability to the protein and comparisons with the mesophile homologues reveal these aromatic clusters are preferentially mutated to non-aromatic residues [230].

The experiments within this chapter focus on the investigation of the physical and chemical properties of the diphenylalanine nanotubes. The extent to which the

diphenylalanine nanotubes can retain structural stability under harsh chemical and thermal conditions may prove important in the scope of possible applications for these novel materials; the ability to withstand extremes of heat, for example during sterilisation would be a prerequisite for any material in consideration for use as tissue engineering scaffolds or biosensors. To this end, the thermal stability of the diphenylalanine nanotubes under wet and dry heating conditions was studied by AFM. Further analysis of the resultant artefacts of heating was investigated by time-of-flight secondary-ion mass spectrometry (TOF-SIMS).

As our understanding of the physical and chemical properties of the nanotubes increases the focus turns to their potential uses and the means of how to manipulate these structures to broaden the scope of possible applications. The use of magnets has previously been demonstrated for the orientation and improved growth of protein crystals for X-ray diffraction studies in the elucidation of protein structures [231-234]. This method of orientation has also been used as a tool to align biofibrils (collagen, tubulin and amyloid) in preparation for X-ray fibre diffraction analysis [41, 235-241].

The behaviour of a substance within an externally applied magnetic field is determined by the magnetic nature of the material. Diamagnetism is an intrinsic form of magnetism; in diamagnetic materials, atoms have no permanent magnetic moments in the absence of an applied magnetic field. However, in an externally applied magnetic field a small magnetic moment is induced in the opposite direction to the applied field. The magnetization of a diamagnetic material is proportional to the applied magnetic field strength and the magnetic susceptibility of the material (a constant). The diamagnetic susceptibility of a material is closely related to its structure. The magnetic alignment of proteins occurs primarily due to the intrinsic diamagnetic nature of the peptide bond due to the ordered arrangement within the secondary structure conformations of the polypeptide chain (α -helix and β -sheet) [242, 243]. However, in highly aromatic structures where there are many conjugated rings, the net anisotropy of the structure is derived predominantly by the aromatic ring. The aromatic ring has 10 fold greater intrinsic diamagnetic anisotropy than the peptide bond due to the ordered and close π - π stacking interactions [244]. Consequently, given the high aromatic

content of the diphenylalanine nanotubes, the closing experiments within this chapter have investigated the use of magnetic fields for the alignment of the diphenylalanine nanotubes by AFM.

The work presented in this chapter was initiated in collaboration with Ehud Gazit's group from The University of Tel Aviv in Israel. The thermal stability experiments have been published in the journals *Langmuir* [245] and *Journal of the American Chemical Society* [246].

4.2 Experimental

4.2.1 Materials

Diphenylalanine peptide was purchased from Bachem, Switzerland. 1,1,1,3,3,3-hexafluoro-2-propanol was purchased from Sigma Aldrich, UK. For solution imaging isopropanol and acetone were purchased from Fischer. Amylin (20-29) with azide or alkyne group coupled to the N-terminus were synthesised as outlined in Chapter 3.

4.2.2 Method

4.2.2.1 Preparation of peptide samples

Stock solutions were prepared by diluting the lyophilised diphenylalanine peptides in 1,1,1,3,3,3-hexafluoro-2-propanol (HFIP) to a concentration of 100 mg/ml. The peptide stock solutions were diluted in ultrapure water (pH 6, resistivity 18.2 M Ω cm) to a final concentration of 2 mg/ml and vortex mixed for 20 seconds.

4.2.2.2 Atomic force microscopy

All AFM images were generated using a Multimode Nanoscope IIIa AFM (Digital Instruments, Veeco Metrology Group, Santa Barbara, USA). Imaging was performed using the J-type scanner using silicon TESP probes (supplied by Veeco

Metrology Group) mounted on cantilevers with nominal spring constants of 42 N/m and resonant frequency of 320 kHz. Scan rates employed were 0.5-0.8 Hz.

Data analysis was performed using the Nanoscope analysis software package v5.30r3.sr3 (Digital Instruments, Veeco Metrology Group, Santa Barbara, USA) and SPIP program (Image Metrology A/S, Denmark). Images show topography and phase data (where indicated), contrast scale bars are presented alongside images where appropriate. The upper z range value is stated above each scale bar with lighter colours indicating higher topographical features and greater phase contrast respectively.

4.2.2.3 Air AFM imaging

A sample of the diluted (2 mg/ml) diphenylalanine peptide stock solution was further diluted to 0.2 mg/ml in ultrapure water (pH 6, resistivity 18.2 MΩcm), to prevent molecular overcrowding of the scan area, immediately prior to imaging. A 10 µl aliquot sample was dropped onto freshly cleaved mica and dried under N₂ and imaged in air using the AFM.

4.2.2.4 Solution AFM imaging

Imaging of biomolecules in solution by AFM requires the stable immobilisation of the biomolecule to the substrate. For the imaging of the diphenylalanine nanotubes in solution two strategies were investigated; altering the substrate and changing the solution environment.

Mica, highly ordered pyrolytic graphite (HOPG), gold and silicon substrates were all investigated for imaging the nanotubes in water. All substrates were cleaned prior to use; mica and HOPG substrates were freshly cleaved, gold and silicon substrates were UV cleaned (for 10 minutes). Aliquot (10 µl) samples of freshly diluted (final concentration of 0.2 mg/ml) diphenylalanine nanotube solution were dropped onto each substrate and immediately imaged by AFM using the liquid cell.

Using freshly cleaved mica as the substrate, different aqueous solvents were investigated for nanotube solution imaging. The solvents investigated were 50 and 75 % v/v isopropanol or acetone in water. 100 mg/ml stock solutions of diphenylalanine in HFIP were diluted to give a final peptide concentration of 2 mg/ml in 50 or 75 % v/v isopropanol or acetone and vortex mixed. Aliquot samples were dropped onto freshly cleaved mica and imaged immediately using the liquid cell. Solvent volume was maintained during imaging using a closed liquid cell and syringe system.

4.2.2.5 AFM imaging of autoclaved samples

The autoclaved samples were prepared by our collaborators at the University of Tel Aviv. A sample of the diluted (to 2 mg/ml) of diphenylalanine peptide stock solution was autoclaved at 121 °C, 1.2 atmospheres. An aliquot sample of the autoclaved nanotube solution was deposited onto freshly cleaved mica and air dried at room temperature. Samples were imaged in air at room temperature by tapping mode AFM in Nottingham.

4.2.2.6 *In situ* heat imaging

The thermal stability of the nanotube samples was investigated by heating of the samples using the internal heater stage of the AFM J-scanner. The heat stage has a built-in thermostat which monitors the temperature of the system, allowing the sample to be heated bottom-up to a desired temperature, which is maintained by a feedback coolant system.

Aliquot samples of the diluted (2 mg/ml) diphenylalanine nanotube solution were dropped onto freshly cleaved mica and dried in an N₂ stream. Samples were mounted within the AFM and then heated successively to the desired temperatures; 25, 50, 100, 150 and 200 °C. At each temperature, the system was allowed to equilibrate for 5 minutes before imaging commenced, throughout which the temperature was maintained. Immediately after each image was captured, the temperature was increased to the next desired temperature. To allow for comparisons to be drawn, the same nanotubes were imaged and the imaging parameters were kept as constant as possible throughout the experiment.

4.2.2.7 *Ex situ* heat imaging

The same AFM experimental set up was used as for the *in situ* imaging, with exception that the samples were heated to the desired temperature and the system was equilibrated for 5 minutes. Following this, the system was allowed to cool to room temperature and equilibrated for a further 5 minutes prior to imaging. Immediately after imaging the sample was heated to the next desired temperature. The temperature increments were 25, 100, 125 and 150 °C. Several different nanotube samples were studied, and in each sample the same nanotubes were imaged with the imaging parameters kept as constant as possible.

4.2.2.8 Optical microscopy imaging of AFM cantilever following high-temperature AFM imaging

Optical images of the AFM cantilevers used in the high-temperature *in situ* imaging of the diphenylalanine nanotubes were generated using the Leica TCS confocal microscope (Leica Microsystems (UK) Ltd) at x 2.5 and x 10 magnification.

4.2.2.9 Time-of-flight secondary-ion mass spectrometry analysis

The composition of the crystalline deposits observed on the AFM cantilevers following high-temperature imaging of the peptide nanotubes was investigated using time-of-flight secondary-ion mass spectrometry analysis (TOF SIMS) [247]. TOF SIMS spectra were obtained using a Ion-TOF SIMS IV instrument (GmbH, Germany). The primary ion was a gallium beam with kinetic energy of 15 kV (20 μ A), which delivers Ga^+ cluster ions over a raster scan area of 300 x 300 cm^2 . High-resolution mass spectra were generated of the AFM cantilever.

4.2.2.10 Magnetic anisotropy

4.2.2.10.1 Diphenylalanine nanotubes

An aliquot (10 μ l) sample of the diluted stock solution (2 mg/ml) of diphenylalanine nanotubes was dropped onto freshly cleaved mica and allowed to evaporate completely for 1 to 2 hours inside a closed container at room

temperature. The experiment was performed in four magnetic fields; 0.5, 3, 7 and 12 Tesla. A control experiment was also performed at 0 Tesla. In the 0.5 Tesla experiment, the sample was placed horizontally in the gap of a C-shaped bench magnet. For the 3 and 7 Tesla experiments, the samples were placed in the homogenous field of a horizontal bore solenoid magnet of the magnetic resonance imaging suite. In the 12 Tesla experiment, the aliquot sample was 'hung' vertically on the mica surface within the 5 cm-diameter vertical bore of a solenoid magnet. In each case the mica surface was positioned parallel to the direction of the magnetic field.

4.2.2.10.2 Amylin (20-29) fibrils

For comparative purposes to determine the effects of a high magnetic field on fibrils formed by a peptide with low aromatic content, samples of functionalised amylin (20-29) were investigated as a control. The sample comprised a 50:50 mix of the modified amylin (20-29) with either an azide or alkyne group attached to the N-terminus. A 50:50 mix of both forms of the lyophilised peptide were dissolved in ultrapure water (pH 6, resistivity 18.2 MΩcm) to a final peptide concentration of 150 µg/ml and left to form fibrils in a sealed eppendorf tube overnight at room temperature. A section of freshly cleaved mica was immersed in the peptide solution and placed within the 5-cm vertical bore of the 12 Tesla solenoid magnet. The solution was left to evaporate overnight at room temperature.

4.2.2.10.3 AFM imaging and data analysis

Following exposure to the magnetic fields, the dried sample residues were imaged using the AFM. Analysis of the AFM images was performed using the SPIP program. Nanotube orientations relative to the direction of the magnetic field were measured using the angle function within the SPIP program. Thus enabling the nanotube anisotropy relative to the applied magnetic field to be determined by calculating the average projected length of the nanotubes on the direction of the magnetic field. This was then graphed as a polar plot using the statistical program Origin (OriginLab Corp. USA).

4.3 Results

4.3.1 AFM imaging of diphenylalanine nanotubes

Samples of the nanotubes formed by diphenylalanine peptide were imaged by AFM using both tapping mode air and liquid imaging.

The AFM images presented in figure 4.3 are typical of the dried diphenylalanine nanotube samples imaged in air. Figure 4.3a is a low resolution topography image of a selection of nanotubes. The nanotubes are discrete, long and unbranched structures displaying a range of diameters in agreement with the published values measured from electron microscopy images [86, 220]. The nanotubes in the image all display the typical uniformity in diameter along their axis and have half-height widths of 256.2, 296.1 and 353.4 nm and respective heights of 105.74, 166.21, and 133.65 nm.

Figure 4.3b is a topography image of a nanotube; the higher-resolution image highlights the uniform and smooth surface topography of the tubular structures, which do not have any discernable surface feature. A 3D representation of the nanotube is presented in figure 4.3c demonstrating the tubular nature of the structure. A profile of the nanotube cross-section (location is highlighted by the line in figure 4.3b) is presented in figure 4.3d. The nanotube has a half-height width of 247.02 (± 4.14) nm and respective height of 117.35 (± 2.71) nm.

Solution imaging by AFM allows biomolecules to be studied in their hydrated state generating a better understanding of the native structure in a liquid environment. However, obtaining a stable image of the nanotubes will require sufficient immobilisation of the structures to the substrate during imaging. To this end, several substrates including mica, gold, silicon wafer and HOPG were investigated. However, none of the substrates assayed resulted in sufficient immobilisation of the nanotubes in ultrapure water for stable imaging. Investigations using organic solvents revealed that v/v aqueous concentrations of isopropanol also proved ineffective but 50% and higher concentrations of acetone

were sufficient and proved effective for the stable imaging of the nanotubes using a mica substrate.

The AFM images presented in figure 4.4 are of a typical diphenylalanine nanotube imaged in solutions of 50% v/v acetone. The low-resolution topography image presented in figure 4.4a has been zoomed in to give the higher-resolution image shown in figure 4.4b. The nanotube has a uniform surface topography with no branching or surface features. Pockets of material can be observed on the substrate surface and at the edges of the nanotubes. A further high-resolution zoom in of a section of the nanotube where the surrounding material can be observed is shown in figure 4.4c no further topographical information can be discerned. A 3D representation of this image surface is presented in figure 4.4d and a profile of the cross-section highlighted by the line is presented in figure 4.4e. The nanotube has a half-height width of 282.4 (± 6.3) nm and height of 111.2 (± 3.6) nm along its axis. Collectively, the images and profile illustrate the uniform nature of the nanotube surface topography and demonstrate that the nanostructure has a slightly flattened tubular morphology. These observations are in agreement with our findings from the air images of the dried nanotube samples.

4.3.2 AFM imaging of autoclaved diphenylalanine nanotubes.

Samples of diphenylalanine nanotubes were autoclaved and imaged in air by AFM to assess the thermal stability of the nanotubes following wet heat treatment. The images presented in figure 4.5 are typical of the autoclaved nanotube samples.

Figure 4.5a is a low-resolution topography image of a group of nanotubes displaying a range of widths between 235 to 432 nm and heights of 46 to 231 nm. The higher-resolution topography image presented in figure 4.5b, together with the profile presented in figure 4.5c of the nanotube cross-section (highlighted by line in figure 4.5b) demonstrate the uniform and smooth surface topography of the nanotube. Collectively, these images show that the nanotubes do not lose any observable structural integrity following autoclave treatment.

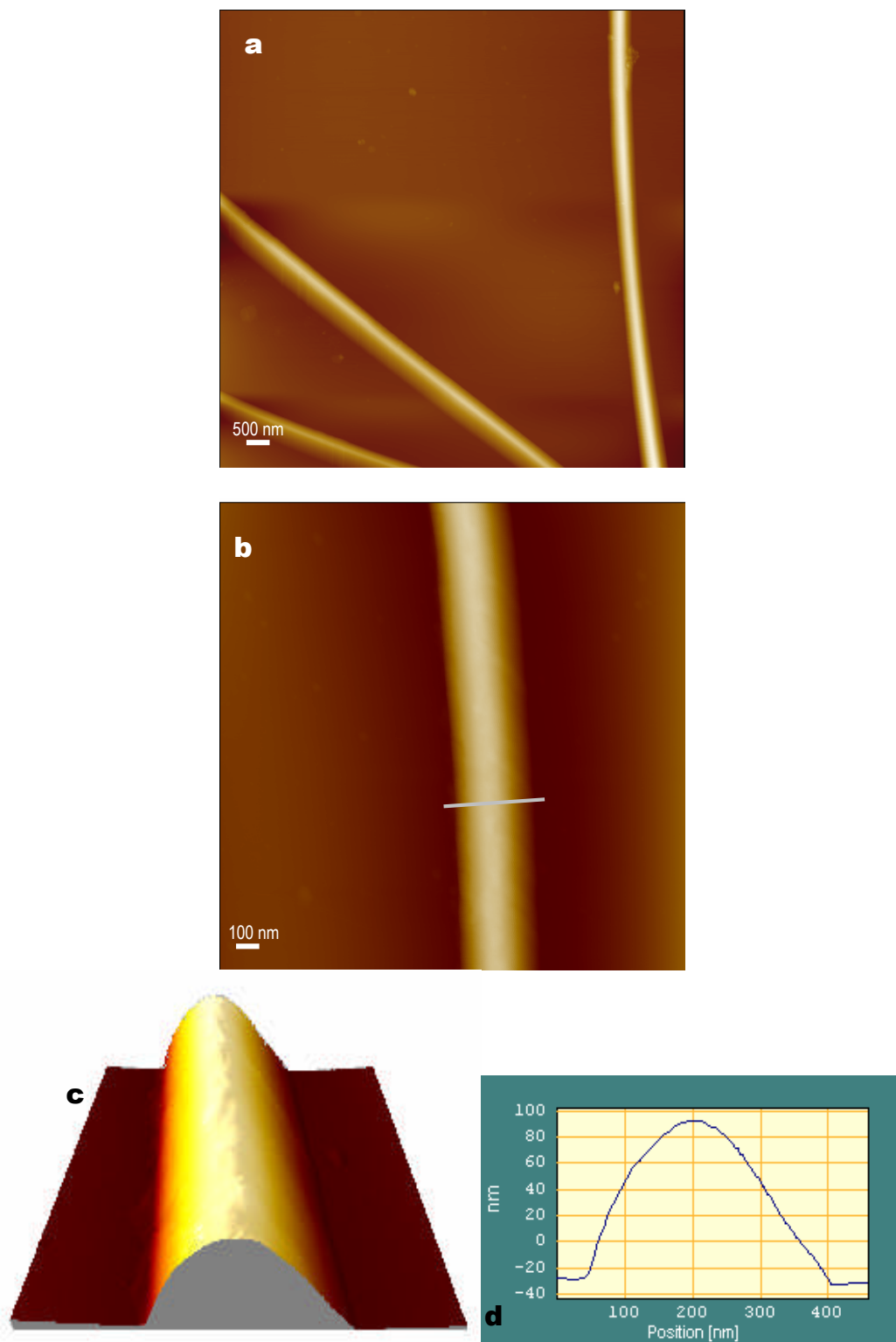


Figure 4.3: *Ex situ* AFM images of diphenylalanine nanotubes. **Figure 3a** is a topography image of diphenylalanine nanotubes dried onto freshly cleaved mica and imaged by tapping mode AFM in air. **Figure 3b** is a higher-resolution topography image; the line denotes the position of the cross-sectional profile presented in **figure 3d**. A 3D representation of the nanotube is presented in **figure 3c**.

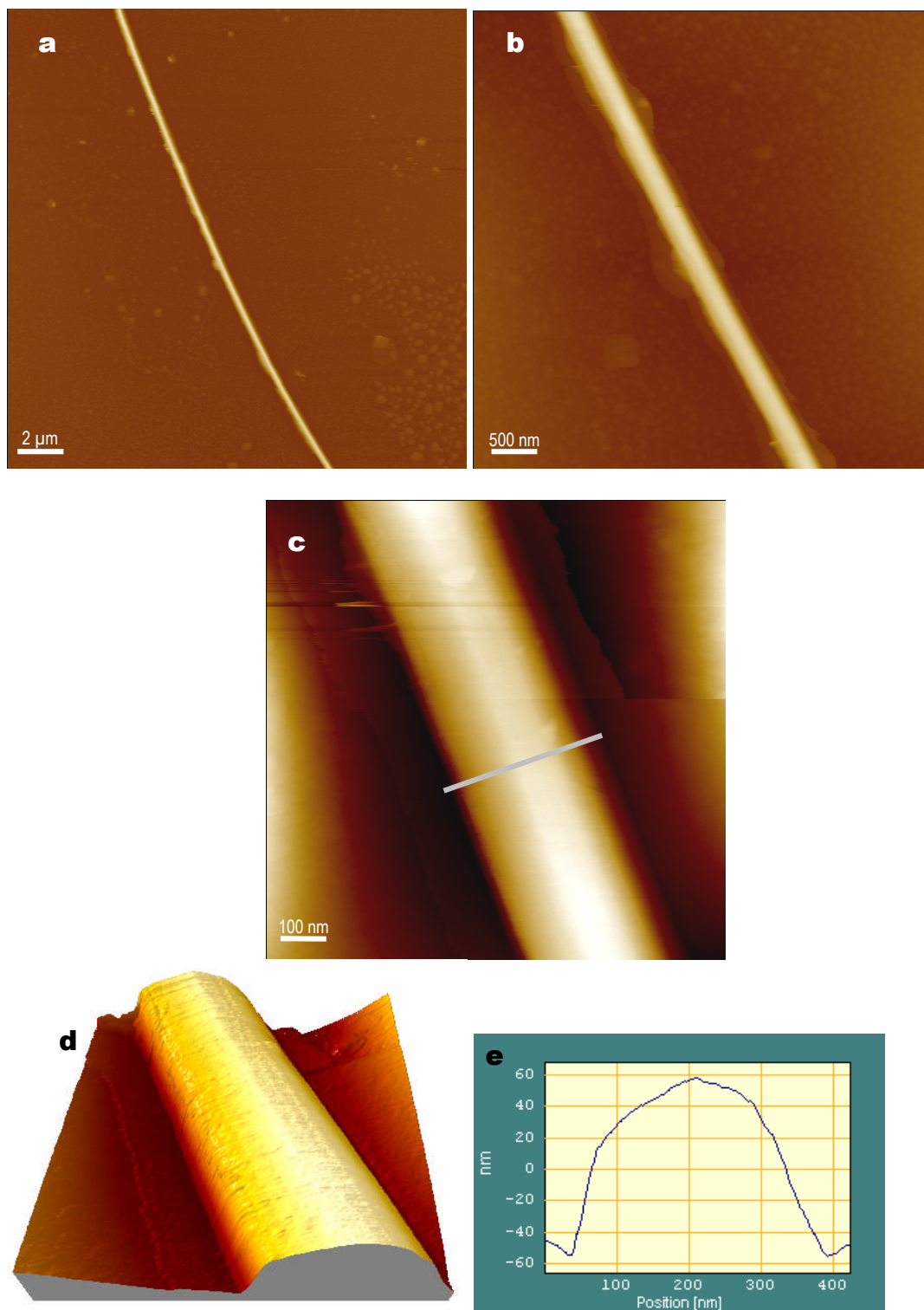


Figure 4.4: AFM *in situ* images of diphenylalanine nanotubes in 50% v/v acetone. **Figure 4a** is a topography image of the nanotubes imaged *in situ* 50% v/v acetone on mica. **Figure 4b and 4c** are higher-resolution topography images, a 3D representation of the nanotube surface topography is shown in **figure 4d**. **Figure 4e** is a profile of the nanotube cross-section highlighted by the line in figure 4c.

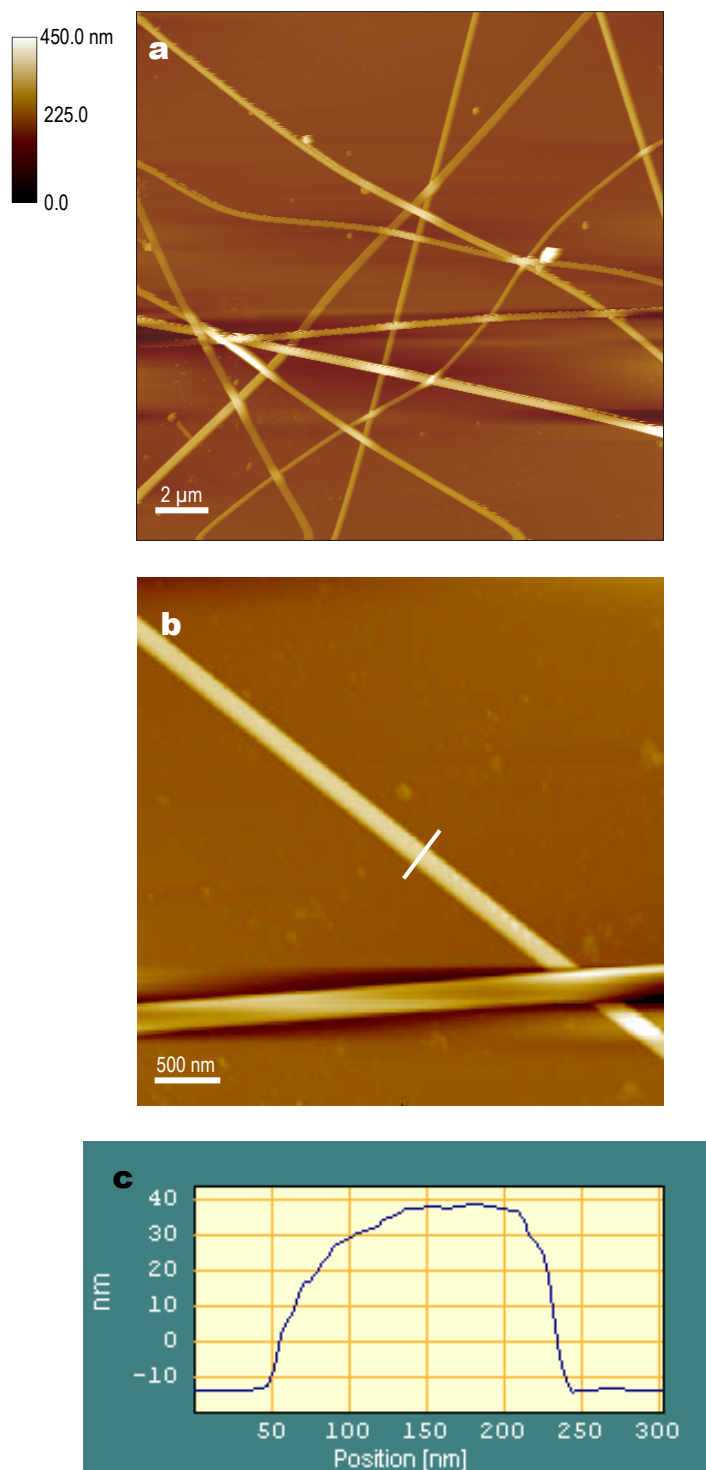


Figure 4.5: AFM images of diphenylalanine nanotubes after autoclave treatment. Autoclave conditions were 121 °C at 1.2 atmospheres. **Figure 5a** is a topography image of diphenylalanine nanotubes after autoclave treatment. Z range contrast bar is shown. **Figure 5b** is a higher-resolution topography image of diphenylalanine nanotubes after autoclave treatment; the line indicates the positioning of the cross-sectional profile, which is shown in figure 5c.

4.3.3 AFM *in situ* heat imaging

Samples of diphenylalanine nanotubes were dried onto freshly cleaved mica and heated from the bottom-up using the heating stage of the AFM J-scanner to assess the thermal stability of the nanotubes during dry heating. Samples were imaged at room temperature and then heated to the desired temperature, following an equilibrium period an AFM image was captured before the sample was heated to the next temperature. The images presented in figure 4.6 are the series of typical high-resolution AFM topography images captured (left), with cross-sectional profiles (middle) and 3-D representations of the surface (right) of an exemplar nanotube at each of the temperature increments of 24, 50, 100 and 150°C.

Figure 4.6a shows the nanotube at room temperature (24°C) it has a typically smooth surface topography and uniform half-height width along its axis of 469 nm and height of 62.3 nm. When the nanotube was heated to 50°C no observable change in the nanotube morphology (figure 4.6b) or dimensions was noted. The topography image and 3D representation of the surface shown in figure 4.6c are of the nanotube at 100°C. Loss of structural integrity can clearly be seen, with an apparent breakdown in the nanotube wall and deformation of the tubular structure with a prominent trough visible in the cross-sectional profile. Loss of outer wall integrity also results in considerable variation in morphology along the nanotube axis. The nanotube has a half-height width of 487 nm and height of 59 nm. Figure 4.6d is a topography image, profile and 3D representation of the nanotube at 150°C. The increased temperature results in loss of spatial volume, due to an apparent collapse of the nanotube; with a narrower half-height width of 167 nm and height of 12.3 nm. Occasionally along the nanotube axis pockets of higher topography and width can be observed, however there is still a considerable reduction in dimension sizes by comparison with the nanotube at lower temperatures. Furthermore, in the 150°C (figure 4.6d) image granular material can be observed on the mica surface which is not seen at lower temperatures. Attempts to image the nanotubes at temperatures above 150°C were unsuccessful.

4.3.4 AFM *ex situ* heat imaging

Ex situ heat imaging of the nanotube samples was performed to investigate whether the mechanical forces imposed by the AFM tip during high temperature

imaging were responsible for the observed loss in nanotube structural integrity. For the *ex situ* heat imaging experiment, the nanotube samples were heated and then cooled before imaging at room temperature. The images presented in figure 4.7 are a series of typical high-resolution AFM topography images (left), with cross-sectional profiles (middle) and 3-D representations of the surface (right) of the same pair of nanotubes imaged at room temperature after heating to 24, 100, 125 and 150°C. The cross-sectional profiling positions are indicated by the line in each topography image.

The images presented in figure 4.7a are of the nanotubes at 24°C. The nanotubes are typical tubular structures with smooth surface topography and uniform half-height width of 164 nm and height 96 nm. Figure 4.7b shows the nanotubes after heat treatment to 100°C. The morphology of the nanotubes remains similar with a slight loss in dimensions; half-height width 159 nm and height 81 nm. The jagged appearance of the 3D representation and in the topography image along an edge of the nanotube is most likely attributable to noise artefact during imaging rather than a feature of the nanotubes. The images presented in figure 4.7c show the nanotubes after heat treatment to 125°C. There is a slight change in surface topography with a loss of the smooth outer wall appearance and depressions along the surfaces of the nanotubes. However, a marginal increase in nanotube width to 168 nm and height to 88.2 nm is observed. A further increase in temperature to 150°C results in a considerable loss in the structural integrity of the nanotubes. The images presented in figure 4.7d of the nanotubes after heat treatment to 150°C show this dramatic change in structure and topography. Pockets of narrow and wide segments can be observed along the entire axis of the nanotubes. The cross-sectional profiles highlight the difference in dimensions between the wider (top) and narrower (bottom) sections. The wider sections have greater widths (256 nm) than those measured at lower temperatures but have considerably lower heights around 24 nm, suggesting that in these regions the nanotubes have collapsed and flattened. Whereas in the narrower segments, there is almost complete loss of structure with the cross-sectional width measuring 203 nm and height of 8 nm. In similarity to the *in situ* heat imaging background debris can be observed deposited on the mica surface only in the 150 °C images. Furthermore, attempts to image the nanotubes after heating to 200 °C were also unsuccessful.

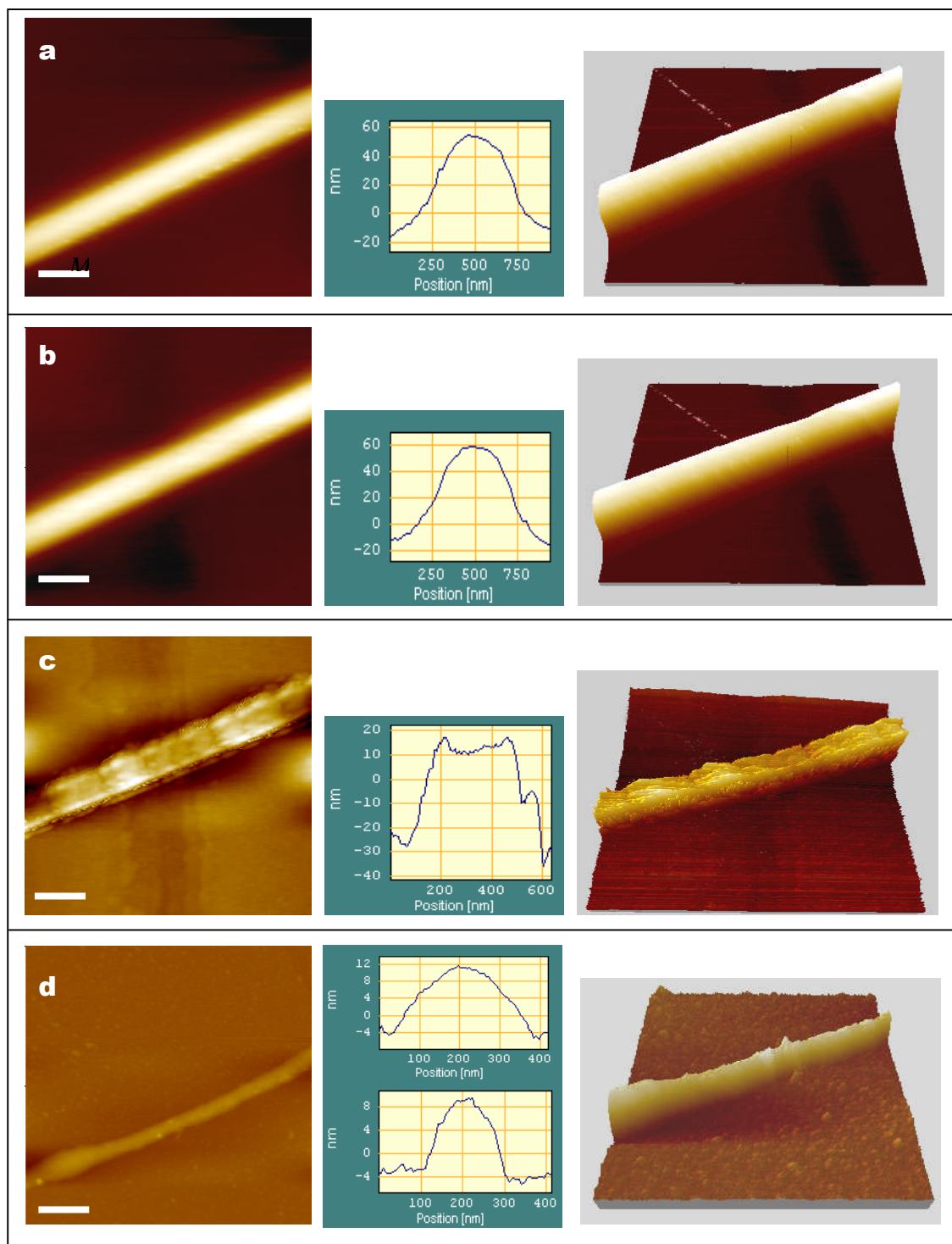


Figure 4.6: *In situ* heating of diphenylalanine nanotubes. AFM topography images (left) of the same nanotube sample heated to a) 24 °C, b) 50 °C, c) 100 °C and d) 150 °C. Nanotube samples were heated successively to each temperature. Cross-sectional line profiles (middle) and 3D representation of the surface (right) are shown. Samples were heated to each temperature and allowed to equilibrate for 5 minutes and then the temperature was maintained throughout imaging. Immediately after each image was captured, the temperature was increased. Scale bars represent 500 nm.

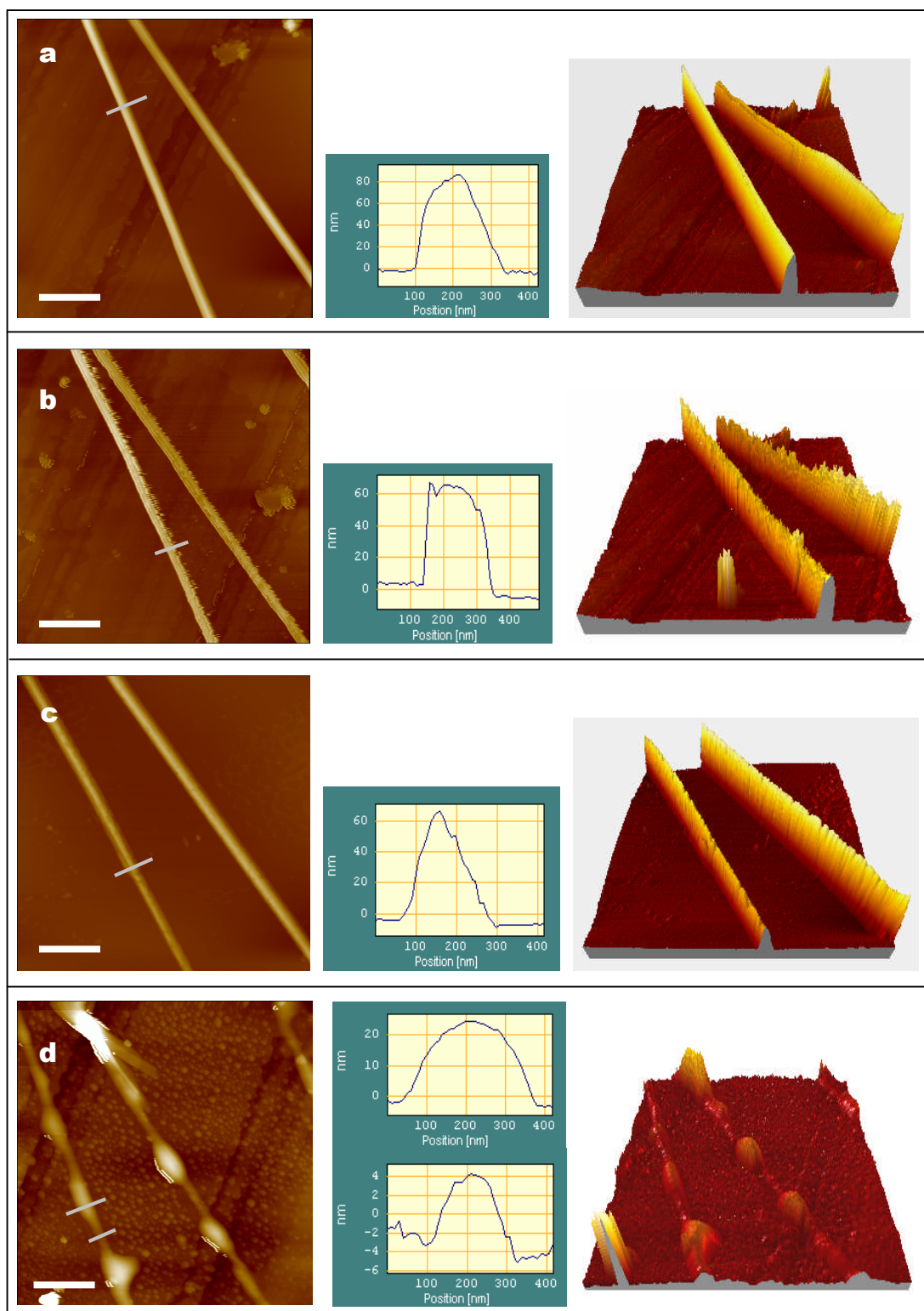


Figure 4.7: *Ex situ* heating of diphenylalanine nanotubes. AFM topography images of the same nanotube sample after heating to a) 24 °C, b) 100 °C, c) 125 °C and d) 150 °C. Samples were heated to the desired temperature, allowed to equilibrate for 5 minutes, then cooled to room temperature and equilibrated for a further 5 minutes before imaging. Following imaging the samples were immediately heated to the next temperature. Cross-sectional line profiles (middle) and 3D representation of the surface (right) are shown. Scale bars represent 1 μm .

For comparative purposes the average dimensions of the nanotube cross-sections at each temperature for both the *in situ* and *ex situ* heat imaging experiments are presented in graphical form in figure 4.8. Figure 4.8c shows the change in half-height width and figure 4.8d the change in peak height with temperature for the *in situ* imaging. The width of the nanotube remains reasonably constant up to 100°C, after which there is a 66% loss in width. Similarly, the height measurements follow the same trend, with a dramatic loss in height of 82 % occurring when the temperature was raised to 150°C. The changing nanotube half-height width for the *ex situ* imaging are presented in figure 4.8a and peak height in figure 4.8b. The width of the nanotube remains moderately constant up to temperatures of 125°C however, a further increase in temperature results in an increase in width. The large error bars in these points are due to the variation in morphology of the nanotubes with pockets of narrow and wide segments along the nanotube axis. The height of the nanotube decreases marginally up to 125°C; however at 150°C there is a dramatic loss of 81% in height.

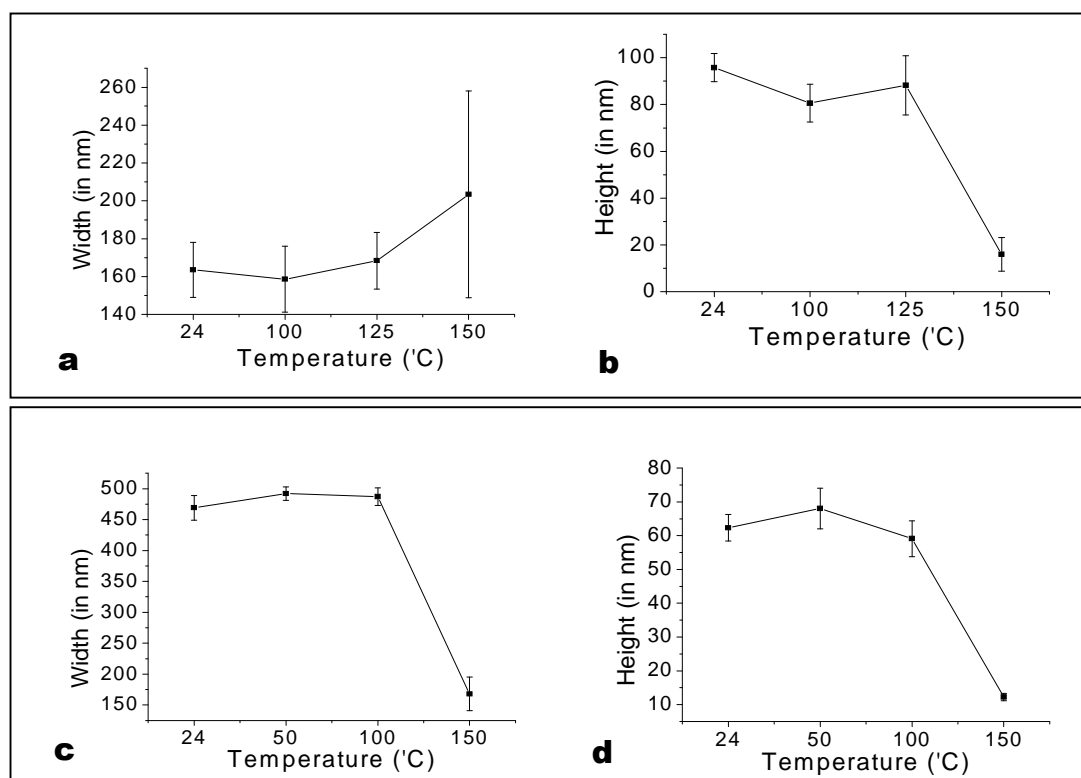


Figure 4.8: Graphical comparison of the change in widths and heights of the diphenylalanine nanotubes with increasing temperature. *Ex situ* heating: the change in nanotube **8a)** half-height width and **8b)** height with temperature. *In situ* heating: the change in nanotube **8c)** half-height width and **8d)** height with temperature.

4.3.5 Optical microscopy images of AFM cantilever following high-temperature AFM imaging

Further investigation using optical microscopy of the AFM cantilevers used for the *ex situ* and *in situ* temperature imaging revealed the presence of crystalline deposits on the cantilevers and chips. The optical microscopy images of the AFM cantilevers and chip used for the high-temperature *in situ* imaging are presented in Figure 4.9. The image shown in figure 4.9a is of a cantilever at a magnification of 2.5 and a higher-resolution image at x 10 magnification is shown in figure 4.9b. Extensive deposition of crystalline material along the edges of both the chip and cantilever is observed with coverage particularly concentrated as larger crystals around the tip region of the cantilever. The presence of this crystalline material particularly around the tip region is most likely the cause of the unstable imaging experienced in both the *in situ* and *ex situ* imaging experiments at 200 °C. The presence of the deposited material would not only interfere with the reflection of the laser but may also act as faux tips. Crystalline material was also observed on the cantilevers used for *ex situ* imaging but to a lesser extent, which may be attributable to the cantilever being a greater distance away from the sample surface during heating.

4.3.6 TOF-SIMS analysis

TOF SIMS analysis was performed to determine the composition and origins of the crystalline deposits which formed on the AFM cantilevers during high temperature imaging.

Presented in figure 4.10 is the positive spectrum for the TOF SIMS analysis of the silicon cantilevers. The spectrum reveals that despite extensive cleaning by a process of plasma etching (20 Pa O₂ at 100 W for 60 seconds) and UV cleaning (10 minutes) prior to imaging, a residual contamination of poly(dimethylsiloxane) (PDMS) was found to be present on the cantilevers. The presence of PDMS is most likely attributed to the packaging conditions used for the storage of new AFM cantilevers. However, by subtracting the peaks corresponding to the PDMS contaminant (the spectrum reference for PDMS rubber from The Static SIMS Library (SurfaceSpectra Ltd) can be found in appendix B) three peaks of interest are observed at *m/u* 77, 91 and 120 (highlighted by arrows in figure 4.10). The

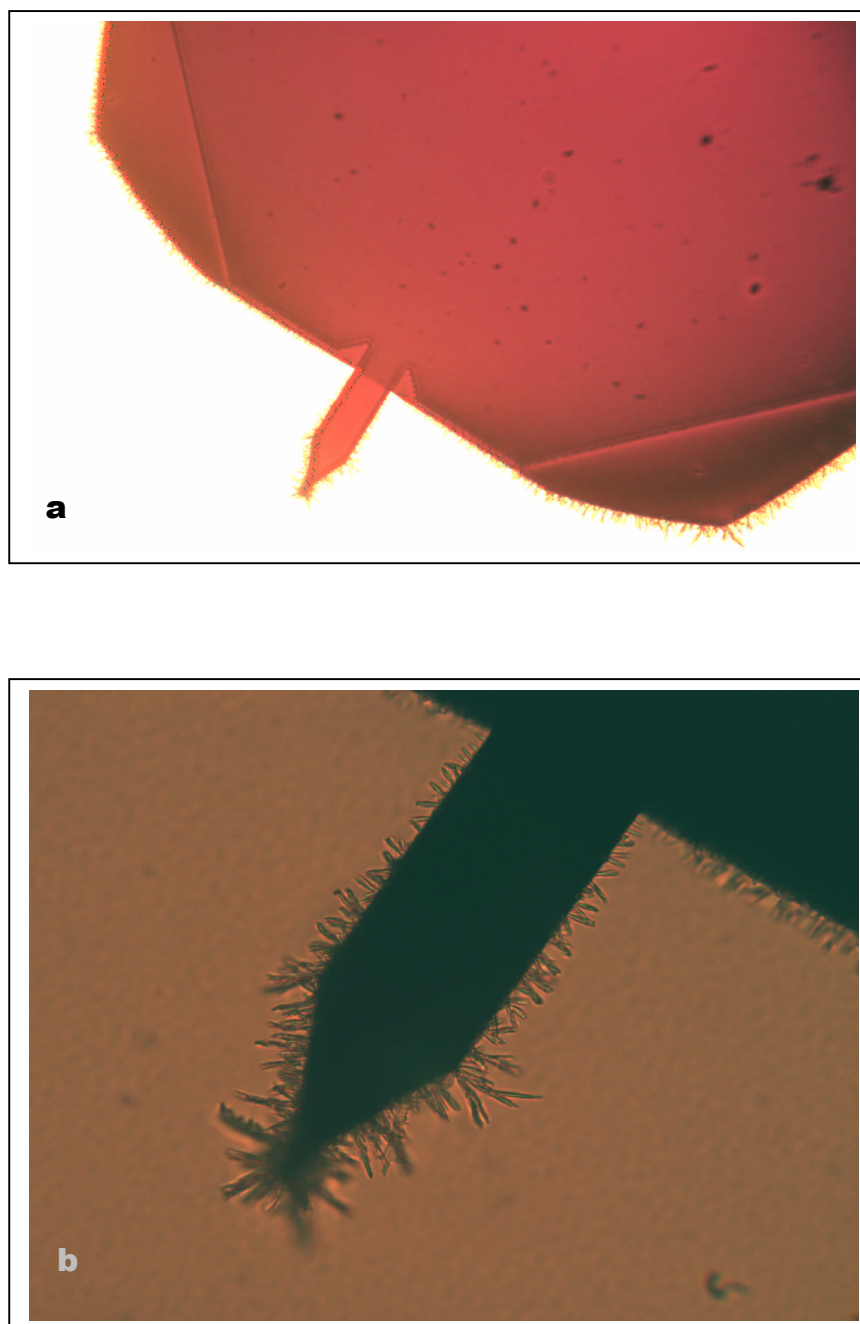


Figure 4.9: AFM cantilever tips with crystalline deposits formed during high temperature (200 °C) imaging of diphenylalanine nanotubes. Optical microscopy images of the AFM cantilevers at **a)** x 2.5, and **b)** x 10 magnifications.

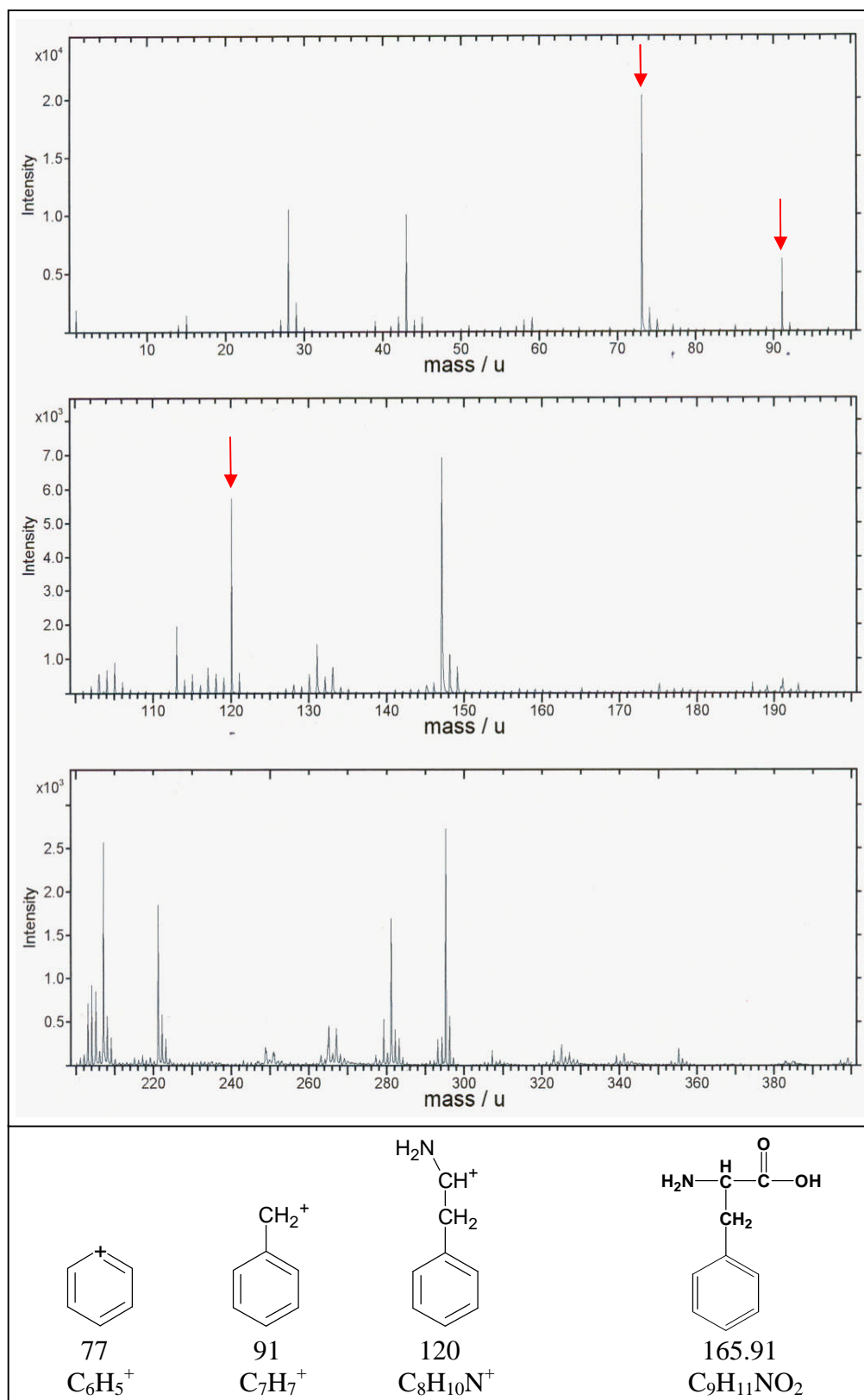


Figure 4.10: TOF SIMS spectrum of AFM cantilevers with crystalline deposits following heat treatment of the diphenylalanine nanotubes. The positive TOF SIMS spectrum, with peaks of interest highlighted by the arrows at m/u of 77, 91 and 120. The suggested chemical structures of the molecules for these peaks and the structure of phenylalanine (far right) are presented below.

proposed chemical structures for these molecular weights are shown below the spectrum in figure 4.10 and correspond to hydrocarbon compounds of C_6H_6 (m/u 77), C_7H_7 (m/u 91) and C_8H_{10} (m/u 120). All three structures are fragments comprising an aromatic ring, suggesting that the compounds can be attributed to the varying degrees of fragmentation of phenylalanine, specifically containing the aromatic side chain. The spectrum analysis therefore demonstrates that the crystalline deposits observed on the AFM cantilever comprise aromatic fragments of phenylalanine.

4.3.7 Magnetic Anisotropy

In the following experiments the influence of varying magnetic field strengths on the orientation and alignment of the diphenylalanine nanotubes has been investigated. Solutions of diphenylalanine nanotubes were evaporated under different magnetic field strengths and the residues were imaged by AFM.

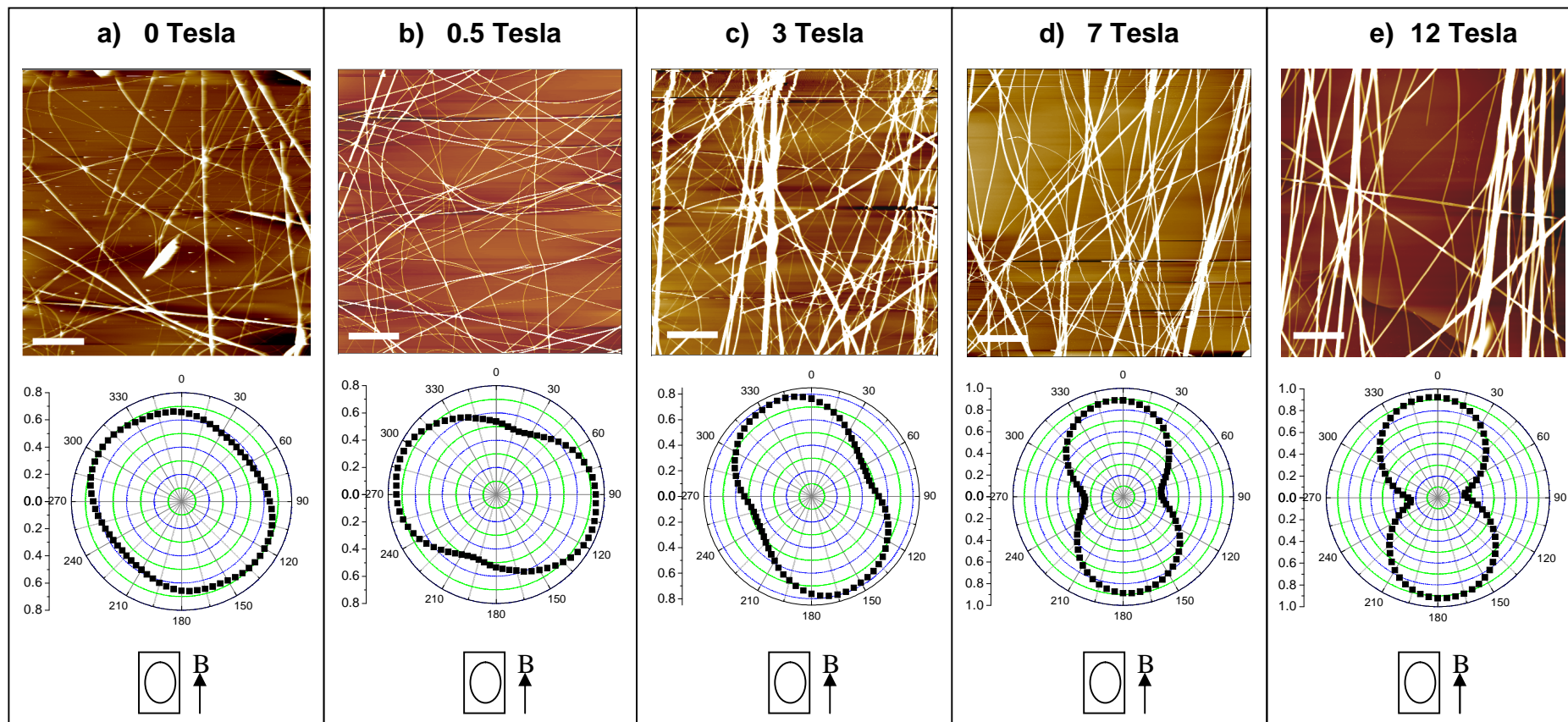
Presented in figure 4.11 are the AFM topography images and respective polar plots of nanotube samples that have been evaporated in different magnetic fields of 0, 0.5, 3, 7 and 12 Tesla. The polar plots show the distribution of nanotube orientation relative to the magnetic field direction for each image and therefore give an indication of nanotube anisotropy with the magnetic field. In the simplest interpretation of the polar plot, the ellipticity of the plot is an indication of the materials anisotropy: a circular plot would denote no alignment of the nanotubes, whereas a figure of eight shape indicates perfect alignment; intermediate of these extremes would give a plot with an hour glass shape with the smaller the neck indicating more alignment.

The morphology and range of half-height widths (0.5 to 2.0 μm) displayed by the nanotubes in all the samples exposed to the magnetic fields are in agreement with that observed in the control samples not exposed to an applied magnetic field (figure 4.11a). Furthermore, the dimensions and morphology displayed are concurrent with published data from early EM studies of diphenylalanine nanotubes [86, 220].

The topography image and polar plot shown in figure 4.11a are of the control sample at 0 Tesla magnetic field. Both the circular polar plot and the lack of visible orientation of the nanotubes in the topography image indicate there is no alignment in the sample. Similarly in the 0.5 Tesla sample (figure 4.11b), there is no evidence in the topography image that there is alignment of the nanotubes by the magnetic field. However, the shape of the polar plot suggests there is slight alignment of the nanotubes within the sample but very weakly associated with the direction of the magnetic field. In the topography image presented in figure 4.11c of the 3 Tesla sample some of the nanotubes appear orientated with the direction of the magnetic field. The polar plot for the sample provides further support for this indicating a slight preference for alignment in a direction close to that of the magnetic field. The topography images presented in figures 4.11d and e of the 7 and 12 Tesla samples, respectively, clearly display alignment of the nanotubes with their long axis parallel to the direction of the magnetic field. The polar plots provide further support for this, with the 12 Tesla sample displaying a stronger anisotropy with the direction of the field strength.

An observation worth noting is the small, yet significant, number of nanotubes that remain misaligned in the highest field strengths (12 Tesla, see figure 4.11e). Although the majority are aligned, it may be supposed that the nanotubes which are not, have been restrained either due to substrate interactions or have been pinned in place by neighbouring under and over lying nanotubes and are thus unable to orientate in the field.

A quantitative comparison of the alignment of the nanotubes with increasing magnetic field strength may be drawn by plotting the ratio of the maximum to minimum average projection values of the nanotubes in each image versus the relative magnetic field strength. The plotted graph is presented in figure 4.12 and a linear relationship between the ratio of projected value to magnetic field strength can be seen. Concluding therefore that as the magnetic field strength increases, the degree of diphenylalanine nanotube anisotropy to the magnetic field increases.



Increasing magnetic field strength

Figure 4.11: AFM images of diphenylalanine nanotubes with the relative anisotropy polar plots under differing field strengths. Topography images of the diphenylalanine nanotubes after exposure to magnetic field strengths of **a) 0 Tesla**, **b) 0.5 Tesla**, **c) 3 Tesla**, **d) 7 Tesla** and **e) 12 Tesla**, the direction of the applied magnetic field (B) relative to the sample is also shown. Scale bar represents $25\ \mu\text{m}$. Beneath each AFM image are the polar plots calculated to determine the anisotropy of the nanotubes relative to the magnetic field.

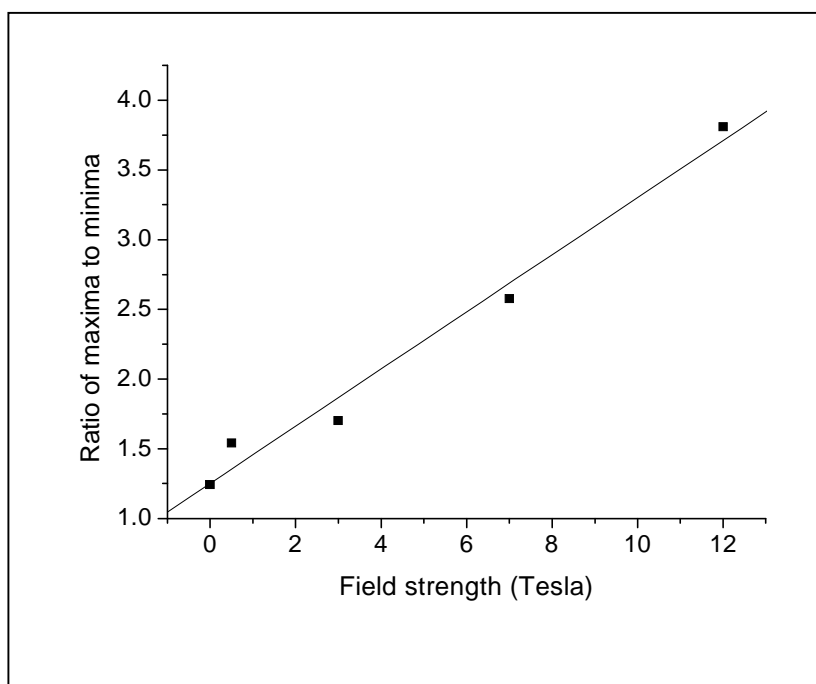


Figure 4.12: Ratio of maximum to minimum alignment versus applied magnetic field. The line graph is the change in the ratio of the maximum alignment value to the minimum value versus the increase in magnetic field strength. The maximum and minimum alignment values are obtained from the maximum and minimum average projection values for the sample.

To establish whether the observed alignment of the diphenylalanine nanotubes is an inherent characteristic of peptide-based fibrillar structures, a control experiment was performed using samples of amylin (20-29) fibrils. Samples of azide and alkyne functionalised amylin (20-29) peptides were allowed to pre-form before placing in a 12 Tesla magnetic field to evaporate overnight. The AFM topography image and relative polar plot of the sample are presented in figure 4.13. The morphology and dimensions of the amylin fibrils concur with those previously observed in Chapter 3. The samples of amylin (20-29) biofibrils do not display any preferred orientation in the AFM topography image and together with the circular appearance of the corresponding polar plot indicate no alignment under the 12 Tesla magnetic field.

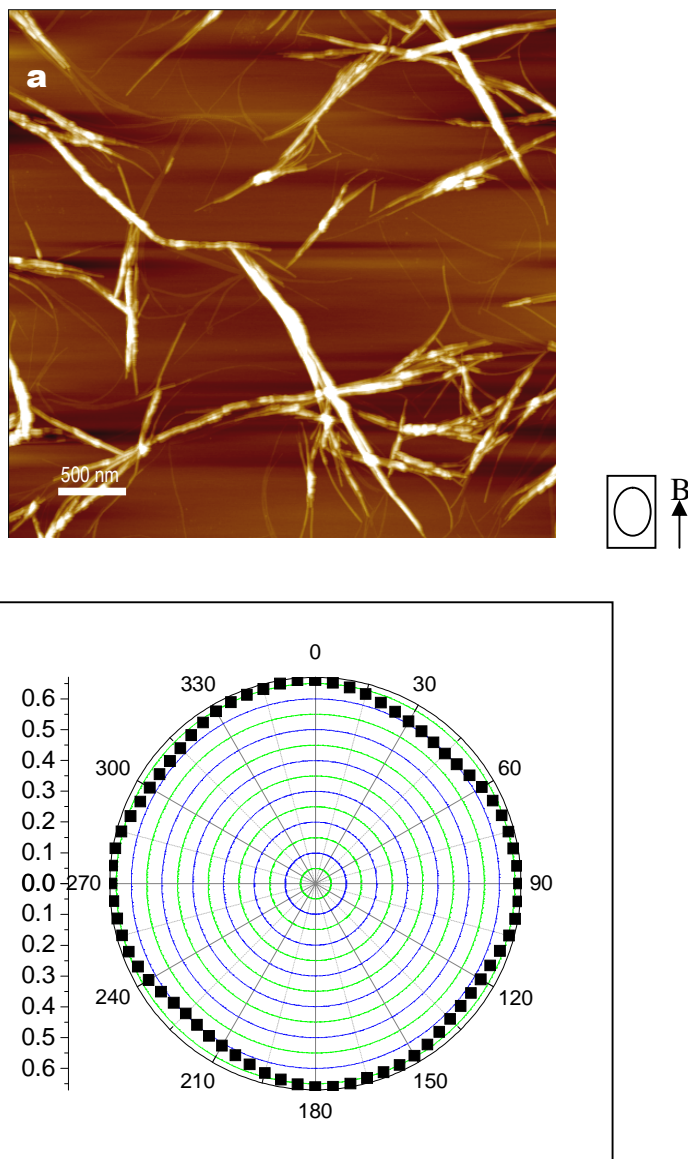


Figure 4.13: Ex situ AFM image of amylin (20-29) following exposure to 12 T magnetic field. Figure 13a is a topography image of amylin (20-29) fibrils after overnight exposure to a 12 T magnetic field. The direction of the applied magnetic field (B) relative to the sample is shown. **Figure 13b** is the polar plot calculated to determine the anisotropy of the peptide fibrils relative to the magnetic field.

4.4 Discussion

The focus of the experiments presented in this chapter are the nanotubes which self-assemble from the core recognition motif of the β -amyloid polypeptide; a simple dipeptide of phenylalanine. The dipeptide readily self-assembles under mild conditions to form discrete tubular structures. The mechanical properties of the diphenylalanine nanotubes reveal these structures to have a high degree of rigidity and stiffness by comparison with other bionanomaterials [220]. Here we have investigated the physical properties of the nanotubes by AFM, building on and corroborating current knowledge of the thermal and chemical stability from EM, CD spectroscopy and thermo gravimetric experiments [245]. One advantage AFM possesses over EM which is of particular relevance to the study of the thermal and chemical stability, is the ability to directly visualise specimens without drying and coating; a preparative process which could directly influence or alter the properties of the nanotubes.

In this chapter diphenylalanine nanotubes have been successfully imaged by AFM in both dry conditions and in solution. AFM imaging of the nanotubes in solution required an aqueous organic solvent environment with stable images generated in solutions of 50% acetone using mica as the substrate. The diphenylalanine nanotubes observed display the same characteristics irrespective of imaging in a dried or hydrated form: the nanotubes were discrete, long tubular structures with uniform morphologies displaying diameters in the range of 0.1 to 2 μm (figures 4.3 and 4.4) and were in agreement with published EM data [86, 220, 221, 229]. In addition, imaging of the nanotubes in aqueous acetone further demonstrates the chemical stability of these structures in an organic solvent.

The thermal stability of the diphenylalanine nanotubes was investigated under wet heating and dry heating conditions using the AFM. AFM images of samples following autoclaving (121°C, 1.2 atmospheres) demonstrate that the nanotubes retain structural integrity following wet heating conditions. The ability to withstand autoclave treatment is a highly desirable property when considering the potential applications for these nanostructures. The ability to undergo autoclaving as a sterilisation technique may be a prerequisite for use of the nanotubes in any

application that required aseptic conditions, for example as tissue engineering scaffolds or biosensors.

The AFM *in situ* and *ex situ* dry heat imaging of the diphenylalanine nanotubes demonstrates the thermal stability up to 100°C with no deterioration in morphology or structure (figures 4.6a & b and 4.7a & b). However, as the temperature is progressively increased above this, structural changes begin to occur in the nanotubes (figures 4.6c & d and 4.7c & d); there is loss in structural integrity and the nanotubes appear to collapse. Furthermore, significant deposition of granular material on the mica substrate can be seen at temperatures of 150°C (figures 4.6d and 4.7d), and crystalline deposits (figure 4.10) form on the AFM cantilever at temperatures of 200°C (figure 4.9), preventing the generation of stable images.

The AFM images clearly demonstrate the changes in diphenylalanine nanotube structure as the samples are heated above 100°C. However, to establish whether the deterioration in nanotube structure observed in the *in situ* heating experiment was due solely to the temperature or was a result of the mechanical deformation caused by the oscillating AFM probe during high-temperature imaging, the samples were heated and then imaged at room temperature (*ex situ* heating). Ideally for a direct comparison of the *in situ* and *ex situ* AFM heating, the same sample of nanotubes would be heated. However the nature of the experiment prevents this as the same nanotube cannot be reheated, and as such the example nanotubes were chosen on the basis of their similarity in dimension. Imaging parameters were kept as constant as possible and the AFM tapping tips that were used have a nominal spring constant of 42 N/m and were raster scanned across the sample surface at a rate of 0.5-0.8 Hz with an oscillating downward tapping frequency of 320 kHz. The results clearly indicate the collapse of the nanotubes as they are progressively heated by both *in situ* and *ex situ* AFM heating. Furthermore, a dramatic loss of ~80% in height upon heating the nanotubes to 150°C was observed in both *in situ* and *ex situ* heating conditions (figure 4.8). The data strongly suggests that at higher temperatures the nanotubes lose structural integrity and that the degradation and deformation is not solely attributable to the mechanical forces of the oscillating AFM tapping tip; temperature alone is the

controlling factor. However, once the nanotubes are heated to 150°C, the samples will be deformed no matter at what temperature the sample is imaged.

In a recent study, thermo-gravimetric analysis (TGA) was used to assay the thermal degradation of diphenylalanine nanotubes. In TGA studies the change in weight of a sample as a function of increasing temperature is measured [245]. The thermogram (figure 4.14) from this experiment shows a 15% loss in nanotube mass at around 50°C followed by a steady decrease in weight as the temperature increases, which is attributed to loss of water from the nanotubes. At around 150°C there is an acute 10 % drop in mass, followed by a plateau at 175°C until a dramatic loss in weight at temperatures above 300°C. Considering this data together with our AFM and TOF SIMS findings we can suggest that at temperatures up to 100°C, the limited changes observed in nanotube integrity are due to loss of water from the diphenylalanine nanotubes. As the temperature was raised to 150°C, in both the *in situ* and *ex situ* AFM heating images there was considerable degradation of the nanotubes and loss of structural integrity together with the appearance of granular deposits on the mica substrate. This is concurrent with a dramatic loss of 10 % mass noted in the TGA data between 150 and 175°C.

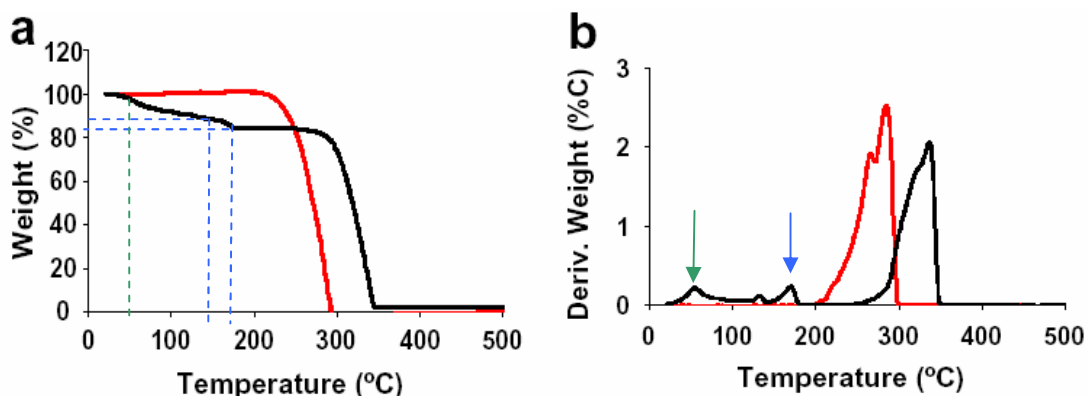


Figure 4.14: TGA data of diphenylalanine nanotubes and alanine dipeptides (Source Adler-Abramovich *et al* 2006 [245]) The black line indicates the diphenylalanine nanotube experiment. A sample of alanine dipeptides, which do not self-assemble to form nanotubes, was also studied as the control (red line). The colour of the dotted line in **figure 14a** corresponds to the feature highlighted by the same colour arrow in **figure 14b**.

Consideration of these findings together with our TOF SIMS analysis of the phenylalanine crystal deposits on the cantilevers, suggests that the observed deterioration and loss in mass at temperatures at and above 150°C is due to the loss of free phenylalanine from the nanotubes. Phenylalanine will at temperatures of 130°C, sublime under vacuum and decomposes at 283°C, whereas diphenylalanine does not [248]. Therefore we suggest that as the temperature is raised, sublimation of phenylalanine molecules and their fragments from the nanotubes occurs, collecting as crystal deposits on the cantilever within the AFM.

The evidence suggests therefore that heat-induced degradation of the nanotube's structural integrity occurs initially by the loss of water from the hollow water-filled nanotubes; as the temperature is increased, the nanotubes appear to deform suggesting that the walls are collapsing with loss of nanotube structural integrity. Thermal degradation of the diphenylalanine building blocks occurs as the temperature is further increased with loss of free phenylalanine from the tubes due to sublimation, resulting in the observed flat ribbon-like structure.

The thermal stability study of diphenylalanine nanotubes suggests that the nanotubes will withstand autoclaving as a potential sterilisation technique. Furthermore, the dry heating experiments demonstrate that it may be possible to use heat and localised mechanical forces to selectively deform the diphenylalanine nanotube. One key factor in developing novel applications for these nanotubes is the ability to control and manipulate their use as innovative materials.

In the final section of this chapter the application of magnetic fields to directly manipulate the orientation of diphenylalanine nanotubes has been investigated. The AFM images of diphenylalanine nanotube samples evaporated in different magnetic field strengths (figure 4.11) provide direct evidence for the alignment of the nanotubes in high magnetic fields (12 Tesla). Furthermore, a linear correlation is observed when the degree of sample anisotropy under each magnetic field is plotted against field strength (figure 4.12). By comparison when the control sample of amylin (20-29) fibrils was positioned within the highest strength (12 Tesla) magnetic field, no anisotropy was observed (figure 4.13).

The alignment of the nanotubes within a magnetic field arises due to the net diamagnetic susceptibility of the structure. When a substance is placed in a magnetic field it will experience a force tending to turn it into the position of minimum potential energy, thus leading to the alignment of like-substances in a sample. The diamagnetic anisotropy of most proteins is attributed to the anisotropy of the peptide bond, resulting from the resonance of its planar partial double-bond [244]. The cumulative contribution of the individual peptide bond anisotropies to the net anisotropy of the protein arises due to the regular structural organisation of the polypeptide chain in secondary structures (α helix and β -sheets).

However, the aromatic ring has anisotropy 10 times greater than that of the peptide bond [242]. In most proteins the aromatic content is very low, but within the diphenylalanine nanotubes there is 1 aromatic ring per peptide bond. Therefore the dominant contributor to the net diamagnetic anisotropy of the nanotubes is most likely the aromatic rings. The large diamagnetic anisotropy of the aromatic rings arises due to π - π interactions that govern the regular packing of the phenylalanine side chains within the nanotubes.

In diamagnetic material, the orbital motion of electrons creates atomic current loops (magnetic moments), which produce magnetic fields. When placed inside an applied magnetic field the moving charges will generate fields opposing the applied field. In terms of the aromatic side chains of the phenylalanine, the delocalised ring of π -electrons of each aromatic ring act as a magnetic dipole and will align opposing the applied magnetic field. The resultant torque imposed as the aromatic rings try to align in the magnetic field causes the rotation of the nanotubes and alignment in the sample. From the AFM images we can observe that the nanotubes are aligning with their long axis parallel to the magnetic field. Consequently, our experimental observations may provide empirical evidence to support or rule out future models for the arrangement of the diphenylalanine residues within the nanotubes. Currently, within the collaborative group, work is underway to generate a model of the nanotube structure based around a constraint on the average ring orientation of the dipeptides within the nanotubes. The constraint was derived from the magnetic alignment direction of the nanotubes

within the AFM images and may provide an insight into the possible ultrastructure of the nanotubes.

4.5 Conclusion

Diphenylalanine peptide nanotubes were for the first time successfully imaged in solution using the AFM. The thermal stability of the nanotubes under wet and dry heating was probed using the AFM, revealing their structural stability following autoclave treatment and under dry heating up to 100°C. As the temperature is progressively increased the nanotubes lose structural integrity due to the thermal degradation of the diphenylalanine building blocks, as free phenylalanine sublimates from the nanotube resulting in loss of mass and spatial volume. Furthermore, we show that high magnetic fields can be used to directly align the diphenylalanine nanotubes. The findings presented in this chapter display the ability to directly manipulate the diphenylalanine nanotubes demonstrating their potential to produce well-ordered functional and exploitable nanomaterials with considerable thermal stability.

Chapter

5

General Conclusions

The work presented in this thesis has focussed on the investigation of self-assembling peptides utilising both *in situ* and *ex situ* AFM. Short peptide sequences are well established as model systems for the study of amyloid. This is due to the comparative ease with which the shorter fragments can be synthesised and prepared. However, pivotal to this work is the identification that key fragments within the full-length amyloidogenic polypeptides are crucial to the self-assembly mechanism and readily assemble in isolation to form amyloid-like nanostructures.

The ability of short peptide fragments to self-assemble into fibrillar structures demonstrates that the capacity for well-ordered fibril formation is retained within these shortened sequences. However, the structures which assemble from these fragments are often morphologically distinct. Consequently, amyloid formation by the full-length polypeptide chain is more complex than might be revealed from fibrillisation studies of these key fragments and the influence of the remaining polypeptide chain must be considered if a true representation of the mechanism is to be determined. However, the ability of the self-assembling peptide to form a variety of distinct amyloid and amyloid-like structures with unique properties and exploitable characteristics makes their use as potential nanomaterials highly versatile.

Within this thesis two peptide systems have been studied; the peptide fragment corresponding to amino acid residues 20 to 29 of the human amylin polypeptide and an aromatic dipeptide corresponding to residues 19 and 20 of the β -amyloid polypeptide. The former peptide contains the minimal core amyloidogenic fragment (NFGAIL) of the amylin polypeptide, and the latter is the smallest

fragment of the β -amyloid polypeptide known to self-assemble. Both peptides readily self-assemble into fibrillar structures under simple conditions.

In the introductory chapter of this work, an overview of the current understanding of amyloid assembly, characterisation and properties has been presented, highlighting the important role the AFM has contributed to the many advancements made in understanding this complex world of peptide self-assembly. Within this final chapter, the findings and general conclusions of the experimental studies presented in this thesis will be discussed in light of the current understanding of amyloid formation and the implications for the development of strategies for the generation of novel controllable and specialised fibrillar materials. Nanofibrillar material have already been utilised in applications ranging from microelectronics to tissue engineering scaffolds for regenerative growth.

The first experimental study presented within this thesis addressed the self-assembly of the amylin (20-29) peptide fragment. This fragment has long been recognised to play a key role in the interactions governing amylin assembly into amyloid fibrils and has been studied by several research groups as a model for amyloid formation. However, these studies have predominantly concentrated on the mature fibrils, with no direct visual observation of the early stages in fibrillisation. To this end, a preliminary AFM study which focussed on younger solutions of amylin (20-29) was undertaken. The formation of fibrils was observed by *ex situ* imaging after an initial lag period of only 4 hours, with visible fibril polymorphisms noted in samples aged 18 hours. In samples of fibrils aged up to 6 hours, periodicity was noted in the fibrils, reminiscent of the pre-fibrillar globular protofilaments noted in other amyloid samples [56]. However, over the time-course studied these younger fibril morphologies were replaced by mature fibrils (aged >18 hours) which were straight flat ribbon-like structures displaying a range of morphologies, in agreement with those previously observed by EM and AFM [43, 44, 49].

One of the major contributions that the AFM has facilitated in the study of amyloid formation is the capacity to directly visualise dynamic events in an

aqueous environment, providing vital insights into the fibril assembly mechanisms. Within Chapter 2, the influence of a range of solution conditions on amylin (20-29) fibril formation was directly visualised by *in situ* AFM. AFM images revealed that a range of morphologies including truncated ribbons, long unbranched fibrils, shorter fibrils and globular aggregates were formed dependent on the pH, electrolyte composition and ionic strength of the solution. Fibril dimensions were also influenced by electrolyte composition. Successful *in situ* imaging of the amylin (20-29) fibrils facilitated kinetic studies to be made for the first time on the growth of fibrils. Growth rates varied between individual fibrils, ranging from 2 to 11 nm min⁻¹ on the mica surface. By comparison the published rate of full-length amylin fibrillisation is much slower at 1.1 nm min⁻¹ [44].

The findings within Chapter 2 demonstrate that different amyloid assembly pathways may be triggered by variations in environmental conditions. Similar findings have been reported for other amyloid fibrils [128] and provide further support that these well-ordered supramolecular structures may assemble via various pathways which may also include off-pathway events. Understanding the mechanisms that underpin amyloid fibril assembly are vital to the development of a full knowledge of amyloid, not only from a medical perspective for the development of therapeutics, but also for the recognition that these highly-ordered structures may be exploited as novel peptide-based nanofibrillar material.

The studies presented in Chapter 3 address the potential use of the amylin (20-29) peptide fibrils as specifically functionalised structures. This work investigates whether fibrils can be assembled from naturally occurring peptides which have been chemically modified to produce nanofibrillar structures that display a specific function. Azide and alkyne functional moieties were successfully coupled to the N-terminal of the amylin (20-29) peptide sequence. AFM investigations revealed the modified peptides readily self-assemble to form fibrillar structures displaying similar morphologies to non-functionalised amylin (20-29) fibrils. Furthermore, Congo red binding indicated that the modified fibrils have retained the core β -sheet ultrastructure and thus are amyloidogenic in nature. However, the fibrils that formed displayed smaller widths and heights suggesting that the moieties may influence the packing and assembly of the fibrils. These findings

demonstrate that the additional steric bulk of the functional moieties do not impose any detrimental effects on the fibril forming potential of the peptide fragments, but may influence the higher-order fibrillar packaging.

These observations have two implications, in the first instance, they provide further information regarding the interactions and packaging of the peptide fibrils within the amyloid core. This suggests that fibril formation will proceed providing the ordered β -sheet core can still form; any additional steric bulk outside of the core amyloidogenic region may influence the structural hierarchy but not the capacity to form amyloid. Secondly, this result demonstrates that fibrillar structures displaying all the intrinsic characteristics of amyloid may be self-assembled from chemically tailored individual building blocks, generating functionalised supramolecular structures. During attempts to form covalently linked fibrillar networks of the azide and alkyne functionalised fibrils using the 1,3-dipolar cycloaddition reaction of alkyne and azides an increase in the fibril population dimensions was observed that was dependent on the catalyst concentration present and the stage during fibril formation that the ions were added. Despite no significant change in morphology or aggregation into novel fibrillar network, this increase in dimensions suggests that the reaction may have been successful but with low efficiency. This can most likely be attributed to unfavourable conformational and steric presentation of the functional moieties for the formation of triazole ring linkers between fibrils. However, this does not rule out the potential of this chemistry for other applications including the generation of decorated fibrils with function specific ligands or the immobilisation of fibrils to a functionalised support or scaffold.

The focus of Chapter 4 is the second of the two peptide systems, the diphenylalanine peptide. The structures that readily self-assemble under mild conditions from the dipeptide are large, water-filled nanotubes which display a range of dimensions from 100s of nanometres in diameter and microns in length. The scope of possible applications for these diphenylalanine nanotubes is already being explored with proven success in microelectronics and biosensors. As with all material engineering, understanding the fundamental properties and principles

of the building blocks will enable their full potential to be realised and novel applications for the materials to be developed.

In the opening experiments of Chapter 4, the AFM is used to study the physical properties of the diphenylalanine nanotubes. *In situ* imaging of the nanotubes in an organic solvent demonstrates their chemical stability even with prolonged exposure and repeated imaging. Furthermore, the nanotubes exhibited considerable thermal stability under both dry and wet heating conditions; indicating that the nanotubes retain structural integrity at high temperatures. The ability to withstand wet heating conditions suggests that the nanotubes may be used in applications requiring sterilisation, such as biosensors and tissue engineering. During *in situ* and *ex situ* dry heating of the nanotubes a loss of wall integrity was observed at 125°C with loss of structural integrity at temperatures above 150°C. TOF SIMS analysis identified the decomposition of structure to be the result of sublimation of free phenylalanine from the nanotubes. Suggestive that the nanotubes may be degraded at higher temperatures, indicative of their potential use as thermally degradable devices.

In the final experiment of this thesis the potential to directly control and orientate the diphenylalanine nanotubes using magnetic fields is examined. X-ray crystallographers have previously probed the use of magnetic fields to produce highly-orientated crystals for the elucidation of biomolecular structures, including some amyloid fibrils. Following evaporation of phenylalanine nanotubes samples within different magnetic fields, AFM imaging revealed the nanotubes became increasingly orientated with the direction of the magnetic field with intensifying field strengths. Under magnetic field strength of 12 T there was almost complete alignment of the nanotubes. Consequently, strong magnetic fields may be a useful tool for future manipulation of the diphenylalanine nanotubes, demonstrating the potential to produce well-ordered functional and exploitable nanomaterials with considerable thermal stability.

Throughout this thesis the results generated are testament to the effectiveness and versatility of the AFM in the study of peptides which self-assemble into amyloid and amyloid-like structures. The high-resolution images generated provide

detailed information on both static and dynamic events during fibrillisation, as well as providing insights into the physical properties of these fibrillar structures. The application of AFM in the study of amyloid and their resultant fibrillar nanostructures can only strengthen with the continuing developments in the technology. From achieving higher-resolution images by improved tip geometries through the utilization of carbon nanotubes, to the development of high-speed scanning to enable real-time images of amyloid fibrillisation events.

In conclusion, the results presented throughout this thesis have revealed the potential of self-assembling peptides for the production of fibrillar nanostructures. By direct modification and manipulation, the ideal intrinsic or engineered properties of the fibrillar structures can be utilized to generate novel architectures and functionalised well-ordered nanomaterials.

References

1. Arai M. and Kuwajima K. (2000) Role of the Molten Globule State in Protein Folding. *Advances in Protein Chemistry*, **53**: 209-282.
2. Wickner S., Maurizi M.R., and Gottesman S. (1999) Posttranslational Quality Control: Folding, Refolding, and Degrading Proteins. *Science*, **286**(5446): 1888-93.
3. Hartl F.U. (1996) Molecular Chaperones in Cellular Protein Folding. *Nature*, **381**: 571-580.
4. Ellis R.J. and Hart F.U. (1999) Principles of Protein Folding in the Cellular Environment. *Current Opinion in Structural Biology*, **9**: 102-10.
5. Muchowski P.J. (2002) Protein Misfolding, Amyloid Formation, and Neurodegeneration: A Critical Role for Molecular Chaperones? *Neuron*, **35**: 9-12.
6. Jaenicke R. and Seckler R. (1997) Protein Misassembly *in vitro*. *Advances in Protein Chemistry*, **50**: 1-60.
7. Prusiner S.B., Scott M.R., DeArmond S.J., and Cohen F.E. (1998) Prion Protein Biology. *Cell*, **93**(3): 337-48.
8. Chiti F., Webster P., Taddei N., Clark A., Stefani M., Ramponi G., and Dobson C.M. (1999) Designing Conditions for *in vitro* Formation of Amyloid Protofilaments and Fibrils. *Proceedings of the National Academy of Science*, **96**: 3590-3594.
9. Hilbich C., Kisters-Woike B., Reed J., Masters C.L., and Beyreuther K. (1991) Aggregation and Secondary Structure of Synthetic Amyloid β A4 Peptides of Alzheimer's Disease. *Journal of Molecular Biology*, **218**: 149-163.

10. Cohen A.S. and Calkin S E. (1959) Electron Microscopic Observations on a Fibrous Component in Amyloid of Diverse Origins. *Nature*, **183**(4669): 1202 - 1203.
11. Muchowski P.J., Scheffer G., Sittler A., Wanker E.E., Hayer-Hartl M.K., and Hartl F.U. (2000) Hsp70 and Hsp40 Chaperones can Inhibit Self-assembly of Polyglutamine Proteins into Amyloid-like Fibrils. *Proceedings of the National Academy of Science, USA*, **97**: 7841-6.
12. Soto C. (2001) Protein Misfolding and Disease; Protein refolding and Therapy. *FEBS Letters*, **498**: 204-7.
13. Dobson C.M. (1999) Protein Misfolding, Evolution and Disease. *Trends in Biochemical Sciences*, **24**: 329-32.
14. Chapman M.R., Robinson L.S., Pinkner J.S., Roth R., Heuser J., Hammer M., Normark S., and Hultgren S.J. (2002) Role of *E. coli* Curli Operon in Directing Amyloid Fiber Formation. *Science*, **295**: 851-5.
15. Anguiano M., Nowak R.J., and Lansbury Jr P.T. (2002) Protofibrillar Islet Amyloid Polypeptide Permeabilizes Synthetic Vesicles by a Pore-like Mechanism that May Be Relevant to Type II Diabetes. *Biochemistry*, **41**: 11338-43.
16. Caughey B. and Lansbury Jr P.T. (2003) Protofibrils, Pores, Fibrils, and Neurodegeneration: Separating the Responsible Protein Aggregates from The Innocent Bystanders. *Annual Review of Neuroscience*, **26**: 267-98.
17. Gazit E. (2004) The Role of Prefibrillar Assemblies in the Pathogenesis of Amyloid Disease. *Drugs of the Future*, **29**(6): 1-7.
18. Dobson C.M. (2003) Protein Folding and Misfolding. *Nature*, **426**: 884-890.
19. Westermark G.T., Wilander, Westermark P., and Johnson (1987) Islet Amyloid Polypeptide-like Immunoreactivity in the Islet β -cells of Type-II

- (Non-Insulin Dependent) Diabetic and Non-Diabetic Individuals. *Diabetologia*, **30**: 887-92.
20. Glover J.R., Kowal A.S., Schirmer E.C., Patino M.M., Liu J.J., and Lindquist S.L. (1997) Self-Seeded Fibers Formed by Sup35, the Protein Determinant of [PSI⁺], a Heritable Prion-like Factor of *S-cerevisiae*. *Cell*, **89**(5): 811-9.
21. Fändrich M., Fletcher M.A., and Dobson C.M. (2001) Amyloid Fibrils from Muscle Myoglobin. *Nature*, **410**: 165-6.
22. Lansbury P.T. Jr. (1999) Evolution of Amyloid: What Normal Protein Folding may tell us about Fibrillogenesis and Disease. *Proceedings of the National Academy of Science, USA*, **96**: 3342-4.
23. Kelly J.W. (1997) Amyloid Fibril Formation and Protein Misassembly: A Structural Quest into Amyloid and Prion Diseases. *Structure*, **5**: 595-600.
24. Tennent G.A., Lovat L.B., and Pepys M.B. (1995) Serum Amyloid P-Component Prevents Proteolysis of the Amyloid Fibrils of Alzheimer-Disease and Systemic Amyloidosis. *Proceedings of the National Academy of Science, USA*, **92**(10): 4299-4303.
25. Westermark P. (1994) Amyloid and Polypeptide Hormones: What is their Interrelationship? *Amyloid*, **1**: 47-58.
26. Jimenez J.L., Tennent G., Pepys M., and Saibil H.R. (2001) Structural Diversity of *ex vivo* Amyloid Fibrils Studied by Cryo-Electron Microscopy. *Journal of Molecular Biology*, **311**: 241-7.
27. Glenner G.G., Eanes E.D., and Page D.L. (1972) The Relation of the Properties of Congo Red-Stained Amyloid Fibrils to the β -Conformation. *The Journal of Histochemistry and Cytochemistry*, **20**(10): 821-6.
28. Puchtler H., Sweat F., and Levine M. (1962) On the Binding of Congo Red by Amyloid. *The Journal of Histochemistry and Cytochemistry*, **10**: 355-.

29. Eanes E.D. and Glenner G.G. (1968) X-Ray Diffraction Studies on Amyloid Filaments. *Journal of Histochemistry and Cytochemistry*, **16**(11): 673-7.
30. Pauling L. and Corey R. (1951) Configuration of Polypeptide Chains with Favoured Orientation Around Single Bonds: Two New Pleated Sheets. *Proceedings of the National Academy of Science*, **37**: 729-39.
31. Serpell L.C., Sunde M., and Blake C.C.F. (1997) The Molecular Basis of Amyloidosis. *Cellular and Molecular Life Sciences*, **53**(11-12): 871-87.
32. Blake C.C.F. and Serpell L.C. (1996) Synchrotron X-ray Studies Suggest that the Core of the Transthyretin Amyloid Fibril is a Continuous β -sheet Helix. *Structure*, **4**: 989-998.
33. Sunde M. and Blake C.C.F. (1997) The Structure of Amyloid Fibrils by Electron Microscopy and X-ray Diffraction. *Advances in Protein Chemistry*, **50**: 123-159.
34. Sunde M., Serpell L.C., Bartlam M., Fraser P.E., Pepys M.B., and Blake C.C.F. (1997) Common Core Structure of Amyloid Fibrils by Synchrotron X-ray Diffraction. *Journal of Molecular Biology*, **273**: 729-739.
35. Serpell L.C., Sunde M., Benson M.D., Tennent G.A., Pepys M.B., and F. P.E. (2000) The Protofilament Substructure of Amyloid Fibrils. *Journal of Molecular Biology*, **300**(5): 1033-1039.
36. Serpell L.C., Sunde M., Fraser P.E., Luther P.K., Morris E.P., Sangren O., Lundgren E., and Blake C.C. (1995) Examination of the Structure of the Transthyretin Amyloid Fibril by Image Reconstruction from Electron Micrographs. *Journal of Molecular Biology*, **254**: 113-8.
37. Shirahama T. and Cohen A.S. (1967) High Resolution Electron Microscopic Analysis of the Amyloid Fibril. *Journal of Cellular Biology*, **33**: 679-706.

38. Stromer T. and Serpell L.C. (2005) Structure and Morphology of the Alzheimer's Amyloid Fibril. *Microscopy Research and Technique*, **67**: 210-7.
39. Chamberlain A.K., MacPhee C.E., Zurdo J., Morozova-Rocke L.A., Hill A.O., Dobson C.M., and D. J.J. (2000) Ultrastructural Organisation of Amyloid Fibrils by Atomic Force Microscopy. *Biophysical Journal*, **79**: 3282-93.
40. Khurana R., Ionescu-Zanetti C., Pope M., Li J., Nielson L., Ramirez-Alvarado M., Regan L., Fink A.L., and Carter S.A. (2003) A General Model for Amyloid Fibril Assembly Based on Morphological Studies Using Atomic Force Microscopy. *Biophysical Journal*, **85**: 1135-44.
41. Malinchik S.B., Inouye H., Szumowski K.E., and Kirschner D.A. (1998) Structural Analysis of Alzheimer's Beta(1-40) Amyloid: Protofilament Assembly of Tubular Fibrils. *Biophysical Journal*, **74**(1): 537-45.
42. Roher A.E., Baudry J., Chaney M.O., Kuo Y-M., Stine W.B., and Emmerling M.R. (2000) Oligomerisation and Fibril Assembly of the Amyloid- β Protein. *Biochimica et Biophysica Acta*, **1502**: 31-43.
43. Goldsbury C., Cooper G.J.S., Goldie K.N., Mueller S.A., Saafi E.L., Grujters W.T.M., Misur M.P., Engel A., Aebi U., and Kistler J. (1997) Polymorphic Fibrillar Assembly of Human Amylin. *Journal of Structural Biology*, **119**: 17-27.
44. Goldsbury C., Kistler J., Aebi U., Arvinte T., and Cooper G.J.S. (1999) Watching Amyloid Fibrils Grow by Time-lapse Atomic Force Microscopy. *Journal of Molecular Biology*, **285**: 33-39.
45. Ionescu-Zanetti C., Khurana R., Gillespie J.R., Petrick J.S., Trabachino L.C., Minert L.J., Carter S.A., and Fink A.L. (1999) Monitoring the Assembly of Ig Light-chain Amyloid Fibrils by Atomic Force Microscopy. *Proceedings of the National Academy of Science*, **96**(23): 13175-13179.

46. Booth D.R., Sunde M., Bellotti V., Robinson C.V., Hutchinson W.L., Fraser P.E., Hawkins P.N., Dobson C.M., Radford S.E., Blake C.C.F., and P. M.B. (1997) Instability, Unfolding and Aggregation of Human Lysozyme variants Underlying Amyloid Fibrillogenesis. *Nature*, **385**: 787-793.
47. Macphee C.E. and Dobson C.M. (2000) Formation of Mixed Fibrils Demonstrates the Generic Nature and Potential Utility of Amyloid Nanostructures. *Journal of American Chemical Society*, **122**: 12707-13.
48. Padrick S.B. and Miranker A.D. (2001) Islet Amyloid Polypeptide: Identification of Long-Range Contacts and Local Order on the Fibrillogenesis Pathway. *Journal of Molecular Biology*, **308**: 783-4.
49. Goldsbury C., Goldie K.N., Pellaud J., Seeling J., Frey P., Muller S.A., Kistler J., Cooper G.J.S., and Aebi U. (2000) Amyloid Fibril Formation from Full-length and Fragments of Amylin. *Journal of Structural Biology*, **130**: 352-62.
50. Kajava A.V., Aebi U., and Stevens A.C. (2005) The Parallel Superpleated Beta-Structure as a Model for Amyloid Fibrils of Human Amylin. *Journal of Molecular Biology*, **348**: 247-52.
51. Antzutkin O.N., Leapman R.D., Balbach J.J., and Tycko R. (2002) Supramolecular Structural Constraints on Alzheimer's β -Amyloid Fibrils from Electron Microscopy and Solid-State Nuclear Magnetic Resonance. *Biochemistry*, **41**(51): 15436-50.
52. Petkova A.T., Buntkowsky G., Dyda F., Leapman R.D., Yau W.M., and Tycko R. (2004) Solid State NMR Reveals a pH-Dependent Antiparallel β -Sheet Registry in Fibrils Formed by a β -Amyloid Peptide. *Journal of Molecular Biology*, **335**(1): 247-60.
53. Petkova A.T., Ishii Y., Balbach J.J., Antzutkin O.N., Leapman R.D., Delaglio F., and Tycko R. (2002) A Structural Model for Alzheimer's β -Amyloid Fibrils Based on Experimental Constraints from Solid State

- NMR. *Proceedings of the National Academy of Science, USA*, **99**(26): 16742-7.
54. Kirschner D.A., Abraham C., and Selkoe D.J. (1986) X-Ray Diffraction from Intraneuronal Paired helical Filaments and Extraneuronal Amyloid Fibres in Alzheimer's Disease Indicates Cross- β Conformation. *Proceedings of the National Academy of Science*, **83**: 503-7.
55. Jimenez J.L., Nettleton E.J., Bouchard M., Robinson C.V., Dobson C.M., and Saibil H.R. (2002) The Protofilament Structure of Insulin Amyloid Fibrils. *Proceedings of the National Academy of Science, USA*, **99**(14).
56. Blackley H.K.L., Sanders G.H.W., Davies M.C., Roberts C.J., Tendler S.J.B., and Wilkinson M.J. (2000) *In-situ* AFM Study of β -Amyloid Fibrillisation. *Journal of Molecular Biology*, **298**: 833-40.
57. Goldsbury C., Frey P., Olivier V., Aebi U., and M. S.A. (2005) Multiple Assembly Pathways Underlie Amyloid- β Fibril Polymorphisms. *Journal of Molecular Biology*, **352**: 282-98.
58. Chiti F., Stefani M., Taddei N., Ramponi G., and Dobson C.M. (2003) Rationalization of the Effects of Mutations on Peptide and Protein Aggregation. *Nature*, **424**: 805-8.
59. Chiti F., Taddei N., Baroni F., Capanni C., Stefani M., Ramponi G., and Dobson C.M. (2002) Kinetic Partitioning of Protein Folding and Aggregation. *Nature Structural Biology*, **9**(2): 137-43.
60. Tartaglia G. G., Cavalli A., Pellarin R., and Caflisch A. (2004) The role of aromaticity, exposed surface, and dipole moment in determining protein aggregation rates. *Protein Science*, **13**(7): 1939-1941.
61. Azriel R. and Gazit E. (2001) Analysis of the Minimal Amyloid-forming Fragment of the Islet Amyloid Polypeptide -An Experimental Support for the Key Role of the Phenylalanine Residue in Amyloid Formation. *Journal of Biological Chemistry*, **276**(36): 34156-61.

62. Gazit E. (2002) A Possible Role for π -Stacking in the Self-Assembly of Amyloid Fibrils. *FASEB*, **16**: 77-83.
63. Wurth C., Guimard N.K., and Hecht M.H. (2002) Mutations that Reduce Aggregation of the Alzheimer's A β 42 Peptide: An Unbiased Search for the Sequence Determinants of A β Amyloidogenesis. *Journal of Molecular Biology*, **319**: 1279-90.
64. Green J.D., Goldsbury C., Kistler J., Cooper G.J.S., and Aebi U. (2004) Human Amylin Oligomer Growth and Fibril Elongation Define Two Distinct Phases in Amyloid Formation. *Journal of Biological Chemistry*, **279**(13): 12206-12.
65. Jarrett J.T., Berger E.P., and Lansbury Jr P.T. (1993) The Carboxy Terminus of the β -Amyloid Protein is Critical for the Seeding of Amyloid Formation: Implications for the Pathogenesis of Alzheimer's Disease. *Biochemistry*, **32**: 4693-7.
66. Lomakin A., Chung D.S., Benedek G.B., Kirschner D.A., and Teplow D.B. (1996) On the Nucleation and Growth of Amyloid β -protein Fibrils: Detection of Nuclei and Quantitation of Rate Constants. *Proceedings of the National Academy of Science, USA*, **93**: 1125-29.
67. Serag A.A., Altenbach C., Gingery M., Hubbell W.L., and Yeates T.O. (2001) Identification of a Subunit Interface in Transthyretin Amyloid Fibrils: Evidence for Self-Assembly from Oligomeric Building Blocks. *Biochemistry*, **40**: 9089-96.
68. Walsh D.M., Condron M.M., Lomakin A., Benedek G.B., and Teplow D.B. (1997) Amyloid β -Protein Fibrillogenesis. Detection of a Protofibrillar Intermediate. *Journal of Biological Chemistry*, **272**(35): 22364-72.
69. Harper J.D. and Lansbury Jr P.T. (1997) Models of Amyloid Seeding in Alzheimer's Disease and Scrapie: Mechanistic Truths and Physiological

- Consequences of the Time-Dependent Solubility of Amyloid Proteins. *Annual Review of Biochemistry*, **66**: 385-407.
70. Krebs M. R.H., Morozova-Roche L. A., Daniel K., Robinson C.V., and D. C.M. (2004) Observation of sequence specificity in the seeding of protein amyloid fibrils. *Protein Science*, **13**(7): 1933-1938.
71. Biere A.L., Wood S.J., Wypych J., Steavenson S., Jiang Y., Anafi D., Jacobsen F.W., Jarosinski M.A., Wu G-M., Louis J-C., Martin F., Narhi L.O., and Citron M. (2000) Parkinson's Disease-associated α -Synuclein is More Fibrillogenic than β - and γ -Synuclein and Cannot Cross-seed its Homologs. *Journal of Biological Chemistry*, **275**(44): 34574-9.
72. Jarret J.T. and Lansbury Jr P.T. (1992) Amyloid Fibril Formation requires a Chemically Discriminating Nucleation Event: Studies of an Amyloidogenic Sequence from the Bacterial Protein OsmB. *Biochemistry*, **31**: 12345-52.
73. Cohen F.E. (2000) Prions, Peptides and Protein Misfolding. *Molecular Medicine Today*, **6**(7): 292-3.
74. Monti M., Garolla di Bard B.L., Calloni G., Chiti F., Amoresano A., Ramponi G., and Pucci P. (2004) The Regions of the Sequence Most Exposed to the Solvent within the Amyloidogenic State of a Protein Initiate the Aggregation Process. *Journal of Molecular Biology*, **336**: 253-62.
75. McGaughey G.B., Gagnes M., and Rappe A.K. (1998) π -Stacking Interactions. Alive and Well in Proteins. *The Journal of Biological Chemistry*, **273**(25): 15458-63.
76. Makin O.S., Atkins E., Sikorski P., Johansson J., and Serpell L.C. (2005) Molecular Basis for Amyloid Fibril Formation and Stability. *Proceedings of the National Academy of Science*, **102**(2): 315-320.
77. Kowalewski T. and Holtzman D.M. (1999) *In situ* Atomic Force Microscopy Study of Alzheimer's β -Amyloid Peptide on Different

- Substrates: New Insights into Mechanism of β -Sheet Formation. *Proceedings of the National Academy of Science*, **96**: 3688-93.
78. Kelly J.W. (2000) Mechanisms of Amyloidogenesis. *Nature Structural Biology*, **7**(10): 824-6.
79. Massi F. and Straub J.E. (2001) Energy Landscape Theory for Alzheimer's Amyloid β -Peptide Fibril Elongation. *Proteins*, **42**: 217-229.
80. Pallitto M.M. and Murphy R.M. (2001) A Mathematical Model of the Kinetics of β -Amyloid Fibril Growth from the Denatured State. *Biophysical Journal*, **81**(3).
81. Serio T.R., Cashikar A.G., Kowal A.S., Sawick G.J., Moslehi J.J., Serpell L.C., Arnsdorf M.F., and Lindquist S.L. (2000) Nucleated Conformational Conversion and the Replication of Conformational Information by a Prion Determinant. *Science*, **289**: 1317-21.
82. Zerovnik E. (2002) Amyloid Fibril Formation. Proposed Mechanisms and Relevance to Conformational Disease. *European Journal of Biochemistry*, **269**: 3362-71.
83. Serag A.A., Altenbach C., Gingery M., Hubbell W.L., and Yeates T.O. (2002) Arrangement of Subunits and Ordering of β -Strands in an Amyloid Sheet. *Nature Structural Biology*, **9**(10): 734-9.
84. Gazit E. (2005) Mechanisms of Amyloid Fibril Self-Assembly and Inhibition. Model Short Peptides as a Key Research Tool. *FEBS Journal*, **272**: 5971-8.
85. Sanchez de Groot N., Pallares I., Aviles F.X., Vendrell J., and Ventura S. (2005) Prediction of "Hot Spots" of Aggregation in Disease-Linked Polypeptides. *BMC Structural Biology*, **5**: 18-32.
86. Reches M. and Gazit E. (2003) Casting Metal Nanowires Within Discrete Self-Assembled Peptide Nanotubes. *Science*, **300**: 625-7.

-
87. Tenedis K., Waldner M., Bernhagen J., Fischle W., Bergmann M., Weber M., Merkle M-L., Voelter W., Brunner H., and Kapurniotu A. (2000) Identification of a Penta- and Hexapeptide of Islet Amyloid Polypeptide (IAPP) with Amyloidogenic and Cytotoxic Properties. *Journal of Molecular Biology*, **295**: 1055-71.
88. Westermark P., Engstrom U., Johnson K.H., Westermark G.T., and Betsholtz C. (1990) Islet Amyloid Polypeptide: Pinpointing Amino Acid Residues Linked to Amyloid Fibril Formation. *Proceedings of the National Academy of Sciences, USA.*, **87**: 5036-40.
89. Balbach J.J., Ishii Y., Antzutkin O.N., Leapman R.D., Rizzo N.W., Dyda F., Reed J., and Tycko R. (2000) Amyloid Fibril Formation by A β 16-22, a Seven-Residue Fragment of the Alzheimer's β -Amyloid Peptide, and Structural Characterization by Solid State NMR. *Biochemistry*.
90. Jaikaran E.T.A.S., Higham C.E., Serpell L.C., Zurdo J., Gross M., Clark A., and Fraser P.E. (2001) Identification of a Novel Human Islet Amyloid Polypeptide β -Sheet Domain and Factors Influencing Fibrillogenesis. *Journal of Molecular Biology*, **308**: 515-25.
91. Reches M., Porat Y., and Gazit E. (2002) Amyloid Fibril Formation by Pentapeptide and Tetra peptide Fragments of Human Calcitonin. *Journal of Biological Chemistry*, **277**(38): 35475-80.
92. Wu C., Lei H., and Duan Y. (2005) The Role of Phe in the Formation of Well-Ordered Oligomers of Amyloidogenic Hexapeptide (NFGAIL) Observed in Molecular Dynamics Simulations with Explicit Solvent. *Biophysical Journal*, **88**(4): 2897-2906.
93. Findeis M.A., Musso G.M., Arico-Muendel C.C., Benjamin H.W., Hundal A.M., L. J-J, Chin J., Kelley M., Wakefield J., Hayward N.J., and Molineaux S.M. (1999) Modified-Peptide Inhibitors of Amyloid -Peptide Polymerization. *Biochemistry*, **38**: 6791-800.

-
94. Tjernberg L.O., Näslund J., Lindqvist F., Johansson J., Karlström A.R., Thyberg J., Terenius L., and Nordstedt C. (1996) Arrest of β -Amyloid Fibril Formation by a Pentapeptide Ligand. *Journal of Biological Chemistry*, **271**: 8545-8.
95. Tracz S.M., Abedini A., Driscoll M., and R. D.P. (2004) Role of Aromatic Interactions in Amyloid Formation by Peptides Derived from Human Amylin. *Biochemistry*, **43**: 15901-8.
96. Kirschner D.A., Inouye H., Duffy L.K., Sinclair A., Lind M., and Selkoe D.J. (1987) Synthetic Peptide Homologous to β protein from Alzheimer's Disease forms Amyloid-like Fibrils *in vitro*. *Proceedings of the National Academy of Sciences, USA.*, **84**: 6953-57.
97. Kudva Y.C., Mueske C., Butler P.C., and Eberhardt N.L. (1998) A Novel Assay *in vitro* of Human Islet Amyloid Polypeptide Amyloidogenesis and Effects of Insulin Secretory Vesicle Peptides on Amyloid Formation. *Biochemical Journal*, **331**: 809-13.
98. Levine H. (1993) Thioflavine T Interaction with Synthetic Alzheimer's Disease β -Amyloid Peptides: Detection of Amyloid Aggregation in Solution. *Protein Science*, **2**: 404-10.
99. Ban T., Hamada D., Hasegawa K., Naiki H., and Goto Y. (2003) Direct Observation of Amyloid Fibril Growth Monitored by Thioflavin T fluorescence. *Journal of Biological Chemistry*, **278**: 16462-65.
100. Glenner G.G., Eanes E.D., and W. C.A. (1988) Amyloid Fibrils Formed from a Segment of the Pancreatic Islet Amyloid Protein. *Biochemical and Biophysical Research Communication*, **155**(2): 608-14.
101. Antzutkin O.N., Balbach J.J., Leapman R.D., Rizzo N.W., Reed J., and Tycko R. (2000) Multiple Quantum Solid-state NMR Indicates a Parallel, not Antiparallel, Organisation of β -sheets in Alzheimer's β -Amyloid Fibrils. *Proceedings of the National Academy of Science*, **97**(24): 13045-50.

-
102. Griffiths J.M., Ashburn T.T., Auger M., Costa P.R., Griffin R.G., and Lansbury Jr P.T. (1995) Rotational Resonance Solid-State NMR Elucidates a Structural Model of Pancreatic Amyloid. *Journal of American Chemical Society*, **117**: 3539-46.
103. Jaroniec C.P., MacPhee C.E., Bajaj V.S., McMahon M.T., Dobson C.M., and Griffin R.G. (2004) High-resolution Molecular Structure of a Peptide in an Amyloid Fibril Determined by Magic Angle Spinning NMR Spectroscopy. *Proceedings of the National Academy of Science*, **101**(3): 711-16.
104. Barrow C.J., Yasuda A., Kenny P.T.M., and Zagorski M.G. (1992) Solution Conformations and Aggregational Properties of Synthetic Amyloid β -Peptides of Alzheimer's Disease. *Journal of Molecular Biology*, **225**: 1075-93.
105. Makin O.S. and Serpell L.C. (2004) Structural Characterisation of Islet Amyloid Polypeptide Fibrils. *Journal of Molecular Biology*, **335**: 1279-88.
106. Colombo G., Daidone I., Gazit E., Amadei A., and Di Nola A. (2005) Molecular Dynamics Simulation of the Aggregation of the Core-Recognition Motif of the Islet Amyloid Polypeptide in Explicit Water. *Proteins: Structure, Function, and Bioinformatics*, **59**(3): 519-527.
107. Zanuy D., Porat Y., Gazit E., and Nussinov R. (2004) Peptide Sequence and Amyloid Formation: Molecular Simulations and Experimental Study of a Human Islet Amyloid Polypeptide Fragment and its Analogs. *Structure*, **12**: 439-55.
108. Binnig G., Quate C.F., and Gerber Ch. (1986) Atomic Force Microscope. *Physical Review Letters*, **56**(9): 930-3.
109. Hafner J.H., Cheung C.L., Woolley A.T., and Lieber C.M. (2001) Structural and Functional Imaging with Carbon Nanotube AFM Probes. *Progress in Biophysics and Molecular Biology*, **77**(1): 73-110.

-
110. Weisenhorn A.L., Hansma P.K., Albrecht T.R., and Quate C.F. (1989) Forces in Atomic Force Microscopy in Air and Water. *Applied Physics Letters*, **54**: 2651-3.
111. Hansma P.K., Cleveland J.P., Radmacher M., Walters D.A., Hillner P.E., Bezanilla M., Fritz M., Vie D., Hansma H.G., Prater C.B., Massie J., Fukunaga L., Gurley J., and Elings V. (1994) Tapping Mode Atomic Force Microscopy in Liquids. *Applied Physics Letters*, **64**: 1738-40.
112. Putman C.A.J., Vanderwerf K.O., de Groot B.G., Vanhulst N.F., and Greve J. (1994) Tapping Mode Atomic Force Microscopy in Liquid. *Applied Physics Letters*, **64**: 2454-6.
113. Zhong Q., Inniss D., Kjoller K., and Elings V.B. (1993) Fractured Polymer/Silica Fibre Surface Studied by Tapping Mode Atomic Force Microscopy. *Surface Science Letters*, **290**: L688-92.
114. Magonov S.N., Elings V., and Whangbo M.H. (1997) Phase Imaging and Stiffness in Tapping-Mode Atomic Force Microscopy. *Surface Science*, **375**: L385-91.
115. Chen X., Roberts C.J., Zhang J., Davies M.C., and Tendler S.J.B. (2002) Phase Contrast and Attraction-Repulsion Transition in Tapping Mode Atomic Force Microscopy. *Surface Science*, **519**: L593-8.
116. Schmitz I., Schreiner M., Friedbacher G., and Grasserbauer M. (1997) Phase Imaging as an Extension to Tapping-Mode AFM for the Identification of Material Properties on Humidity-Sensitive Surfaces. *Applied Surface Science*, **115**: 190-8.
117. Tamayo J. and Garcia R. (1996) Deformation, Contact Time and Phase-Contrast Time in Tapping Mode Scanning Force Spectroscopy. *Langmuir*, **12**: 4430-5.
118. Luthi R., Meyer E., Howald I., Haefke H., Anselmetti D., Dreier M., Ruetsche M., Bonner T., Overney R.M., Fromer J., and Guntherodt H.J.

- (1994) Progress in Non-Contact Dynamic Force Microscopy. *Journal of Vacuum Science and Technology B*, **12**: 1673-1676.
119. Garcia N. and Binh V.T. (1992) Van der Waals Forces in Atomic Force Microscopy Operating in Liquids: A Spherical-Tip Model. *Physical Review B*, **46**: 7946-8.
120. Hartmann U. (1991) Van der Waals Interactions Between Sharp Probes and Flat Sample Surfaces. *Physical Review B*, **43**: 2402-7.
121. Burnham N.A. and Colton R.J. (1989) Measuring the Nanomechanical Properties and Surface Forces of Materials Using an Atomic Force Microscope. *Journal of Vacuum Science and Technology A*, **7**: 2906-13.
122. Allison D.P., Hinterdorfer P., and H. W. (2002) Biomolecular Force Measurements and the Atomic Force Microscope. *Current Opinion in Biotechnology*, **13**: 47-51.
123. Ellis J.S., Allen S., Chim Y.T.A., Roberts C.J., Tendler S.J.B., and Davies M.C. (2006) Molecular-Scale Studies on Biopolymers Using Atomic Force Microscopy. *Advances in Polymer Science*, **193**: 123-72.
124. Leckband D. (2000) Measuring the Forces that Control Protein Interactions. *Annual Review of Biophysical and Biomolecular Structures*, **29**(1-26).
125. Green J., Goldsbury C., Mini T., Sunderji S., Frey P., Kistler J., Cooper G., and Aebi U. (2003) Full-length Rat Amylin Forms Fibrils Following Substitution of Single Residues from Human Amylin. *Journal of Molecular Biology*, **326**: 1147-1156.
126. Khurana R., Gillespie J.R., Talapatra A., Minert L.J., Ionescu-Zanetti C., Millett I., and Fink A.L. (2001) Partially Folded Intermediates as Critical Precursors of Light Chain Amyloid Fibrils and Amorphous Aggregates. *Biochemistry*, **40**: 3525-35.

127. Kad N.M., Myers S. L., Smith D.P., Smith A., Radford S.E., and Thomson N.H. (2003) Hierarchical Assembly of β_2 -Microglobulin Amyloid *in vitro* Revealed by Atomic Force Microscopy. *Journal of Molecular Biology*, **330**: 785-97.
128. Gosal W.S., Morten I.J., Hewitt E.W., Smith D.A., Thomson N.H., and Radford S.E. (2005) Competing Pathways Determine Fibril Morphology in the Self-assembly of β_2 -Microglobulin into Amyloid. *Journal of Molecular Biology*, **351**: 850-64.
129. Kad N.M., Thomson N.H., Smith D.P., Smith D.A., and Radford S.E. (2001) β_2 -Microglobulin and its Deamidated Variant, N17D Form Amyloid Fibrils with a Range of Morphologies *in vitro*. *Journal of Molecular Biology*, **313**: 559-71.
130. Cheng H. and Olvera de la Cruz M. (2004) Rod-Like Polyelectrolyte Adsorption onto Charged Surfaces in Monovalent and Divalent Salt Solutions. *Journal of Polymer Science Part B: Polymer Physics*, **42**: 3642-53.
131. Hansma H.G. and Laney D.E. (1996) DNA Binding to Mica Correlates with Cationic Radius: Assay by Atomic Force Microscopy. *Biophysical Journal*, **70**: 1933-39.
132. Karrasch S.E., Dolder M., Schabert F., Ramsden J., and Engel A. (1993) Covalent Binding of Biological Samples to Solid Supports for Scanning Probe Microscopy in Buffer Solution. *Biophysical Journal*, **65**: 2437-46.
133. Purton J.A., Allan N.L., and Blundy J.D. (1997) Impurity Cations in the Bulk and the {001} Surface of Muscovite: An Atomistic Simulation Study. *Journal of Material Chemistry*, **7**(9): 1947-51.
134. Sedman V.L., Allen S., Chan W.C., Davies M.C., Roberts C.J., Tendler S.J.B., and Williams P.M. (2005) Atomic Force Microscopy Study of Human Amylin (20-29) Fibrils. *Protein and Peptide Letters*, **12**: 79-83.

-
135. Zhu M., Souillac P.O., Ionescu-Zanetti C., Carter S.A., and Fink A.L. (2002) Surface-catalyzed Amyloid Fibril Formation. *Journal of Biological Chemistry*, **277**(52): 50914-22.
136. Blackley H.K.L., Patel N., Davies M.C., Roberts C. J., Tendler S. J. B., Wilkinson M.J., and Williams P.M. (1999) Morphological Development of β (1-40) Amyloid Fibrils. *Experimental Neurology*, **158**(2): 437-443.
137. Brown C.L., Aksay I.A., Saville D.A., and Hecht M.H. (2002) Template-Directed Assembly of a *de Novo* Designed Protein. *Journal of American Chemical Society*, **124**: 6846-48.
138. Kowaleski T. and Holtzman D.M. (1999) *In situ* AFM study of Alzheimer's β -Amyloid Peptide on Different Substrates: New Insights into Mechanisms of β -sheet Formation. *Proceedings of the National Academy of Sciences, USA.*, **96**: 3688-93.
139. Engel M.F.M., Yigittop H., Elgersma R.C., Rijkers D.T.S., Liskamp R.M.J., de Kruijff B., Hoppener J.W.M., and Killian J.A. (2006) Islet Amyloid Polypeptide Inserts into Phospholipid Monolayers as Monomers. *Journal of Molecular Biology*, **356**: 783-9.
140. Green J., Kreplak L., Goldsbury C., Blatter X.L., Stolz M., Cooper G.S., Seeling A., Kistler J., and Aebi U. (2004) Atomic Force Microscopy Reveals Defects Within Mica Supported Lipid Bilayers Induced by the Amyloidogenic Human Amylin Peptide. *Journal of Molecular Biology*, **342**: 877-87.
141. Yip C.M. and McLaurin J. (2001) Amyloid- β Peptide Assembly: A Critical Step in Fibrillogenesis and Membrane Disruption. *Biophysical Journal*, **80**: 1359-71.
142. Yip C.M., Darabie A.A., and McLaurin J. (2002) A β 42-Peptide Assembly on Lipid Bilayers. *Journal of Molecular Biology*, **318**: 97-107.

143. O'Nuallain B. and Wetzel R. (2002) Conformational Abs Recognizing a Generic Amyloid Fibril Epitope. *Proceedings of the National Academy of Science, USA*, **99**: 1485-90.
144. Harper J.D., Wong S.S., Lieber C.M., and Lansbury Jr P.T. (1997) Atomic Force Microscopic Imaging of Seeded Fibril Formation and Fibril Branching by the Alzheimer's Disease Amyloid- β Protein. *Chemical Biology*, **4**: 119-25.
145. Humphris A.D.L., Miles M.J., and Hobbs J.K. (2005) A Mechanical Microscope: High-Speed Atomic Force Microscopy,. *Applied Physics Letters*, **86**(3): 034106.
146. McMaster T.J., Brayshaw D., Miles M.J., Walsby A.E., and Dunton P. (2005) A New Ultra High Speed AFM Technique for Biophysics: 3-Dimensional Imaging of Surfaces, Molecules and Processes with True Millisecond Resolution. *Biophysical Journal*, **88**(1): 541A-541A Pt2 Sup. S.
147. Meersman F. and Dobson C.M. (2006) Probing the Pressure-Temperature Stability of Amyloid Fibrils Provides New Insights into Their Molecular Properties. *Biochimica et Biophysica Acta*, **1764**: 452-60.
148. Hatters D.M., MacRaidl C.A., Daniels R., Gosal W.S., Thomson N.H., Jones J.A., Davis J.J., MacPhee C.E., Dobson C.M., and Howlett G.J. (2003) The Circularization of Amyloid Fibrils Formed by Apolipoprotein C-II. *Biophysical Journal*, **85**: 3979-90.
149. Jansen R., Grudzielanek S., Dzwolak W., and Winter R. (2004) High Pressure Promotes Circularly Shaped Insulin Amyloid. *Journal of Molecular Biology*, **338**: 203-6.
150. Malisaukas M., Zamontin V., Jass J., Noppe W., Dobson C.M., and M.-R.L. A. (2003) Amyloid Protofilaments from the Calcium-Binding Protein Equine Lysozyme: Formation of Ring and Linear Structures Depends on pH and Metal Ion Concentration. *Journal of Molecular Biology*, **330**: 879-90.

151. Fisher T.E., Oberhauser A.F., Carrion-Vasquez M., Marszalek P.E., and Fernandez J.M. (1999) The Study of Protein Mechanics with the Atomic Force Microscope. *Trends in Biochemical Sciences*, **4**: 379-84.
152. Kis A., Kasas S., Babic B., Kulik A.J., Benoit W., Briggs G.A.D., Schonenberger C., Catsicas S., and Forro L. (2002) Nanomechanics of Microtubules. *Physical Review Letters*, **89**(24): 248101.
153. Smith D.A., Brockwell D.J., Zinober R.C., Blake A.W., Beddard G.S., Olmsted P.D., and Radford S.E. (2003) Unfolding Dynamics of Proteins Under Applied Force. *Philosophical Transactions of the Royal Society A: Mathematical, Physical and Engineering Sciences*, **361**(1805): 713-30.
154. Guo S. and Akhremitchev B.B. (2006) Packing Density and Structural Heterogeneity of Insulin Amyloid Fibrils Measured by AFM Nanoindentation. *Biomacromolecules*, **7**(5): 1630-6.
155. Kellermayer M.S.Z., Grama L., Karsai A., Nagy A., Kahn A., Datki Z.L., and Penke B. (2005) Reversible Mechanical Unzipping of Amyloid Beta-Fibrils. *Journal of Biological Chemistry*, **280**(9): 8464-70.
156. Rief M., Pascual J., Saraste M., and Gaub H.E. (1999) Single Molecule Force Spectroscopy of Spectrin Repeats: Low Unfolding Forces in Helix Bundles. *Journal of Molecular Biology*, **286**: 553-61.
157. Brockwell D.J., Beddard G.S., Paci E., West D.K., Olmsted P.D., Smith D.A., and Radford S.E. (2005) Mechanically Unfolding the Small, Topologically Simple Protein L. *Biophysical Journal*, **89**: 506-19.
158. MacPhee C.E. and Woolfson D.N. (2004) Engineered and Designed Peptide-Based Fibrous Biomaterials. *Current Opinion in Solid State and Materials Science*, **8**: 141-9.
159. Zhang S. (2003) Fabrication of Novel Biomaterials Through Molecular Self-Assembly. *Nature Biotechnology*, **21**(10): 1171-8.

160. Scheibel T., Parthasarathy R., Sawicki G., Lin X.M., Jaeger H., and Lindquist S.L. (2003) Conducting nanowires built by controlled self-assembly of amyloid fibers and selective metal deposition. *Proceedings of the National Academy of Science*, **100**(8): 4527-4532.
161. Serio T.R., Cashikar A.G., Moslehi J.J., Kowal A.S., and Lindquist S.L. (1999) Yeast prion $\psi(+)$ and its determinant, Sup35p. *Methods in Enzymology*, **309**: 649-673.
162. Broglia R.A., Tiana G., Pasquali S., Roman H.E., and V. E. (1998) Folding and Aggregation of Designed Proteins. *Proceedings of the National Academy of Science*, **95**: 12930-33.
163. Hosseinkhani H., Hosseinkhani M., and Kobayashi H. (2006) Design of Tissue-engineered Nanoscaffold Through Self-assembly of Peptide Amphiphile. *Journal of Bioactive and Compatible Polymers*, **21**(4): 277-96.
164. Reches M. and Gazit E. (2006) Designed Aromatic Homo-Dipeptides: Formation of Ordered Nanostructures and Potential Nanotechnological Applications. *Physical Biology*, **3**: S10-9.
165. Zhang S., Holmes T.C., Lockshin C., and Rich A. (1993) Spontaneous Assembly of a Self-Complementary Oligopeptide to Form a Stable Macroscopic Membrane. *Proceedings of the National Academy of Science*, **90**: 3334-8.
166. Kahn S.E., D'Alessio D.A., Schwartz M.W., Fujimoto W.Y., Ensinck J.W., Taborsky G.J. Jr., and Porte D. Jr. (1990) Evidence of Cosecretion of Islet Amyloid Polypeptide and Insulin by Beta-cells. *Diabetes*, **39**: 634-8.
167. Cooper G.J.S., Willis A.C., C. A., Turner R.C., Sim R.B., and Reid K.B.M. (1987) Purification and Characterisation of a Peptide from Amyloid-Rich Pancreases of Type-2 Diabetes Mellitus. *Proceedings of the National Academy of Sciences, USA*, **84**: 8628-32.

168. Kahn S.E., Andrikopoulos S., and V. C.B. (1999) Islet Amyloid: A Long Recognised but Underappreciated Pathological Feature of Type 2 Diabetes. *Diabetes*, **48**: 640-5.
169. Roberts A.N., Leighton B., Todd J.A., Cockburn D., Schofield P.N., Sutton R., Holt S., Boyd Y., Day A.J., Foot E.A., Willis A.C., Reid K.B.M., and Cooper G.J.S. (1989) Molecular and Functional Characterisation of Amylin, a Peptide Associated with Type-2 Diabetes Mellitus. *Proceedings of the National Academy of Science, USA*, **86**: 9662-6.
170. Steiner D.F., Ohagi S., Nagamatsu S., Bell G.I., and Nishi M. (1991) Perspectives in Diabetes: Is Islet Amyloid Polypeptide a Significant Factor in Pathogenesis or Pathophysiology of Diabetes? *Diabetes*, **40**: 305-9.
171. Janson J.J., Soeller W.C., Roche P.C., Nelson R.T., Torchia A.J., Kreutter D.K., and Butler P.C. (1996) Spontaneous Diabetes Mellitus in Transgenic Mice Expressing Human Islet Amyloid Polypeptide. *Proceedings of the National Academy of Science, USA*, **93**(14): 7283-8.
172. Lorenzo A., Razzaboni B., Weir G.C., and Yankner B.A. (1994) Pancreatic Islet Cell Toxicity of Amylin Associated with Type-2 Diabetes Mellitus. *Nature*, **368**: 756-60.
173. Charge S.B.P., de Koning E.J.P., and Clark A. (1995) Effect of pH and Insulin on Fibrillogenesis of Islet Amyloid Polypeptide *in vitro*. *Biochemistry*, **34**: 14588-93.
174. Mazor Y., Gilead S., Benhar I., and G. E. (2002) Identification and Characterisation of a Novel Molecular-Recognition and Self-Assembly Domain Within the Islet Amyloid Polypeptide. *Journal of Molecular Biology*, **322**: 1013-24.
175. Nilsson M.R. and Raleigh D.P. (1999) Analysis of Amylin Cleavage Products Provides New Insights into the Amyloidogenic Region of Human Amylin. *Journal of Molecular Biology*, **294**: 1375-1385.

-
176. Porat Y., Stepensky A., Ding F. X., Naider F., and Gazit E. (2003) Completely Different Amyloidogenic Potential of Nearly Identical Peptide Fragments. *Biopolymers*, **69**: 161-4.
177. Stolz M., Stoffler D., Aebi U., and Goldsbury C. (2000) Monitoring Biomolecular Interactions by Time-Lapse Atomic Force Microscopy. *Journal of Structural Biology*, **131**: 171-80.
178. Ashburn T.T.M., Auger M., and Lansbury Jr P.T. (1992) The Structural Basis of Pancreatic Amyloid Formation- Isotope Edited Spectroscopy in the Solid State. *Journal of American Chemical Society*, **114**: 790-1.
179. Abedini A. and Raleigh D.P. (2006) Destabilization of Human IAPP Amyloid Fibrils by Proline Mutations Outside of the Putative Amyloidogenic Domain: Is there a Critical Amyloidogenic Domain in Human IAPP? *Journal of Molecular Biology*, **355**: 274-81.
180. Higham C.E., Jaikaran E.T.A.S., Fraser P.E., Gross M., and Clark A. (2000) Preparation of Synthetic Human Islet Amyloid Polypeptide (IAPP) in a Stable Conformation to Enable Study of Conversion to Amyloid-like Fibrils. *FEBS Letters*, **470**: 55-60.
181. Kaye R., Bernhagen J., Greenfield N., Sweimeh K., Brunner H., Voelter W., and Kapurniotu A. (1999) Conformational Transitions of Islet Amyloid Polypeptide (IAPP) in Amyloid Formation *in vitro*. *Journal of Molecular Biology*, **287**: 781-96.
182. Rhoades E., Agarwal J., and Gafni A. (2000) Aggregation of an Amyloidogenic Fragment of Human Islet Amyloid Polypeptide. *Biochimica et Biophysica Acta*, **1476**: 230-8.
183. Muller D.J., Amrein M., and Engel A. (1997) Adsorption of Biological Molecules to a Solid Support for Scanning Probe Microscopy. *Journal of Structural Biology*, **119**: 172-88.

-
184. Gosal W.S., Myers S.L., Radford S.E., and Thomson N.H. (2006) Amyloid Under the Atomic Force Microscope. *Protein and Peptide Letters*, **13**: 261-70.
185. Nilsson M.R., Nguyen L.L., and Raleigh D.P. (2001) Synthesis and Purification of Amyloidogenic Peptides. *Analytical Biochemistry*, **288**: 76-82.
186. Chan W.C. and White P.D., *Fmoc Solid Phase Peptide Synthesis: A Practical Approach*, ed. C. White. 2000: Oxford University Press.
187. Garcia R. and Perez R. (2002) Dynamic Atomic Force Microscopy Methods. *Surface Science Reports*, **47**: 197-301.
188. Pashley R.M. (1981) DLVO and Hydration Forces between Mica Surfaces in Li⁺, Na⁺, K⁺ and Cs⁺ Electrolyte Solutions: A Correlation of Double-Layer and Hydration Forces with Surface Cation Exchange Properties. *Journal of Colloid and Interface Science*, **83**(2): 531-545.
189. Pashley R.M. and Israelachvili J.N. (1984) DLVO and Hydration Forces Between Mica Surfaces in Mg²⁺, Ca²⁺, Sr²⁺ and Ba²⁺ Chloride Solutions. *Journal of Colloid and Interface Science*, **97**(2): 446-55.
190. Zanuy D. and N. R. (2003) The Sequence Dependence of Fiber Organisation. A Comparative Molecular Dynamics Study of the Islet Amyloid Polypeptide Segments 22-27 and 22-29. *Journal of Molecular Biology*, **329**: 565-884.
191. Eakin C.M., Attenello F.J., Morgan C.J., and Miranker A.D. (2004) Oligomeric Assembly of Native-like Precursors Precedes Amyloid Formation by β -2 Microglobulin. *Biochemistry*, **43**: 7808-15.
192. Uversky V.N., Li J., and Fink A.L. (2001) Metal-triggered Structural Transformations, Aggregation, and Fibrillation of Human α -Synuclein. *Journal of Biological Chemistry*, **276**(47): 44284-96.

-
193. Krebs M.R.H., Bromley E.H.C., Rogers S.S., and Donald A.M. (2005) The Mechanism of Amyloid Spherulite Formation by Bovine Insulin. *Biophysical Journal*, **88**: 2013-21.
194. Lee K-B., Park S-J., Mirkin C.A., Smith J.C., and Mrksich M. (2002) Protein Nanoarrays Generated By Dip-Pen Nanolithography. *Science*, **295**: 1702-5.
195. Zhang S., Yanc L., Altmana M., Lässlea M., Nugenta H., Frankele F., Lauffenburgera D.A., Whitesidesc G.M., and Rich A. (1999) Biological surface engineering: a simple system for cell pattern formation. *Biomaterials*, **20**(13): 1213-20.
196. Liu G-Y. and Amro N.A. (2002) Positioning Protein Molecules on Surfaces: A Nanoengineering Approach to Supramolecular Chemistry. *Proceedings of the National Academy of Science*, **99**(8): 5165-70.
197. McMasters M.J., Hammer R.P., and McCarley R.L. (2005) Surface-Induced Aggregation of Beta Amyloid Peptide by Omega-Substituted Alkanethiol Monolayers Supported on Gold. *Langmuir*, **21**(10): 4464-70.
198. Patel N., Davies M. C., Hartshorne M., Heaton R. J., Roberts C. J., Tendler S. J. B., and Williams P. M. (1997) Immobilization of Protein Molecules onto Homogeneous and Mixed Carboxylate-Terminated Self-Assembled Monolayers. *Langmuir*, **13**: 6485-90.
199. Santoso S., Hwang W., Hartman H., and Zhang S. (2002) Self-assembly of Surfactant-like Peptides with Variable Glycine Tails to Form Nanotubes and Nanovesicles. *Nano Letters*, **2**: 687-91.
200. Smith A.M., Banwell E.F., Edwards W.R., Pandya M.J., and Woolfson D.N. (2006) Engineering Increased Stability into Self-Assembled Protein Fibers. *Advanced Functional Materials*, **16**(8): 1022 - 1030.
201. *The Chemistry of the Azido Group*, ed. Patai S. 1971: Interscience.

202. *The Chemistry of the C-C Triple Bond. Part I*, ed. Patai S. 1978: Interscience.
203. Huisgen R., *1,3-Dipolar Cycloaddition Chemistry-Introduction, Survey, Mechanism.*, ed. Padwa A. Vol. 1. 1984, New York: Wiley-Interscience. 1-176.
204. Rostovtsev V.V., Green L.G., Fokin V.V., and Sharpless K.B. (2002) A Stepwise Huisgen Cycloaddition Process: Copper (I)-Catalysed Regioselective "Ligation" of Azides and Terminal Alkynes. *Angewandte Chemie International Edition*, **41**(14): 2596-99.
205. Bock V.D., Miemstra H., and van Maarseveen J.H. (2006) Cu^I-Catalyzed Alkyne-Azide "Click" Cycloadditions from a Mechanistic and Synthetic Perspective. *European Journal of Organic Chemistry*, **2006**(1): 51-68.
206. Rodionov V.O., Fokin V.V., and Finn M.G. (2005) Mechanism of the Ligand-Free Cu(I)-Catalyzed Azide-Alkyne Cycloaddition Reaction. *Angewandte Chemie International Edition*, **44**(15): 2210-5.
207. Gothelf K.V. and Jorgensen K.A. (1998) Asymmetric 1,3-Dipolar Cycloaddition Reactions. *Chemical Review*, **98**: 863-909.
208. Huisgen R. (1963) 1,3-Dipolar Cycloadditions Past and Future. *Angewandte Chemie International Edition*, **2**(10): 565-98.
209. Gilchrist T.L., *Heterocyclic Chemistry*. 3rd ed. 1992: Longman.
210. Link A.J. and Tirrell D.A. (2003) Cell Surface of *Escherichia coli* via Copper(I)-Catalysed [3+2] Cycloaddition. *Journal of American Chemical Society*, **125**: 11164-65.
211. Wang Q., Chan T.R., Hilgraf R., Fokin V.V., Sharpless K.B., and Finn M.G. (2003) Bioconjugation by Copper (I)-Catalysed Azide-Alkyne [3+2] Cycloaddition. *Journal of American Chemical Society*, **125**: 3192-3.
212. Lewis W.G., Magallon F.G., Fokin V.V., and Finn M.G. (2004) Discovery and Characterisation of Catalysts for Azide-Alkyne Cycloaddition by

- Fluorescence Quenching. *Journal of American Chemical Society*, **126**(30): 9152-3.
213. Speers A.E., Adam G.C., and Cravatt B.F. (2003) Activity-Based Protein Profiling *In Vivo* Using a Copper(I)-Catalysed Azide-Alkyne [3 + 2] Cycloaddition. *Journal of American Chemical Society*, **125**: 4686-87.
214. Franke R., Doll C., and Eichler J. (2005) Peptide Ligation Through Click Chemistry for the Generation of Assembled and Scaffolded Peptides. *Tetrahedron Letters*, **46**: 4479-82.
215. Dyke J.M., Groves A.P., Morris A., Ogden J.S., Dias A.A., Oliveira A.M.S., Costa M.L., Barros M.T., Cabral M.H., and Moutinho A.M.C. (1997) Study of the Thermal Decomposition of 2-Azidoacetic Acid by Photoelectron and Matrix Isolation Infrared Spectroscopy. *Journal of American Chemical Society*, **119**(29): 6883 - 6887.
216. Deiters A., Cropp T.A., Mukherji M., Chin J.W., Anderson C., and Schultz P.G. (2003) Adding Amino Acids with Novel Reactivity to the Genetic Code of *Saccharomyces Cerevisiae*. *Journal of American Chemical Society*, **125**: 11782-3.
217. Sunde M. and Blake C.C.F. (1998) From the Globular to the Fibrous State: Protein Structure and Structural Conversion in Amyloid Formation. *Quarterly Reviews of Biophysics*, **31**(1): 1-39.
218. Tornøe C.W., Christensen C., and Meldal M. (2002) Peptidotriazoles on Solid Phase: [1,2,3]-Triazoles by Regiospecific Copper(I)-Catalysed 1,3-Dipolar Cycloadditions of Terminal Alkynes to Azides. *Journal of Organic Chemistry*, **67**: 3057-64.
219. Wamhoff H., *1,2,3-Triazoles and their Benzo Derivatives*, in *Comprehensive Heterocyclic Chemistry*, Katritzky A.R., Editor. 1984, Pergamon Press. p. 669-732.

-
220. Kol N., Adler-Abramovich L., Barlam D., Shneck R.Z., Gazit R., and Rousso I. (2005) Self-Assembled Peptide Nanotubes Are Uniquely Rigid Bioinspired Supramolecular Structures. *Nano Letters*, **5**(7): 1343 -1346.
221. Song Y., Challa S.R., Medforth C.J., Qiu Y., Watt R.K., Pena D., Miller J.E., van Swol F., and Shelnutt J.A. (2004) Synthesis of Peptide-Nanotube Platinum-Nanoparticle Composites. *Chemical Communications*, **9**: 1044-45.
222. de Pablo P.J., Schaap I.A.T., MacKintosh F.C., and Schmidt C.F. (2003) Deformation and Collapse of Microtubules on the Nanometer Scale. *Physical Review Letters*, **91**: 98101-4.
223. Yemini M., Reches M., Gazit E., and Rishpon J. (2005) Peptide Nanotubes Modified Electrodes for Enzyme-Biosensors Applications. *Analytical Chemistry*, **77**: 5155-9.
224. Yemini M., Reches M., Rishpon J., and Gazit E. (2005) Novel Electrochemical Biosensing Platform Using Self-Assembled Peptide Nanotubes. *Nano Letters*, **5**(1): 183-6.
225. Mahler A., Reches M., Rechter M., Cohen S., and Gazit E. (2006) Rigid, Self-Assembled Hydrogel Composed of a Modified Aromatic Dipeptide. *Advanced Materials*, **18**(11): 1365-70.
226. Holmes T.C., de Lacalle S., Su X., Liu G., Rich A., and Zhang S. (2000) Extensive Neurite Outgrowth and Active Synapse Formation on Self-Assembling Peptide Scaffolds. *Proceedings of the National Academy of Science*, **97**(12): 6728-33.
227. Langer R. and Vacanti J.P. (1993) Tissue Engineering. *Science*, **260**(5110): 920-6.
228. Silva G. A., Czeisler C., Niece K. L., Beniash E., Harrington D.A., Kessler J.A., and Stupp S.I. (2004) Selective Differentiation of Neural Progenitor Cells by High-Epitope Density Nanofibers. *Science*, **303**: 1352-1355.

-
229. Reches M. and Gazit E. (2004) Formation of Closed-Cage Nanostructures by Self-Assembly of Aromatic Dipeptides. *Nano Letters*, **4**(4): 581-85.
230. Kannan N. and Vishveshwara S. (2000) Aromatic Clusters: A Determinant of Thermal Stability of Thermophilic Proteins. *Protein Engineering*, **13**(11): 753-61.
231. Astier J.P., Veesler S., and Boistelle R. (1998) Protein Crystals Orientation in a Magnetic Field. *Acta Crystallographica Section D*, **54**: 703-6.
232. Bras W., Diakun G.P., Diaz J.F., Maret G., Kramer H., Bordas J., and Medrano F.J. (1998) The Susceptibility of Pure Tubulin to High Magnetic Fields: A Magnetic Birefringence and X-Ray Fiber Diffraction Study. *Biophysical Journal*, **74**(3): 1509-21.
233. Sakurazawa S., Kubota T., and Ataka M. (1999) Orientation of Protein Crystal Grown in a Magnetic Field. *Journal of Crystal Growth*, **196**: 325-31.
234. Wakayama N.I. (2003) Effects of a Strong Magnetic Field on Protein Crystal Growth. *Crystal Growth and Design*, **3**(1): 17-24.
235. Chen Z., Krause G., and Reif B. (2005) Structure and Orientation of Peptide Inhibitors Bound to Beta-amyloid Fibrils. *Journal of Molecular Biology*, **354**(4): 760-76.
236. Glucksman M.J., Hay R.D., and Makowski L. (1986) X-ray Diffraction from Magnetically Orientated Solutions of Macromolecular Assemblies. *Science*, **231**: 1273-5.
237. Inouye H., Fraser P.E., and Kirschner D.A. (1993) Structure of Beta-Crystallite Assemblies Formed by Alzheimer Beta-Amyloid Protein Analogues: Analysis by X-Ray Diffraction. *Biophysical Journal*, **64**: 502.
238. Inouye H. and Kirschner D.A. (1997) X-Ray Diffraction Analysis of Scrapie Prion: Intermediate and Folded Structures in a Peptide Containing

- Two Putative Alpha-Helices. *Journal of Molecular Biology*, **268**(2): 375-89.
239. Serpell L.C., Blake C.C., and Fraser P.E. (2000) Molecular Structure of a Fibrillar Alzheimer's A-Beta Fragment. *Biochemistry*, **39**(43): 13269-75.
240. Sikorski P., Atkins E.D.T., and Serpell L.C. (2003) Structure and Texture of Fibrous Crystals Formed by Alzheimer's A β (11–25) Peptide Fragment. *Structure*, **11**: 915-26.
241. Yamagishi A., Takeuchi T., Higashi T., and Date M. (1989) Diamagnetic Orientation of Polymerised Molecules Under High Magnetic Field. *Journal of the Physical Society of Japan*, **58**(7): 2280-3.
242. Pauling L. (1979) Diamagnetic Anisotropy of the Peptide Group. *Proceedings of the National Academy of Science*, **76**(5): 2293-4.
243. Worcester D.L. (1978) Structural Origins of Diamagnetic Anisotropy in Proteins. *Proceedings of the National Academy of Science*, **75**(11): 5475-7.
244. Pauling L. (1936) The Diamagnetic Anisotropy of Aromatic Molecules. *Journal of Chemical Physics*, **4**: 673.
245. Adler-Abramovich L., Reches M., Sedman V.L., Allen S., Tendler S. J. B., and Gazit E. (2006) Thermal and Chemical Stability of Diphenylalanine Peptide Nanotubes: Implications for Nanotechnological Applications. *Langmuir*, **22**(3): 1313-20.
246. Sedman V.L., Adler-Abramovich L., Allen S., Gazit E., and Tendler S.J.B. (2006) Direct Observation of the Release of Phenylalanine from Diphenylalanine Nanotubes. *Journal of American Chemical Society*, **128**(21): 6903-8.
247. Braun R.M., Blenkinsopp P., Mullock S.J., Corlett C., Willey K.F., Vickerman J.C., and Winograd N. (1998) Performance Characteristics of a Chemical Imaging Time-of-Flight Mass Spectrometer. *Rapid Communications in Mass Spectrometry*, **12**(18): 1246-52.

248. *The Merck Index*, ed. Budavari S. Vol. 11th Edition, Centennial Edition. 1989, New Jersey, USA: Merck & Co. Inc.

Appendix A

Animations

The animations on the enclosed CD contain time-lapse sequence of images of amylin (20-29) fibrillisation in 100 mM sodium acetate (pH5.5). The images presented are also displayed in figure 2.19.

To view animation in full, copy and paste file to Desktop and open.

Appendix B

TOF SIMS spectra for poly(dimethylsiloxane)

The positive spectra for poly(dimethylsiloxane) (PDMS) rubber. Spectra from The Static SIMS Library (SurfaceSpectra Ltd).

